Engineering Library

MAR 24 49

Journal of Research

of the

National Bureau of Standards

FEBRUARY 1949

VOLUME 42 NUMBER 2

PERIODICALS OF THE NATIONAL BUREAU OF STANDARDS

Journal of Research

The National Bureau of Standards is the principal agency of the Federal Government for fundamental research in physics, chemistry, and engineering. It has the custody of the national standards of physical measurement in terms of which all working standards in research laboratories and industry are calibrated, and carries on necessary research leading to improvement in such standards and methods of measurement. It also has a general responsibility for basic research in physics, chemistry, and engineering, and for developments of improved methods for testing materials and equipment. It determines physical constants and properties of materials, tests and calibrates standard measuring apparatus and reference standards, and studies technical processes. The results of the Bureau's research and investigations are published in the JOURNAL OF RESEARCH.

Research Papers

Reprints of individual articles appearing in the JOURNAL OF RESEARCH. They are made available to serve the needs of research workers, technical groups, and others for the separate papers relating to the special subjects in which they are interested.

Technical News Bulletin

Contains short but complete summaries of research, development, and testing in progress at the Bureau, accounts of the Bureau's national and international activities, scientific and technical announcements of new plans and programs, and a list of publications by members of the staff. It is a prompt and reliable source of official information of value to those who desire to keep in touch with the general activities of the Bureau.

Basic Radio Propagation Predictions

The CRPL–D series, Basic Radio Propagation Predictions, is issued as a monthly publication for those concerned with radio communication in determining the best sky-wave frequencies over any path at any time of day for average conditions for the month of prediction, which is made 3 months in advance. Charts of extraordinary-wave critical frequency for the F2 layer, of maximum usable frequency for a transmission distance of 4,000 km, and of percentage of time occurrence for transmission by sporadic E in excess of 15 Mc, for a distance of 2,000 km, are included.

ANNUAL SUBSCRIPTION Send order, with remittance, to Superintendent of Documents, U. S. Government Printing Office, Washington 25, D. C.	United States, Canada, Cuba, Mexico, Newfoundland, Republic of Panama	Other countries
JOURNAL OF RESEARCH of the National Bureau of Standards:		
12 monthly issues (2 volumes), paper covers	$4.50	$5.50
Bound volume (½ year, 1 volume), blue buckram	3.00	3.50
RESEARCH PAPERS	(*)	(*)
TECHNICAL NEWS BULLETIN, 12 monthly issues	1.00	1.35
BASIC RADIO PROPAGATION PREDICTIONS, 12 monthly issues	1.00	1.25

*The prices of the separate Research Papers appearing in this JOURNAL are given in the Contents. If 100 or more copies of any separate are ordered, a discount of 25 percent is allowed. Those who desire copies of separate Research Papers should send their orders and remittance without delay to the Superintendent of Documents, U. S. Government Printing Office, Washington 25, D. C. This will aid him to determine the number of copies to be printed for sale. Research Papers are not printed from electrotypes and usually no more reprints can be had when the first and only printing is exhausted.

The printing of this publication has been approved by the Director of the Bureau of the Budget, April 23, 1947.

U. S. DEPARTMENT OF COMMERCE
Charles Sawyer, Secretary
NATIONAL BUREAU OF STANDARDS
E. U. Condon, Director

FEBRUARY 1949
VOLUME • 42
NUMBER 2

JOURNAL OF RESEARCH

of the

NATIONAL BUREAU OF STANDARDS

Contents

RP		Page
1953.	A spiral contractometer for measuring stress in electrodeposits. Abner Brenner and Seymour Senderoff. (Price 10 cents)	89
1954.	Calculation of stress in electrodeposits from the curvature of a plated strip. Abner Brenner and Seymour Senderoff. (Price 15 cents)	105
1955.	Laboratory wear tests with automotive gear lubricants. Samuel A. McKee, James F. Swindells, Hobart S. White, and Wayne Mountjoy. (Price 10 cents)	125
1956.	The system BaO-B_2O_3. Ernest M. Levin and Howard F. McMurdie. (Price 10 cents)	131
1957.	Separation of the 177° to 200° C fraction of petroleum and the isolation of normal undecane. Morton B. Epstein, Beveridge J. Mair, Charles B. Willingham, and Frederick D. Rossini. (Price 10 cents)	139
1958.	Winter measurements of ozone over the Organ Mountains, New Mexico. Ralph Stair. (Price 10 cents)	145
1959.	Effect of convection currents on the distribution of striae in pots of optical glass. Conrad A. Faick, Arthur E. Williams, and Gerald F. Rynders. (Price 15 cents)	153
1960.	Expansion effects of annealing borosilicate thermometer glasses. Arthur Q. Tool and James B. Saunders. (Price 10 cents)	171
1961.	Zeeman effect and g-values for neutral nitrogen and oxygen. Carl C. Kiess and George Shortley. (Price 15 cents)	183

For sale by the Superintendent of Documents, U. S. Government Printing Office, Washington 25, D. C. - Price 60 cents
$4.50 per year on subscription

UNITED STATES GOVERNMENT PRINTING OFFICE, WASHINGTON : 1949

U. S. Department of Commerce
National Bureau of Standards

Research Paper RP1953
Volume 42, February 1949

Part of the Journal of Research of the National Bureau of Standards

A Spiral Contractometer for Measuring Stress in Electrodeposits

By Abner Brenner and Seymour Senderoff

An improved instrument for the measurement of stress in electrodeposits is described. Its operation entails the electrodeposition of a metal coating on the outside of a metal helix and the measurement of the change in radius of curvature of the helix induced by the stress in the electrodeposit. The change in radius of curvature is read from a dial on the instrument. Formulas for the calculation of stress are given, and sources of error and correction factors for them discussed. Data are presented to demonstrate the reproducibility of measurements and the validity of the results. The variation of stress with plate thickness has been investigated and shown to be related to the variation in grain size of the deposit. The advantages of the instrument and fields for its application are indicated.

I. Introduction

It has been known for many years that frequently there is stress, either tensile or compressive, in electrodeposited metal coatings. This was discovered as early as 1877 by Mills [1] [1], who called it "electrostriction." In 1909 Stoney [2] made the first quantitative measurements of stress in electroplates, using as the measuring instrument a straight metal strip, which was insulated on one side. Since then most investigators [3 to 11] in this field have used the same instrument, with certain refinements that will be noted later. The evaluation of stress by X-ray diffraction measurements has been attempted by a number of investigators [8, 12, 13, 14], but these results are difficult to interpret owing, among other factors, to the effect of grain size on X-ray patterns.

The main purpose of this paper is to describe an improved instrument for measuring stress in electrodeposits and to present formulas which may be used to calculate the stress. As there has been some confusion in the literature on the formulas for this calculation, a rigorous mathematical derivation and a discussion of the various formulas to show the correlation among them, and the conditions of applicability of each, are presented in RP1954.

The second purpose of this paper is to demonstrate the effect of certain variables on the stress in electrodeposits.

Many authors have indicated the important effects of stress on the quality of plated articles. Excessively high stress may cause peeling, blistering, or cracking of the deposit and thereby render the base metal more susceptible to corrosion. It may also induce failures by the phenomenon of "stress corrosion."

It is desirable to use stress measurements not only in researches on plating, but also in production control to safeguard the quality of work. An instrument for such a purpose should be rugged, easily operated, self-contained, and comparatively inexpensive. The Stoney instrument and its modifications have proved valuable as research tools, but they do not adequately meet these other criteria.

Stoney [2], Phillips and Clifton [10], and Soderberg and Graham [11], placed a straight metal strip in a suitable fixture and plated the strip on one side only. Stoney permitted the strip to bend continuously during plating, whereas in the other two studies the strip was held rigid during plating and was allowed to bend some time after plating was stopped. In all three cases the radius of curva-

[1] Figures in brackets indicate the literature references at the end of this paper.

ture of the bent strip was determined by measuring the camber (sagitta of the arc) of the bent strip. To do this, some type of special gage, such as was recommended by Phillips, or a microscope with a calibrated vernier focussing adjustment, is required.

Barklie and Davies [5], Marie and Thon [6], Jacquet [7], Hume-Rothery and Wyllie [8], and Martin [9], set the strip in a suitable fixture, allowed it to bend during plating, and observed and measured the displacement of one end of the strip through a microscope with a calibrated eyepiece. By this procedure, the displacement actually measured was four times that measured by Stoney's method for strips with equal radii of curvature.

Kohlschutter and Vuilleumier [3, 4], attached a thin glass pointer to the bottom of the strip at an acute angle, so that it emerged from the solution and passed across a scale when the strip bent during plating. This apparatus is fragile; it is difficult to attach the glass to the metal; and in addition, the sensitivity of the instrument is reduced by the weight of the glass at the end. The scale deflections observed are difficult to convert to absolute values of stress.

It will be noted that the first two methods require special auxiliary gages or calibrated microscopes for measurement and that the measured linear displacements are very small. The Kohlschutter apparatus is fragile, and it is difficult to determine the absolute values of stress from the observations made with it.

The new instrument developed at this Bureau meets to a reasonable degree the criteria for an instrument suitable for both production control and research. We have designated it the "spiral contractometer."

II. Description and Operation of the Spiral Contractometer

The spiral contractometer is based on the use of a helix, instead of a straight strip, for the measurement of stress. A flat strip is wound to form a helix and is plated on one side only. The stress in the deposit causes the helix to wind more tightly or to unwind, depending on whether the stress is compressive or tensile. When the plate is deposited under compression and relieves its stress by expanding, it exhibits "compressive stress." When the plate is deposited under tension and relieves its stress by contracting, it exhibits "tensile stress." The change in the radius of curvature of the helix is a measure of the stress in the plate. The change in radius of curvature is actually measured by the angular displacement of one end of the helix while the other end is held rigid. This angular displacement may be magnified conveniently by the use of gears and may then be read directly on the dial of the instrument. Figure 1, A, shows the assembled contractometer. Figure 1, B, shows the instrument with the helix detached. Figure 2 shows a modified instrument with the dial face vertical instead of horizontal. The parts of the instrument are shown in figure 3.

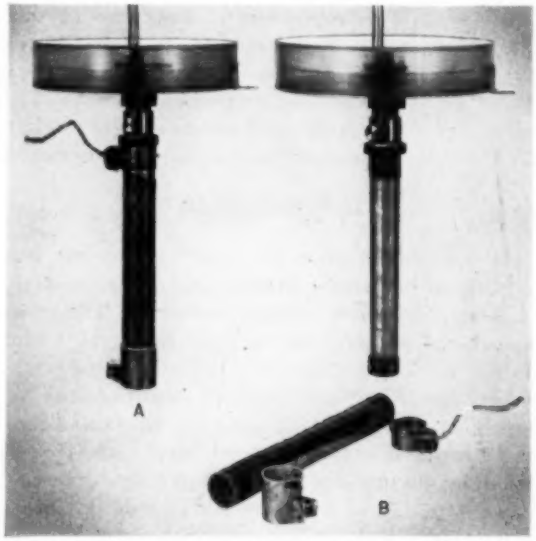

FIGURE 1. *Spiral contractometer.*

A, Contractometer completely assembled for stress determination; B, contractometer with helix removed.

The basic assembly (fig. 3) consists of a stainless steel disk, 7, to the center of which is anchored a housing and bearings, 4, for the pointer gear, 5. The pointer, 2, is rigidly anchored to its gear, which rotates freely with its shaft in the bearings. The entire pointer assembly is counterbalanced with a weight on the other side of the gear. One end of an arm, 3, is attached rigidly to the torque rod, 9. At the other end is a gear segment, 6, which meshes with the pointer gear. The pitch diameter of the gear on the arm is ten times as great as that of the pinion (or pointer gear) and gives tenfold magnification of the angular dis-

FIGURE 2. *Model of contractometer with vertical dial face.*

placement of the torque rod. The top end of the torque rod rotates freely in a small hole in the disk.

The guard tube (B) is slid on over the collar, 8, and anchored with its set screw. The plastic base, 10, is than attached to the torque rod with its countersunk set screw. The helix does not touch the guard tube. To attach it for a run, it is slid over the assembly and than locked in place, on the collar, 11, and the plastic base, 10, by clamps *D* and *E*. These clamps serve not only to hold the helix tightly, but also, by acting as electrical guards, give a very uniform current distribution over the active length of the helix. By loosening the set screw on the guard tube (*B*) the assembly is slid up or down over the collar, 8, until the lever arm, 3, is raised clear of the dial disk, 7, and the gears, 5 and 6, properly mesh. By rotating the guard tube, the pointer may be set at any desired place on the dial. The set screw is then tightened, the plastic cap (*F*) is placed on the instrument, and the entire assembly is suspended in a plating solution by the hanger, 1, so that the solution level is somewhere on the top clamp (*D*). By connecting the positive lead to a suitable anode and the negative lead to the wire on clamp *D*, plating on the helix proceeds. Since the top of the helix is firmly anchored, only the bottom turns during the plating. The rotation is transmitted to the pointer with a tenfold magnification and is read in degrees on the graduations at the edge of the disk.

Between normal operations the instrument need not be completely disassembled except for occasional cleaning. In that case, the disassembling and assembling can be done in less than 5 min. For successive runs, only the helix and clamps need be removed or replaced, leaving the rest of the instrument assembled.

Since the helix is the heart of the instrument, it merits some detailed description. The helix is made by winding a metal strip of uniform width and thickness on a ¾-in. steel rod at a pitch such that there are neither spaces nor overlaps between the coils. The width of the strip is about 0.7 in. (18 mm). The thickness is determined by the rigidity desired for a particular application. The range of 0.01 to 0.03 in. (0.25 to 0.75 mm) has been found most useful for this work. For deposits with very high stresses, thicker strips may be used. When the winding is completed, the ends are anchored to the rod by screws. The helix is then fully annealed in vacuo, in order to relieve the stresses due to cold working and thus prevent uncoiling. After annealing, the rod is mounted in a lathe and the helix is cut off at the desired length. The helix is then stretched lengthwise until the coils are separated from each other by a distance of about 0.02 to 0.04 in. (0.5 to 1.0 mm). The inside rod is then removed and the helix is ready for use.

As there is some effort involved in properly preparing a helix and in measuring and calibrating it, it is fortunate that one helix can be used for many determinations. It was found that by using an 18:8 stainless steel helix for metal deposits that can be stripped with nitric acid, and a copper

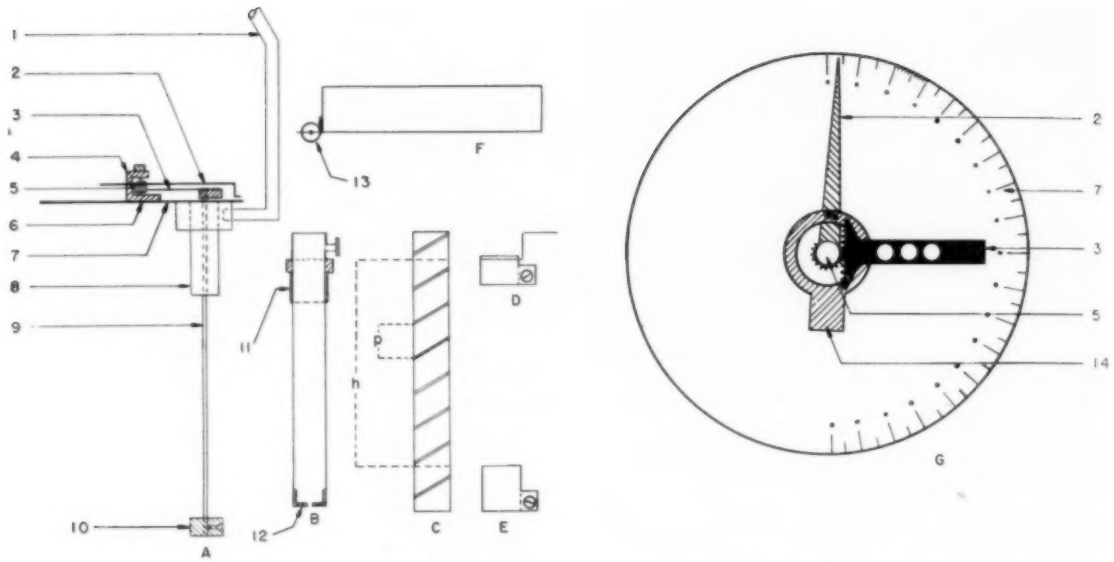

FIGURE 3. *Schematic drawing of contractometer and its parts.*

A, Basic assembly; B, guard tube; C, helix; D, top clamp with soldered wire lead; E, bottom clamp; F, plastic cap with removable calibration assemble; G, top view of dial face. 1, hanger; 2, pointer; 3, lever arm; 4, housing and bearings; 5, gear on pointer; 6, gear segment on lever arm; 7, dial face graduated in degrees; 8, collar; 9, torque rod; 10, plastic base with set screw; 11, plastic collar; 12, plastic bearing; 13, removable pulley for calibration; 14, balancing weight on pointer.

helix for metals that can be stripped with hydrochloric acid, the helices can be reused almost indefinitely without appreciable change in their dimensions, elastic moduli, or deflection constants, provided reasonable precautions in handling and storing are used. When stainless steel helices are used, it is generally necessary to apply a special nickel strike, followed by a cyanide copper strike, to obtain good adherence of the deposit whose stress is being measured.

The steps involved in a stress determination are:

1. Clean the helix and apply a strike plate if desired.
2. Dry and weigh the helix.
3. Stop-off the inside of the helix by dipping a test-tube brush in thinned stop-off lacquer and passing it once through the helix.
4. Wipe the outside of the helix with acetone to remove the excess stop-off lacquer.
5. Dip in hot alkali and in an acid dip (or other suitable preplating dips) and rinse.
6. Mount the helix on the contractometer, set the clamps, adjust the pointer to the desired position, and replace the cap on the dial.
7. Immerse in the plating solution and start the plating.

The helix may be allowed to twist as plating progresses and a record kept of the displacements with time by taking periodic readings; or the pointer may be clamped before the plating starts and released at the end of the run. The clamping of the pointer prevents the helix from twisting until the plating is completed. Successive stress determinations by these two methods gave the same results within the experimental error.

8. At the end of a run, remove the helix, dissolve the lacquer from the inside of the helix with acetone, and clean and dry the helix.
9. Weigh the helix to determine the average thickness of the deposit.
10. Strip the deposit from the helix by suitable means.

The stress is calculated from the observed deflection, the physical constants and dimensions of the helix, and the average thickness of the coating, which is determined from the increase in weight of the helix.

For this calculation the following dimensions of

the helix are measured with an accuracy of a few percent:

1. The outside diameter of the helix.
2. The thickness of the strip.
3. The pitch of the helix.
4. The height of the exposed portion of the helix between the clamps (or the plated portion) with the helix considered as a cylinder.

The first two are measured with a micrometer. The third and fourth quantities are determined by compressing the helix so that the coils just touch each other, and the appropriate distances measured with a centimeter rule. The height is h, and the pitch is p in figure 3, C.

As will be shown later, the calculation is simplified if the deflection constant of the helix, that is, the torque required to cause a deflection of 1 degree is determined. This can be done by attaching a cotton thread to the lever arm near the gear segment, drawing the string through a hole in the side of the plastic cap and over the removable pulley, 13 (fig. 3) on the cap. With a helix clamped in place as described previously, weights are attached to the end of the string and the deflection is read on the dial. It is desirable to load the string with about 10 or 20 g as a zero load and to measure the deflection caused by increasing the load. The string is kept approximately perpendicular to the lever arm by rotating the cap in a plane parallel to the dial. By measuring the distance on the lever arm from the string to the torque rod, and using the known load in grams, a deflection constant that shows the relation of the bending moment to the degrees of deflection may be calculated for the helix.

III. Calculation of Stress

Although on certain projects it may be sufficient to express the stress at any stage by a scale deflection, as some investigators have done, it is preferable to express the results in absolute values. The formulas by which this may be accomplished are based on those of Stoney, with certain modifications to adapt them for use with a helix instead of a straight strip.

The following symbols will be used throughout this section:

S = stress.
S_T = true (or corrected) stress.
E = Young's modulus of basis metal strip.
E_c = Young's modulus of coating.
p = pitch of strip.
t = thickness of basis strip.
d = thickness of deposit.
$\Delta(1/r)$ = change of curvature induced by deposit.
h = height of plated portion of helix.
D = angular deflection of helix in radians.
$\overline{D}$ = angular deflection of dial needle in degrees.
M = bending moment.
K = deflection constant of helix.
C = outside diameter of helix.

The basic formula used in this work is:

$$S=\frac{Et^2}{6d}\times\Delta\left(\frac{1}{r}\right). \tag{1}$$

The change in curvature induced by the deposit (the difference between the initial and final curvature of the helix) is:

$$\Delta\left(\frac{1}{r}\right)=\frac{Dp}{\pi Ch}. \tag{2}$$

Substituting in eq 1 and rearranging terms,

$$S=\frac{Et^2p}{6\pi Ch}\times\frac{D}{d}, \tag{3}$$

with E in pounds per square inch; t, C, h, p, and d in inches; and D in radians; S is in pounds per square inch. E, t, C, h, and p are constants of the helix; d is determined from the weight of deposit; and D from the deflection of the needle on the instrument.

The derivation of this formula entails the assumption that the thickness of the deposit is negligible compared to the thickness of the basis metal strip. When the thickness of the deposit is appreciable, it must be considered for accurate results and this is done in Stoney's second formula:

$$S_T=\frac{E(t^2+td)}{6d}\,\Delta\left(\frac{1}{r}\right). \tag{4}$$

Equation 4 may be written in terms of eq 1 and a correction factor thus:

$$S_T=S\left(1+\frac{d}{t}\right). \tag{5}$$

A final refinement of the formula is required in order to take into account the difference in modulus which may exist between the basis metal and

the deposit. This is done with a fair degree of accuracy (though it is not mathematically exact), by

$$S_T = S\left(1+\frac{E_c}{E}\times\frac{d}{t}\right). \quad (6)$$

One of the important advantages of the spiral contractometer is the fact that it is possible to calibrate it and thus eliminate errors due to differences in the physical properties of the helix from the published values usually associated with the metal from which it is made. The deflection constant of the helix is evaluated by

$$M = K\overline{D} \quad (7)$$

where M=bending moment=weight of applied load $\times$ distance from fulcrum. The stress may be calculated from this deflection constant by

$$S = \frac{2K}{pt}\times\frac{\overline{D}}{d}. \quad (8)$$

If K is in inch-pound per degree, $\overline{D}$ in degrees, p, t, and d in inches, then S is in pounds per square inch. S_T is obtained from S by eq 6, as indicated previously.

From the data obtained in calibrating a helix, its modulus can be calculated by

$$E = \frac{2.16\times10^4 KCh}{p^2t^3}, \quad (9)^2$$

where K is known from the calibration, and p, t, C, and h are measured dimensions of the helix. The use of these formulas in a typical stress determination is demonstrated in the appendix, p. 103.

The detailed discussion and derivation of these formulas appears in RP1954, but a few comments are in order here. The value of stress obtained by using the simpler approximate formulas 3 and 8, can be seen to approach the true stress (S_T) as d/t approaches zero. Even when d/t is as high as 0.1, the values differ by only 10 percent, which may be considered to be the magnitude of the experimental error in a measurement of this type. In the experimental work described in this paper, the largest d/t ratio used was 0.05, and many experiments were made with d/t ratios of 0.03 or less. Best practice requires that d/t be kept as low as practicable because of the departure of the behavior of the helix from the simple flexure theory and the increase in certain other errors as the radius of curvature decreases. When, however, d/t in a particular experiment happens to be large or if higher accuracy is desired, it is simple to apply the correction factor of eq 6 to obtain an exact value for stress when $E_c/E=1$. Even when the moduli of the basis metal and coating differ, the value of S_T obtained from eq 6 will differ from that obtained by the far more complicated exact formula by only a few percent, at most.

Lastly, it should be noted that the formula presented by Soderberg and Graham [11], i. e.,

$$S_T = \frac{E(t+d)^3}{6dt}\times\Delta\left(\frac{1}{r}\right),$$

while slightly different from eq 4, does not actually conflict with it. As shown in RP1954, the slight difference between the two is a result of the different experimental conditions used for measuring stress. In the present case, the strip is allowed to bend during plating, and in their experiment, it was held rigidly during plating. These cases require somewhat different mathematical treatment. The magnitude of the differences between stresses obtained by using the two formulas varies with d/t and is about 10 percent when $d/t=0.05$.

In summary it may be said that for most ordinary applications of the spiral contractometer stress may be simply calculated by using eq 3, or better, by using eq 8. For high accuracy when d/t and E_c/E are high, the value thus obtained may be multiplied by a simple correction factor, as in eq 6, to obtain values of stress differing from the exact value by only a small fraction of the experimental error usually attending a stress determination.

IV. Evaluation of the Instrument

Some of the factors that may affect the precision or accuracy of the instrument were studied. The current distribution over the helix was investigated by determining microscopically the thickness of metal deposited over the length of the helix. Under the most unfavorable conditions, which involved plating on the helix when it was immersed in a large plating tank, the average deviation of the plate thickness on the helix was

[2] This equation applies to an instrument with a gear ratio of 10:1. The general formula is

$$E = \frac{2.16\times10^3 KCh}{p^2t^3}g$$

where g is the gear ratio.

±3 percent from the mean. A stop-off lacquer must be used on the interior of the helix to prevent plating there. If too thick a layer is used it may affect the deflection constant of the helix. With a lacquer coating weighing about 0.2 g/dm², the calibration constant of the helix was changed by about 15 percent. However, a lacquer coating of about 0.05 g/dm ², (about 0.0002 in., or 0.005 mm, thick), had no significant effect on the deflection constant of the helix, and afforded satisfactory protection to the inside. In some experiments, plating on the inside of the helix was prevented by making the guard tube cathodic to the helix, in order that the inner surface of the helix would be anodic. This method works fairly well with acid solutions of copper and nickel, but not with solutions having good throwing power, such as the cyanide copper solution. There is also some uncertainty in determining the actual current on the outside of the helix.

Data presented in table 1 show that within experimental error, the nature of the helix used had no effect on the measurement of stress. Helices of 18:8 stainless steel and of copper, each in several different thicknesses, gave about the same results.

TABLE 1. *Reproducibility of measurements with copper and stainless steel helices of various thicknesses*

Run	Helix	Type	t	d	S	S_T	Correction factor $\left(1+\frac{Ec}{E}\times\frac{d}{t}\right)$
			in.	*(in.×10⁻⁴)*	*lb/in.²×10³*	*lb/in.²×10³*	
1	D	Cu	0.0197	6.58	15.5	16.5	1.06
2	E	Cu	.0224	6.07	15.5	16.3	1.05
3	E	Cu	.0224	6.36	14.5	15.3	1.05
4	F	Cu	.0219	6.16	13.8	14.5	1.05
5	F	Cu	.0219	6.10	17.4	18.3	1.05
6	G	Cu	.0228	5.98	18.1	19.0	1.05
7	G	Cu	.0228	5.98	13.2	14.0	1.05
8	H	Cu	.0315	5.58	14.8	15.4	1.04
9	B	Stainless steel	.0131	6.62	14.7	15.5	1.05
10	B	do	.0131	6.62	14.7	15.5	1.05
11	I	do	.0196	6.20	15.8	16.5	1.04
12	J	do	.0333	6.26	16.5	16.9	1.02
Average (all runs)					15.4±7.5%	16.2±7%	
Average Cu helices only (8 determinations)					15.388±8%	16.123±8.5%	
Average stainless steel helices only (4 determinations)					15.425±5%	16.100±3%	
Percentage difference between averages for steel and Cu helices					0.2%	0.2%	

Since the coating on a helix must be stripped after each run, the constancy of the calibration must be known. Stainless steel helix *B*, 0.013 in. (0.33 mm) thick was used during a period of 3 months for about 15 stress determinations. It was calibrated at various times, with the results shown in table 2. The constancy of the deflection constant, *K*, is clearly demonstrated, as well as the reproducibility of the calibration.

A source of error exists in the determination of the deflection constant of the helix by the direct loading method, if the helix is made from a thick metal strip. It was found that considerable torsion of the torque rod then occurred if large moments were applied to the lever arm (3 in fig. 3). On the other hand, no compensating error is involved in measuring the stress in a coating, since only a negligible amount of torsion in the torque rod is required to turn the pointer. In a calibration, one can check whether or not the torsion in the torque rod is significant by keeping

TABLE 2. *Constancy of the calibration constant of stainless steel helices*

Elapsed time	k	K
Days	*deg/g-cm*	*in.-lb/deg*
0	2.13	4.06×10^{-4}
25	2.15	4.03×10^{-4}
40	2.14	4.05×10^{-4}
91	2.12	4.10×10^{-4}
Average (helix *B*)	2.14±0.6%	4.06×10^{-4}±0.6%

the bottom of the helix at rest when the turning moment is applied to the lever arm.

The reproducibility of the instrument was determined by making 12 stress determinations in a purified Watts nickel solution of the following composition:

	N	*g/liter*	*oz/gal*
$NiSO_4.7H_2O$	1.8	240	32
$NiCl_2.6H_2O$	0.38	45	6
H_3BO_3	.5 (*M*)	30	4
pH = 3.0 to 3.5			

The determinations were made at 55°C and 2.5 amp/dm^2 (23 amp/ft^2), with approximately 30-min runs, each giving approximately 0.0006 in. (0.015 mm) of nickel deposit. Five copper helices and three stainless steel helices of varying thicknesses were used for the 12 runs. The copper helices were electrocleaned as cathode, dipped in a 20-percent HCl solution, rinsed and dried. After weighing them and stopping off the inside as described previously, they were wiped with acetone, dipped in the hot alkali cleaner, then in a 20-percent HCl solution, and rinsed. They were then mounted on the instrument and plated. The stainless steel helices were electrocleaned anodically, dipped in 20-percent HCl, struck with nickel for 30 sec at 6 v in a Woods nickel solution, rinsed, and struck with copper for 10 sec at 4 v in a cyanide copper solution. They were then rinsed, dried, and treated in the same way as the copper helices.

Table 2 shows the results of these runs. It can be seen that the average deviation from the mean in the series is less than ± 8 percent, which may be considered satisfactory for a measurement of this type. A large part of these variations probably lies in the plating procedures rather than in the instrument. The average stress determined with the stainless steel helices differs by 1 percent from that obtained with the copper helices, which is well within the experimental error. The average deviation from the mean is less with the steel helices than with the copper. This may be caused by the greater dimensional stability of the steel helices and their smaller tendency to be permanently deformed on handling. For highest precision it seems advisable, therefore, to use stainless steel helices whenever applicable, that is, with any metal deposits that can be stripped with HNO_3.

The validity of the results obtained with the instrument, that is, the extent to which the instrument measures stress and not some extraneous factors, cannot be directly determined, since there is no absolute method for measuring stress in deposits. The validity of the determinations of stress is confirmed by comparison with results obtained by other methods of measurement in baths of various types.

An indication of the validity of the calculations of stress was obtained by comparing the value of Young's modulus for a helix, as calculated from the deflection constant, with the known value. From the average value of K for the stainless steel helix described in table 2, and eq 9, the modulus is calculated to be 29.2×10^6 lb/in^2.[3] This compares with 29×10^6 lb/in.^{2} for E of 18:8 stainless steel as given in the literature [15]. A similar calculation of E for the copper helices D—G in table 1 gives an average value of 15.3×10^6 lb/in.^{2} Timoshenko [16] lists 16×10^6 as E for cold-rolled copper and Soderberg and Graham [11] report the value as 15.6×10^6.

It should be noted here that helices whose $k<$ approximately 0.75°/g-cm give low values for E. This is explained by the fact that a portion of the bending moment applied in calibration is absorbed by the twisting of the torque rod of the instrument as indicated above. With the stiffer helices, such as H, I, and J, the portion absorbed by the torque rod becomes appreciable compared to the twisting of the helix, whereas with the weaker helices this portion is negligible. It is interesting to note, however, that a stress determination taken with a stiffer helix gives results equivalent to those obtained with the thinner helices, if the deflection observed with the stiff helices is used in eq 3 with the known modulus rather than in eq 8 with the calibration constant.

If it is necessary to consistently use stiff helices in some application, it would be desirable to use a thicker torque rod in order that the helices with lower values of k could be calibrated.

In comparing values for stress in electrodeposits, the thickness of the deposit must be specified. The variation of stress with thickness will be considered later in some detail. Typical values for stress in nickel deposits plated from a carefully purified and electrolyzed Watts nickel

[3] This calculation is shown in detail in the appendix.

solution of composition specified above, at 55° C, 2.5 amp/dm² and pH 3.0 to 3.5 are shown in table 3.

TABLE 3. *Best values of stress in nickel deposited from Watts bath*

Plating conditions: Watts nickel, temperature=55° C, pH=3.0 to 3.5, current density=2.5 amp/dm².

Stress		Thickness
S	S_T	
lb/in.²	*lb/in.²*	*Inch*
15,000	16,000	0.0006
12,000	13,000	.001
9,000	11,000	.002

In the literature the published values for stress in nickel coatings from a Watts nickel solution vary from 13,000 to 25,000 lb/in.² [17, 5, 10, 11]. As in most cases the thickness of plate, conditions of plating, or other pertinent data are not given, and as the stress varies with these factors and also with the purity of the plating solution, comparisons of table 3 with the published values are not of much value.

As all previous data on the stress in coatings, as well as those obtained with the helix, are based on the deformation of a metal strip, an attempt was made to measure stress by different procedures. A direct measurement of the contraction per unit length was made on a nickel shell deposited under stress and then freed of its base material. Brass tubes 6 in. (15 cm) long, 5/16 in. (0.5 cm) in diameter, and 0.028 in. (0.07 cm) in wall thickness were plated with 0.002 in. (0.05 mm) of nickel from a Watts nickel solution. Shallow scratches were cut at intervals along the length of the tubes with a fine diamond tipped tool. The distances between these scratches were measured in a travelling microscope with an accuracy of better than ±0.0001 in. (0.002 mm). The brass was then removed by immersing the tube in a chromic and sulfuric acid mixture and bubbling air up through the tube. When the brass had completely dissolved, the distances between the scratches on the nickel tube were again measured. An average contraction in length of 3.0×10^{-4} in./in. was observed. By applying Hooke's Law and a small correction for circumferential and relieved stresses, a value of 10,300 lb/in.² was obtained. Since the accuracy of measurement was about ±0.0001 in. and the contraction in 4 in. (10 cm) (the greatest length measured) was about 0.0012 in. (0.03 mm), the accuracy of the measurement may be considered as approximately ±10 percent. As the accuracy of the measurements with the contractometer is also about ±10 percent, the agreement between the stress indicated for a 0.002-in. (0.05-mm) plate in table 3, and this value may be considered fair.

Another instance of agreement with an independent method of measurement was secured in the following manner. A shell of chromium, approximately 0.005 in. thick (0.13 mm), was plated on a copper tube at 85° C, 80 amp/dm². On dissolving the copper, the chromium developed a single longitudinal crack, having the full length of, and extending completely through the wall of, the shell. The amount by which the shell opened up at the crack is a measure of the internal stress in the chromium. The opening and the dimensions of the shell were measured with a microscope, and the average stress was calculated by the formulas given by Rosenthal and Mazia [18]. The average stress was found to be 53,200 lb/in². Chromium was plated under similar conditions on the spiral contractometer, and a value of 60,000 lb/in². was obtained. Again, the agreement may be considered satisfactory.

To more fully establish the validity of the determinations of stress made with the spiral contractometer, they were compared with the results of measurements made under similar conditions by the commonly accepted method of the bending of a flat strip. Simultaneous stress determinations were made with the spiral contractometer and a strip contractometer according to the method of Barklie and Davies [5]. Both instruments were used in the same solution at the same time. The results tabulated in table 4 show agreement of the two methods within 3 percent, which is within their experimental error.

TABLE 4. *Comparison of spiral contractometer with the flat strip contractometer*

Run	Spiral contractometer			Strip contractometer		
	S	S_T	$\left(1+\frac{d}{t}\right)$	S	S_T	$\left(1+\frac{d}{t}\right)$
	lb/in.²	*lb/in.²*		*lb/in.²*	*lb/in.²*	
1	15,000	16,000	1.06	16,000	17,000	1.06
2	14,700	15,600	1.06	14,500	15,400	1.06
Average [1]	14,900	15,800	.....	15,300	16,200	.....

[1] Difference in average S=2.6%. Difference in average S_T=2.5%.

To study the response of the instrument to solution variants known to affect stress, the effects of impurities, high pH, chloride, hydrogen peroxide, and organic materials were investigated. The results shown in table 5 are in general agreement with the work of others [3, 9, 10, 11]. There is some disagreement in the literature on the effect of hydrogen peroxide. The difficulty in measuring its effect may be associated with its decomposition with time. To check this effect further the strip contractometer was run simultaneously with the spiral contractometer in experiments 7, 8, and 9 (table 5), and the results are in excellent agreement.

TABLE 5. *Effect of changes in bath composition on the stress in the nickel deposits*

Thickness of deposit, 0.0006 in.

Bath	Solution	S	Variable
		lb/in.²	
1	Watts Nickel (as made up with commercial salts), pH=3.0	32,000	Impurities.
2	No. 1 purified with H_2O_2 and carbon, and electrolyzed, pH=3.0	15,000	Do.
3	Purified Watts nickel, pH=6.0	24,500	pH.
4	Electrotyping Ni bath (contains NH_4^+), pH 5.8	16,000	pH.
5	Electrotyping Ni bath (contains NH_4^+), pH 6.2	15,000	pH.
6	Electrotyping Ni bath (contains NH_4^+), pH 6.8	33,000	pH.
7	Purified Watts Ni+1 g/l H_3O_3 (30%), pH=4.2	Very high (off scale) Very high (off scale)[a]	H_2O_2.
8	Bath 7 after standing 1 hr at 54° C	62,000 [a] 60,000	H_2O_2. H_2O_2.
9	Bath 7 after standing overnight at 54° C	15,000 [a] 16,000	H_2O_2. H_2O_2.
10	Bath 9 +1 g/l of Nacconol EP and 0.02 g/l of cinchonine, pH=4.2	36,000	Wetting agent and organic brightener.
11	Bath 10+2 g/l of saccharin	4,500	Saccharin.
12	Bath 11+additional 2 g/l of saccharin	2,700	Do.
13	2 N $NiCl_2$, pH=5.0	31,000	Chloride.

[a] Determination with straight-strip contractometer.

It has been observed that in runs made with either the spiral or strip contractometer, the stress usually decreased with thickness. This relation is shown in figures 4 and 5. The same phenomenon was observed by Kohlschutter and Vuilleumier [3], and by Vuilleumier [4] in their work with the contractometer. They explained this on the basis of the progressive coarsening of the grain of the deposit with increasing thickness. Hughes, in commenting on Vuilleumier's paper suggested that the change might be due only to the stiffening of the strip, caused by increasing its thickness with the plating. That the effect is real and not due to increasing stiffness of the helix is shown by using the deflection constant for the plated helix in the calculation of stress. The increased stiffness of the helix accounts for only a small proportion (10%) of the decrease in stress as the deposit increases from 0.0001 to 0.002 in. in thickness.

The stress which is determined for a coating of a given thickness is an average stress and is not a suitable quantity for studying the change of stress

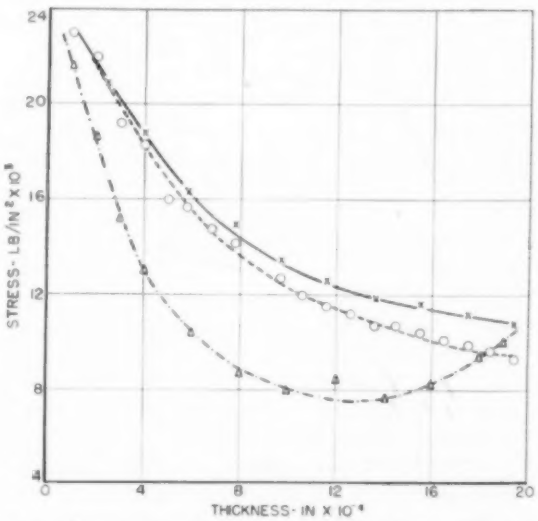

FIGURE 4. *Stress in nickel, deposited from a carefully purified Watts nickel-plating solution.*

....., Uncorrected stress (S); ——, true stress (S_T); _ _ _ _, instantaneous stress (S_i).

with thickness of deposit. Suppose that a deposit had a high initial stress, which then decreased to a constant value as the coating became thicker, then the average stress would show a continual decrease with thickness which would mask the fact that the stress had become constant. Therefore, it is more sound to relate the thickness of the coating to the stress in the increment of coating deposited at that particular thickness. This stress will be referred to as the "instantaneous stress." It is readily determined from the slope of the curve for the average stress as shown in the appendix. In figures 4 and 5 the curves of the instantaneous stress are compared with the curves for the average stress. It will be seen that the instantaneous stress decreases rapidly until a thickness of about 0.0005 in. is reached.

The decrease of stress with thickness seems to be best explained on the basis of a change of grain size of the deposit. The following experiments were made to test this hypothesis.

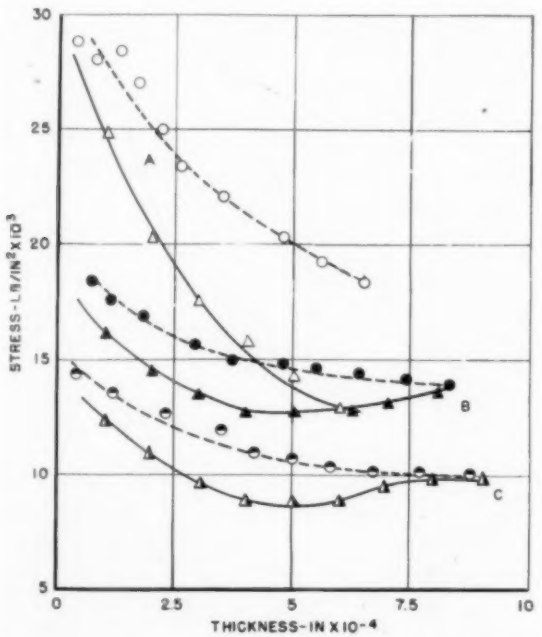

FIGURE 5.—*Stress in nickel, deposited from pilot plant Watts nickel solution.*

A, Stress of plate deposited on stainless steel helix; B, stress of plate deposited on bright (small grain) side of electroformed nickel helix; C, stress of plate deposited on dull (large grain) side of electroformed nickel helix; ·····, true stress; ———, instantaneous stress.

A sheet of nickel approximately 0.014 in. (0.34 mm) thick was electroformed on a polished stainless steel base in a Watts nickel solution. The sheet was removed from the stainless steel base, and two longitudinal strips were cut from the center and formed into helices. One of the helices was wound so that the initially deposited bright surface of the nickel (the side originally adjacent to the stainless steel) was on the outside, and the other helix was wound so that the finally deposited dull surface (the side adjacent to the solution) was on the outside. These helices were annealed at 500° C for 1 hr and were prepared for stress determinations as described previously. The helices were electrocleaned cathodically, activated by a 10-sec cathodic treatment in 10-percent H_2SO_4 and run in the nickel solution to a thickness of approximately 0.0008 in. (The stress determination was run in the same solution in which the helices were electroformed.) The curves of figure 5 show the relation of thickness to stress found with the two helices. A curve for a run on a stainless steel helix in the same solution was included for comparison. It will be noted that the lowest stress was obtained when plating on the coarse-grained surface of the helix (curve c), the stress was higher when plated on the fine-grained surface (curve b) and still higher when plating was done on the stainless steel helix (curve a). It will also be noted that the slopes of curves b and c are much smaller than that of curve a. An insight into this behavior can be obtained from inspection of the photomicrographs taken of cross sections of the two nickel helices with their subsequently applied deposits (fig. 6).

In each of the pictures the plate applied during the stress determination is on the right. In a and c the bright side of the helix is on the right, in b and d, the dull side is on the right. In figure 6, a, and 6, b, the progressive coarsening of the grain structure of the helix from the bright side toward the dull side can be seen. In figure 6, c, and 6, d, it can be seen that the grain structure of the nickel plate in both cases is finer than that on which it was deposited, but the grain size of the plate in figure 6, d, is larger than that in 6, c, and there are more instances of continuance of the basis structure in 6, d, than 6, c. We may conclude, therefore, that the order of the stresses and the slopes of the curves shown in the curves of figure 5 are related to the grain size of the deposited nickel, and

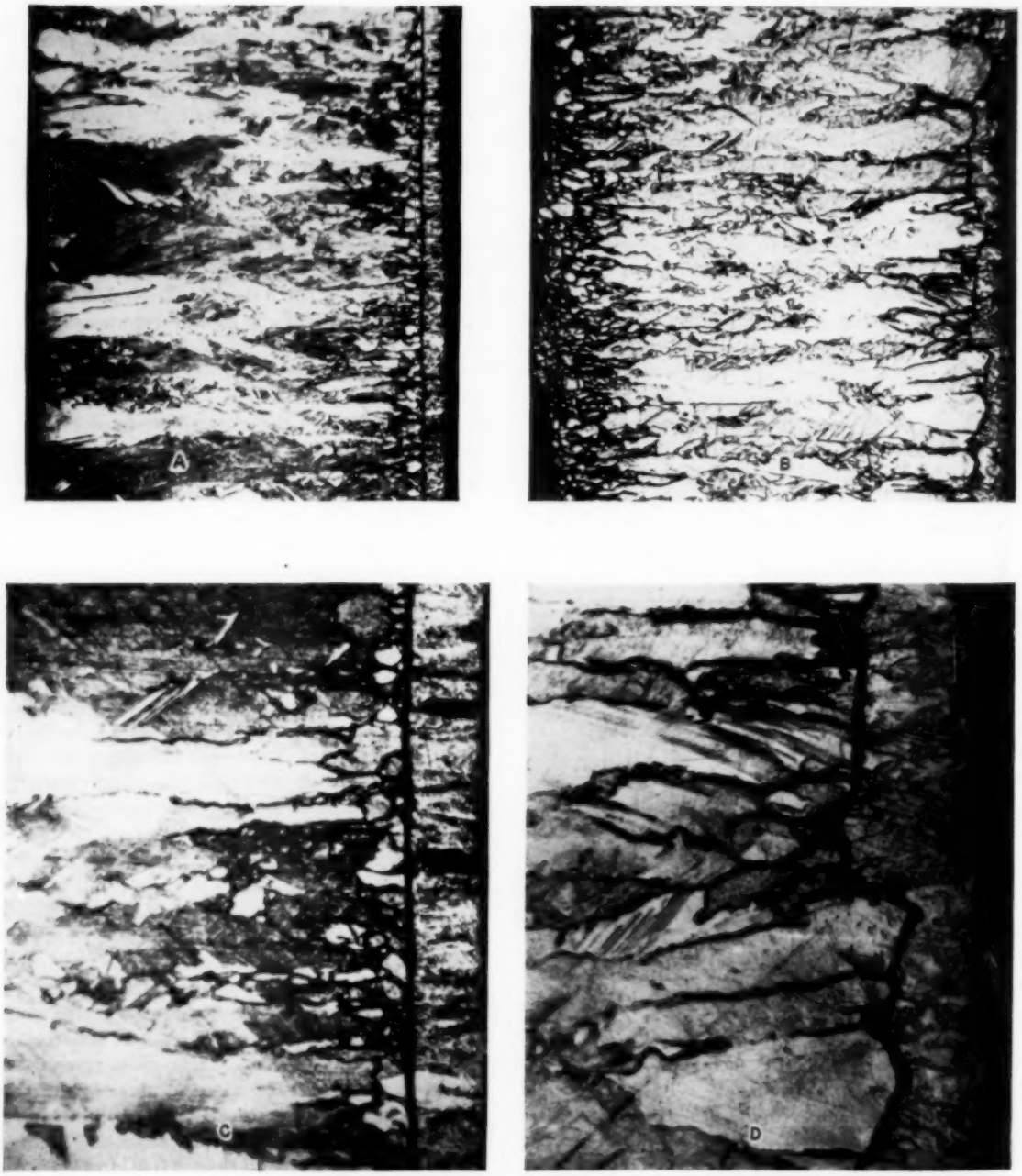

FIGURE 6.—*Photomicrographs of cross sections of nickel plates on nickel helices.*

In each case the nickel plate is on the right and the helix on the left. A, nickel plate on bright side of helix, ×150; B, nickel plate on dull side of helix, ×150; C, nickel plate on bright side of helix, ×500; D, nickel plate on dull side of helix, ×500.

the amount of continuance of the basis structure. If there had not been some grain growth on the bright side of the helix (probably during annealing) curve 5, b, would probably have approached 5, a, more closely, and if perfect continuance of the structure of the base nickel had been obtained, curve 5, c, probably would have more nearly approached a straight line. Close examination of figure 6, a, and 6, b, shows that the rate of grain growth of nickel observed in the electroformed helix approximately corresponds to the rate of decrease of stress with increasing thickness shown in figure 4. It is rapid at first and then levels off. The low stress of certain bright nickel deposits, in spite of their very fine grain, does not detract from the plausibility of this analysis, because these plates invariably have a definite laminated structure and frequently contain impurities, such as compounds of sulfur or carbon. These extraneous factors may provide planes or areas for internal stress relief and introduce entirely new factors into the consideration of the mechanical forces in the deposit.

To determine whether the difference noted in curves 5,b and 5,c may be caused by the difference in micro-roughness of the surfaces of the two helices, a stress determination was run on a stainless steel helix, to a thickness of nickel of approximately 0.001 in. (0.025 mm). The contractometer was then removed from the solution and rinsed, and the deposit was electropolished to a mirror-bright surface in about 5 min. After rinsing, the contractometer was returned to the nickel solution, and the stress determination was continued. A stress-thickness curve for the entire run duplicated figure 4 with only the slightest indication of any response to the electropolishing. As electropolishing smooths a surface without affecting the crystal structure, the measured stress must be related to the crystal structure and not to the micro-roughness of the surface.

From these tests it may be concluded that the stress in nickel deposits decreases with increasing grain size. The explanation of this is beyond the scope of this paper, but it may be related to inclusions at the grain boundaries as suggested by O'Sullivan [19], or possibly to the attraction between crystal faces as suggested by Blum and Rawdon [20]. The explanation of this phenomenon, together with the fundamental causes of stress in electrodeposits, is an important subject, on which further research is required.

V. Application of the Spiral Contractometer

The spiral contractometer may prove to be a valuable tool in the field of electrodeposition, both in research and in production control. A typical research application was the measurement of the stress of chromium deposits reported in the paper on properties of chromium by Brenner et al. [21]. In this study, the stress of chromium deposits produced at various temperatures was measured with the spiral contractometer. It was found that the high-temperature crack-free deposits (frequently referred to as "stress-free") actually were under high stress. The "low-stress" deposits produced in the vicinity of the "bright range" were low in stress as a result of stress-relief by cracking. It was shown that when they were very thin, these deposits also built up considerable stresses before they cracked. It was concluded that the high-temperature conditions produced chromium of higher tensile strength (probably because of its lower oxide content), so that the high stresses of the chromium deposits could exist without producing cracking. Figure 7 shows the results obtained with chromium, and in addition, the curve for nickel drawn on the same scale for comparison.

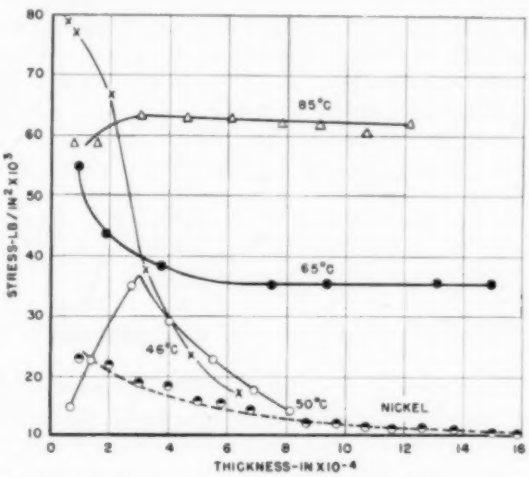

FIGURE 7. *Stress in chromium plate deposited at various temperatures.*

A curve for stress in nickel is included for comparison.

Cracking of a deposit is not in itself an indication of the magnitude of stress, but rather it is an indication that the maximum stress at certain points exceeds the tensile strength of the material. Cracking can be induced either by conditions that increase the stress or lower the tensile strength. Inclusions, such as oxides, or basic salts, therefore, may not actually raise the stress, but they may lower the tensile strength of the deposit.

The spiral contractometer has been used to measure stresses of metals deposited from other solutions such as cobalt, cobalt-tungsten alloys; and "electroless nickel and cobalt" where metal deposition is accomplished by chemical reduction, without the use of current. This latter use suggests a possibility of its application for measuring stresses in nonmetallic or organic coatings that are applied by brushing or spraying.

Other research problems that might be aided by the spiral contractometer are the search for stress-reducing agents, the determination of plating conditions that give minimum stress, and the determination of the effects on stress of addition agents used for various purposes in plating solutions.

An important field of application of the spiral contractometer is in production control. By periodic stress determinations in an operated plating tank, the presence of contamination can be detected. Purifying treatments can be followed with the contractometer, and the effectiveness and completeness of the treatment determined. During production, periodic stress determinations can be made with this instrument while plating is done in the tank, and with current from the regular busbar. The instrument may also be valuable in "trouble-shooting", especially when the adhesion is to be improved. By a simple measurement, abnormal plating stresses may be detected, and thus either eliminated or confirmed as a cause of poor adhesion.

VI. Summary and Conclusions

A new instrument for the measurement of stress in electrodeposits has been described. The spiral contractometer has been shown to be a rugged, easily operated unit that gives measurements of stress that are reproducible in nickel solutions to within ± 10 percent. The values obtained with this instrument agree well with reported values, with measurements made with another type of contractometer, and with measurements by procedures based on different principles. The instrument is sensitive enough and accurate enough for research work. The convenience of its use should encourage its application to routine control of plating solutions and plated products. The advantages of the design of this instrument as compared to others are (1) Convenience: No auxiliary optical or other types of measuring equipment are required. The measurement of deflection is taken from a dial on the instrument. This permits the instrument to be hung in an operating plating tank and measurements to be taken on the site. (2) Sensitivity: The length of strip that may be conveniently used when wound as a helix is four to eight times that usually used in the straight-strip instruments. This gives a greater deflection for a given change in curvature. The deflection can be conveniently magnified to any desired degree by the gear system of the instrument. (3) The measurements are made at the plating temperature, thereby eliminating thermal errors. (4) The use of a coiled strip greatly reduces or eliminates errors caused by transverse bending. (5) The instrument can be easily calibrated, thus permitting simpler calculations and eliminating errors due to variation of the physical properties of the helix.

The values for stress in pure nickel deposits of various thicknesses and deposited under clearly defined conditions have been established.

A simple formula for the calculation of stress in electrodeposits has been presented and it has been shown to be sufficiently accurate for most work. Where special conditions require it, a correction factor for use with that formula has been derived, by which values of higher accuracy may be calculated without the use of complicated formulas requiring extended computations. In addition, another paper has been prepared for publication in which the formulas for calculating stress are rigorously derived and the relations of previously suggested formulas are shown.

The change in stress of nickel deposits with thickness has been investigated and shown to be related to the increase in grain size as plating progresses.

The authors acknowledge the cooperation and assistance of the staff of the Bureau's Electrodepo-

sition Section, as well as members of other sections of the Bureau. In particular we acknowledge the contribution of R. Crosthwaite, who assisted in the designing of the instrument, and that of W. Ramberg and S. Levy of the Engineering Mechanics Section, who advised us on matters relating to the theory of elasticity.

VII. References

[1] E. J. Mills, Proc. Roy. Soc. (London) **26,** 504 (1877).
[2] G. G. Stoney, Proc. Roy. Soc. (London) **A82,** 172 (1909).
[3] V. Kohlschutter and E. Vuilleumier, Z. Electrochem. **24,** 300 (1918).
[4] E. Vuilleumier, Trans. Electrochem. Soc. **42,** 99 (1922).
[5] R. H. D. Barklie and H. J. Davies, Proc. Inst. Mech. Eng., p. 731 (1930), I.
[6] C. Marie and N. Thon, J. Chim. Phys. **29,** 11 (1932).
[7] P. Jacquet, Compt. Rend. **194,** 456 (1932).
[8] W. Hume-Rothery and M. R. Wyllie, Proc. Roy. Soc. (London) **A181,** 331 (1943); **A182,** 415 (1944).
[9] B. Martin, Proc. Am. Electroplaters' Soc., p. 206 (1944).
[10] W. Phillips and F. L. Clifton, Proc. Am. Electroplaters' Soc., p. 97 (1947).
[11] K. G. Soderberg and A. K. Graham, Proc. Am. Electroplaters' Soc., p. 74 (1947).
[12] W. A. Wood, Phil. Mag. **15,** 553 (1933); **20,** 964 (1935); **24,** 772 (1937).
[13] E. M. Mahla, Trans. Electrochem. Soc. **77,** 145 (1940).
[14] M. R. J. Wyllie, J. Chem. Phys. **16,** No. 1, 52 (1948).
[15] Metals Handbook of Am. Soc. Metals, p. 541 (1939).
[16] S. Timoshenko, Strength of materials, part I, p. 5, 2nd ed. (D. Van Nostrand and Co., New York, N. Y., 1940).
[17] A. W. Hothersall, Proc. Am. Electroplaters' Soc., p. 4 (1946); J. Inst. Metals, Symposium on Internal Stress in Metals and Alloys, Preprint No. 1082 (1947).
[18] H. Rosenthal and J. Mazia, Symposium on Stress Corrosion Cracking of Metals, p. 122 (1944), Am. Soc. Testing Materials and Am. Inst. Mining Met. Engrs.
[19] J. B. O'Sullivan, Trans. Faraday Soc. **26,** 89 (1930).
[20] W. Blum and H. S. Rawdon, Trans. Electrochem. Soc. **44,** 397 (1923).
[21] A. Brenner, P. Burkhead, and C. W. Jennings, Proc. Am. Electroplaters' Soc., p. 32 (1947); J. Research NBS **40,** 31 (1948) RP1854.

VIII. Appendix

Some calculations based on data taken with the spiral contractometer are demonstrated herein.

The calculation of stress of run 9, table 1, follows:

Dimensions of Helix (Helix B)

C = outside diameter of helix = 0.765 in. (1.94 cm).
p = pitch of helix = 0.678 in. (1.72 cm).
t = thickness of strip = 0.0131 in. (0.33 mm).
h = height of plate = 4.49 in. (11.4 cm).
$k = 5.57/2.60 = 2.14$ deg/g-cm.
$K = 4.05 \times 10^{-4}$ in.-lb/deg (deflection constant).

h and p are measured by mounting the plated helix on a ¾-in. rod, compressing it longitudinally until the coils of the helix just touch each other and measuring the height of the deposit and the pitch of the helix with a centimeter rule.

K is obtained as follows: In calibrating this helix it was found that the average deflection of the pointer for 0- to 25-g loads was 5.57 deg/g with the load attached to the lever arm at a distance of 2.60 cm from the torque rod, and $k = 5.57/2.60 = 2.14$ deg/g-cm.

$K = 8.68 \times 10^{-4}/k = 4.05 \times 10^{-4}$ in.-lb/deg since 1 g-cm = 8.68×10^{-4} in.-lb).

The weight of nickel on the helix = 1.04 g.

$$d = \frac{g}{G \times 2.54 \times \pi C h},$$

where,
g = weight of plate in grams.
G = density of nickel.
C = diameter of helix in centimeters.
h = height of plated portion of helix.
d = thickness of plate in inches.

$$d = \frac{1.04}{8.9 \times 2.54 \times 3.14 \times 1.94 \times 11.4}$$

$d = 1.04/1575 = 6.62 \times 10^{-4}$ in.

It will be noted that for a given helix and plated metal the denominator is constant. The plate thickness may therefore be obtained by merely dividing its weight by the constant denominator.

The pointer deflection, D, observed for this deposit was 107°.

Substituting values in eq 8

$$S = \frac{2K}{pt} \times \frac{D}{d} = \frac{2 \times 4.05 \times 10^{-4}}{0.678 \times 1.31 \times 10^{-2}} \times \frac{107}{6.62 \times 10^{-4}} =$$

$$9.13 \times 10^{-2} \times 1.615 \times 10^{5} = 14{,}700 \text{ lb/in}^2.$$

It will be noted here that the first term, $2K/pt$, is constant for a given helix and that the stress is determined by multiplying the ratio, D/d, by this constant.

To determine stress by use of the known E of the helix instead of K, the observed deflection of the pointer in degrees, D, is converted to deflection of the helix in radians, D.

107°/10 = 10.7° = deflection of helix, since the gear ratio is 10:1.

$10.7° \times \pi/180 = 1.87 \times 10^{-1}$ radians = D

Substituting in eq 3,

$$S = \frac{Et^2 p}{6\pi C h} \times \frac{D}{d} = \frac{29 \times 10^{6} \times 1.72 \times 10^{-4} \times 6.78 \times 10^{-1}}{6 \times 3.14 \times 7.65 \times 10^{-1} \times 4.49} \times$$

$$\frac{1.87 \times 10^{-1}}{6.62 \times 10^{-4}} = 52.4 \times 282 = 14{,}800 \text{ lb/in}^2.$$

E stainless steel, helix B $=29\times10^6$ lb/in^2.

Again the first term, $E\ell^2p/6\pi Ch$, is constant for a given helix.

The correction factor to obtain the true stress, S_T, is applied according to eq 6.

$S_T=S(1+E_e/Ed/t)$

$=14.7\times10^3(1.050)$ $\quad E_e/E$ for nickel on steel $=1$

$=15{,}500$ lb/in^2. $\quad d/t=6.62\times10^{-4}/1.31\times10^{-2}$

$=0.050$

The modulus of the helix is calculated from the calibration data as follows:

Table 2 gives $K=4.06\times10^{-4}$ in.-lb/deg for helix B.

Substituting in eq 9

$$E=2.16\times10^4KCh/p^2\ell^2$$

$$=2.16\times10^4\times4.06\times10^{-4}\times7.65\times10^{-1}\times 4.49/4.60\times10^{-1}\times2.25\times10^{-6}$$

$$=29.2\times10^6\text{lb/in.}^2$$

There is no need to calculate the modulus of a helix for a stress determination, but it serves as a good check on the physical condition of a helix.

Calculation of Instantaneous Stress (S_i)

At thickness t, $S_a=1/t\int_0^t S_i\,at$, where S_a=stress (corrected) shown by the contractometer at thickness t.

$S_at=\int_0^t S_i\,dt$; and differentiating with respect to t, $S_a+tdS_a/dt=S_i$

But since dS_a/dt is the slope of the stress versus thickness curve, at thickness t,

$dS_a/dt=m/t$ and $S_i=S_a-m$ (see fig. 8).

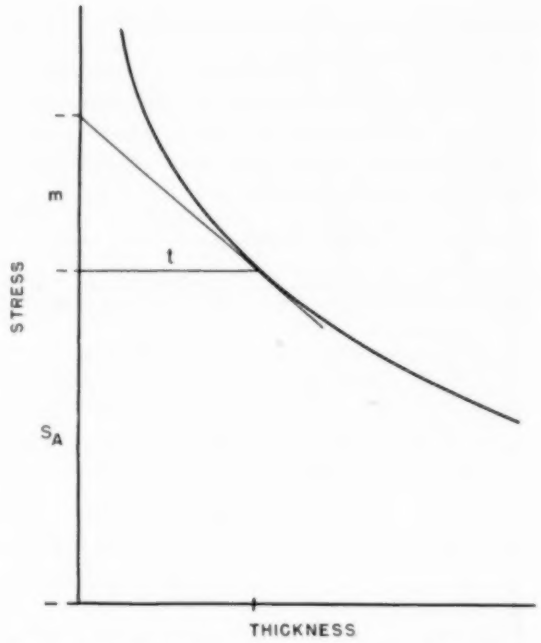

FIGURE 8. *Diagram showing calculation of instantaneous stress (S_i).*

The tangent of the S_T curve in figure 5 at various thicknesses was found graphically, and its intercept, y, on the stress axis noted on the graph. Since $m=y-S_a$, and S_a can be read from the curve, S_i can be determined at any thickness.

WASHINGTON, June 18, 1948.

U. S. Department of Commerce
National Bureau of Standards

Research Paper RP1954
Volume 42, February 1949

Part of the Journal of Research of the National Bureau of Standards

Calculation of Stress in Electrodeposits from the Curvature of a Plated Strip

By Abner Brenner and Seymour Senderoff

Formulas are derived for the calculation of stress in electrodeposits from the curvature developed in a plated strip. All the formulas are derived from the fundamentals of the theory of elasticity and the relationships among the various formulas are shown. Simplified formulas are derived and their limits of applicability demonstrated. Correction factors for a number of variables and specific formulas for different experimental procedures are presented.

I. Introduction

The methods of determining the stress in an electro deposit by the curvature of a strip that is plated on only one side has been described in a preceding paper [1].[1]

The calculation of stress in electrodeposits was first worked out by Stoney [2]. He derived two equations, but only the first one has been used by later investigators, apparently because the second one was written down without making clear either its derivation or meaning. His first equation,

$$S=\frac{Et^2}{6rd},$$

where S is stress in the coating, E is Young's modulus of elasticity of the basis metal, t is the thickness of the basis metal, d is the thickness of the coating, r is the radius of curvature of the bent strip, is really a differential expression in which the thickness of the coating is considered to be infinitesimal compared to the thickness of the basis metal. The equation is therefore approximate, but it can be used without much error in those cases in which the thickness of the coating does not amount to more than a few percent of the thickness of the basis metal. The error involved in using the Stoney equation for thin coatings is usually less than the experimental error, which is ordinarily about 5 to 10 percent.

[1] Figures in brackets indicate the literature references at the end of this paper.

There are occasions however, when it is desirable to measure the stress in thick deposits, which are to be used for electroforming, or to study the variation of stress with thickness. Such a situation could be met by plating on a basis metal of such thickness that the deposit would still contribute only a small proportion of the total thickness. It would nevertheless be an advantage to make measurements of stress, particularly of deposits of low stress, by plating a thick coating on a relatively thin strip of basis metal, because the sensitivity of the measurement is thereby increased. The error involved in using the Stoney equation begins to exceed the experimental error when the thickness of the coating is 5 percent or more of the thickness of the basis metal. For example, in Soderberg's [3] work, in which the thickness of the coatings amounted to as much as 25 percent of the thickness of the basis metal, the error involved in using the Stoney equation would have been more than 50 percent. This was recognized by Soderberg who then made a more satisfactory analysis of the calculations involved than had been made previously.

Although on the practical side, the Stoney equation is sufficiently accurate for most calculations of the stress in electrodeposited coatings, the theoretical side is not so satisfactory. There exists a lack of clarity in the definition of what is meant by the stress in the deposit, and a lack of recognition that the same formula cannot be used

for data obtained by slightly different methods of applying the simple bent strip technique.

Barklie's [4] derivation of the Stoney equation is very similar to that given by Stoney. According to his derivation, his formula yields the approximate stress in the coating on the curved beam. This stress will be referred to as the equilibrium stress. It is smaller than the true stress, because some of the force has been relieved by the bending of the coating. A minor situation that has caused confusion is that Stoney and Barklie both considered that the neutral axis of the bent strip was distant from the surface by about one-third the thickness of the strip, instead of at the center of the strip as would ordinarily be expected. Actually, this confusion does not affect their derivations. The neutral axis is usually defined as that longitudinal axis of a beam, which undergoes no additional strain (no change in length) when the beam is bent. According to this definition the neutral axis lies at the center of a simple beam. Barklie and Stoney considered the neutral axis to be that axis along which the stress was zero after bending. It will be shown later that this axis is not the same as the neutral axis as above defined. Stoney and Barklie did not consider the effect of the difference in Young's modulus of the coating and of the basis metal on the calculation of stress, apparently because for thin coatings this effect is negligible. Soderberg took account of these moduli in his derivation.

Because of the rather confused situation regarding the calculation of stress in electrodeposits from the data obtained by the deflection of a strip, it was considered worth while to give a more rigorous derivation of the involved formulas than has been done previously. An added advantage in having the exact formulas is that in a given case one can determine whether or not the Stoney formula is a sufficiently accurate approximation. The need for clarifying the situation was further shown by the recent appearance of another paper on stress, by Heussner, Balden, and Morse [5], in which another set of formulas, differing slightly from those given by Soderberg, was proposed.

It has not been recognized previously that slight variations in the procedure of measuring stress by the curved-strip method require different methods of calculation. There are three methods of measuring the stress of electrodeposits by the curvature of a strip.

Method I. The deposit is plated on a basis metal, which is so rigidly held that neither contraction nor bending of the plated strip can occur. The constraints are then released and the flat plated strip is allowed to assume its equilibrium curvature. This is the method used by Soderberg, who developed a suitable formula for the calculation.

Method II. The deposit is plated on a strip that is constrained from bending but not from undergoing contraction. The constraints are then released, and the flat plated strip is allowed to assume its equilibrium curvature. Experimentally, this method is more easily realized than method I, because bending can be more readily prevented than can the rather minute longitudinal changes.

Method III. The deposit is plated on a strip that is allowed to bend continuously during plating. This is the method that is most commonly used, but there has been no satisfactory discussion in the literature of the calculations involved for either this method or for method II.

In the following discussion, the formulas for the different methods of measurement will be derived. For thin coatings, all formulas reduce to Stoney's formula. In the summary, the error involved in using Stoney's formula for thick coatings will be considered in more detail, and examples will be given.

1. Symbols

A_b = coefficient of thermal expansion of basis metal.
A_c = coefficient of thermal expansion of coating.
b = width of strip.
C = diameter of helix.
c = distance of neutral axis to outside surface of coating in a plated beam whose basis metal and coating have different moduli of elasticity.
d = thickness of coating.
D = angular deflection of torque rod in radians.
D' = angular deflection of torque rod in degrees.
$\overline{D}$ = angular deflection of geared pointer in degrees.
E = Young's modulus of elasticity.
E_b = Young's modulus of elasticity of basis metal.
E_c = Young's modulus of elasticity of coating.
F = force.

G=gear ratio.
h=height of plated (or active) portion of helix.
I=moment of inertia.
K=calibration constant of helix with deflection of geared pointer measured in degrees.
K'=calibration constant of helix with deflection of torque rod measured in degrees.
L=projected length of helix.
L'=true length of helix.
M=bending moment.
M_b=bending moment of basis metal.
M_c=bending moment of coating.
p=pitch of helix.
$R=E_c/E_b$=ratio of modulus of coating to modulus of basis metal.
r=radius of curvature.
$\Delta(1/r)$=change in curvature.
S_b=stress in basis metal.
S_{bm}=maximum stress in basis metal.
S_c=stress in coating.
S_{eq}=stress at equilibrium.
S_s=stress as calculated by Stoney's formula.
σ=generalized stress.
S=true stress.
ΔT=temperature change.
t=thickness of basis metal.
y=distance of fibers from neutral axis.

II. Derivation of Equations for the Stress in an Electrodeposit

In deriving equations for stress, only elementary considerations of beam theory are involved. This presentation is more detailed than would be required for presentation to a specialist in the theory of elasticity. Before beginning the derivations, it is necessary to clearly define what is meant by the stress in a coating. When a coating is plated upon a thin strip of metal that is restrained from bending, the strip is compressed by the tension in the coating, and the latter is thereby also shortened and loses some of its stress. If the constraints are now released and the strip is allowed to curve, the stress in the coating is still further relieved. These losses in stress depend on the dimensions of the basis metal, and hence the final equilibrium stress in the coating is not a constant quantity but depends upon the experimental conditions. To be independent of the mode of measurement, the stress in a coating is defined as the stress that exists in the coating when it is deposited upon a rigid, incompressible surface, or for practical purposes, upon a basis metal thick enough to undergo no appreciable deformation. This will be referred to as the "true stress."

There are two basic conditions that must be satisfied by the internal, longitudinal fiber stresses of a beam in equilibrium.

$$F=\int \sigma dA=0, \tag{1}$$

and

$$M=\int \sigma y dA=0, \tag{2}$$

taken over any cross section of the beam. The first equation states that the sum, F, of the longitudinal forces within the beam is zero, i. e., that the internal compressive forces are equal to the internal tensile forces. The second equation states that at equilibrium the internal bending moment, M, of the beam is zero about any axis. The variable, y, is the distance of the fibers, of stress σ, from the chosen axis, and dA is the element of area of the cross section.

Before considering the application of these general equations to the curvature of a plated strip, it will be helpful to examine first the stresses that exist in a plated strip that has been allowed to assume its equilibrium curvature. In figure 1 is shown the system of stresses that exists in a strip that has been plated according to method I. The distribution of the longitudinal stresses is the same over any cross section, $ABCD$, of the beam. The stresses vary along the direction of the radius of curvature, that is from AB to DC. The stresses do not vary in the direction of the width, b, of the beam, that is from AD to BC, and therefore the system of stresses normal to the cross section can be represented by a two-dimensional graph, DL, as shown in the figure. The magnitude of the tensions in the coating are represented by the length of the vectors directed to the right and the magnitude of the compressive stresses by the vectors directed toward the left. It will be noted that the outer fibers of the basis metal, as well as the coating, are under tension, but that most of the basis metal is under a compressive stress. The neutral axis of the beam is at the midpoint and is the curved surface represented by the dotted line PFU. The method of constructing the stress diagram will be considered later.

The tensile force in the coating is the summation of the stresses, represented by $EKLD$ over the

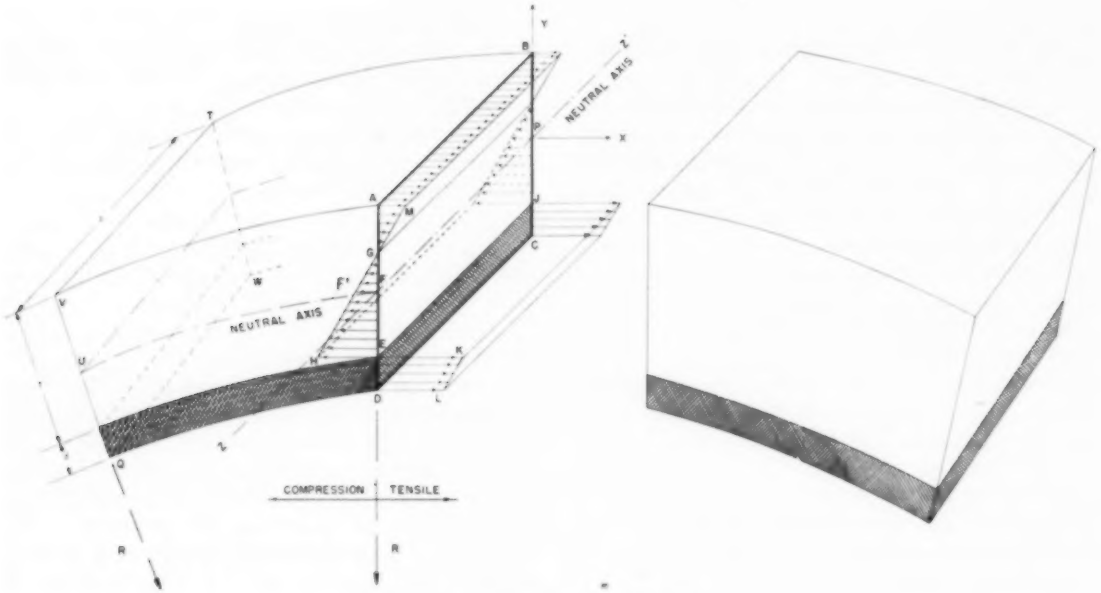

FIGURE 1. *Stresses in a plated strip.*

The cross-hatched area is the coating.

area of the cross section, *DEJC*, of the coating. The stress can be considered constant over the elemental strips of area, *bdy*. Tensile force in coating $=b\int_D^E \sigma dy = b(\text{area } EKLD)$. Similarly, the internal forces in the basis metal consists of a compressive force represented by b(area *EHG*) and a tensile force represented by b(area *GAM*). The first condition of equilibrium as applied to this beam is:

$$\text{Force} = b(\text{area } EKLD + \text{area } GAM) - b(\text{area } EHG) = 0. \quad (3)$$

Tensile forces − compressive forces = 0; or, area area *EKLD* + area *GAM* = area *EHG*.

In figure 1, the internal bending moment of a fiber is represented by the product of a stress, and its distance from the neutral axis, for example, $KE \times EF$. The internal bending moment of the coating is the aggregate of the products of each fiber stress by its lever arm, summed over the area of the cross section of the coating *DEJC*.

$$\text{Bending moment of coating} = b\int_D^E \sigma y dy. \quad (4)$$

The integral represents the moment of the area *EKLD* with respect to the neutral axis. When the stress, σ, is tensile (arrows to the right in fig. 1), it is considered positive. When the stress is compressive (arrows to the left), it is considered negative. y is positive or negative, depending upon whether the area under consideration is above or below the reference axis. In later summing up these moments, each must be given its proper sign.

$$\text{Bending moment of the coating} = b(\text{moment of area } EKLD). \quad (5)$$

The bending moment of the basis metal strip is represented similarly by the moments of areas *EHG* and *GAM* with respect to the neutral axis. The second condition of equilibrium can now be represented graphically as, b(moment of area *EKLD*) + b(moment of area *FEHF'*) + b(moment of area *FF'G*) + b(moment of area *GAM*) = 0. Or by using the absolute values of the moments

$$\text{Moment of area } EKLD = \text{moment of area } GAM + \text{moment of area } FEHF' - \text{moment of area } FF'G. \quad (6)$$

The moments of the areas were considered with respect to the neutral axis for illustrative purposes. However, the sum of the moments, with proper regard to sign, is zero with respect to any axis, for example with respect to an edge, AB, of the beam. If the beam is not at its equilibrium curvature, the net bending moment is not zero and tends to make the beam assume the equilibrium curvature.

Qualitatively, the effect of the stresses in the beam is to give the cross section, $ABCD$, the appearance of having rotated around ZZ' as axis with respect to another cross section, $QVTW$.

The stress in a coating may be calculated from the equilibrium curvature of the beam by different methods. The two general conditions of equilibrium may be applied to the curved beam to determine the equilibrium stress, which is then corrected for the stresses that have been relieved by contraction and curvature. Stoney and Barklie applied this method partially, but this procedure is not very easy to use, because the distribution of stresses in the beam is rather complicated, particularly for methods II and III. A simpler approach is to consider that the plated beam reaches its final equilibrium in stages and to calculate for each stage the relation between the stress in the coating and the geometrical changes of shape that occur. This method will be illustrated graphically for method I by constructing the diagrams of the stresses that exist in the coating and basis metal strip at each stage. Only two-dimensional graphs are necessary to show the stresses, as they are to be interpreted in the sense of the plane graph $DLKHMA$ of figure 1.

1. Equations for Method I

The formulas for method I will now be discussed for the simple case in which the moduli of the basis metal and coating are the same.

In figure 2, A, is shown the stress, S, in the coating. There is no resultant stress in the basis metal, because it has been held rigid and has not been allowed to deform. The stress, S, is thus the true stress in the coating. In figure 2, B, the stresses are shown in the coating and basis metal after the constraints have been partially removed and the beam has been allowed to shorten, but not to curve. As the coating also contracts slightly, its stress is somewhat reduced. It can be shown that the compressive stress in the basis metal is

$$S\left(\frac{d}{t+d}\right). \tag{7a}$$

The stress in the coating is diminished by this same amount to the new value

$$S\left(\frac{t}{t+d}\right). \tag{7b}$$

The first condition of equilibrium is illustrated here by the equality of the area $MNPR$ and the area $LMGH$, that is, by the equality of the tensile forces and the compressive forces.

The internal bending moment in the straight beam (see fig. 2, B), which tends to make it curve is equal to the sum of the bending moments of the basis metal and the coating. This is represented by the moments of areas $MNPR$ and $LMGH$ with respect to the neutral axis. Since the forces in the basis metal and coating are equal and opposite, the internal bending moment, M, is equivalent to a couple with the forces applied at the center of the basis metal and of the coating, that is with a distance of $(t+d)/2$ between the lines of application of the two forces, F_2,

$$M=F_2\left(\frac{t+d}{2}\right)$$

$$F_2=b \text{ (area } MNPR)=S\left(\frac{t}{t+d}\right)db$$

or

$$F_2=b \text{ (area } LMGH)=S\left(\frac{d}{t+d}\right)tb.$$

Therefore,

$$M=\frac{Stdb}{2}. \tag{7c}$$

This same result could have been obtained directly from the stresses in the beam as shown in figure 2, A. The initial tensile force of the coating is equal to the stress times the area of the cross section or, $F_1=Sdb$. The force may be considered to act at the midpoint of the coating at a distance of $t/2$ from the neutral axis. The product of the force and the distance gives the same result as before, $Stdb/2$.

When the straight beam is now allowed to bend, a new distribution of the internal stresses occur.

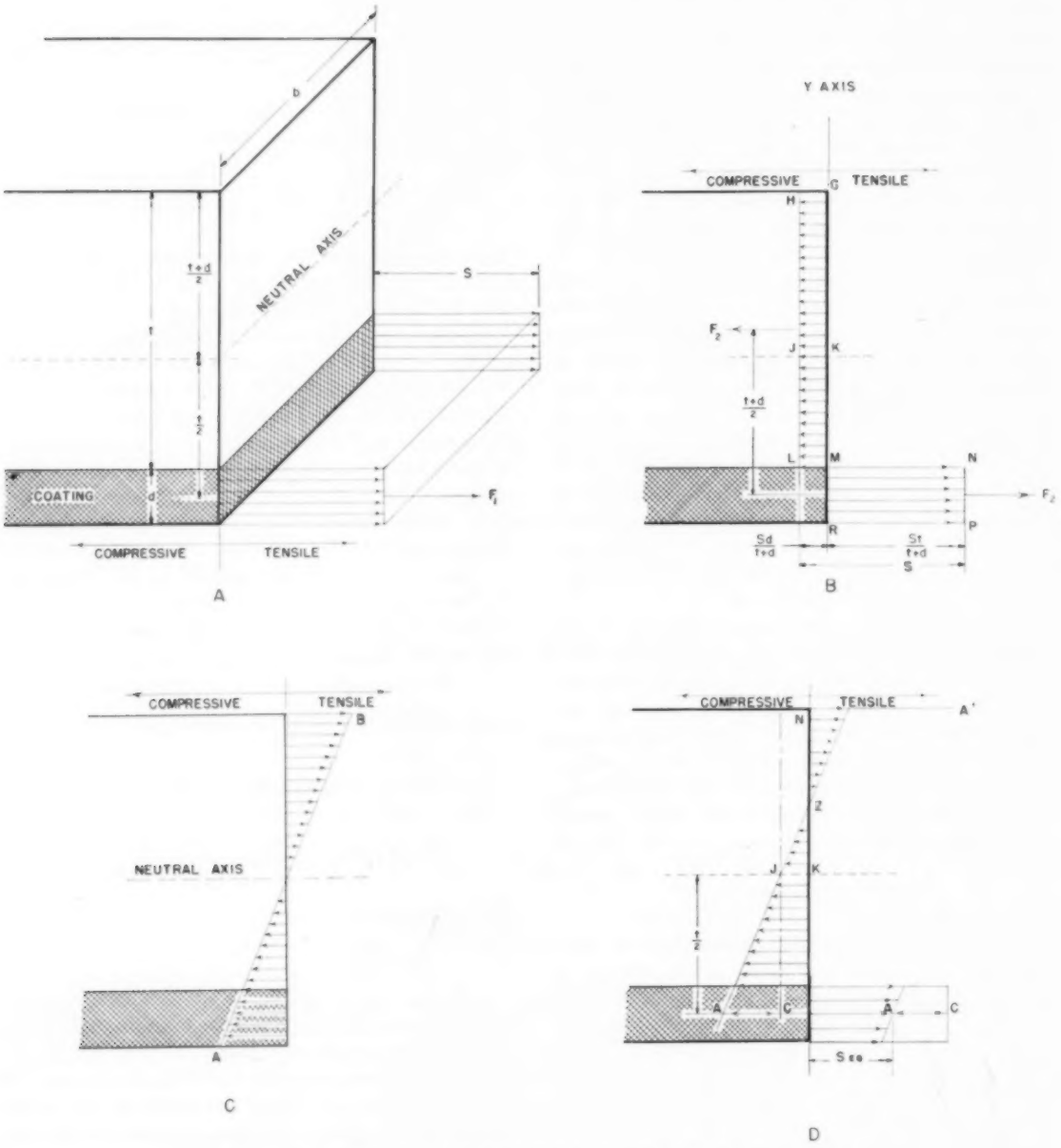

FIGURE 2. *Stresses in a strip held rigid during plating and then released.*

A, Stresses in rigidly held plated strip; B, stresses after contraction only had occurred; C, system of forces superimposed on forces of B as a result of curvature; D, stresses in the free strip at equilibrium; combination of stresses in B and C.

Regardless of what system of stresses may have existed previously in a beam, an additional system of stresses shown in figure 2, C, is produced and superimposed on the initial stresses. Bending of the beam continues until the bending moment of the stresses shown in figure 2, C, is equal and opposite to the bending moment calculated for the stresses in figure 2, B. The algebraic addition of this new system of fiber stresses to those shown in figure 2, B, gives the final system of stresses shown in figure 2, D. It can be shown graphically that both conditions of equilibrium are satisfied by stresses in figure 2, D. In figure 2, C, the tensile force is equal to the compressive force, and thus if the first condition of equilibrium were satisfied by figure 2, B, it will still be satisfied on adding the stresses in 2, B, to those of figure 2, C. The bending moment of the stresses in figure 2, C, is equal and opposite to the bending moment of the stresses calculated for figure 2, B, and thus the sum of the two system of stresses gives a resultant bending moment of zero for figure 2, D.

The equality between the initial bending moment of the flat plated strip, as typified in figure 2, A, or 2, B, and the bending moment of the new stresses produced by curvature typified in figure 2, C, forms the basis for the calculation of the stress in the coating. The bending moment of the stresses of figure 2, C, depends upon the curvature and the dimensions of the beam, and is readily calculated from measurements made directly on the beam.

$$M=\frac{EI}{r}=\frac{E(t+d)^3b}{12r}, \tag{8}$$

where r is the radius of curvature of the neutral axis.

Here E is taken to be the modulus of both the coating and the basis metal. I is the moment of inertia of the cross section, $ABCD$ (fig. 1), of the beam with respect to the trace, FP, of the neutral axis in the plane of the cross section. In the previous discussion it was shown that the initial bending moment of the beam (fig. 2, B) was numerically equal to the bending moment impressed by curvature (fig. 2, C). Thus, the bending moment in eq 7 can be equated to the bending moment in eq 8:

$$\left.\begin{aligned} M&=\frac{Stdb}{2}=\frac{E(t+d)^3b}{12r}\\ S&=\frac{E(t+d)^3}{6tdr}\end{aligned}\right\}. \tag{9}$$

This is the equation derived by Soderberg.

Some other useful relationships may be made clear by use of the diagrams in figure 2. The stresses in figure 2, C, are proportional to their distance, y, from the neutral axis, and are given by the expression,

$$\sigma=\frac{Ey}{r}, \tag{10}$$

which is the basic relation of simple beam theory. The slope of the stress line, AB, with respect to the y axis is

$$\frac{E}{r}. \tag{11}$$

As the beam bends, the line AB can be visualized as rotating further from the y axis. It will be noted that the compressive stress along the neutral axis, denoted by JK, is the same before bending (fig. 2, B) as after bending (fig. 2, D). This is because there is no strain (or change of length) at the neutral axis as a result of the bending. Certain other features of the stresses in the beam have already been pointed out in the discussion of figure 1.

Figure 2, D, shows that the point of zero stress in the beam occurs not at the neutral axis, but at a point, Z, which is distant from the surface of the basis metal by about one-third the thickness of the basis metal when the coating is thin. The point of zero stress can be determined readily with the aid of the diagram.

By eq 11

$$\frac{JK}{KZ}=\frac{E}{r}. \tag{12}$$

JK is equal to the initial compressive stress in the basis metal (fig. 2, B).

$$JK=S\left(\frac{d}{t+d}\right)=\frac{E(t+d)^3}{6rtd}\left(\frac{d}{t+d}\right)=\frac{E(t+d)^2}{6rt}, \tag{13}$$

by substituting for S, using eq 9.

Substituting for JK, as given by eq 13, into eq 12,

$$KZ=\frac{(t+d)^2}{6t} \tag{14}$$

$$NZ=KN-KZ=\frac{t+d}{2}-\frac{(t+d)^2}{6t}=\frac{t}{3}+\frac{d}{6}-\frac{d^2}{6t}. \quad (15)$$

When d is small, NZ is approximately equal to $t/3$. Z is the point that Stoney and Barklie called the neutral axis.

It is of interest to calculate the average equilibrium stress in the coating, that is, the stress at the midpoint of the coating after bending has taken place. The equilibrium stress, S_{eq}, illustrated by figure 2, D, differs from the stress in figure 2 B, by the stress AC, which results from curvature.

$$\left.\begin{aligned} S_{eq}&=S\left(\frac{t}{t+d}\right)-AC=\frac{E(t+d)^3}{6rtd}\left(\frac{t}{t+d}\right)-\frac{Et}{2r}\\ S_{eq}&=\frac{E(t^2-td+d^2)}{6rd}\end{aligned}\right\} \quad (16)$$

The relative difference between the equilibrium stress and the true stress (relative difference$=S_{eq}-S)/S$ can be shown to be $-(4d/t)+10(d/t)^2$, which is fairly large. If d/t is about 5 percent, which is the value in some experiments, the equilibrium stress is about 18 percent smaller than the true stress.

In the measurement of stress it is necessary that the elastic limit of the basis metal be not exceeded. From figure 2, D, it is apparent that the maximum stress in the basis is a compressive stress occurring at the interface with the coating. For method I, this stress can be shown to be given by the formula

$$S_{bm}=\frac{Sd(4t^2-td+d^2)}{(t+d)^3} \quad . \quad (17)$$

If the coating is thinner than the basis metal, this stress is always less than the stress in the coating. By differentiation of eq 17, it can be shown to attain a maximum value of $5S/9$ when the thickness of the coating is one-half the thickness of the basis metal. This simple relation serves as a convenient means of determining whether the elastic limit of the basis metal is likely to be exceeded.

2. Equation for Method II

The stress in the coating will now be calculated for method II, in which it is assumed that the basis metal is prevented from bending but not from contracting during plating, and is allowed to bend subsequently. The stress distribution in this beam differs from that in method I because, although bending is prevented, contraction of the basis metal can take place progressively as the coating becomes thicker. The calculation is complicated by the situation that the earlier layers of coating are compressed by the tension in the succeeding layers in the same way that the basis metal is compressed. Before bending occurs there thus exists a stress distribution in the coating, as shown in figure 3, B, with the greatest tension in the layer of coating last deposited. It is of interest to make this calculation for method II because it approximates practice more closely than the conditions laid down for method I, inasmuch as it is difficult to prevent the contraction of a thin strip during plating, even if it is bolted down. If it turns out that the calculated value for method II differs from that for method I by less than the experimental error, then the simpler calculation can be used.

Stress S_b in the basis metal produced as a result of the successive additions of coating to a total thickness of d will be calculated first. It has already been noted (eq 7b) that the compressive stress produced in the basis metal of thickness t, by the addition of a coating of thickness d with a tensile stress S, is $S_b=S(d)/(t+d)$. If the coating is added in increments dx, the equation becomes $dS_b=S(dx)/(t+x)$, where x is the thickness of the coating that has been previously laid down. The total compressive stress in the basis metal is

$$S_b=S\int_0^d\frac{dx}{t+x}=S\ln\left(\frac{t+d}{t}\right)=S\ln\left(1+\frac{d}{t}\right). \quad (18)$$

It will be noted that when d is small, this equation approaches that for method I (eq 7b), since $S\ln(t+d)/t=S(d)/(t+d)+1/2(d)/(t+d)^2+\ldots$, and the second and higher term may be neglected for thin coatings. An expression for the tension in the coating as a function of the distance, x, from the surface of the basis metal is now required for the purpose of calculating the bending moment of the beam. Qualitatively, it may be observed (fig. 3, B) that the coating has the minimum stress at the interface with the basis metal and that the stress at the outer surface of the coating has the initial value, S.

Consider now the stress in an increment of coating dx, at the distance x from the basis metal,

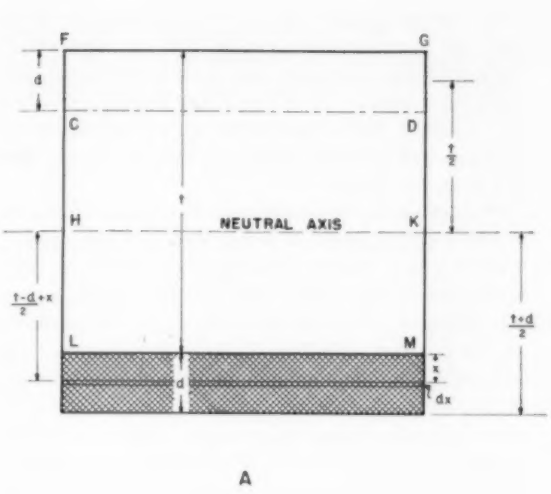

A

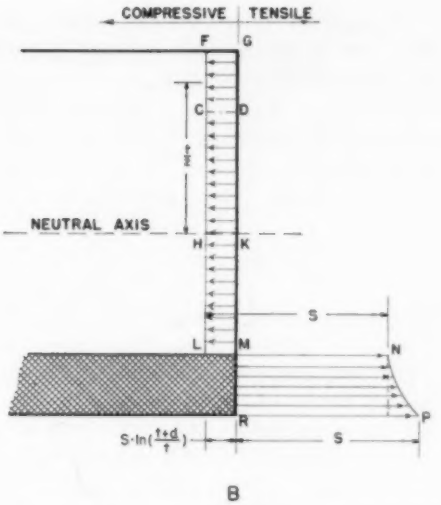

B

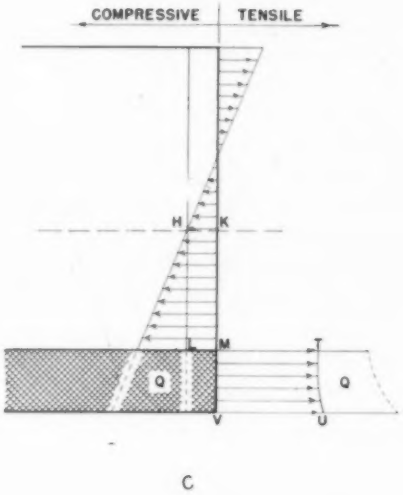

C

FIGURE 3. *Stresses in a strip allowed to contract during plating, but not bend, and then allowed to curve after the plating was completed.*

A, Diagram of dimensions involved in computation; B, stresses in strip before bending took place; C, stresses in strip after it curved.

before any subsequent metal is deposited. The stress in this last increment is S, because the increment does not produce any finite contraction of the base metal. However, its stress is decreased by the effect of the layers of thickness dx, subsequently deposited upon it. The decrease in stress undergone by this increment of coating will be the same as the increase of stress undergone by the basis metal, namely

$$S \ln\left(\frac{t+d}{t}\right) - S \ln\left(\frac{t+x}{t}\right) = S \ln\left(\frac{t+d}{t+x}\right). \quad (19a)$$

The stress at any point x, in the coating is

$$\left.\begin{aligned} S_c &= S - S \ln\left(\frac{t+d}{t+x}\right) \\ S_c &= S\left[1 + \ln\left(\frac{t+x}{t+d}\right)\right] \end{aligned}\right\} \quad (19b)$$

The moment of the coating with respect to the neutral axis is (see fig. 3, A)

$$M_c = bS\int_0^d \left[1 + \ln\left(\frac{t+x}{t+d}\right)\right]\left(\frac{t-d}{2} + x\right) dx, \quad (20)$$

since the variable lever arm of the fiber stresses is $(t-d)/(2)+x$.

Integration by parts gives the following expression

$$M_c = \frac{Sbtd}{2}\left(1 - \ln\left(\frac{t+d}{t}\right) + \frac{d}{2t}\right). \quad (21)$$

The amount of the basis metal about the neutral axis is

$$M_b = \frac{Sbtd}{2} \ln\left(\frac{t+d}{t}\right), \quad (22)$$

because only the area $FCDG$ (which equals $d \times S \ln (t+d)/t$ contributes to the moment. The moments of areas $HLMK$ and $CHKD$ are equal and opposite, and hence cancel.

Equating the initial internal bending moment of the beam to the bending moment imposed by the curvature, as given in eq 8

$$\left.\begin{aligned} M_c+M_b&=\frac{E(t+d)^3b}{12r}\\ \frac{Sbtd}{2}\left(1+\frac{d}{2t}\right)&=\frac{E(t+d)^3b}{12r}\\ S&=\frac{E(t+d)^3}{6rtd\left(1+\frac{d}{2t}\right)}=\frac{E(t+d)^3}{3rd(2t+d)}\end{aligned}\right\} \quad (23)$$

On comparing this formula for stress with the one for method I, it will be seen that the relative difference between the two values of S is $1/2\times d/t$. Since d/t usually is not over 10 percent, the difference between the two methods of calculation of S would be about 5 percent, or within the experimental error. This difference cannot be determined experimentally, because the frequently observed variation of stress with thickness detracts too much from the reproducibility.

The stresses in the coating before and after bending are shown in figure 3, B, and C. It will be noted that the stress in the outer fibers of the coating are higher than in the inner fibers even after bending, in contrast to the coating shown in figure 2, D, for method I. The equilibrium stresses in the coating, represented by area *MTUV* in figure 3, C, are obtained by subtracting area Q from area *MNPR* in figure 3,B.

3. Equations for Method III

Method III deals with the bending of the strip as plating proceeds and is the most common method of measurement employed for determining stress in coatings. Before deriving the expression for method III it will be advantageous to consider, qualitatively, the mechanical differences between method I, which is the simplest to visualize, and method III. In method I the mean length of the lever arm of the fiber stresses in the coating is $t/2$. In method III, the length of the lever arm varies from $t/2$ for the first increment of coating laid down to $(t+d)/2$ for the final increment. The longer average lever arm causes the bending moment to be greater in method III. In method I the curvature of the beam is determined by the final thickness of the beam, $t+d$. In method III, the thickness of the beam varies from t to $t+d$ as the plating proceeds, and on the average is less than in method I. This smaller average cross section of beam also leads to a greater bending of the beam in method III. From both causes, a given thickness of coating will produce more curvature by method III than by method I.

To derive the formula for calculating stress by method III, consider a beam that has been plated with a thickness of coating x, so that the total thickness of the beam is $t+x$. The deposition of an increment of coating of thickness dx produces an increment of internal bending moment, dm, about the neutral axis, which is situated at the center of the beam at a distance, $(t+x)/2$, from the strip dx. The strip increases in curvature from radius r_1 to radius r_2 by the amount $(1/r_2-1/r_1=d(1/r)$. The internal bending moment of the increment dx is represented by a couple that is given by eq 7C, except that t must be replaced by $t+x$ and d is replaced by the increment dx

$$dm=S\left(\frac{t+x}{2}\right)bdx. \quad (24)$$

It may be noted that this is the same as the bending moment of a fiber of stress S, and cross section, bdx, with a lever arm of length $(t+x)/2$, extending to the center of the beam. The bending moment impressed by curvature of the beam is given by eq 8, except that $1/r$ is replaced by $d(1/r)$ and M by dM.

$$dM=\frac{Eb(t+x)^3}{12}d\left(\frac{1}{r}\right). \quad (25)$$

Equating eq 24 to eq 25

$$S\left(\frac{t+x}{2}\right)bdx=\frac{Eb(t+x)^3}{12}d\left(\frac{1}{r}\right). \quad (26)$$

On separating variables and integrating:

$$\left.\begin{aligned} S\int_0^d\frac{dx}{(t+x)^2}&=\frac{E}{6}\int_0^{1/r}d\left(\frac{1}{r}\right)=\frac{E}{6r}\\ S&=\frac{Et(t+d)}{6rd}\end{aligned}\right\} \quad (27)$$

This formula is the simplest of those for the three methods and, it is closer to the simple Stoney formula than the formulas of methods I and II. The relative difference from Stoney's approximation is d/t, which was usually less than 5 percent

for the experiments done with the spiral contractometer [1]. In reviewing the literature, it was found that eq 27 was first written down by Stoney, in the form

$$S=\frac{4E(t^2+td)z}{d^2} \qquad (28)$$

which is the same as eq 27 with r replaced by $L^2/8Z$. This latter expression is the formula that Stoney used for calculating r; L is the length of the plated strip, and Z is the camber of the curved strip (see eq 50A). This formula will be discussed in more detail later. Equation 28 seems to have been entirely ignored by later investigators, probably because Stoney did not give its derivation or indicate its application. It was also passed over by the authors until the above derivation had been arrived at and the similarity of eq 27 with eq 28 was discovered. The diagram for the stresses involved in method III is shown in figure 4. The distinguishing feature is that the stress in the outer fiber of the coating is considerably higher than in the inner fibers. The stress is equal to S, the initial stress, since the last increment of coating does not undergo bending or contraction.

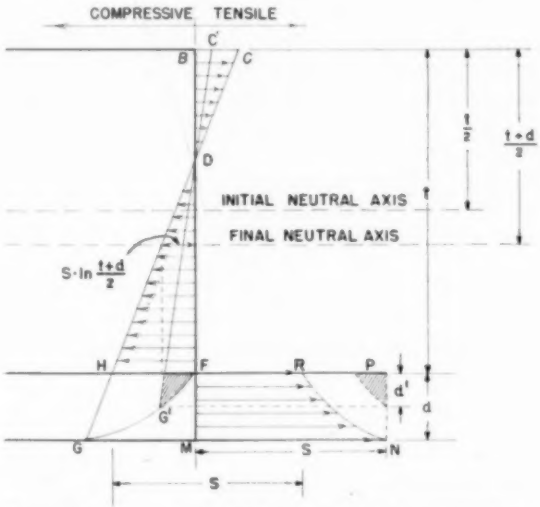

FIGURE 4. *Stress in a plated strip allowed to continuously curve during plating.*

The stresses in the coating are not as readily calculated as in methods I and II, because each increment of coating is deposited in a curved condition, and the stress relief resulting from the subsequent curvature is not given by the simple relation, Ey/r (eq 10). In addition, the compression of the first increments of coating by the tension in the latter increments produces a stress relief, given by eq 19A. The stress in the coating at a distance x from the interface with the basis metal is given by the equation

$$Sx=S\left[1+\ln\frac{t+x}{t+d}-\frac{3(t-d+2x)(d-x)}{(t+d)(t+x)}\right]. \qquad (29)$$

In figure 4, area $GHIF$ represents the compressive force that is generated in the coating as a result of the bending of the beam and the tension of the outer layers of the coating. This area is subtracted from the initial tensile force of the coating (area $FMNP$) to give the final stresses $FMNR$ in the coating. Area $GHIF$ may be considered to have been swept out by the end of the line GDC when it starts from its initial position FDB and goes through the intermediate position $C'DG'$, as the coating increases in thickness.

III. Calculation of Stress When the Young's Moduli of the Coating and Basis Metal are Different

The treatment up to this point has dealt with measurements in which the moduli of the basis metal and coating were the same. The moduli of the common metals range from 2.4×10^6 lb/in.^{2} for lead to 30×10^6 lb/in.^{2} for steel. However, by suitable choice of basis metal, the modulus of the coating need not differ from that of the basis metal by more than a factor of 2. The effect of differences in moduli is negligible when the thickness of the coating amounts to only a few percent of the thickness of the basis metal, but may be significant with thicker coatings.

When the basis metal and the coating have different moduli, the neutral axis no longer passes through the center of mass of the cross section, at $(t+d)/2$, and the moment of inertia of the cross section does not enter simply into eq 8. For method I, Soderberg has derived an expression for the stress of a coating plated on a basis metal of different modulus, but it is too lengthy to be convenient for calculation. In the following derivation, which is similar to that given previously for method I, a simpler expression than that given by Soderberg will be obtained. Also, a simple

empirical formula can be given that will simplify calculations still further.

In the following discussion the ratio of the modulus of the coating to that of the basis metal will be denoted by $R(R=E_c/E_b)$. When the moduli of the coating and basis metal differ, the initial stresses (fig. 2,C) in the coating and basis metal are given by the expressions $S(t)/(t+Rd)$ and $S(d)/(t+Rd)$, instead of by eq 7a and 7b. The bending moment of the coating is equivalent to a couple and is calculated in the same manner as was done for eq 7c, except that the equal and opposite forces in the coating and basis metal are now given by the expression $F=S(t)/(t+Rd)db$ or $F=S(d)/t+Rd)tb$. The distance between the points of application of the forces is $(t+d)/2$, as before. The initial bending moment of the coating is

$$M=\left(\frac{Stdb}{t+Rd}\right)\left(\frac{t+d}{2}\right). \tag{30}$$

The expression for the opposing bending moment impressed by curvature is similar to that in eq 8, except that the moment of inertia, I, of the cross section must be replaced by a more complicated expression. For purposes of calculation, the beam consisting of materials of two different moduli is replaced by an equivalent T-beam, in which the widths of the basis metal and the coating are proportional to their moduli. Thus, the basis metal strip is considered to have a width b, and the coating a width equal to Rb. The neutral axis of this equivalent beam (and also the neutral axis of the original beam) is located in the basis metal at a distance, c, from the outside surface of the coating. This distance is given by the expression

$$c=\frac{t^2+2td+Rd^2}{2(t+Rd}. \tag{31}$$

The moment of inertia of the cross section of the T-beam with respect to the neutral axis is given by the expression

$$I=\frac{b[R(t+d)^4-t^4-Rd^4)(R-1)}{12(t+Rd)}. \tag{32}$$

To simplify later calculations, the Rd^4 quantity in the (t^4-Rd^4) term in eq 32 will be considered negligible and dropped. That this may be done is shown by the fact that in the extreme case when the thickness of the coating is one-half that of the basis metal, and the ratio of their moduli is 2, the error thus introduced is less than 1 percent. On substituting I from eq 32 into eq 8, replacing E with E_b, and setting this equal to the right-hand side of eq 30, an expression for S is obtained

$$S=\frac{E_c(t+d)^3}{6rdt}-\frac{(E_c-Eb)t^3}{6rd(t+d)}, \tag{33}$$

or

$$S=\frac{E_b[R(t+d)^4-(R-1)t^4]}{6rdt(t+d)}.$$

It will be noticed that the first member of the formula is of the same form as eq 9. The second member of the formula is of a similar form except that t and $(t+d)$ are interchanged, and the expression is multiplied by the difference E_c-E_b, of the moduli. The following semi-empirical formula was found to agree within a few percent with eq 33.

$$S=\frac{E_b(t+Rd)^3}{6rdt}, \tag{34}$$

and is much simpler to use.

The derivation of the expression for the stress in an electrodeposited coating, measured by method III is somewhat more involved than that given for method I, but fortunately a simple semi-empirical formula will serve for most purposes. The derivation follows along the same lines as that given for eq 27. The increment of bending moment dm, which is added to the beam by each increment of coating of thickness dx, is given by an expression similar to eq 24 except that the distance of the increment of coating from the neutral axis is not equal to $(t+x)/2$ as in the case of equal moduli, but is given by eq 31. The equation for the change of internal bending moment with deposition of coating is

$$dm=S\left[\frac{t^2+2tx+Rx^2}{2(t+Rx)}\right]bdx. \tag{35}$$

The increment of the opposed bending moment that is developed by the bending of the beam is given by an expression similar to eq 8, except that M and $1/r$ are replaced by the corresponding differentials and I is given by eq 32.

$$dm=\frac{E_b b[R(t+x)^4-t^4(R-1)]}{12(t+Rx)}d\left(\frac{1}{r}\right). \tag{36}$$

Equations 35 and 36 yield the following equation for the stress

$$S\int_0^d \frac{t^2+2tx+Rx^2}{R(t+x)^4-(R-1)t^4}\,dx=\frac{E}{6r}. \qquad (37)$$

By making the change of variable to $z=(t+x)/t$, breaking the fraction into partial fractions and integrating, the following expression is obtained for the stress

$$S\left[\left(\frac{1+H^2}{2H}\right)\tanh^{-1}\left(\frac{H-Q}{1-HQ}\right)+\left(\frac{1-H^2}{2H}\right)\tan^{-1}\left(\frac{H-Q}{1+HQ}\right)-H^2\tanh^{-1}\left(\frac{H^2-Q^2}{1-H^2Q^2}\right)\right]=\frac{E_bt}{6r}, \qquad (38)$$

where $H^4=(E_c-E_b)/E_c$, and $Q=Ht/(t+d)$.

It is of interest to note that eq 38 can be considerably simplified. When the absolute value of x is less than 1, the $\tan^{-1} x$ and $\tanh^{-1} x$ may be represented by a series of the form, $x+ax^3+bx^5\ldots$. The first term approximation is accurate enough for present purposes. On replacing the arc tangents by their arguments and simplifying, the following equation is obtained

$$S=\frac{E_bt(t+d)}{6rd}-\frac{(E_c-E_b)t^3}{6rd(t+d)}. \qquad (39)$$

This equation parallels eq 33, because the first term is the same as the expression for materials of the same modulus (eq 27), and the second term is the same as that of eq 33.

Over a range of thickness of coating of $d=0$ to $t/2$, good agreement with eq 38 is obtained by the simple semiempirical formula

$$S=\frac{E_bt(t+R^{5/4}d}{6rd}. \qquad (40)$$

However, over a more limited range the formula

$$S=\frac{E_bt(t+Rd)}{6rd}, \qquad (41)$$

is quite satisfactory.

IV. Calculation of the Effect of Temperature Changes on the Measurement of Stress

The plated strip of metal constitutes a bimetallic element, such as is used in thermoregulators, and will curve as a result of temperature changes if the two metals differ in coefficient of expansion, which is usually the case. The measurements made with the spiral contractometer are made at the temperature of the plating solution, and the only interest in the effect of temperature changes is to determine the precision of temperature regulation required to keep the error from this cause below 1 percent. After the contractometer is removed from a warm plating solution, an appreciable movement of the pointer occurs, thus showing that the effect of the temperature is not negligible. The effect of temperature change may be serious if the curvature of the plated strip is measured after it is removed from a warm plating solution, as is usually done in applying methods I and II.

In the following discussion of thermal effects, a different approach is employed than that used by Soderberg, and the equations developed are not the same. After a strip has come to an equilibrium curvature under the tension of the coating, the effect of a subsequent temperature change is to alter the curvature. In order to calculate the stress in the deposit, it is first necessary to correct the final observed curvature, $1/r_f$, for the increment of curvature, $\Delta(1/r)$, resulting from the temperature change. This is readily done as follows: The equations for stress, as developed for the three different methods may be written in the form, $S=Q(1/r)$, where $1/r$ is the curvature resulting from the stress in the coating alone. The equation is corrected by subtracting the curvature superimposed upon it by thermal stresses and takes the form

$$S=Q\left[\frac{1}{r_f}-\Delta\frac{(1)}{(r)}\right]=Q\left(\frac{1}{r}\right). \qquad (42)$$

The value of $\Delta(1/r)$ is calculated in the manner used for method I, from the known thermal stresses set up in the beam. The additional internal bending moment, produced in the curved beam by the thermal stresses alone, is equated to the opposing bending moment impressed by the corresponding increment of curvature. Since the longitudinal forces, F, set up by the thermal effect are equal and opposite in the coating and basis metal, their bending moment is equivalent to a couple with the distance, $(t+d)/2$, between their points of application. Equating the bending

moment of the couple to the bending moment impressed by curvature gives

$$F\frac{(t+d)}{(2)}=EI\Delta\frac{(1)}{(r)}=\frac{E(t+d)^3b}{12}\Delta\frac{(1)}{(r)}. \quad (43)$$

$$\Delta\frac{(1)}{(r)}=\frac{6F}{Eb(t+d)^2}. \quad (44)$$

It is now necessary to have an expression for the force, F, in the coating or base metal. It should be remembered that F is the force which existed before the strip was allowed to undergo the additional increment of curvature, $\Delta(1/r)$ (just as in method I, where the bending moments were calculated from the forces in the uncurved beam). A condition of equilibrium for the bimetallic strip (assuming that it is held at constant curvature) is that the change in length, or the strain of each metal strip must be equal.

$$A_c\Delta T+\frac{F}{dbE}=A_b\Delta T-\frac{F}{tbE}. \quad (45)$$

A_c and A_b are the coefficients of expansion, and the temperature change is ΔT. The strains produced by thermal expansion are $A\Delta T$. The other two terms represent the strains produced by the force F.

From eq 45, $F=[Etdb(A_b-A_c)\Delta T]/(t+d)$, and substituting in eq 44,

$$\Delta\left(\frac{1}{r}\right)=\frac{6td(A_b-A_c)\Delta T}{(t+d)^3}. \quad (46)$$

Applying this correction for $\Delta 1/r$ to eq 42, the following equations for stress are developed for methods I and III, respectively:

$$S=\frac{E(t+d)^3}{6tdr}-E\Delta T(A_b-A_c). \quad (47)$$

$$S=\frac{Et(t+d)}{6dr}-E\Delta T(A_b-A_c)\left(\frac{t}{t+d}\right)^2. \quad (48)$$

It will be noted that the formulae for stress are the same as the original formula except for the subtraction of a term involving the difference A_b-A_c, of the coefficients of expansion. The correction term in eq 47 agrees with the expression given by Heussner [5] but not with the one given by Soderberg [3]. For metals that differ in coefficient of thermal expansion by 5 x 10^{-6}, for example copper and steel, the correction amounts to about 150 lb/in.^{2}/° C. When measuring low stresses, such as a few thousand pounds per square inch, it would be important to control the temperature of plating within 1 or 2 deg, but a control of 5 deg C would probably be sufficient when measuring stresses above 20,000 lb/in^2.

If the moduli of the coating and the basis metal are different, the appropriate correction term is subtracted from the expressions previously given for the stress in eq 33, 34, or 38 to 41. The correction for method I can be shown to have the same form as that given in eq 47, namely $E_c\Delta T(A_b-A_c)$ (except that E is replaced by E_c). The correction term for method III can be evaluated by the method given, but for practical purposes the same correction term as that given in eq 48 (except that E is replaced by E_c) may be used.

V. Stress Remaining in Coating After Removal of Basis Metal

Some observers have attempted to note the trend of stress with thickness by observing the direction of bending of the deposit after the basis metal was dissolved. However, in order to draw any conclusions, it is first necessary to know, as a basis of reference, the direction of bending when the stress is uniform throughout the deposit. The three diagrams (fig. 2, D, 3, C, and 4), show the stress existing in the coating after bending has taken place. In method I it is obvious that the coating would straighten out if the basis metal were removed, since the coating was uniformly stressed throughout when it was in its initial straight position. When the basis metal is removed, the coating will simply contract slightly and return to its original straight condition. In method II, since the outer fibers of the coating are under slightly higher stress than in method I, the coating should not quite straighten out, but should remain slightly curved. This slight curvature would be difficult to demonstrate in practice, since the tendency for the stress in many coatings to decrease with thickness usually more than compensates for the excess outer stress. The stresses in the coating in method III differ from the two preceding cases in that the outer fibers of the coating have a considerably higher stress than the inner fibers. This indicates that the curved coating should curve still further after the basis metal

is removed. The percentage difference in stress between the inner and outer fibers is approximately equal to $3(d/t)$, which amounts to about 15 percent for $d/t=0.05$, and hence the additional curvature should be detectable if the coatings are moderately thick. By comparison, the percentage difference in stress between the inner and outer fibers in method I is $6(d/t)^2$, which is much smaller, but yet sufficient to bend the coating back nearly straight.

The expected increase in curvature was not observed when the basis metal (copper) was dissolved from a deposit obtained from a Watts nickel bath, probably because the stress in the outer layers decreased as the coating became thicker. However, the curvature of a deposit from a chloride nickel bath increased considerably when the basis metal was dissolved.

It has seemed paradoxical to some platers that a sheet of plated metal, which has been deposited on a rigid backing, does not curl when it is stripped from the basis metal, whereas a thin plated sheet will develop considerable curvature. The explanation of this paradox is that curving will take place only when there are differences of stress between the two faces of a strip. If the stress in an electrodeposited coating is uniform, it is relieved only by contraction of the coating when it is stripped from the basis metal.

VI. Comparison of Formulas

It is interesting to compare the Stoney formula with the other formulas that have been derived for computing stress measured by the three different methods. This comparison will be made by expanding the formulas and comparing only the approximations that involve the first two terms.

In the last column of table 1, the approximation formulas are expressed in terms of the Stoney formula, S_s. The first term of each formula consists of the Stoney formula, and the second term consists of a correction, involving the ratio, d/t, of the thickness of the coating to that of the basis metal. The correction diminishes as the thickness of the coating decreases.

A meaning can be attached to the two terms of the formulas for method I, (eq 9 and 34). The S_s term is the approximate stress in the coating, calculated without regard for the thickness or physical properties of the coating. The second term, $S_s(3Rd)/(t)=E_cT/2r$, can be shown to be the average stress that the coating loses in bending from its initial straight position to a curvature of $1/r$. The midpoint of the coating is approximately at a distance $t/2$ from the neutral axis of the beam. The compressive stress that is set up as a result of curvature is $E_c/2r$ (by eq 10), which is the second term of the formula. This compressive stress diminishes the tensile stress of the coating by this amount.

If carried further, the expansions of the formulas for methods I and II would yield terms containing higher powers of d/t, and therefore their contribution to the calculation would be small. The terms in d^2/t^2 represent the correction involved in the shift of the neutral axis from the center of the unplated beam to the center of the plated beam.

In table 2 are shown the errors involved in

TABLE 1. *First two terms in the expansion of the formulas for stress*

Stoney's equation $S_s=\frac{Et^2}{6rd}$				$=S_s$
Method	Equation			
I	9	$S=\frac{E(t+d)^3}{6td^2r}$	$=\frac{E(t^3+3t^2d)}{6td^2r}+\ldots$	$=S_s\left(1+3\frac{d}{t}\right)+\ldots$
	16	$S_{ss}=\frac{E(t^3-td)}{6rd}+\ldots$		$=S_s\left(1-\frac{d}{t}\right)+\ldots$
	34	$S=\frac{E_s(t+Pd)^3}{6rdt}$	$=\frac{E_s(t^3+3Pt^2d)}{6rdt}+\ldots$	$=S_s\left(1+3P\frac{d}{t}\right)+\ldots$
II	23	$S=\frac{E(t+d)^3}{3dr(2t+d)}$	$=\frac{E(t^3+3t^2d)}{3dr(at+d)}+\ldots$	$=S_s\left(1+\frac{5}{2}\frac{d}{t}\right)+\ldots$
III	27	$S=\frac{Et(t+d)}{6rd}$	$=$	$S_s\left(1+\frac{d}{t}\right)+\ldots$
	41	$S=\frac{E_st(t+Pd)}{6rd}$	$=$	$S_s\left(1+R\frac{d}{t}\right)+\ldots$

819237—49——3

using the approximation formulas for coatings of various relative thickness (compared with the basis metal). It will be noted that if the moduli of the basis metal and coating are the same, the Stoney formula does not cause a serious error if used for method III, provided that d/t is less than 0.1, but that the error is appreciable for method I. However, if the moduli differ appreciably, the Stoney formula would not be a safe one to use for either method. The formulas that are the most convenient to use for calculation have been designated by an asterisk.

TABLE. 2 *Errors involved in using approximation formulas for calculating stress in coatings*

Method of measurement	Formula	Error in using approximation formula for d/t equal to—			
		0.05	0.1	0.2	0.5
Moduli of coating and basis metal are equal					
*Method I. Cathode completely rigid.	$\frac{E(t+d)^3}{6rdt}$	*Per cent* ...	*Per cent* ...	*Per cent* ...	*Per cent* ...
Stoney	$\frac{Et^2}{6rd}$	−14	−25	−42	−70
Two-term approximation	$\frac{Et^2}{6rd}=\left(1+\frac{3d}{t}\right)$	−1	−2	−7	−26
Method II. Cathode restricted from bending.	$\frac{E(t+d)^3}{3rd(2t+d)}$	...	...	...	...
Stoney	$\frac{Et^2}{6rd}$	−11	−21	−36	−63
Two-term approximation	$\frac{Et^2}{6rd}\left(1+\frac{5}{2}\frac{d}{t}\right)$	0	−1	−4	−17
*Method III. Cathode bends during plating.	$\frac{Et(t+d)}{6rd}$	...	...	...	...
Stoney	$\frac{Et^2}{6rd}$	−5	−9	−17	−33
Moduli of coating and basis metal differ by $\frac{E_c}{E_b}=R=2$					
Method I. Exact formula	$\frac{E_c(t+d)^3}{6rdt}-\frac{(Ec-Eb)t^3}{6rd(t+d)}$	...	...	...	...
Stoney	$\frac{Et^2}{6rd}$	−26	−43	−62	−84
*Semiempirical	$\frac{E_b(t+Rd)^3}{6rdt}$	−2	−1	+5	+32
Two-term approximation	$\frac{Et^2}{6rd}\left(1+3R\frac{d}{t}\right)$	−5	−9	−16	−34
Method III. Exact formula	See eq 38	...	...	...	...
Stoney	$\frac{Et^2}{6rd}$	−11	−19	−33	−52
*Two-term approximation	$\frac{Et(t+Rd)}{6rd}$	−2	−3	−6	−4
Empirical	$\frac{Et}{6rd}(t+R^{0.4}d)$	0	0	−1	+4
Simplified	$\frac{E_cd}{6rd}(t+d)-\frac{(E_c-E_b)t^3}{6rd(t+d)}$	+3	+4	+5	12

TABLE 2. *Errors involved in using approximation formulas for calculating stress in coating*—Continued

Method of measurement	Formula	Error in using approximation formula for d/t equal to—			
		0.05	0.1	0.2	0.5
Moduli of coating and basis metal differ by $\frac{E_c}{E_b}=R=4$					
Method III. Exact formula	See eq 38	*Per cent* ...	*Per cent* ...	*Per cent* ...	*Per cent* ...
Stoney	$\frac{Et^2}{6rd}$	...	...	−51	...
Two-term approximation	$\frac{Et(t+Rd)}{6rd}$	...	...	−12	...
Empirical	$\frac{Et}{6rd}(t+R^{0.4}d)$	...	...	+4	...
Simplified	$\frac{E_cd}{6rd}(t+d)-\frac{(E_c-E_b)t^3}{6rd(t+d)}$	...	...	−13	...

VII. Calculation of the Radius of Curvature

The value for the curvature $1/r$ of the strip must be substituted into the formulas for the stress in the coating. The curvature of the bent strip is usually measured indirectly, although it could be determined directly by comparison with a set of curvature gages, as was done by Soderberg [3]. Several different methods of measuring and calculating the curvature have been used, and there is a chance of some confusion. In at least one instance in the literature, an incorrect formula for calculating the curvature resulted through an error in selecting the proper deflection of the bent strip. Three methods of calculating the curvature, or change in curvature, of the plated strip have been used. These involve (a) measuring the camber of the curved strip, (b) measuring the

deflection of the end of the strip, and (c) measuring the angular deflection of the end of a helix.

In figure 5, AOA' represents the strip that has been curved by plating. Initially the strip occupied the position of the straight line ABC. The other lines in the figure are auxiliary lines for aiding the discussion. The method of calculating the curvature that was used by Stoney, involves measuring the sagitta, Z, of the arc AOA'. The curved strip is set on a flat surface with the convex side up, and the camber of the arc measured with a microscope or special micrometer.

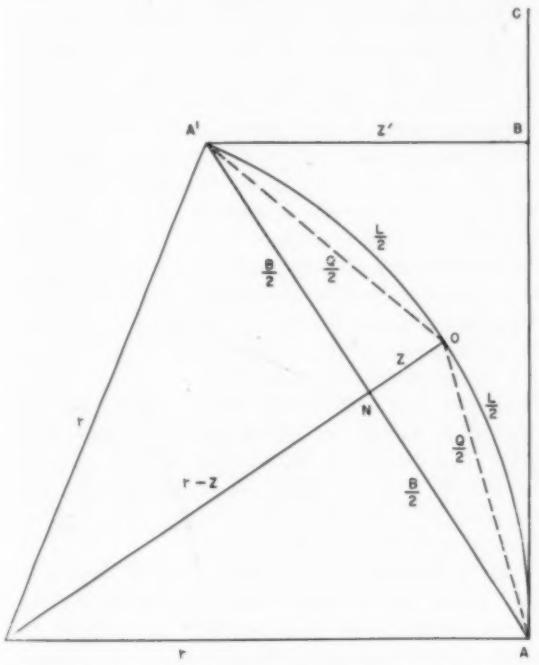

FIGURE 5. *Diagram showing the relation between the radius of curvature of a plated strip and the deflection of the end or center.*

The curvature $1/r$ is calculated from the following formula:

$$\frac{1}{r}=\frac{2Z}{B^2+Z^2}. \tag{49}$$

Another formula is

$$\frac{1}{r}=\frac{8Z}{Q^2}. \tag{50}$$

The broken line $Q=AOA'$ may be replaced by the arc length $AOA'=L$, which is the length of the curved strip, without making an error of more than about 2 percent, providing that the sagitta, Z, is not more than 10 percent of the length of the strip. The formula then becomes

$$\frac{1}{r}=\frac{8Z}{L^2}. \tag{50a}$$

In some experiments the strip is anchored at A, and the strip then curves away from its initial position ABC. The deflection Z' is measured and used to calculate the curvature of the strip. The formula for calculating the curvature is

$$\frac{1}{r}=\frac{2Z'}{B^2}. \tag{51}$$

The arc length L, which is the length of the strip, may be substituted for the chord without much error

$$\frac{1}{r}=\frac{2Z'}{L^2}. \tag{52}$$

By comparing eq 52 with eq 50a, it will be noted that the deflection Z' is approximately four times greater than the sagitta A. The error involved in the approximation of eq 52 is less than 2 percent if the deflection Z' is not greater than 20 percent of the length of the strip. For equal curvatures, the error of this approximation is about twice as large as that of eq 50a.

The main application of the spiral contractometer is for making measurements by method III, as the spiral continuously curves during the plating. However, by anchoring the needle, and releasing it at the conclusion of the plating, the experiment may be conducted according to method II.

Since the spiral is initially curved, the measurement consists not in determining the curvature $1/r$, as was done for an initially straight strip, but in determining the change in curvature of the spiral $\Delta(1/r)=(1/r_2)-(1/r_1)$. This expression is to be substituted for $1/r$ in the formulas that are applied to measurements made with the spiral contractometer. The change in curvature is computed from the angular deflection D, of the spiral as follows. When the curvature of an arc of fixed length is increased, the angle subtended by the arc increases. The change in the angle subtended by the arc is equivalent in the case of the helix of the contractometer to the angular deflection of the torque rod. The arc has an initial curvature of L/r_1 radians and after further bending has a curv-

ature L/r_2 radians. The angular deflection (or change in angle) D, (see fig. 6) is:

$$\left.\begin{aligned} D=FOB-COB=\frac{L}{r_2}-\frac{L}{r_1}=L\left(\frac{1}{r_2}-\frac{1}{r_1}\right)=L\Delta\left(\frac{1}{r}\right) \\ \Delta\left(\frac{1}{r}\right)=\frac{D}{L}=\frac{\pi D'}{180L}. \end{aligned}\right\} \quad (53)$$

The expression D' refers to the angular deflection measured in degrees instead of in radians.

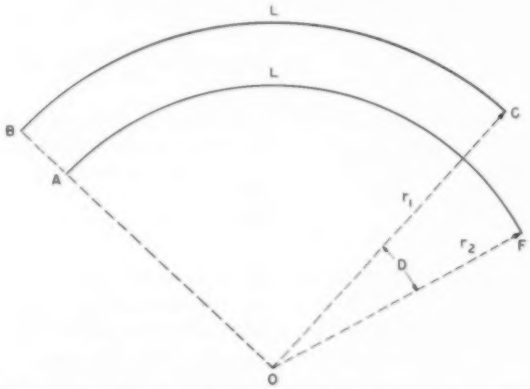

FIGURE 6. *Diagram showing the relation between the radius of curvature and the angle subtended by an arc of constant length.*

The two arcs in the figure are of equal length.

In this discussion the arc has been considered to lie in one plane. However, the same relation holds for a helix, if the curvature of the arc is considered with respect to the axis of the helix. This is equivalent to considering the length of the projection of the arc upon a plane normal to the axis of the helix. The projected length of the helix is approximately constant and is equal to π C times the number of turns, where C is the diameter of the helix. The number of turns of the helix is found most readily by pushing the coils together until the helix forms a cylinder and then dividing the height of the cylinder h, by the pitch, p, of the helix.

$$L=(\pi C)\left(\frac{h}{p}\right)=\frac{\pi Ch}{p}. \quad (54)$$

The pitch is the width of the strip, from which the helix is made, measured in a direction parallel to the axis of the helix. It is related to the actual width b, of the strip by $b=p\cos a$, where a is the helix angle. The projected length of the strip is related to the true length of the strip L', by $L=L'\cos a$.

From eq 53 and 54, the expression for the change in curvature of the helix takes the form

$$\Delta\left(\frac{1}{r}\right)=D'\left(\frac{p}{180Ch}\right). \quad (55)$$

The expression in parentheses is a constant for a given helix, and needs to be determined only once.

No analysis was made of the precision of the relation (eq 55) between the change in curvature and the deflection, as was done in the discussion of the formulas applied to the flat strips. Slight errors may result from end effects, since the diameter of the helix will change slightly as its curvature changes, but the diameter of the ends is maintained constant by the fittings. Another possible source of error is the change in the helix angle as the helix coils or uncoils with the plating operation. A direct observation of the angle showed that the change in the angle in an experiment was not readily observable. It is believed that the angular deflection of the pointer is a more direct measure of the change in curvature than is the linear deflection measured on a flat strip. Therefore, the errors involved in computing the change in curvature are probably smaller than those involved in eq 50a and 52, or well under 1 percent for measurements involving less than one complete turn of the pointer (which is equivalent to a 36° turn of the helix).

One advantage of the spiral contractometer is that the unplated helix can be calibrated with known weights and thus make it unnecessary to know the modulus of the basis metal. An expression will now be derived relating the calibration constant K', of the helix to its Youngs modulus E, in order that K' can be substituted for E in the formulas that have already been developed. The deflection of the torque rod of the contractometer is proportional to the torque M, which is applied by a weight attached with a thread to the lever arm.

$$M=K'D'. \quad (56)$$

The bending moment, M, transferred to the helix is given by an equation similar to eq 8

$$M=EI\Delta\left(\frac{1}{r}\right)=\frac{Et^3p}{12}\Delta\left(\frac{1}{r}\right). \quad (57)$$

It will be noted that the moment of inertia I, of the strip composing the helix, is taken for a cross section that is parallel to the axis of the helix, because the helix curves and uncurves with respect to the axis as a center. On substituting in eq 57 for $\Delta(1/r)$, and for M, using eq 55 and 56, the expression for E is obtained

$$E=\frac{2160K'Ch}{t^3p^2}. \tag{58}$$

The Youngs modulus of the metal composing the helix has been calculated with the aid of this formula, and the agreement with the accepted value of the modulus was within 3 percent.

In calculating the stress in a deposit, Stoney's equation and eq 27 are the ones most frequently used in conjunction with the spiral contractometer. On substituting for E from eq 58 and for $\Delta(1/r)$ from eq 55, Stoney's equation takes the form

$$S_s=\frac{2K'D'}{tpd}. \tag{59}$$

Equation 27 takes the form

$$S=\frac{2K'D'(t+d)}{t^2pd}=S_s\left(1+\frac{d}{t}\right). \tag{60}$$

In using the spiral contractometer, the angular deflection of the torque rod is not read directly, but the deflection in degrees is read from a pointer that is geared to the torque rod. The pointer makes G revolutions for one revolution of the torque rod. Therefore, in using eq 55, in which the deflection D' relates to the torque rod, the observed reading $\overline{D}$, of the pointer must be divded by G or

$$\Delta\frac{(1)}{(r)}=\frac{\overline{D}}{G}\frac{(p)}{(180Ch)}. \tag{61}$$

Also, the calibration constant of the helix is usually determined with direct reference to the deflection of the pointer in degrees rather than of the torque rod. The relation between the constant K, of the readings referred to the pointer, and the constant K' of those referred to the torque rod is:

$$K'=KG. \tag{62}$$

This substitution must be made in calculating E from eq 58. Since

$$K'D'=K\overline{D}, \tag{63}$$

the forms of eq 59 and 60 are unchanged if the constant and the deflection of the pointer are substituted for those of the torque rod.

The authors express their appreciation to W. Ramberg and S. Levy of the Engineering Mechanics Section of this Bureau for their assistance in matters relating to the theory of elasticity.

VIII. References

[1] A. Brenner and S. Senderoff, Proc. Am. Electroplaters' Soc. (publication pending); J. Research NBS **42,** 89 (1949) RP1953.

[2] G. G. Stoney, Proc. Roy. Soc. (London) [A], **82,** 172 (1909).

[3] K. G. Soderberg and A. K. Graham, Proc. Am. Electroplaters' Soc. p. 74 (1947).

[4] R. H. Barklie and J. J. Davies, Proc. Inst. Mech. Eng., p. 731 (1930, I).

[5] C. E. Heussner, A. R. Balden, and L. M. Morse, Plating **35,** 719 (1948).

WASHINGTON, October 29, 1948

U. S. Department of Commerce
National Bureau of Standards

Research Paper RP1955
Volume 42, February 1949

Part of the Journal of Research of the National Bureau of Standards

Laboratory Wear Tests With Automotive Gear Lubricants

By Samuel A. McKee, James F. Swindells, Hobart S. White, and Wayne Mountjoy

In the past, most of the work with the SAE extreme-pressure lubricants testing machine has been confined to the testing of the load-carrying capacity of gear lubricants under certain fixed operating conditions that simulate high speed and shock load. This paper describes a different use of the machine for the determination of the wear with gear lubricants under conditions simulating high torque and low speed. The modifications to the machine and the procedure used are described in detail.

Data were obtained with a straight mineral oil and 11 representative samples of commercial lubricants commonly used in automotive gears, when operating at 225° F and various constant loads. The loads covered were 90, 135, 180, and 225 pounds (scale reading). These data showed marked differences in the performance of the lubricants in the higher load range. The trends shown by these differences were in reasonable agreement with the known service performance of these lubricants.

Other information given includes an indication of run-in wear, the change in surface roughness of the test cups with wear, and the effect of the original surface roughness on the rate of wear.

I. Introduction

Of the various laboratory testing machines that have been commonly used in the study of automotive gear lubricants, the SAE machine, in general, more nearly simulates gear operation.[1,2] The two contacting cylindrical test cups of this machine are rotated at different speeds under load and provide a combined rubbing and rolling action that is typical of loaded gear teeth. A further similarity is a line contact that is constantly changing with respect to the surfaces of both cups, hence no one point on the periphery is under continuous stress.

In the past, most of the work with the SAE machine has been confined to the testing of the load-carrying capacity of gear lubricants under certain fixed operating conditions that simulate shock loading.[3] This paper describes the use of the machine for the determination of the wear with gear lubricants under conditions simulating high torque and low speed.

The machine is particularly adaptable for wear tests in that the test specimens are of such size and shape that accurate indications of wear may be obtained by determinations of loss in weight. Also, any wear that occurs on the test cups does not materially affect the area of contact under a given load. On the other hand, the method of lubricating the test surfaces is not especially suitable for long-time tests, and it seemed advisable to modify the machine in this respect.

II. Modifications of the SAE Machine

Although the primary objective in modifying the lubricating system was long-time operation, it was felt desirable also to provide better temperature control of the upper test cup. The lower test cup is supported in a small oil box with the oil level about half way up the cup, and lubrication

[1] William S. James, SAE Trans. **47,** 312 (1940).
[2] S. A. McKee, F. G. Bitner, and T. R. McKee, SAE Trans. **33,** 402 (1933).
[3] CRC Test procedure (CRC designation L-17-545), CRC Handbook, p. 458 (1946).

between the two cups is effected by the oil carried up by the lower cup as it rotates. Since only the lower cup is cooled by immersion in the oil bath, the upper cup runs at a considerably higher temperature. This is usually quite noticeable in the load-carrying capacity tests. For this reason, it was decided to use an additional oil reservoir of larger capacity with a circulating system for applying a stream of oil to the upper test cup.

The design of the SAE machine is such that one of the major problems in the development of an oil circulating system was the prevention of excessive oil leakage around the test cups and oil box. The system in present use is reasonably satisfactory in this respect.

The arrangement of this circulating system is shown in figure 1. The oil being tested is drawn from the reservoir, A, by the motor-driven pump, B, and delivered through the ¼-in. pipe, C, to the top of the upper test cup, which is covered by the special oil splash guard, D. The oil then drains to the oil box, E. This box is fitted with two ¼-in. overflow pipes, F, so located that the oil level in the box partially immerses the lower test cup. The oil from the overflows falls into open fittings in the ¾-in. drain pipe, G, and drains back to the reservoir. Also, shown in the figure are thermocouples, H, in the oil box and oil reservoir, heater, J, on the oil reservoir, and auxiliary heater, K, on the delivery pipe.

A view of the test cups and oil box assembled except for the splash guards is shown in figure 2. The counterweight, L, is mounted from the oil box to counterbalance the overflow pipes and the overhanging lower test-cup shaft. An oil thrower, M, is mounted on the upper test shaft as shown, and N is a special nut for the upper test cup (a portion of its length is a cylindrical seat for the inner oil guard, which is shown in fig. 3). Figure 3 shows accessory parts and changes in the oil box as follows: P, inner oil guard that rides on upper test shaft; R, plate sealing oil-box bearing; S seal for shaft at other oil-box bearing; T, dams welded to

FIGURE 1. *General view of SAE machine, showing arrangement of special oil-circulating system.*

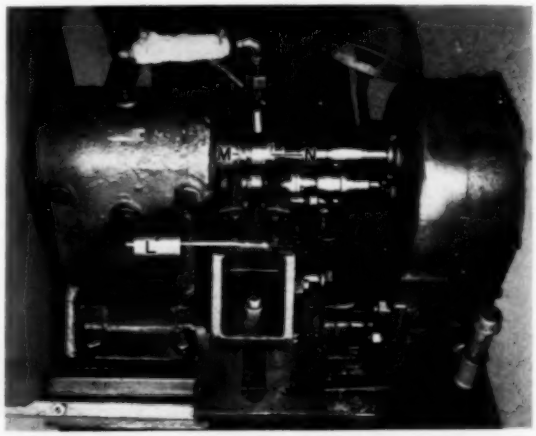

FIGURE 2. *Close-up view of test shafts and oil-box assembly of SAE machine.*

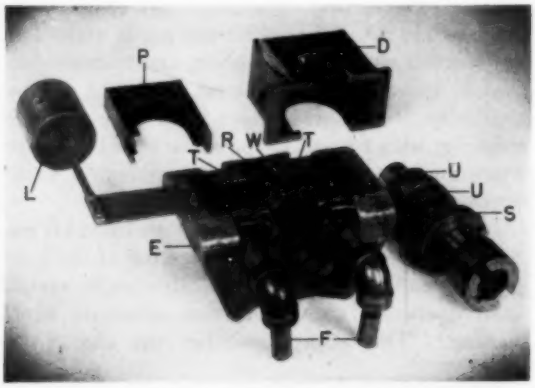

FIGURE 3. *Special parts and changes to oil box and lower test shaft.*

oil box to fit outer oil guard D; U, grooves in spacers on lower test shaft; W, special drain hole in oil-box bearings.

III. Lubricants

The lubricants used in these tests included a Navy Contract 1080 mineral oil, five lubricants conforming to U. S. Army Specification 2–105B,[4] five lubricants conforming to Federal Specification VV–L–761,[5] and one lead-soap active-sulfur lubricant. All were SAE 90 grade. In the figures given in this paper the mineral oil is designated by the number 1080, the Army specification lubricants by the letter A and a number representing a particular lubricant, the Federal specification lubricants by the letter F and the lubricant number, and the lead-soap active-sulfur lubricant by the letters AS.

IV. Test Method

In all the tests, the upper test cup was driven at a speed of 500 rpm with a 3.4 to 1 gear ratio between the upper and lower cups. This provided a 2.4 to 1 ratio of rubbing to rolling at the contacting surfaces. The specimens used were steel Timken test cups T–48651 and in most of the tests had an average surface roughness of from 25 to 30 microinches (rms, Profilometer). A 2-quart sample of oil was used in each run. This was circulated at a rate of about 500 g/min. With a constant oil temperature of 225° F, tests were made at constant loads of 90, 135, 180, and 225 lb (scale readings), respectively. The loading system is such that the corresponding loads on the 2-in. diameter by ½-in. test cups are ten times the scale readings. Tests were also made at 250° F and 180-lb load. The above conditions approximate the range of conditions covered in the usual high-torque low-speed gear tests.

The test cups were weighed before and after each period of operation during a test, the loss in weight being used as a measure of wear during the period. In the first few tests in the program, weighings were made at frequent intervals, and the tests were run for as long as 75 hr. It was found, however, that representative data could be obtained by operating for about 25 hr, making weighings after operating 4, 11, 18, and 25 hr, respectively. Most of the tests were run on this schedule.

V. Wear Data

Data obtained in the tests with the mineral oil, lead-soap active-sulfur lubricant and five Army specification 2–105B lubricants, operating at 90-lb load (scale reading) and at a temperature of 225° F are shown in figure 4, where the loss in weight of both test cups expressed in milligrams is plotted against time in hours. These data indicate that under the conditions present there was a run-in period of high rate of wear for a few hours, after which the wear settled down to a fairly constant rate. In general, this straight portion of the curve is well established by 25 hr of operation, and subsequent test runs were of that duration.

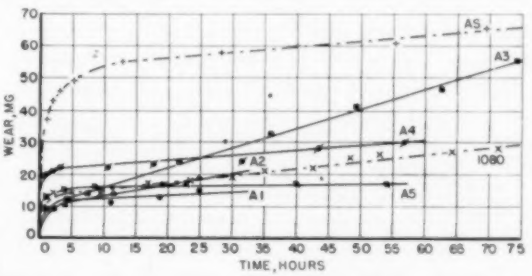

FIGURE 4. *Wear versus time curves for Army specification 2–105 B lubricants operating at 90-lb load and 225° F.*

Wear versus time curves obtained under similar conditions with five Federal Specification VV–L–761 lubricants are given in figure 5. These curves are like those in figure 4 in that they show that there is a run-in period followed by a region where there is a constant rate of wear. The slope of this straight portion of the curve is more significant from the standpoint of estimating gear life than the observed loss in weight for any given length of time. This is illustrated by a comparison of curves 1080, F2, and F5 in figure 5. With these lubricants the losses in weight are quite different, but the slopes of the curves are about alike. Accordingly, if they were extrapolated to estimate long-time wear, the initial differences in loss in weight would lose their significance.

Similar curves for all the lubricants when operating at 225° F and under loads of 135, 180, and 225 lb are given in figures 6, 7, and 8, re-

[4] U. S. Army Specification No. 2–105B, Lubricant, Gear, Universal (Mar. 28, 1946).

[5] Federal Specification VV–L–761 for Lubricants, Enclosed-gear, Hypoid—Gear, and other types (Nov. 28, 1947).

819237—49——4

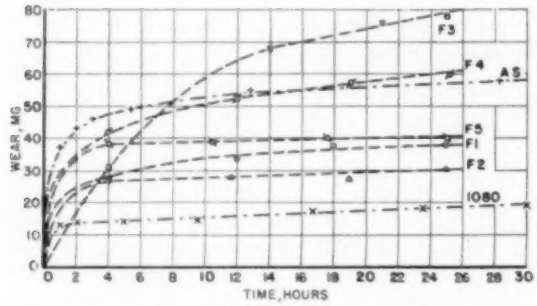

FIGURE 5. *Wear versus time curves for Federal Specification VV–L–761 lubricants operating at 90-lb load and 225° F.*

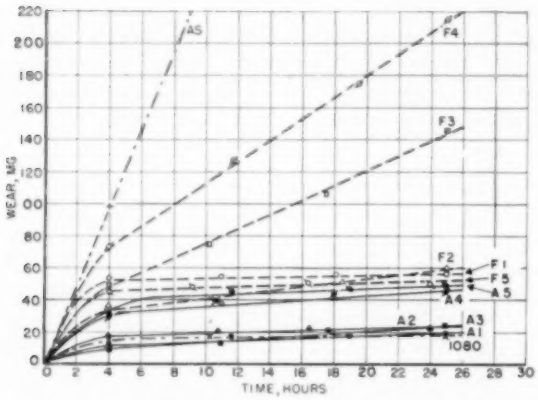

FIGURE 6. *Wear versus time curves for all lubricants operating at 135-lb load and 225° F.*

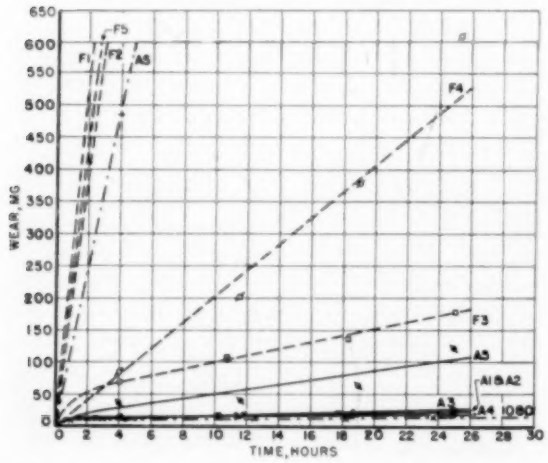

FIGURE 7. *Wear versus time curves for all lubricants operating at 180-lb load and 225° F.*

spectively. From these figures, it will be noted that at the higher loads the rate of wear with some of the lubricants showed a marked increase, whereas with others there was little effect.

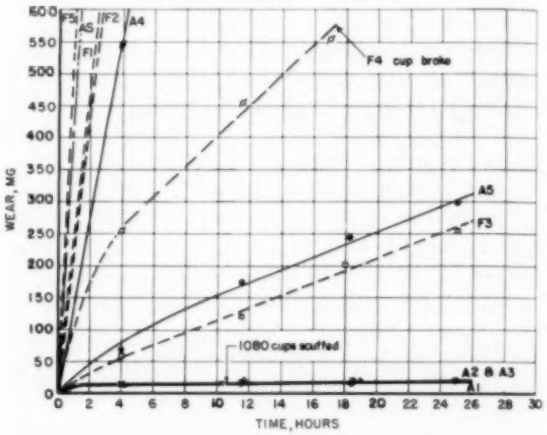

FIGURE 8. *Wear versus time curves for all lubricants operating at 225-lb load and 225° F.*

These effects are summarized in table 1, which gives the values of the rate of wear expressed in milligrams per hour for each lubricant at each operating condition. These values are based on the slopes of the straight portion of the curves. Values for the tests at 225° F are also shown in figure 9, from which it will be noted that when operating at this temperature and the 90-lb load the rate of wear with all the lubricants is relatively low. At the 135-lb load, however, the wear with the lead-soap active-sulfur lubricant and two of the Federal specification lubricants has definitely increased. These differences become accentuated at the two higher loads. At 180 lb, the wear was excessive with the active-sulfur lubricant and with four of the Federal specification lubricants. At 225 lb, the wear was relatively low with three Army specification lubricants, moderate with one Army and one Federal lubricant, excessive with four Federal, one Army, and the active-sulfur lubricant, and scuffing occurred with the mineral oil.

Duplicate tests were not made with all of the lubricants under all operating conditions. However, the results of check tests under some conditions are given in parenthesis in table 1. These indicate that the results are reproducible within practicable limits.

TABLE 1. *Summary of wear data*

Lubricant	Rate of wear after run-in period, mg/hr, at—				
	225° F				250° F
	90 lb	135 lb	180 lb	225 lb	180 lb
1080	0.2 (0.1)	0.1 (0.1)	0.2 (0.2)	Scuffed	0.2
AS	.2	25	120	440	400
A1	.1	0.2	0.3	0.2	0.2
A2	.4	.4	.3	.2	.4
A3	.6	.7	.8	.2	.6
A4	.2 (0.3)	.7	.2	140	.3
A5	.1	.4	3.7 (4.7)	9.9	9.0
F1	.2	0.2	200	240	260
F2	.2	1.3	190	215	200
F3	1.0	4.6 (2.5)	5.2	9.7	4.5
F4	0.6	6.7	21 (24)	[a] 24	10
F5	.1	0.3	220	560	500

[a] Top cup broke: first test at 17 hr; check at 7½ hr.

Although wear data with hypoid gears are not available for a direct comparison, it is believed that these results are in reasonable agreement with the known service performance with these lubricants. The wear with the mineral oil was low up to the point where it would not carry the load, whereas with the lead-soap active-sulfur lubricant (which will carry a high shock load) the wear was relatively high at all but the lightest load.

Values of the rate of wear obtained in the tests with all the lubricants operating at the 180-lb load and 250° F are also given in table 1. These data show no marked difference from the data obtained at 225° F with the same load.

VI. Surface Roughness Data

In most of the tests, Profilometer readings of the surface roughness of the test cups were obtained at intervals during the test run. Typical data showing the changes in surface roughness that took place during the test runs are given in figures 10 and 11. In the figures, the average values of the roughness of the cups in microinches (rms) is plotted against the time in hours when operating with some of the lubricants at 225° F and with loads of 135 and 180 lb, respectively. In all of these tests, the original roughness of the cups averaged about 28 microinches. From a comparison of these figures with the wear data given in figures 6 and 7, it will be noted that in the tests where the rate of wear was relatively low the roughness decreased in the run-in period and tended to level off in a range between 10 and 20 microinches. As the rate of wear increased, there was a trend for the roughness to increase. This was especially noticeable in cases of excessive wear

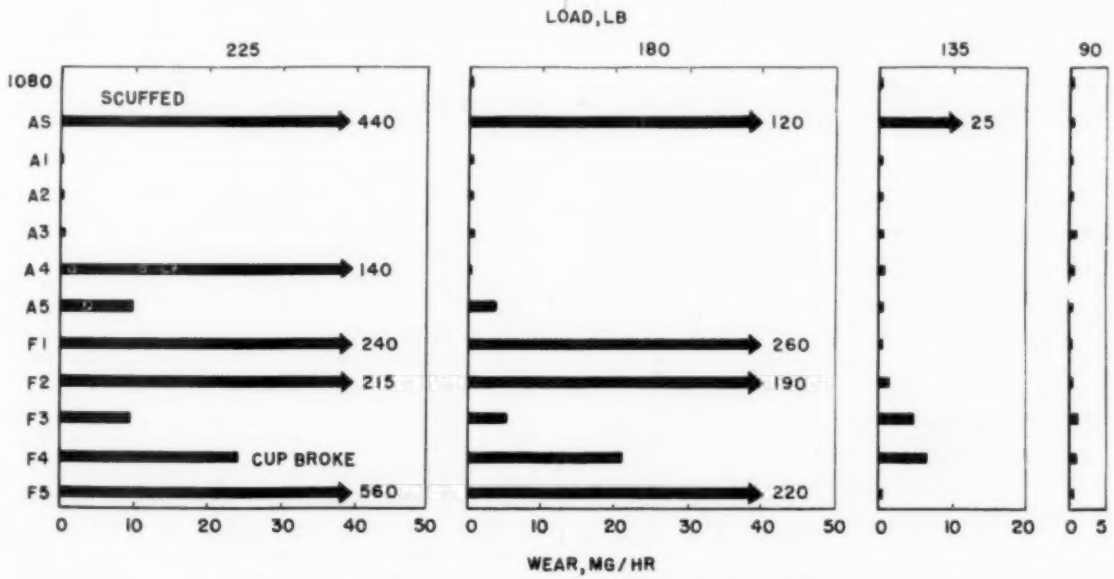

FIGURE 9. *Rate of wear at 225° F for all lubricants at various loads.*

where there was definite "ridging" of the cups, which in some cases was beyond the range of the Profilometer.

Some study was also made of the effect of the original surface roughness of the cups on the rate of wear. Data obtained in tests with the mineral oil and one of the Army specification lubricants operating at 225° F and 135-lb load, using cups with original roughnesses of 14, 28, and 35 microinches (rms), are given in figure 12. Surface roughness versus time curves are shown in the upper part of the figure. These indicate that the net result of operation was to bring the roughness of the cups fairly close together. The wear versus time curves for these tests are given in the lower part of the figure. From these it will be noted that while the run-in wear tended to increase with increase in roughness, the final rate of wear was practically independent of original surface roughness over the range covered. This is of considerable importance in tests of this kind in that comparable data may be obtained with reasonable tolerances in the surface roughness of the cups.

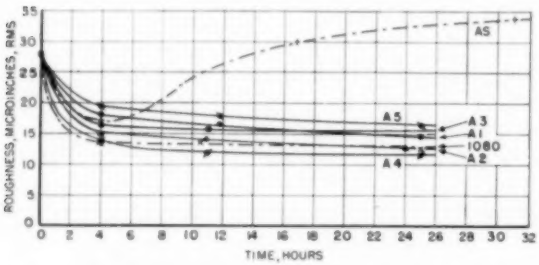

FIGURE 10. *Surface roughness versus time curves for various lubricants operating at 135-lb load and 225° F.*

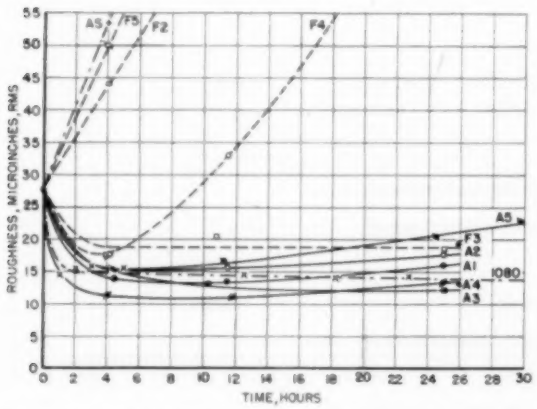

FIGURE 11. *Surface roughness versus time curves for various lubricants operating at 180-lb load and 225° F.*

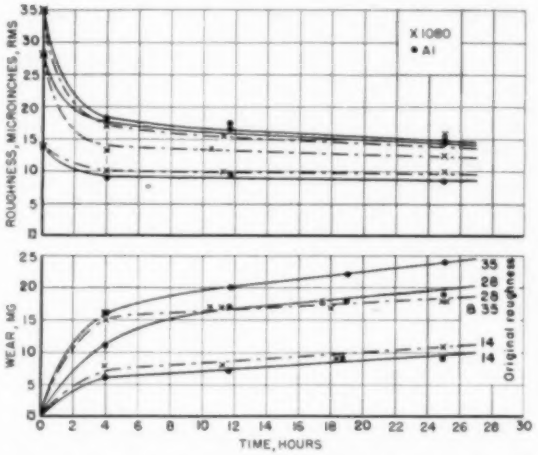

FIGURE 12. *Curves for two lubricants showing surface roughness and wear as functions of time for three values of original surface roughness when operating at 135-lb load and 225° F.*

VII. Conclusion

The results of these tests indicate that this method of operating the SAE machine provides a sensitive measure of the rate of wear obtained with various commercial gear lubricants under conditions simulating high torque and low speed in automotive gears. The data are of interest in that they show significant differences in the performance of lubricants meeting the requirements of the same specification.

The evidence of a run-in wear under some conditions is of considerable importance and should be taken into account in the evaluation of lubricants with respect to wear. One advantage of this type of test is that the rate of wear after the run-in period is not materially affected by the original roughness of the test cups, as is the case with the usual load-carrying capacity tests with this machine.

The lubricants containing the more chemically active additives for withstanding higher shock load tend to show the greater wear. This is in agreement with the known service performance of some of these lubricants, particularly the active-sulfur lubricant and the nonadditive mineral oil.

WASHINGTON, September 27, 1948

U. S. Department of Commerce
National Bureau of Standards

Research Paper RP1956
Volume 42, February 1949

Part of the Journal of Research of the National Bureau of Standards

The System BaO-B_2O_3

By Ernest M. Levin and Howard F. McMurdie

A phase equilibrium diagram of the system BaO-B_2O_3 has been constructed from data obtained essentially by the quenching method. Four congruently melting compounds were identified: $BaO.4B_2O_3$, melting at 879° ±5° C; $BaO.2B_2O_3$, melting at 900° ±5° C; $BaO.B_2O_3$, melting at 1,095° ±5° C; and $3BaO.B_2O_3$, melting at 1,383° ±5° C. Some optical properties of these compounds were determined with the petrographic microscope, and X-ray diffraction data suitable for their identification were obtained. Barium metaborate, $BaO.B_2O_3$, showed an inversion occurring between 100° and 400° C. Mixtures containing less than 30 percent of BaO were found to separate on fusion into two liquid layers, one of which contained 30 percent of BaO, whereas the other was nearly pure B_2O_3. A curve showing indices of refraction of the quenched glasses is also presented.

I. Introduction

The study of this system was undertaken as a preliminary to a study of part of the ternary system, BaO-B_2O_3-SiO_2. The latter system is of fundamental importance to the glass industry, as it serves as a starting point for investigations of the barium crown and dense barium crown glasses, which are characterized by high refractive index and low dispersion. The nature of the high silica-boric oxide portion of the ternary system might also have additional application in studies of enamels and ceramic glazes.

R. Benedikt [1][1] in 1874 prepared $BaO.B_2O_3$ by fusion of a sodium borate and barium chloride in molecular proportions and subsequently leaching out the NaCl from the crystallized melt. H. Ditte [2] in 1873 claimed the preparation of two barium borates: $BaO.2B_2O_3$ and $2BaO.3B_2O_3$. L. Ouvrard [3] in 1901 obtained $3BaO.B_2O_3$.

The first systematic study of the system BaO-B_2O_3 was made by W. Z. Guertler [4] in 1904. The course of the liquidus curve from about 62 to 84 percent of BaO was traced by the combined use of cooling curves and of visual observation of the temperatures at which turbidity of the melts occurred. His diagram indicated maxima at 1,060° C, 1,002° C, and 1,315° C, corresponding to the compounds $BaO.B_2O_3$, $2BaO.B_2O_3$, and $3BaO.B_2O_3$, respectively. In a study on the limits of miscibility of boric anhydride and borates in the fused state, Guertler [5] found that barium oxide melted together with more than 63.2 percent by weight of B_2O_3 separated into two layers. The upper layer was cloudy and soluble in water; the lower one consisted of clear glass that could not be devitrified. Because of the excessive amount of supercooling that occurs in this system, the accuracy of Guertler's results are subject to question.

F. De Carli [6] (1927), using essentially the same method employed by Guertler, extended the liquidus diagram to include the region 33 to 59.5 percent of BaO. He found maxima at 750°, 740°, and 810° C, corresponding to the compounds $BaO.4B_2O_3$, $BaO.3B_2O_3$, and $BaO.2B_2O_3$, respectively. He also observed that melts containing more than 67 percent by weight of B_2O_3 separated into two liquids.

With reference to the "end-members" of the system, the melting point of pure B_2O_3 has been reported variously as 294 ±1° C [7], 460° to 470° C [8], and 450 ±2° C [9]. Kracek, Morey, and Merwin [9] working with small crystals found them to have a density 2.460 and to be nearly or quite uniaxial negative, with ω (or β and γ) =

[1] Figures in brackets indicate the literature references at the end of this paper.

1.64_5 and ϵ (or α) $= 1.61_5$. Crushing either induced a minute lamellar twinning or revealed a twinning caused by inversion. Morey [10] reported that colorless B_2O_3 glass had a density of 1.812 and a refractive index of 1.458.

Barium oxide is colorless, cubic, with a density of 5.72 and with $N_D = 1.980$ [11]. Schumacher [12] has placed its melting point at 1,923° C.

Because of the almost complete absence of optical and X-ray data on the barium borates, as well as the uncertainty as to the number of compounds and their melting points, it was considered desirable to make a comprehensive study of the system BaO-B_2O_3.

II. General Procedure

The general plan followed was to prepare mixtures of BaO and B_2O_3 in varying proportions and to determine their melting points by means of the quenching method. Heating curves obtained by the differential thermocouple method supplemented most of the determinations. The petrographic microscope was used to determine the phases present in the quenched samples. When microscopic identification was uncertain, X-ray diffraction analysis was employed.

1. Preparation of Mixtures

Powdered boric acid (H_3BO_3) was used as a source of B_2O_3 for all mixtures. Both crystalline barium nitrate ($Ba(NO_3)_2$) and powdered barium carbonate ($BaCO_3$), low in nitrate, were used as a source of BaO. All the chemicals were of reagent quality, meeting ACS specifications. Although barium nitrate was satisfactory for preparing mixtures containing less than 78 percent by weight of BaO, it was found unsuitable for mixtures containing more than 78 percent of BaO. In the latter case, the $Ba(NO_3)_2$ appeared to melt before combination with H_3BO_3, making it difficult to obtain homogeneous mixtures by sintering. For mixtures containing more than 78 percent of BaO, barium carbonate was found to be satisfactory.

For each mixture the calculated amounts of boric acid, and barium nitrate or carbonate were thoroughly mixed and ground together for 2 hours in a mechanical grinder. The mixture was then heated slowly over a period of several hours [13] to a final temperature that was below the solidus, usually about 700°C. After approximately 2 hours of sintering, the material was ground to pass a No. 200 sieve and was resintered again at a slightly higher temperature, but still below the solidus. The material was subsequently reground to pass a No. 200 sieve. This treatment, in most cases, gave a sufficiently homogeneous product when examined with the polarizing microscope; however, in a few instances it was necessary to sinter the material for a third time. All sintering was done in platinum by using an electrically heated furnace.

For the preparation of mixtures containing more than 87 percent of BaO, the above procedure was found to be inadequate, since the BaO existed in an uncombined phase and reacted with the platinum crucible. In these instances, it was found expedient to grind together the calculated amount of tribarium borate (containing 86.77 percent of BaO) with the required amount of BaO, formed by igniting barium nitrate.

2. Chemical Analyses

Because of loss of boric acid by volitilization during preparation of the mixtures, it was necessary to analyze the product in each case. To determine BaO, from 0.5 to 1 g of the sample was dissolved in an excess of standard 0.3 *N* hydrochloric acid, followed by titration (to the *p*-nitrophenol end point) of the excess acid with standard 0.3 *N* sodium hydroxide. The B_2O_3 was determined on the same sample by adding mannitol and titrating with the standard sodium hydroxide to the phenolphthalein end point.

In general, it was found that mixtures rich either in BaO or B_2O_3 were hygroscopic, whereas the others were only slightly so. This condition was similar to the one observed for the calcium borates [14]. The percentages of BaO and B_2O_3 were adjusted to total 100 percent on a nonvolatile basis, since any moisture present was expelled in the subsequent heating. All mixtures, however, were stored in a desiccator over magnesium perchlorate.

A check chemical analysis of a few selected samples that had been heated to melting during the differential thermal analysis showed no appreciable change in composition and indicated low volatility of combined B_2O_3.

3. Apparatus and Method

The thermal studies were made by the well established quenching method [15], supplemented in most cases by the differential thermocouple method [16]. Although the latter method did not produce significant results, it indicated the temperatures of phase changes and thus facilitated the quenching determinations. The furnace was of a vertical tube resistance type [17] wound with 80-percent-Pt–20-percent-Rh wire. It was operated in connection with a controller that maintained to within 2 degrees the desired temperatures from which the quenches were made. Temperatures were measured with a Pt vs. Pt+10-percent-Rh thermocouple, which was calibrated periodically against the melting points of gold (1,063° C), $CaO.B_2O_3$ (1,154° C) [14], and $BaO.2SiO_2$ (1,418° C) [18].

Both the quenching and differential thermocouple methods were inadequate for determining the eutectic between $3BaO.B_2O_3$ and BaO, because of the rapid rate of devitrification with the former method and the reaction of barium oxide with platinum with the latter. This eutectic was determined, however, by a method of optical pyrometry. The furnace, sample preparation, and procedure are described in Research Papers 1443 and 1703 [19]. The specimen upon which the optical pyrometer was focused was a small four-sided pyramid about 3/16 in. at the base and grooved on each side. It was ground from a compressed cylinder of material, formed by subjecting about half a gram of a mixture of tribarium borate, barium oxide, and one drop of rubber cement to 36,000 lb/in.^{2}, in a ¼-in.-diameter steel die.

X-ray diffraction powder patterns (with copper Kα radiation) were made of all compounds and certain other samples by using a commercial type Geiger counter X-ray spectrometer equipped with a synchronous-motor-driven scanning unit and attached to an electronic high-speed recorder. A high-temperature X-ray diffraction apparatus [20] was employed for studying inversion forms.

III. Results

1. Binary Compounds

Four binary compounds were found in the system: $BaO.4B_2O_3$, $BaO.2B_2O_3$, $BaO.B_2O_3$, and $3BaO.B_2O_3$. X-ray diffraction data for these compounds are shown in table 1. In the study of the compounds of the system, no evidence of solid solution was found by optical or X-ray diffraction methods.

TABLE 1. *X-ray diffraction data for compounds in the system* $BaO–B_2O_3$, *showing the interplanar spacings* (*d*) *and their relative intensitities* (*RI*)

$BaO.4B_2O_3$		$BaO.2B_2O_3$ [a]		$BaO.B_2O_3$				$BaO.3B_2O_3$ [d]	
				Low temperature form [b]		High temperature form [c]			
d	*RI*	*d*	*RI*	*d*	*RI*	*d*	*RI*	*d*	*RI*
1	2	3	4	5	6	7	8	9	10
A	*Percent*	*A*	*Percent*	*A*	*Percent*	*A*	*Percent*	*A*	*Percent*
6.10	29	6.15	70	6.25	24	6.32	11	4.3	14
5.25	49	4.91	30	3.91	10	3.92	6	3.85	31
4.11	4	4.33	30	3.58	91	3.60	100	3.70	37
3.90	5	3.81	65	3.50	100	...	..	3.24	87
3.70	5	3.55	55	3.11	25	3.13	24	3.06	46
3.57	3	3.39	90	3.05	24	...	..	3.02	64
3.33	100	3.25	70	2.92	12	2.93	5	2.95	39
3.06	17	3.13	100	2.71	6	...	..	2.82	100
2.90	52	3.06	60	2.51	52	2.54	34	2.68	29
2.72	11	2.81	55	2.36	20	2.37	12	2.52	24
2.63	14	2.50	70	2.31	7	...	..	2.36	37
2.52	7	2.35	35	2.12	15	2.18	6	2.28	4
2.41	6	2.30	45	2.06	58	2.08	42	2.23	20
2.24	39	2.11	40	2.02	23	2.03	8	1.96	39
2.17	3	2.04	45	1.955	10	...	..	1.934	27
2.14	18	2.00	35	1.924	7	...	..	1.887	20
2.11	11	...	..	1.829	20	1.867	12	1.862	44
2.05	3	...	..	1.814	12	1.806	6	1.790	29
2.00	7	...	..	1.756	7	...	..	1.734	24
1.979	8	...	..	1.639	6	1.640	3	1.707	12
1.936	6	...	..	1.602	11	1.612	10	1.345	10
1.911	6	...	..	1.503	7	1.509	7	...	..
1.731	3	...	..	1.486	7	...	..	...	..
1.665	3	...	..	1.466	6	...	..	...	..
1.615	6	...	..	1.382	13	...	..	...	..
1.547	3	...	..	1.363	11	1.367	4	...	..
1.516	5	...	..	...	..	...	..	...	..
1.410	5	...	..	...	..	...	..	...	..
1.354	3	...	..	...	..	...	..	...	..
1.253	3	...	..	...	..	...	..	...	..

[a] Weak pattern, poorly crystalline. Only *d* values with *RI* greater than 29 recorded.

[b] Only *d* values with *RI* greater than 5 recorded.

[c] Data obtained with high-temperature X-ray apparatus, at 700° C. Weak pattern. The *d* values are not corrected for temperature coefficient.

[d] Compound hydrates and carbonates rapidly. Pattern determined in sections with fresh samples for each.

$BaO.4B_2O_3$.—This compound occurs as the primary phase in all the mixtures containing up to about 41 percent of BaO. It melts congruently at 879±5°C. It appears as irregular grains, many striated as in polysynthetic twinning. It

is uniaxial negative or biaxial negative with a very small optic axial angle; ω (or β and γ)= 1.594,[2] ϵ (or α)=1.559. Index of glass=1.558.

$BaO.2B_2O_3$.—This compound occurs as the primary phase in mixtures containing approximately 41 to 56 percent of BaO. It melts congruently at 900±5° C. It crystallizes in small irregular grains, biaxially positive, moderately birefringent, with medium optic axial angle; α=1.595, β=1.610, γ=1.668. Index of glass= 1.615.

$BaO.B_2O_3$.—This compound occurs as the primary phase in mixtures containing approximately 56 to 78 percent of BaO. It melts congruently at 1,095±5° C. It appears as irregular grains, highly birefringent, uniaxial negative; ω=1.667, ϵ=about 1.528. Index of glass=1.66. Elongated grains tend to show optic axis figures, with the microscope, which suggests 001 or 0001 cleavage.

Grains of the material examined under the microscope immediately after quenching appear clear and smooth; but after the material has stood for several minutes, the grains have an etch-like appearance over their surface, which interferes with index determinations. At first the change was ascribed to a hydration process, but a sample exposed for 18 hours in the laboratory atmosphere of high relative humidity showed no increase in weight. Studies with the high-temperature X-ray apparatus indicate the existence of two reversible polymorphic forms of the barium metaborate. The temperature of inversion could not be ascertained, as the transition is not sharp, but occurs over a range of 100° to 400° C. From table 1 (columns 3, 4, 5, 6), it can be seen that the two forms are similar, but that the high temperature form has fewer spacings, the most notable reductions occurring at about 3.5 and 3.05 A. The heat effect of the inversion must be small, as the differential heating curve shows no discontinuity below the melting point.

$3BaO.B_2O_3$.—This compound occurs as the primary phase in mixtures containing approximately 78 to 87 percent of BaO. It melts congruently at 1,383±5° C. As ordinarily prepared, it crystallizes poorly as "egg-shaped" grains, biaxial negative (?), with low birefringence and undulatory extinction α=1.756, γ=1.768.

[2] Indices, unless stated otherwise, are considered accurate to ±0.003.

Tribarium borate hydrates and carbonates rapidly when left in the air. A sample exposed to the air (relative humidity above 90%) overnight in the X-ray holder gave a sharp pattern of $BaCO_3$. For more carefully controlled conditions, figure 1 shows the gain in weight of a half gram sample

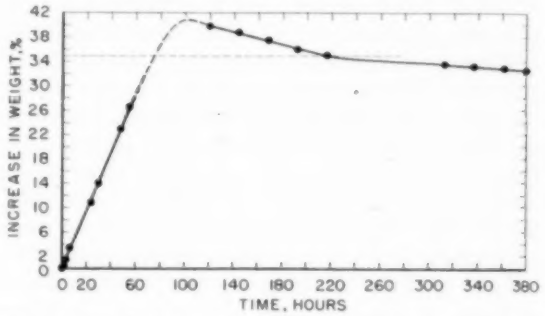

FIGURE 1. *Gain in weight of $3BaO.B_2O_3$ when exposed to the atmosphere at 21° C and 56-percent relative humidity.*

when exposed to the atmosphere at 21° C and 56-percent relative humidity. The maximum gain is approximately 40.8 percent, occurring after about 100 hr of exposure. Assuming that this increase in weight is due almost entirely to hydration and an accompanying decomposition, the condition of the $3BaO.B_2O_3$ at the end of 100 hr can be represented as $3Ba(OH)_2+2H_3BO_3+6H_2O$. Unquestionably, the material is also carbonating during the first 100 hr, but the hydration reaction is greater. During this portion of the experiment, the material appears moist and spongy; but later, as the carbonation reaction predominates, it becomes hard and compact. At approximately 215 hr the gain in weight of the sample is about 35 percent and corresponds to complete conversion of the material to $BaCO_3$ and H_3BO_3. The presence of these products was verified with the aid of the polarizing microscope.

The experimental results did not confirm the existence of the compounds $BaO.3B_2O_3$ and $2BaO.B_2O_3$ reported by De Carli [6] and Guertler [4], respectively.

The composition of $BaO.3B_2O_3$ (42.33% of BaO) is close to that of the determined eutectic between $BaO.4B_2O_3$ and $BaO.2B_2O_3$ (40.6% of BaO). A sample of sintered material and a sample of glass, both of the composition $BaO.3B_2O_3$ were heated for 66 hr at 853° C, which temperature was about 6° below the eutectic. Optical

and X-ray examination of the products showed them to consist of two conjugate phases. The same two primary phases were present when a mixture of the eutectic composition was heated about 2 deg below the melting temperature for 66 hr.

By similar methods, it was concluded that the composition $2BaO.B_2O_3$ (81.50% of BaO) did not represent a unique compound but a mixture of two conjugate phases, $BaO.B_2O_3$ and $3BaO.B_2O_3$.

2. Phase Equilibrium Diagram

The phase equilibrium diagram is shown in figure 2. Mixtures containing less than 30.2 percent of BaO were found on fusion to separate into two immiscible liquids (for convenience designated as L_1 and L_2 in fig. 2.) The heavier glass, which was seen under the microscope to be full of minute spherules of higher index. That the spherules were of approximately the same chemical composition as the heavier glass was indicated by the following experiment: A sample of the glass containing 2.99 percent of BaO was agitated with water for 10 min.; the solution filtered, and the filtrate analyzed volumetrically for BaO and B_2O_3. The filtrate was found to contain 1.98 percent of BaO and 94.49 percent of B_2O_3, based on the original sample weight. The composition of the undissolved glass calculated from these data was 28.6 percent of BaO and 71.4 percent of B_2O_3. A complete separation of the two glasses by differential solubility in water was not possible because of the appreciable solubility of the heavier glass, as noted previously.

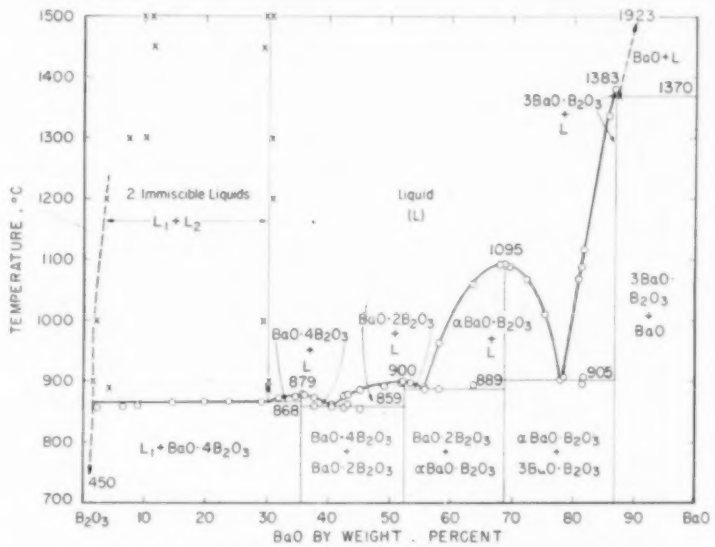

FIGURE 2. *Phase equilibrium diagram for the system* $BaO\text{-}B_2O_3$.

of the two liquids (L_2) on cooling formed a clear glass, with a refractive index of 1.536 and a density of about 2.66 (25° C). It was soluble in hydrochloric acid and appreciably soluble in water. In one experiment, 0.5 g of the heavier glass, ground to pass a No. 200 sieve, was agitated for 30 min in 50 ml of water (27° C). Under these conditions, about 42 percent of the glass was found to have dissolved. Glass L_2 contained about 30 percent of BaO, by analysis.

The other liquid (L_1) on cooling formed a cloudy

The index of the lighter glass, quenched from just above the liquidus (about 870° C), was 1.455. Within the error of measurement, this value was sufficiently close to that of B_2O_3 glass (1.458) to indicate almost pure B_2O_3.

An attempt was made to determine the change in composition of the conjugate liquids L_1 and L_2 with temperature. Table 2 shows the results of chemical analyses of the mechanically separated layers of charges quenched in air from various temperatures above the liquidus.

Although the data for the heavier liquid (L_2) show some variation, no significant change in composition occurs up to 1,500° C. Data for the lighter liquid (L_1) are erratic and more difficult of interpretation. When examined with the microscope, the lighter glass always contained spherules of higher index, indicating that some of liquid L_2, which had been in solution at higher temperatures, had separated out. Also, as the proportion of occluded material appeared to increase as the temperature from which the quenches were made increased, it seems probable that the solubility of liquid L_2 in L_1 had increased with temperature. The results of the chemical analyses, however, are not considered an accurate measure of the extent of solubility of the two liquids at the various temperatures, because of the uncertainty that true and final equilibrium conditions prevailed. This conclusion is indicated by the wide divergence of plotted values from a smooth curve (fig. 2).

TABLE 2. *Composition of the immiscible liquids in the system* BaO-B_2O_3 *at various temperatures*

Temperature	Composition of L_1		Composition of L_2	
	BaO	B_2O_3	BaO	B_2O_3
°C	*Percent*	*Percent*	*Percent*	*Percent*
885	.....	.....	30.25	69.75
890	4.35	95.65	30.26	69.74
900	[a] 1.58	98.42	30.38	69.62
1,000	[a] 2.08	97.92	29.47	70.53
1,200	3.79	96.21	30.90	69.10
1,300	10.23	89.77	30.78	69.22
1,300	[a] 7.42	92.58	.....	.....
1,450	11.52	88.48	29.54	70.46
1,500	11.25	88.75	30.69	69.31
1,500	10.01	89.99	29.95	70.05

[a] Water soluble extract.

To the BaO side of the immiscibility region, the phase diagram consists of congruently melting compounds and simple eutectics. Table 3 shows the compositions and melting temperatures for the compounds and eutectics in the system. It may be noted that the $BaO.B_2O_3$-$3BaO.B_2O_3$ eutectic is as low as 905° C, even with the high BaO content of about 80 percent. From this point to the melting point of pure BaO (1,923° C), the change in temperature is more than 1,000° C.

TABLE 3. *Composition and melting point of compounds and eutectics in the system* BaO–B_2O_3

Compound	Eutectic	Composition		Temperature (±5° C)
		BaO	B_2O_3	
		Percent	*Percent*	
$BaO.4B_2O_3$	.....	35.51	64.49	879
	$BaO.4B_2O_3$-$BaO.2B_2O_3$	40.6	59.4	859
$BaO.2B_2O_3$	.....	52.41	47.59	900
	$BaO.2B_2O_3$-$BaO.B_2O_3$	55.7	44.3	889
$BaO.B_2O_3$	.....	68.77	31.23	1,095
	$BaO.B_2O_3$-$3BaO.B_2O_3$	77.9	22.1	905
$3BaO.B_2O_3$	.....	86.85	13.15	1,383
	$3BaO.B_2O_3$-BaO	87.3	12.7	1,370

3. Index of Refraction of the Quenched Glasses

Figure 3 shows the index of refraction of quenched glasses and of compounds in the system. Mixtures containing more than about 82 percent of BaO could not be quenched to glasses because of the rapid rate of devitrification; and, for the same reason, binary glasses containing above 70 percent of BaO were increasingly difficult to make. Below 30 percent, in the region of liquid immiscibility, two glasses of constant refractive indices always formed, but the amounts of each varied in accordance with the inverse law. The indices are not assumed to represent accurate values for properly annealed glasses, but only an approximation. It is of interest to note that crystalline $BaOB_2O_3$ has a lower average index of refraction than that of glass of identical composition. Such a phenomenon is rather unusual.

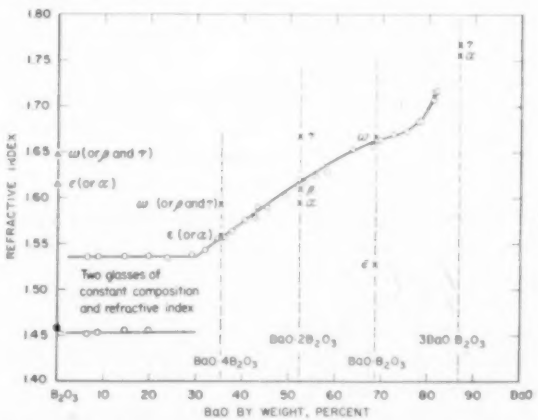

FIGURE 3. *Refractive indices of compounds and of quenched glasses in the system* BaO–B_2O_3.

○, Glasses; ●, B_2O_3 glass from Morey [10]; ×, compounds; △, B_2O_3 crystals from Kracek, Morey, and Merwin [9].

IV. Summary

A phase equilibrium diagram for the system BaO-B_2O_3 has been constructed. A region of liquid immiscibility was found, extending from about 1.6 to 30.2 percent of BaO, and from 868° to above 1,500° C. Optical properties, melting points, and X-ray diffraction data were determined for four compounds identified in this system. Some of the data is summarized in table 4, together with the melting points determined by previous investigators. All of the compounds melted congruently, and only one, $BaO.B_2O_3$ showed an inversion, occurring between 100° and 400° C. A curve showing indices of refraction of the quenched glasses is presented.

TABLE 4. *Some optical properties of barium borate compounds and comparison of melting points, as determined by various investigators*

Compound	Optical properties		Melting point determined by—		
	Character	Indices of refraction	Guertler 1904	De Carli 1927	Levin and McMurdie
			°C	°C	±5° C
$BaO.4B_2O_3$	Uniaxial (−), or biaxial (−) with 2 V small	ω (or β and γ) 1.594 ε (or α) 1.559		751	879
$BaO.2B_2O_3$	Biaxial (+); 2 V medium	α 1.595 β 1.610 γ 1.668		810	900
$BaO.B_2O_3$	Uniaxial (−)	ω 1.667 ε about 1.528	1,060		1,095
$3BaO.B_2O_3$	Biaxial (− ?)	α 1.756 γ 1.768	1,315		1,383

The authors express their appreciation to E. S. Newman for his aid in obtaining thermal data with an automatically recording unit, and to S. M. Lang, for his help in determining the $3BaO.B_2O_3$-BaO eutectic by an optical pyrometer method.

V. References

[1] R. Benedikt, On some salts of boric acid, Ber. deut. chem. ges. **7,** 703 (1874).

[2] H. Ditte, Production by the dry method of several crystalized borates, Compt. rend. **77,** 785, 892 (1873).

[3] L. Ouvrard, On the borates of magnesium and the alkaline earth metals, Compt. rend. **132,** 257 (1901).

[4] W. Guertler, On the melting points of mixtures of the alkaline earths with boric anhydride, Z. anorg. chem. **40,** 337 (1904).

[5] W. Guertler, On the limits of miscibility of boric anhydride and borates in the fused state, Z. anorg. chem. **40,** 225 (1904).

[6] F. De Carli, Anhydrous borates of silver, barium, and zinc, Atti Reale acad. Naz. Lincei [6], **5,** 41 (1927).

[7] N. W. Taylor and S. S. Cole, Crystalline boric oxide, J. Am. Chem. Soc. **56,** 1648 (1934).

[8] L. McCulloch, A crystalline boric oxide, J. Am. Chem. Soc. **59,** 2650 (1937).

[9] F. C. Kracek, G. W. Morey, and H. E. Merwin, The system, water-boron oxide, Am. J. Sci. **35A,** 143 (1938).

[10] G. W. Morey, Properties of glass, ACS Monograph series No. 77, 227, 370 (Reinhold Pub. Corp., New York, N. Y., 1938).

[11] A. N. Winchell, The microscopic characters of artificial inorganic solid substances or artificial minerals, 2 ed., p. 186 (John Wiley & Sons, Inc., New York, N. Y. 1931).

[12] E. E. Schumacher, The melting points of barium, strontium, and calcium oxides, J. Am. Chem. Soc. **48,** 396 (1926).

[13] M. S. Maksimenko, V. N. Krylov, and M. A. Lipinskii, Dehydration of boric acid to boric anhydride, J. Applied Chem. (USSR) **19,** 154 (1946).

[14] E. T. Carlson, The system CaO–B_2O_3, BS J. Research **9,** 825 (1932) RP510.

[15] E. S. Shepherd, G. A. Rankin, and F. E. Wright, Binary systems of alumina with silica, lime, and magnesia, Am. J. Sci. [4] **28,** 293 (1909).

[16] S. Speil, L. H. Berkelhamer, J. A. Pask, and B. Davies, Differential thermal analysis. Its application to clays and aluminous minerals, U. S. Bur. Mines Tech. Pap. 664, 81 p. (1945).

[17] H. S. Roberts, The Geophysical Laboratory furnace thermostat, J. Opt. Soc. Am. Rev. Sci. Instr. **11,** 171 (1925).

[18] K. T. Greene and W. R. Morgan, The system sodium disilicate-barium disilicate, J. Am. Ceram. Soc. **24,** 114 (1941).

[19] R. F. Geller, A resistor furnace with some preliminary results up to 2,000° C., J. Research NBS **27,** 555 (1941) RP1443; R. F. Geller, P. J. Yavorsky, B. L. Steierman, and A. S. Creamer, Studies of binary and ternary combinations of magnesia, calcia, baria, beryllia, alumnia, thoria, and zirconia in relation to their use as porcelains, J. Research NBS **36,** 277 (1946) RP1703.

[20] A. Van Valkenburg, Jr., and H. F. McMurdie, High-temperature X-ray diffraction apparatus, J. Research NBS **38,** 415 (1947) RP1782.

WASHINGTON, October 7, 1948.

U. S. Department of Commerce
National Bureau of Standards

Research Paper RP1957
Volume 42, February 1949

Part of the Journal of Research of the National Bureau of Standards

Separation of the 177° to 200° C Fraction of Petroleum and the Isolation of Normal Undecane[1,2]

By Morton B. Epstein,[3] Beveridge J. Mair, Charles B. Willingham, and Frederick D. Rossini

This report describes the separation of the 177° to 200° C fraction of petroleum (Ponca, Okla., crude) by means of regular distillation, azeotropic distillation, adsorption, and crystallization. A regular distillation at high efficiency with high reflux ratio separated the original petroleum into a series of substantially constant-boiling fractions. Appropriate blends of material of nearly the same boiling point were subjected to azeotropic distillation to produce a separation of the aromatic hydrocarbons from the paraffinic and cycloparaffinic hydrocarbons, with a partial separation of the latter two classes from each other. The fractions intermediate between the aromatic hydrocarbons and the paraffins plus cycloparaffins were further processed by adsorption to separate all the aromatic hydrocarbons. The azeotropic distillation yielded fractions very rich in normal undecane, and from these a pure sample of normal undecane was separated by crystallization.

I. Introduction

In continuation of the work of the American Petroleum Institute Research Project 6 on the fractionation and analysis of hydrocarbons in a large quantity of one representative petroleum [1],[4] work was begun several years ago on the 177° to 200° C fraction of the Project's Ponca, Oklahoma, petroleum. This report describes the separation of the 177° to 200° C fraction of this original petroleum by regular distillation, azeotropic distillation, and adsorption into a portion containing all the aromatic hydrocarbons and a portion containing all the paraffinic and cycloparaffinic hydrocarbons, together with the isolation of pure normal undecane by crystallization from the hydrocarbon part of the azeotropic distillate.

[1] This investigation was performed at the National Bureau of Standards as part of the work of the American Petroleum Institute Research Project 6 on the Analysis, Purification, and Properties of Hydrocarbons.

[2] Presented before the Division of Petroleum Chemistry of the American Chemical Society, St. Louis, Mo., September 1948.

[3] Formerly Research Associate on the American Petroleum Institute Research Project 6, now on the American Petroleum Institute Research Project 44, at the National Bureau of Standards.

[4] Figures in brackets indicate the literature references at the end of this paper.

II. Material Investigated

The material investigated consisted of all of the original petroleum (Ponca, Okla., crude) normally boiling between 177° and 200° C. A complete description of the original crude petroleum is given in reference [2]. The last work on the material normally boiling just below 177° C and that just above 200° C is described in references [3] and [4], respectively.

III. Apparatus and Procedure

The percentage of aromatic hydrocarbons in the entire material normally boiling in the range 177° to 200° C was determined in an analytical adsorption experiment with 1-butanol as the desorbing liquid, in accordance with the standard procedures developed in the Thermochemistry and Hydrocarbon Section at this Bureau [7, 8].

The apparatus used and the procedure followed in carrying on the fractionating processes are described in detail in the following previous publications from this section: Regular and azeotropic distillation [5], adsorption [6, 7, 8], crystallization [9].

The regular distillation of the entire material normally boiling in the range 177° to 200° C was performed in columns 5 and 6 described in reference [5], at a pressure of 725 mm Hg and with a reflux ratio of about 125 to 1. The entire material had a volume of 86.5 liters and was distilled in six charges of approximately equal volume.

The charges for azeotropic distillation were prepared by recombining material, which on the average had distilled within a range of 0.7° C during the regular distillations. Each of the 31 charges distilled azeotropically contained approximately 2.8 liters of hydrocarbons. These distillations were performed in columns 7, 8, and 13 described in reference [5], at a pressure of 725 mm Hg and with a reflux ratio of 130 to 1. The distillation of each charge was discontinued when the boiling point of the distillate and the refractive index of the hydrocarbon portion of the distillate had risen to values indicative of the absence of paraffins and cycloparaffins from the material remaining in the still.

The azeotropic distillation of the material normally boiling in the range 177° to 189° C was performed with butyl Cellosolve (ethylene glycol monobutyl ether) as the azeotrope-forming substance (see fig. 1). Over this range, the amount of hydrocarbon material in the distillate decreased roughly linearly with boiling point from 52 to 35 percent. For the material normally boiling above 189° C, methyl Carbitol (diethylene glycol monomethyl ether) was used as the azeotrope-forming substance. With methyl Carbitol, the amount of hydrocarbon material in the distillate decreased from 65 percent for material normally boiling at 189° C to 55 percent for material normally boiling at 200° C.

The hydrocarbon material in the fractions of the azeotropic distillate between the paraffins plus cycloparaffins and the aromatics was further resolved into two portions of these types by adsorption with silica gel in columns 2 cm in diameter and 7.9 meters in length. For these adsorption experiments, 1-butanol was used as the desorbing liquid.

The residue portion from each of the six regular distillations was separated in a manner similar to the foregoing, except that tert-amyl alcohol was used as the desorbing liquid. Intermediate fractions from the adsorption process were reprocessed until the volume of the remaining intermediate portion became negligible.

Normal undecane (see section V) was separated from appropriate fractions by repeated crystallization with centrifuging [9], at −40° C, using a 2 to 1 mixture of hydrocarbon material with acetone. Final purification of the normal undecane was effected by adsorption [6].

IV. Results of the Fractionation

1. Regular Distillation

The results of the regular distillation of one of the six identical charges are shown in figure 1. Of the total of 86.5 liters of material distilled, 0.7 liter was material normally boiling below 177° C, and 7.0 liters was material normally boiling above 200° C. The curve of the refractive index of the distillate in figure 1 shows, near 187° and 194° C, two pronounced dips due to high concentrations of paraffinic hydrocarbons. These dips are attributable, respectively, to concentrates of methyldecanes and of normal undecane. Beneath the plot of refractive index for the fractions of distillate, there is a similar plot for the aromatic-free portion of each of these same fractions.[5] The difference between these plots is represented at the top of the figure by the curve labeled Δn_D, and indicates in a general way the distribution of aromatic hydrocarbons throughout the distillate. A better picture of the distribution of aromatics is shown, however, by the curve giving the actual percentage of aromatic hydrocarbons by volume. This latter is based upon the measured volume of aromatic material recovered from the individual azeotropic distillations and adsorptions. A correction for losses was uniformly applied throughout the boiling range, upon the basis of the results of the analytical adsorption on the entire material.

2. Azeotropic Distillation

The results of the azeotropic distillation are shown for three charges (A, B, and C; see fig. 1) in figure 2. The sharp increase in refractive index

[5] The refractive index for the aromatic-free portion (paraffins and cycloparaffins) of each fraction was obtained by passing 1 ml through a small column of silica gel (200 mm in length and 2 mm in inside diameter). The first drop of filtrate was used to determine the refractive index. See reference [10].

immediately preceding the end of the distillation to values characteristic of aromatic hydrocarbons is apparent for all three charges, and shows that the azeotropic distillation was satisfactorily separating the aromatic hydrocarbons from the paraffins and cycloparaffins. For the nonaromatic portion of any one charge, there are marked variations in refractive index, a consequence of a partial separation of paraffins from cycloparaffins. This separation did not take place among the various distillations in the uniform manner shown by charge A. Thus, with charge B there were two depressions in the refractive index curve before the final sharp increase. With charge C, which was rich in normal undecane, the central portion of the distillate had a refractive index only 0.003 higher than that of pure normal undecane. Flanking each side of the region rich in normal undecane there was material with a higher refractive index, which contained cycloparaffins and possibly bicycloparaffins. It is, in fact, apparent for charge C that a bicycloparaffin was concentrated in the fractions that immediately preceded the appearance of aromatic material in the distillate.

3. Adsorption

The results of the analytical adsorption experiment on the entire material are shown in figure 3, from which the aromatic content of the entire distillate was calculated to be 16.1 ± 0.2 percent by volume. The total volume of aromatic hydrocarbons separated by azeotropic distillation and by adsorption was 13.0 liters, of which 1.7 liters originally distilled outside of the normal boiling range, 177° to 200° C (175.3° to 198.3° C at 725 mm Hg). For the portion of the distillate normally boiling between 177° and 200° C, the percentage of aromatic hydrocarbons was calculated to be 15.3 percent by volume.

The results of a typical adsorption experiment are shown in figure 4. It will be observed that a satisfactory separation of paraffins and cycloparaffins from aromatic hydrocarbons was obtained.

V. Isolation of Normal Undecane

The concentrate of normal undecane produced by the azeotropic distillation was used as the starting material for the isolation of a small (50 ml) sample of substantially pure normal undecane. About 0.9 liter of material with a refractive index, n_D^{25}, of 1.4177 was crystallized as described in section III, yielding approximately 0.3 liter of material with a refractive index of 1.4153. The normal undecane thereby separated was further fractionated by adsorption, as described in section III, and the results of this fractionation are shown in figure 5. The fraction with the lowest refractive index, indicated as A in figure 5, was taken as the best sample from this processing. Values for certain physical properties of this sample are as follows:[6] boiling point at 760 mm Hg, 195.893° C; density at 25° C, 0.73662 g/ml; refractive index, n_D^{25}, 1.41507; specific dispersion, $(n_F - n_C)/d$ at 25° C, 0.00979; freezing point in air at 1-atm, −25.678° C; calculated purity, 99.7 mole percent.

No attempt was made to prepare a sample of the highest purity in the course of this investigation, since normal undecane is being prepared as an API-Standard and API–NBS hydrocarbon [15].

VI. Conclusion

The foregoing describes the separation of the entire 177° to 200° C fraction of the original crude petroleum (Ponca, Okla.) into an aromatic portion and a portion containing the paraffins and cycloparaffins, together with a partial separation of cycloparaffins from paraffins and the isolation of normal undecane from the latter. The next work on the 177° to 200° C fraction of this petroleum will include the isolation of individual compounds from the aromatic portion, the complete separation of the cycloparaffins from the paraffins, and the separation of individual compounds from the latter two portions.

[6] The boiling point, density, and refractive index were determined by A. F. Forziati [11, 12, 13]. The determination of the freezing point and purity was made by L. F. Soule under supervision of A. J. Streiff [14, 15].

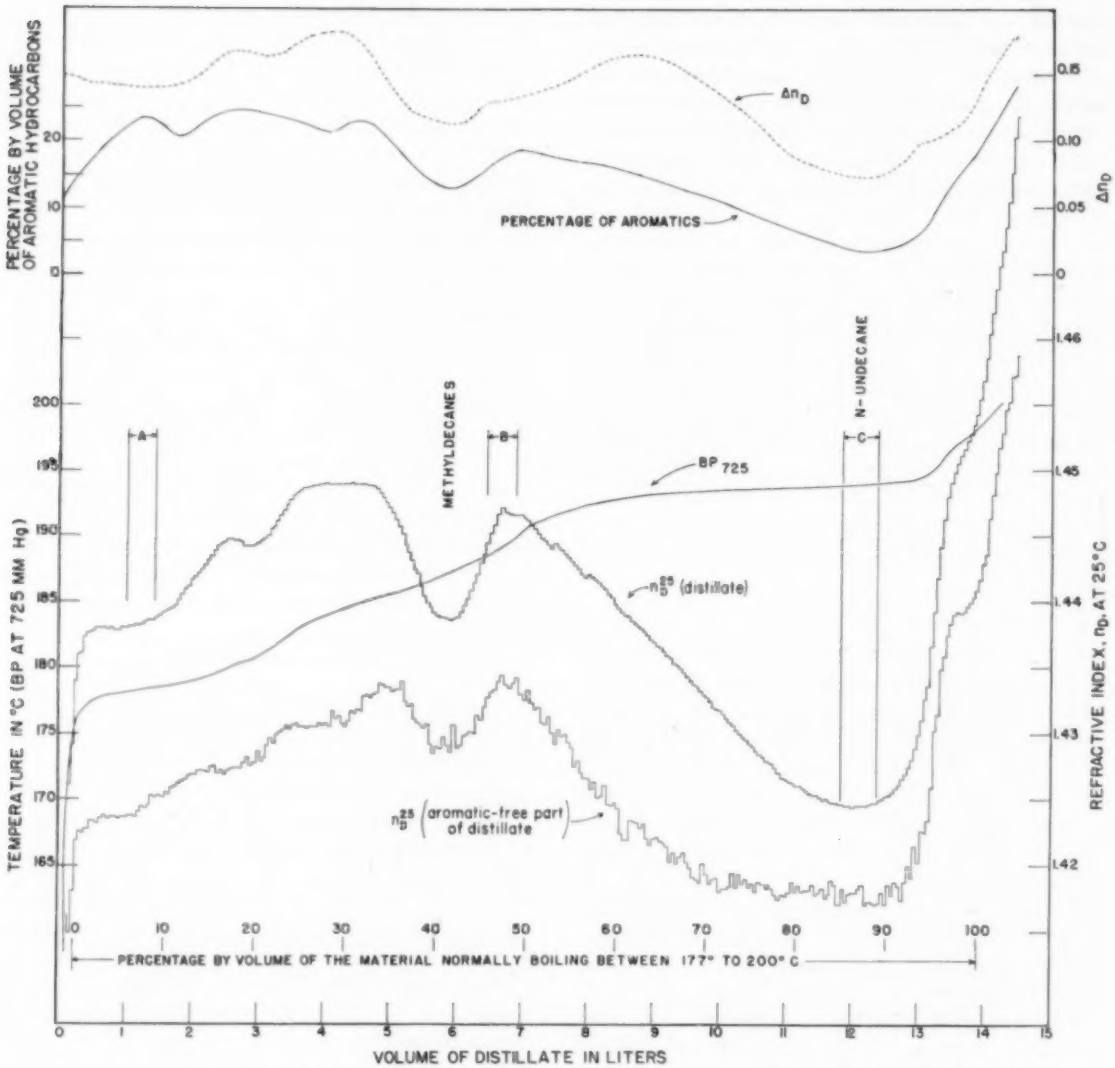

FIGURE 1. *Regular distillation of the 177° to 200° C fraction of petroleum.*

The lower scale of ordinates on the right gives the refractive indices of the fractions of the distillate as obtained and on an aromatic-free basis (see footnote 3). The lower scale of ordinates on the left gives the boiling point of the distillate at a pressure of 725 mm Hg. The upper scale of ordinates on the right gives the difference in refractive index for the two lowermost plots. The upper scale of ordinates on the left gives the percentage of aromatic hydrocarbons by volume. The scale of abscissas gives the volume of the distillate in milliliters. The results of the azeotropic distillation of the portions designated A, B, and C are given in figure 2.

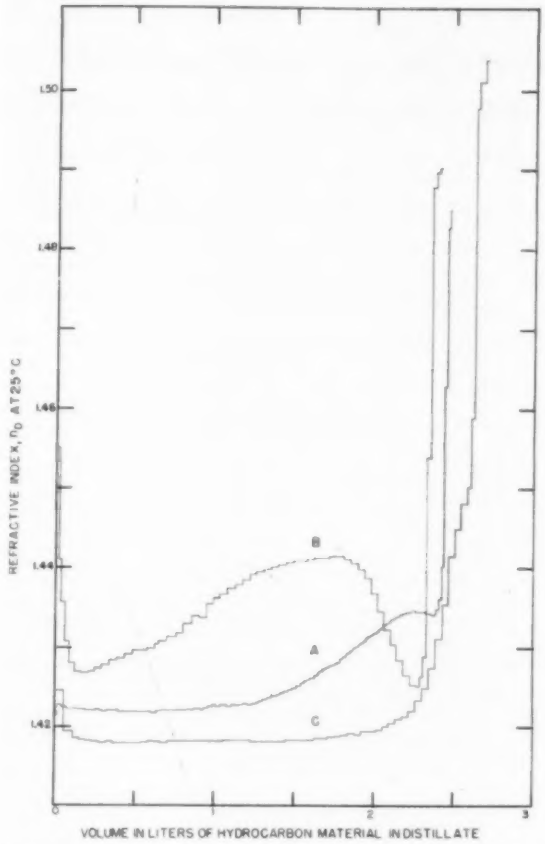

FIGURE 2. *Azeotropic distillation of three representative portions of the 177° to 200° C fraction of petroleum.*

The scale of ordinates gives the refractive index of the hydrocarbon material in the fractions of azeotropic distillate, and the scale of abscissas gives the volume in milliliters of the hydrocarbon material in the distillate. The letters A, B, and C refer to the three charges indicated in figure 1.

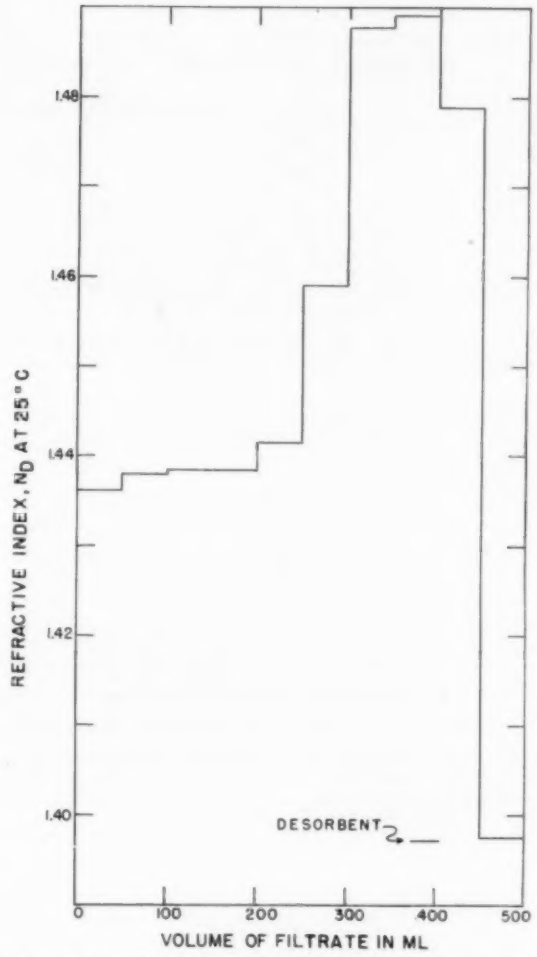

FIGURE 3. *Adsorption of the mixture of paraffins, cycloparaffins, and aromatic hydrocarbons remaining from the azeotropic distillations of the 177° to 200° C fraction of petroleum.*

The scale of ordinates gives the refractive indices of the fractions of the filtrate and scale of abscissas the volume of the filtrate in milliliters.

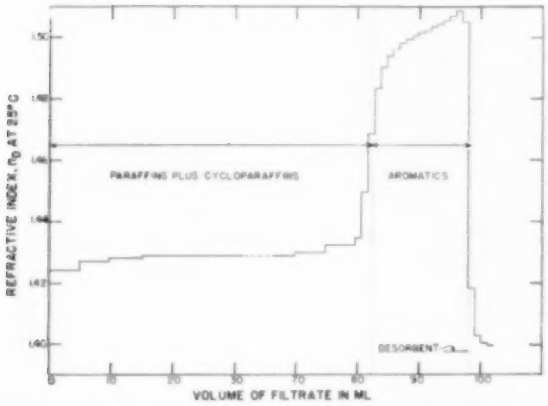

FIGURE 4. *Analytical adsorption experiment on the original 177° to 200° C fraction of petroleum.*

The scale of ordinates gives the refractive indices of the fractions of the filtrate and scale of abscissas the volume of the filtrate in milliliters.

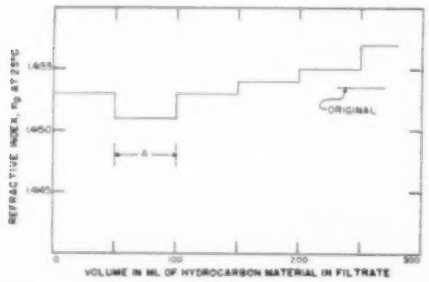

FIGURE 5. *Purification of n-undecane by adsorption.*

The scale of ordinates gives the refractive indices of the hydrocarbon material in the filtrate and the scale of abscissas the volume in milliliters of hydrocarbon material in the filtrate. The portion designated by the letter A was taken as the best sample from this processing.

VII. References

[1] F. D. Rossini, Petroleum Engr. **14,** 223 (1943).

[2] F. D. Rossini, Proc. Am. Petroleum Inst. **19,** (III), 99 (1938); Oil Gas J. **37,** No. 27, 141 (1938); Refiner National Gasoline Mfr. **17,** No. 11, 557 (1938).

[3] B. J. Mair and S. T. Schicktanz, BSJ. Research **11,** 665 (1933) RP614.

[4] B. J. Mair and A. J. Streiff, J. Research NBS **27,** 343 (1941) RP1423.

[5] C. B. Willingham and F. D. Rossini, J. Research NBS **37,** 15 (1946) RP1724.

[6] B. J. Mair, A. L. Gaboriault, and F. D. Rossini, Ind. Eng. Chem. **39,** 1072 (1947).

[7] B. J. Mair, J. Research NBS **34,** 435 (1945) RP1652.

[8] B. J. Mair and F. D. Rossini, ASTM Standards on Petroleum Products, Committee D–2, Year Book, p. 20 (1946); ASTM Standards on Petroleum Products, Committee D–2, Year Book, p. 486 (1947).

[9] B. J. Mair, D. J. Termini, and F. D. Rossini, J. Research NBS **37,** 229 (1946) RP1744.

[10] A. R. Glasgow, Jr., C. B. Willingham, and F. D. Rossini, American Petroleum Institute Research Project 6, National Bureau of Standards. Unpublished.

[11] C. B. Willingham, W. J. Taylor, J. M. Pignocco, and F. D. Rossini, J. Research NBS **35,** 219 (1945) RP1670.

[12] A. F. Forziati, B. J. Mair, and F. D. Rossini, J. Research NBS **35,** 513 (1945) RP1685.

[13] A. F. Forziati, American Petroleum Institute Research Project 6, National Bureau of Standards. Unpublished.

[14] A. R. Glasgow, Jr., A. J. Streiff, and F. D. Rossini J. Research NBS **35,** 355 (1945) RP1676.

[15] A. J. Streiff, F. D. Rossini, et al., American Petroleum Institute Research Project 6, National Bureau of Standards. Unpublished.

WASHINGTON, May 21, 1948.

U. S. Department of Commerce
National Bureau of Standards

Research Paper RP1958
Volume 42, February 1949

Part of the Journal of Research of the National Bureau of Standards

Winter Measurements of Ozone Over the Organ Mountains, New Mexico

By Ralph Stair

This paper gives data on the total amount of ozone above the Organ Mountains at the White Sands Proving Ground in New Mexico from December 16 to 19, 1947, and from January 6 to 8, 1948, as determined from solar ultraviolet measurements by a phototube and filter method. The measurements indicate ozone in the stratosphere in an amount equivalent to a layer about 0.19 centimeter in thickness at normal temperature and pressure for each of the two periods.

I. Introduction

The measurements of the total amount of ozone in the stratosphere over the Organ Mountains in New Mexico recorded in this paper represent additional effort toward a check between the filter method employed at this Bureau and those employed by the Naval Research Laboratory in their V–2 rocket experiments at the White Sands Proving Ground, New Mexico. These measurements were sponsored jointly by the Naval Research Laboratory and the National Bureau of Standards. The data have been reduced in a manner similar to that employed for previous measurements [1, 2].[1]

During the period of the year in which these measurements were made the sun was near its maximum southern position, hence at no time was the mass of the column of air traversed by sunlight less than about 1.73 times that of the zenith air mass of the station. About 3 hr before (or after) solar noon, when the air mass was greater than about 3.00, the ultraviolet radiant energy within the ozone band, 3,000 to 3,400 A, was so nearly completely absorbed that precise measurements were considered unobtainable because of increased dust scattering at low solar altitudes. Hence in the present report only those values for air masses less than about 3.00 are given.

In this method for the determination of total ozone, the results are based on the relative spectral energy emitted by the sun within the spectral region of 3,000 to 3,400 A (see fig. 3). As a matter of fact, because of the high air masses encountered during the winter season, which greatly reduce the solar energy of wavelengths shorter than 3,100 A, together with the low relative spectral response of the phototubes and the low ozone absorption for wavelengths above 3,350 A, it is only between about 3,100 and 3,350 A that an accurate knowledge of the relative solar-energy emission of the sun is required.

It is a known fact that there are large fluctuations in the short ultraviolet emission from the sun [20, 21, 22], which appear to be associated with sun spots and other solar activity. However, no extensive study has been made, either of solar variation at these wavelengths or of ozone changes accompanying increases in short wavelength solar emission because of the difficulties involved in transporting precision instruments above the ozone layer of the stratosphere [17, 18, 19]. According to the records of the U. S. Naval Observatory and the Radio Division of the National Bureau of Standards, there was no unusual solar activity during either period in which the herein recorded ozone measurements were made. A few small sun spots were present in each case, but no pronounced radio or magnetic phenomena commonly associated with excessive solar activity were detected.

It is generally conceded that the photochemical

[1] Figures in brackets indicate the literature references at the end of this paper.

production of ozone occurs principally at altitudes exceeding 30 km [11, 12, 13], which level is above about 90 percent of the total ozone present at any time within the atmosphere. Hence, the major portion of the ozone at a particular time and place has been carried downward by air currents, or other means, so that any fluctuations due to ultraviolet solar variations would become second-order effects. Furthermore, the small changes in the total solar emission, as measured at the earth's surface, are indicative of the fact that changes in the longer wavelengths (3,000 to 3,400 A) transmitted by the atmosphere are relatively small. Although it is not possible, by this method or by any of those dependent upon ultraviolet measurements, to separate changes in the spectral quality of solar radiant flux from true ozone changes, it is believed that changes in solar emission have but a small effect upon the results and may therefore be neglected without making a serious error in the determination of the total amount of stratosphere ozone.

II. Instruments and Methods

In this work at San Augustine Pass in the Organ Mountains, New Mexico, the same two Westinghouse type 767 titanium phototubes (No. 2 and 6) and the same type of amplifier were employed as in the previous work at Mount Evans, Colorado [2] in the summer of 1936, and in the Organ Mountains [1] in the summer of 1947. Two new filters having transmittances intermediate between those for Ba–3 and Ba–1 and between Ba–1 and Ni were substituted for two of the previously employed filters—Cx and Ba–3—in order to keep all of the observed transmittances between about 25 and 75 percent, that is, within the transmission range most sensitive for measurement of ozone changes.

New determinations were made on the relative spectral responses of the phototubes and of the spectral transmittances of the four filters employed. No weight was given to any previous measurements. Small differences in the values employed are therefore the result of physical changes or may be credited to experimental error in either the former or present determinations. The relative spectral responses of the two phototubes and the spectral transmittances of the four filters employed are given in figure 1.

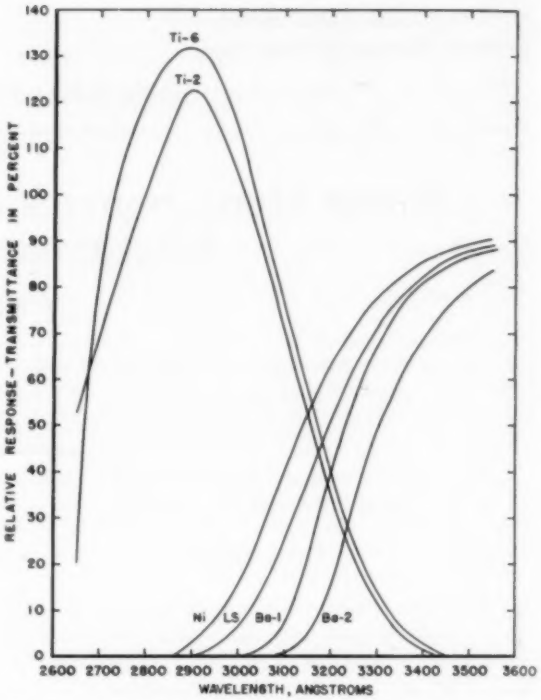

FIGURE 1. *Relative spectral response curves for the two titanium phototubes; also the spectral transmittances of the four filters employed in this work.*

These data were obtained at room temperatures, or slightly above, as affected by the radiant energy employed in the tests, and require a correction if the temperature is excessively different for the field observations. It has been found that the relative spectral response of these phototubes changes but little with temperature over reasonable ranges. However, such is not the case with the glass filters, or of the glass envelopes of the phototubes. Since the phototubes are used within a spectral region where there is no appreciable absorption in the glass (3,000 to 3,400 A), changes in the spectral transmittance of the glass envelope may be neglected. For the filters, a change in temperature of 20 deg C resulted in a change in integrated filter transmittance of about 1 percent, in the 40- to 50-percent range, when the source was simulated sunlight with the phototube used as the receiver. Approximate corrections were made in the case of the December 1947 measurements because of the low temperatures (about 0 °C) encountered. For the January 1948

measurements, no corrections were made, since the weather was warm, being little below normal room temperature at the observing station.

In this work the phototube current is amplified by means of a portable balanced-tube-direct-current amplifier and read on a 0 to 15 microampere Weston model 440 meter. Complete details covering the construction and operation of the amplifier were given in a previous publication [2]. Readings are made without and with each of the four filters in succession. A record is made in which the time of day is tabulated for each set of readings for each filter. Measurements are usually alternately made with two phototubes. The total percentage transmittances of the filters were calculated and plotted as a function of air mass for each of the days on which measurements were made. (See figs. 4, 5, 6, 7).

The determination of the solar air mass as a function of standard time of the station is a rather detailed operation that must be performed before it is possible to interpret the filter-transmittance data intelligently. Reference may be made to a previous paper for details in the determination of air mass at San Augustine Pass [1].

In order to obtain a measure of the total amount of stratosphere ozone at the time of the observations by this method, a solar energy curve outside the atmosphere is either calculated from the measurements or else assumed. For this work, the relative energy curve obtained and employed in the previous work [1] has been used without adjustment. Starting with this relative spectral energy curve, and by a process of arithmetical integration (using 20 A as a unit) a set of transmittance curves for the four filters and two phototubes, as a function of solar air mass was calculated. For these calculations, the Fabry and Buisson [3] transmittance coefficients for ozone and the Rayleigh scattering (atmospheric transmittance) coefficients as used by O'Brien [4] in the reduction of the stratosphere balloon data (*Explorer I* and *II*) have been used. Some of the ozone and scattering (transmittance) curves employed are reproduced in figure 2.

The method is illustrated by an example in table 1, which gives all the steps in the determination of one point (air mass=1.75) on each of the calculated (0.20 cm) ozone curves for phototube Ti-2. This table incidentally gives the relative spectral energy distribution for air mass, $M=0$,

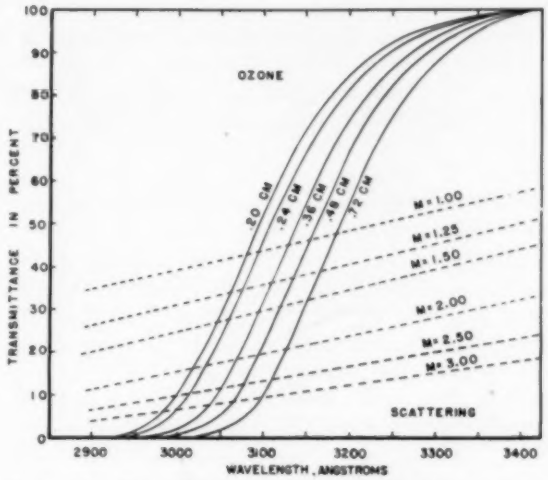

FIGURE 2. *Spectral transmittance of the atmosphere in terms of molecular (Rayleigh) scattering and ozone absorption.*

that is, outside the earth's atmosphere; also the transmittances of the four filters and the relative spectral response of one of the phototubes. For further details regarding this table, reference should be made to previous papers [1, 2].

In figure 8 some of the measurements made during the summer of 1947 [1] are reproduced, together with new calculations of ozone based on the recently determined phototube responses and filter transmittances. The curves shown by the long dashes (in fig. 8) are based on the relative solar spectral energy data of table 1 for $M=0$. The curves shown by the short dashes are based on relative solar energy data (see fig. 3) obtained from V–2 rocket experiments by the Naval Research Laboratory [5]. Similar calculations with the NRL curve are shown in figures 4, 5, 6, and 7 for the winter measurements.

Several things should be noted relative to the choice of the solar energy curve outside the earth's atmosphere. The NBS curve [1] was obtained by a phototube and filter integration method and may not be precise with regard to specific features, since the curve obtained is simply a smooth curve, which appears to best represent the experimental data. On the other hand, the NRL curve is an envelope of the observed spectral emission curve of the sun wherein the Fraunhaufer absorption lines and bands are neglected. If the absorption bands were uniformly distributed, no error would result. The author prefers to use the NBS curve

TABLE 1.—*Method employed in the calculation of ozone values*

This example includes a single set of data for phototube Ti-2 for air mass $M=1.75$ and an ozone value of 0.20 cm ntp

Center of wavelength interval	Relative spectral energy $M=0$	Scattering transmittance $M=1.75$	Transmittance 0.35 cm O_3	Column 2×3×4 relative energy $M=1.75$	Relative response phototube Ti=2	Column 5×6 integrated response	Transmittance of Ni filter	Column 7×8 integrated response	Transmittance of L8 filter	Column 7×10 integrated response	Transmittance of Ba-1 filter	Column 7×12 integrated response	Transmittance of Ba-2 filter	Column 7×14 integrated response
1	2	3	4	5	6	7	8	9	10	11	12	13	14	15
A														
2,940	47	0.157	.....	.....	1.18	.....	0.066	.....	0.02	.....	.....	.....	.....	.....
60	56.5	.182	0.001	0.01	1.14	0.01	.094	.....	0.03	.....	.....	.....	.....	.....
80	58	.191	.004	.04	1.10	.04	.129	.....	.04	.....	.....	.....	.....	.....
3,000	58.5	.198	.020	23	1.04	.24	.167	0.04	.07	0.02	0.001	.....	.....	.....
20	55.5	.207	.046	.53	0.985	.52	.210	.11	.09	.05	.003	.....	.....	.....
40	52	.216	.087	.98	.92	.90	.257	.23	.13	.11	.007	0.01	.....	.....
60	50	.224	.151	1.69	.85	1.44	.304	.44	.17	.24	.018	.03	0.001	.....
80	49.5	.232	.228	2.73	.78	2.13	.353	.76	.21	.44	.039	.08	.003	.....
3,100	49	.241	.331	3.91	.70	2.74	.407	1.12	.26	.70	.076	.21	.008	0.02
20	49.5	.249	.423	5.21	.63	3.28	.458	1.50	.31	1.01	.130	.43	.018	.06
40	52	.258	.500	6.83	.55	3.76	.507	1.91	.36	1.36	.192	.72	.037	.14
60	56	.267	.597	8.93	.475	4.24	.552	2.34	.41	1.75	.263	1.12	.069	.29
80	59	.275	.682	11.07	.41	4.54	.597	2.71	.47	2.11	.336	1.53	.114	.52
3,200	64	.283	.753	13.64	.35	4.77	.634	3.02	.51	2.45	.405	1.93	.168	.80
20	74	.292	.808	17.46	.29	5.06	.670	3.39	.56	2.83	.473	2.39	.232	1.17
40	88	.300	.850	22.44	.24	5.39	.701	3.78	.60	3.25	.534	2.88	.297	1.60
60	94	.309	.885	25.71	.195	5.01	.731	3.66	.65	3.23	.591	2.96	.364	1.82
80	96	.317	.913	27.78	.15	4.17	.756	3.15	.68	2.84	.638	2.66	.426	1.78
3,300	98	.325	.936	29.81	.115	3.43	.776	2.66	.71	2.45	.681	2.34	.483	1.66
20	99	.334	.952	31.48	.085	2.68	.800	2.14	.74	1.99	.718	1.92	.539	1.45
40	99	.343	.965	32.77	.060	1.97	.817	1.61	.77	1.51	.748	1.47	.586	1.15
60	99	.352	.978	34.08	.037	1.26	.832	1.05	.79	0.98	.774	0.98	.629	0.79
80	99	.360	.992	35.35	.021	0.74	.844	0.62	.81	.60	.795	.59	.666	.49
3,400	99	.368	.997	36.32	.010	.36	.856	.31	.83	.30	.813	.29	.697	.25
20	99	.376	.998	37.15	.002	.07	.866	.06	.84	.06	.829	.06	.725	.05
Total	.....	.....	.....	.....	.....	58.75	.....	36.61	.....	30.28	.....	24.60	.....	14.04
Percentage transmittance	.....	.....	.....	.....	.....	.....	.....	62.3	.....	51.5	.....	41.9	.....	23.9

as its use results in closer agreement with the experimental data for high air masses relatively to low air masses. This characteristic is more pronounced in the case of air masses between 1.0 and 1.7 (see fig. 8). For the measurements recorded herein, calculations based on the NRL solar curve indicate ozone in the amount of about 0.04 cm greater than when calculated on the basis of the NBS curve. Between air masses 1.0 and 1.7, the difference is less and ranges between about 0.02 and 0.04 cm (see fig. 8).

III. Amount of Stratosphere Ozone

In figures 4, 5, 6, and 7 are represented the observed data and the calculated effects of assumed amounts of ozone above the San Augustine Pass in the Organ Mountains for the period of December 16 to 19, 1947, and January 6 to 8, 1948. The scattering of the data, which is of the order of about 1 percent and corresponds to about 0.03 cm of ozone, is probably for the greater part random deviation of observations. Although there are some indications of real ozone changes, they are small. According to the Weather Bureau reports, immediately preceding the measurements on December 16 to 19, 1947, polar continental and possibly polar maritime air had moved into the New Mexico area from the northwest. This cold air extended up to 13,000 ft on the 15th, and then became warm again up to 23,000 ft by the 17th. On the morning of the 17th, the tropopause was colder and higher than it had been on

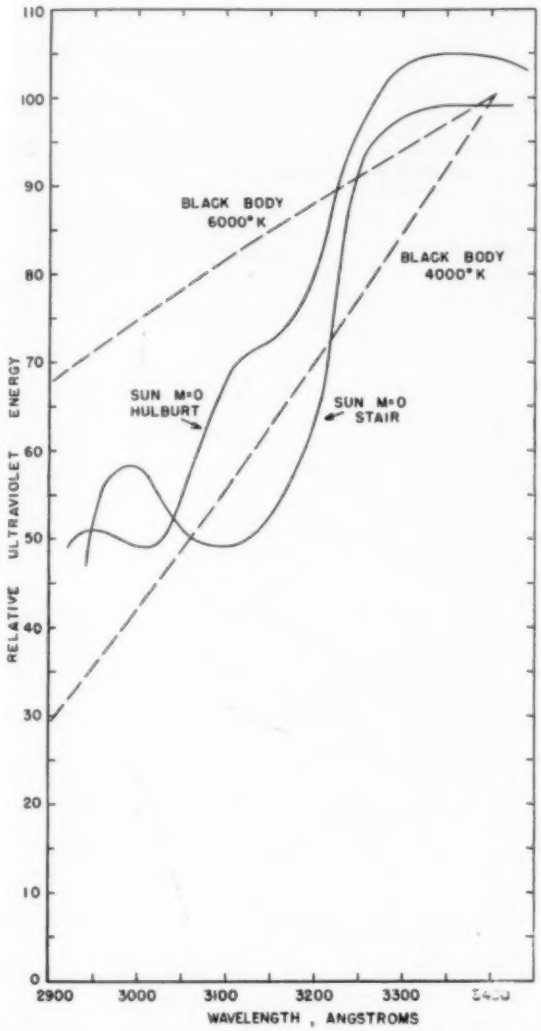

FIGURE 3. *Distribution of energy in the extreme ultraviolet of the solar spectrum.*

The Stair curve is based on previous measurements at Mount Evans, Colo., and at the Organ Mountains, New Mex., and is plotted in terms of microwatts per square centimeter per 10 A. The Hulburt curve is in relative units and is based on V–2 rocket experiments made by the Naval Research Laboratory at White Sands Proving Ground. The curves for black bodies are plotted on relative scales, being arbitrarily set at 100 for 3,400 A.

the 16th (all observations at Albuquerque, New Mex.). This condition continued through the night of the 18th, at which time a second upper cold front has passed the Organ Mountain area. Usually there was a west wind of variable intensity, being somewhat erratic on the 16th in that it shifted to the north and northeast during a part of the day. During the remainder of the 4-day period, there was less wind—at times none. There was an increase in barometric pressure on the 16th, followed by a gradual reduction during the remainder of the period. There is some indication of a decrease in the total amount of ozone during the period (see figs. 4 and 5). This is in agreement with other measurements, in that a decrease in ozone value is to be expected as an anticyclonic mass of air moves into a region [14]. The sky was almost cloudless throughout the day during the 16th and 17th. Much of the sky was covered by thin clouds on the 18th, so that measurements could be made during only part of the afternoon. There was some cloudiness on the 19th, but most of the time the area surrounding the sun was clear.

For several days preceding the ozone measurements on January 6 to 8, 1948, a mass of modified polar continental air had been moving into the Organ Mountain area. There was a continuation of this situation throughout most of the time of the observations, except that on the morning of January 6th the southwestern edge of a high pressure area moved into New Mexico. A light southwest wind was blowing most of the time, and the temperature was high for this season of the year. Haze, local smoke, and clouds produced some interference with the measurements during most of the day of the 6th. Clouds interrupted the work at about 2:15 pm. On the 7th and 8th, there was but little smoke or haze and no clouds throughout the day. The slightly higher ozone values observed on January 6th may be real or may be the result of uncorrected amounts of smoke and haze.

The mean values of ozone, when all of these measurements are considered, appear to be about 0.19 cm for each of the two periods. The data obtained with phototube Ti–6 are higher than those obtained with Ti–2. Any difference must be experimental error, since for the previous calibration of the phototubes as employed for the June and July measurements [1] the data were the reverse in relative amount. Furthermore, the lack of complete agreement for the calculated amount of stratosphere ozone between the measurements with the four filters may also be considered experimental error and indicates the degree of precision that may be expected in this work.

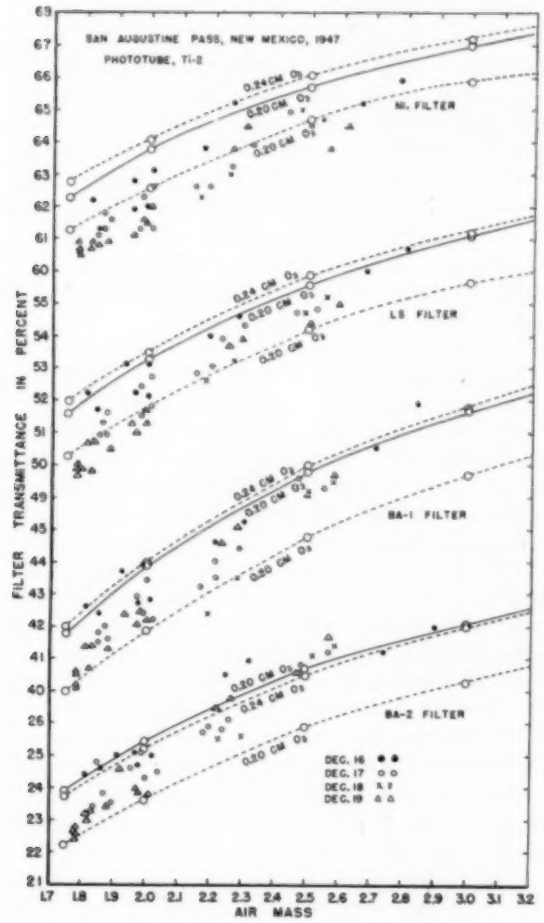

FIGURE 4. *Amount of ozone in the stratosphere, based on observations with titanium phototube 2.*

Calculations based on the Stair solar energy curve (solid lines) and the Hulburt solar energy curve (dotted lines) for air mass, $M=0$.

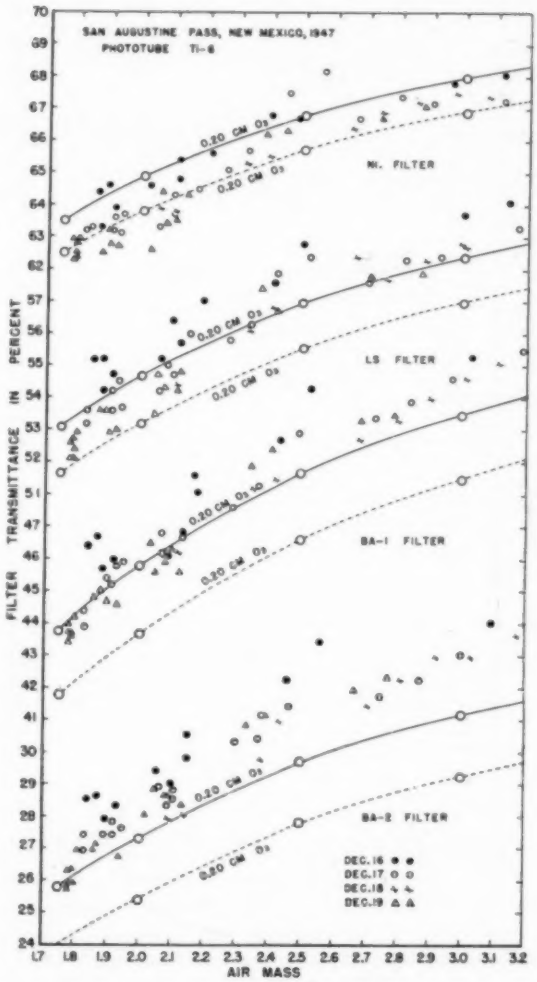

FIGURE 5. *Amount of ozone in the stratosphere, based on observations with titanium phototube 6.*

Calculations based on the Stair solar energy curve (solid lines) and the Hulburt solar energy curve (dotted lines) for air mass, $M=0$.

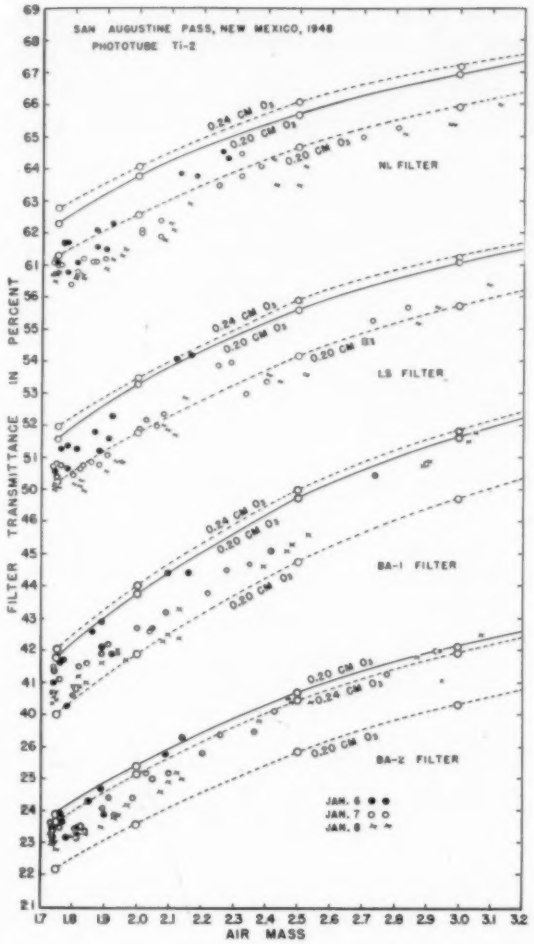

FIGURE 6. *Amount of ozone in the stratosphere, based on observations with titanium phototube 2.*

Calculations based on the Stair solar energy curve (solid lines) and the Hulburt solar energy curve (dotted lines) for air mass, $M=0$.

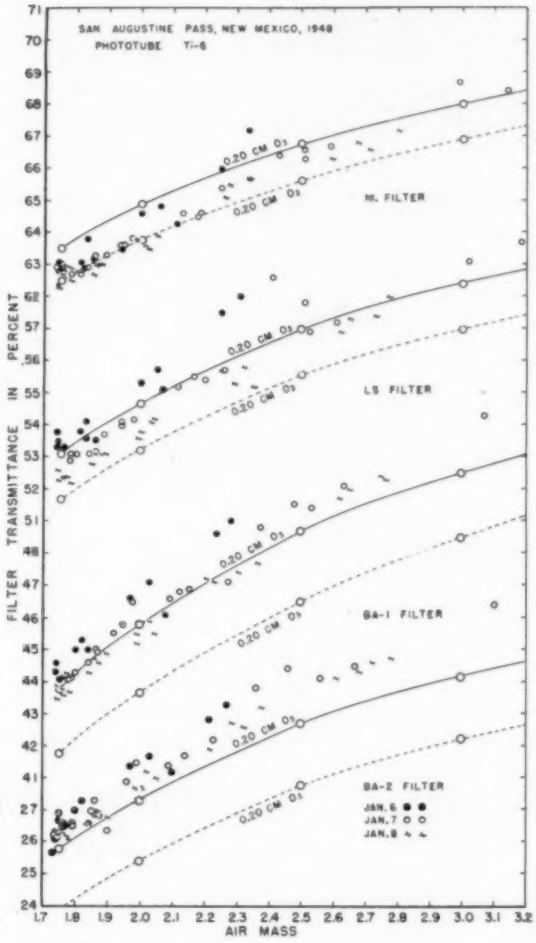

FIGURE 7. *Amount of ozone in the stratosphere, based on observations with titanium phototube 6.*

Calculations based on the Stair solar energy curve (solid lines) and the Hulburt solar energy curve (dotted lines) for air mass, $M=0$.

IV. Conclusion

Although, as previously noted in connection with ozone measurements by this method, the preliminary calibrations and calculations for a particular phototube and filters for a particular station are somewhat involved, when these are once made, it is possible, from a set of curves, to determine precisely the total ozone value from measurements with a single phototube and filter within a few minutes. The simplicity and low cost of the equipment, together with the fact that it is readily portable, makes its use practical in connection with outlying weather stations, should ozone measurements be found useful in connection with weather forecasting. Certain measurements and theoretical considerations indicate [13, 15] that total ozone concentrations, and variations from month-to-month or day-to-day are definitely associated with weather changes but are probably the effect of weather and associated air currents rather than the cause. If such is the case, measurement of total ozone

819237—49——5

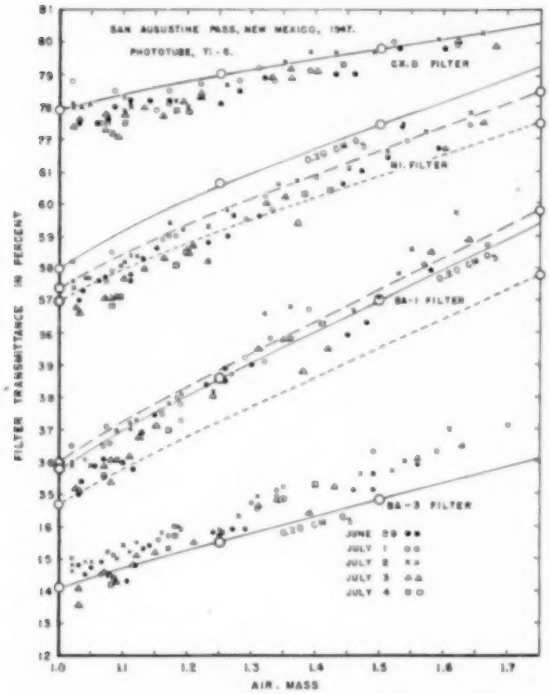

FIGURE 8. *Amount of ozone in the stratosphere, based on observations with titanium phototube 6 in June and July 1947.*

Calculations based on Stair solar energy curve (solid lines, using previously determined constants for phototube and filters; long dashes, using new calibration data for phototube and filters) and on Hulburt solar energy curve (short dashes) for air mass, $M=0$; all curves for 0.20-cm ozone ntp.

may have an indirect usefulness in forecasting and a very important application in fundamental studies of air movements at high altitudes.

The total amounts of ozone determined for the San Augustine Pass in the Organ Mountains (in Dec. 1947 and Jan. 1948) are in general agreement with other determinations for the same latitude and season of the year [6, 9, 10, 11, 16], when it is taken into consideration that the observed values reported herein were made during anticyclone periods when the ozone value should be lower than normal [14].

The author expresses appreciation to the Naval Research Laboratory, which jointly sponsored and financed this work; to John A. Reilly, James A. Stark, and others at the White Sands Proving Ground for valuable assistance in the observational program; and to Edwin M. Margolin of this Bureau for assistance in the reduction of the data.

V. References

[1] Ralph Stair, J. Research NBS **40,** 9 (1948) RP1851.
[2] R. Stair and I. F. Hand, Monthly Weather Rev. **67,** 331 (1939).
[3] C. Fabry and H. Buisson, J. Phys. [5] **3,** 196 (1913); Astrophys. J. **54,** 297 (1921); Compt. rend. **192,** 457 (1931).
[4] B. O'Brien, Nat. Geogr. Soc. Contrib. Tech. Papers, Stratosphere Series, No. 2, p. 49 (1936).
[5] E. O. Hulburt, J. Opt. Soc. Am. **37,** 405 (1947).
[6] G. M. B. Dobson, Proc. Roy. Soc. (London) [A] **129,** 411 (1930).
[7] F. W. P. Götz, Gerlands Beitr. Geophys. **31,** 119 (1931).
[8] G. M. B. Dobson, A. W. Brewer, and B. M. Cwilong, Proc. Roy. Soc. (London) [A] **185,** 144 (1946).
[9] F. W. P. Götz, Ergeb. kosmischen Phys. **III,** 253 (1938).
[10] F. W. P. Götz, Vierteljahrsschr. Naturforsch. Ges. Zurich **89,** 250 (1944).
[11] Richard Ansel Craig, Thesis on The observations and photochemistry of atmospheric ozone and their meteorological significance, Mass. Inst. of Tech. (1948).
[12] O. R. Wulf and L. S. Deming, Terr. Mag. **41,** 299, 375 (1936); **42,** 195 (1937).
[13] Oliver Reynolds Wulf, Proc. Eighth American Scientific Congress **VII,** 439 (1940).
[14] G. M. B. Dobson, D. N. Harrison, and J. Lawrence, Proc. Roy. Soc. (London) [A] **114,** 521 (1927); [A] **122,** 456 (1928).
[15] E. Tonsberg and K. L. Olsen, Geof. Pub. **13,** No. 12 (1944).
[16] G. M. B. Dobson and A. R. Meetham, Quart. J. Roy. Meteorolog. Soc. (London) **60,** 265 (1934).
[17] R. Stair and W. W. Coblentz, J. Research NBS **20,** 185 (1938) RP1075.
[18] R. Stair, J. Research NBS **22,** 295 (1939) RP1181.
[19] W. W. Coblentz and R. Stair, J. Research NBS **22,** 573 (1939) RP1207.
[20] C. G. Abbot, Smithsonian Misc. Coll. **77,** No. 5.
[21] Edison Pettit, Publ. Astron. Soc. Pacific (1925).
[22] G. M. B. Dobson, Proc. Roy. Soc. (London) [A] **104,** 254 (1923).

WASHINGTON, September 28, 1948.

U. S. Department of Commerce
National Bureau of Standards

Research Paper RP 1959
Volume 42, February 1949

Part of the Journal of Research of the National Bureau of Standards

Effect of Convection Currents on the Distribution of Striae in Pots of Optical Glass

By Conrad A. Faick, Arthur E. Williams, and Gerald F. Rynders

The striae distribution in pots of optical glass was studied and the role of convection currents in causing this distribution established. Tracing the convection currents and studying the effect of various cooling techniques on such currents was achieved through the introduction of copper oxide into the melts on their removal from the furnace.

I. Introduction

In all optical glass manufacture a large proportion of the glass in a pot is rejected for defects of one kind or another. Striae, or streaks of different composition within the glass mass, constitute one of the major defects. They are present in all pots of optical glass. However, the amount of glass rejected because of striae is dependent entirely on its distribution in the glass. Fenner [1],[1] Roberts [2], and Wright [3] state that convection currents, set in motion after a pot of glass is removed from the furnace, are largely responsible for the amount of glass rejected for striae.

Other factors, such as pot solution [4], volatilization, and effectiveness of stirring probably determine the amount of striae present, but their distribution is due primarily to convection currents. If the stirring is adequate to keep ahead of striae formation, and the pot of glass at the time of removal from the furnace is free from striae, except possibly for a thin layer in contact with the pot and on the surface of the glass, the problem of striae control becomes one of reduction or control of convection currents.

This paper deals with a study of the striae bands found in optical glass, the role of convection currents in striae distribution, and variations of cooling techniques used to reduce or control convection currents.

[1] Figures in brackets indicate the literature references at the end of this paper.

II. Location and Shape of Striae Bands

It has been the practice at the National Bureau of Standards [5] to tank inspect all optical glass prior to molding it into lens blanks. This inspection of a large number of melts revealed the tendency for striae to be concentrated in certain portions of the melt and to follow a characteristic pattern. For closer study of the striae distribution, samples were selected from definite portions of the melt. Usually, 15 samples were inspected for each melt, representing the center and four quadrants at three different levels, i. e., top, middle, and bottom.

From observation of the striae in the samples, sketches were often made that showed the pattern of the striae and permitted an estimate of the amount present. The sketches shown in figure 1 illustrate the position of the samples chosen and a typical striae pattern. The characteristic of the striae, as revealed by these studies, was a heavy vertical band, originating at the bottom of the pot, going up the center, then spreading across the top and going down the sides. Sometimes this heavy band spread out at the top like branches on a tree; but frequently almost all of it deviated to one side, probably because unsymmetrical cooling caused a migration in one direction. The distance of the striae from the top, sides, and bottom was measured on the selected samples and found to vary between ½ and 4 in., the average distance being 1½ in.

The characteristic striae pattern usually found in a pot of optical glass is illustrated by a few selected samples, which were photographed [6] through the windows of the immersion tank of the inspection apparatus. These are shown in figures 2 to 7, inclusive.

Figure 2 shows the bands down the side of the pot and a loop of striae, probably representing the end of the center band, brought up into the glass by convection currents. Figure 3 shows a heavy band of striae curving around the lower corner of the pot; figure 4 shows the heavy central vertical band, which is believed to be the origin of most of the striae in the glass. Figure 5 shows the heavy vertical band curving toward the side near the surface. Also, there is shown a band of striae parallel to the surface that does not appear to be related to the former. Figure 6, the top edge, shows the end of the heavy vertical band curving downward after having moved across the top of the pot. It also shows a heavy band very close to the pot wall, which may be the source of the horizontal layer (A) shown in figure 5.

Figure 7 shows the striae in a sample from the top left side of a melt, and a cloud of "seeds" associated with it.[2]

III. Cooling Procedure

Since the magnitude of the convection currents depends largely on the method of cooling a pot of glass after removal from the furnace [2], a brief description of the cooling technique will be given before describing the experiments made to trace the convection currents.

After a pot of glass is removed from the furnace, an insulated can is provided to cool the melt to room temperature. This can consists of a sheet metal cylinder lined with 4½ in. of insulating brick, and a lid with 9 in. of insulation. A base-metal thermocouple is in the lid. A triangular suspension is attached to the outer shell and the whole assembly placed over the pot by means of an overhead hoist.

The can is suspended over the pot, at a height determined largely by experience, and allowed to hang in this position for several hours, then lowered to cover the pot. The time of lowering the can is determined by the temperature indicated by the thermocouple in the lid. This temperature is purely an arbitrary value, but is usually somewhere near the critical temperature of the glass as shown by its expansion curve. Variations in the height at which the can is suspended and the temperature at which it is lowered are the means of controlling the type of fracture produced. Figure 8 shows a cooling can in its position over a pot of glass.

IV. Study of Convection Currents

1. Temperature Distribution in a Pot of Glass

Regular production borosilicate melts, 517/645, containing approximately 1,000 lb of glass, were used for the study of convection currents. The first melt of the series was used to determine the time-temperature distribution in the glass during the cooling down period after removal from the furnace. Following the regular production schedule [5], the melt was transferred from the furnace at a temperature of 1,025° C to piers beneath the suspended cooling can. After placing 16 base-metal thermocouples in the melt, the can was lowered to the position shown in figure 8 and a blower placed beneath the pot. When the temperature indicated by the thermocouple in the lid reached 575° C, the can was completely lowered.

These thermocouples were connected to a 16-point strip-chart recorder and a continuous time-temperature record obtained. Figure 9 shows the locations of the thermocouples after the pot of glass was broken open for inspection. Couples 17, 18, 19, and 20 were intended to go down the center of the pot, but the support broke at the time of immersion, allowing them to deviate to one side. It was assumed that the temperature distribution would be symmetrical about the center line of the pot. A comparison of the temperature shown by the deviated couples with the adjacent column of couples tends to substantiate this assumption.

Assuming symmetrical temperature distribution, a series of drawings were made showing the probable isotherms at various times during cooling of the melt. From the time-temperature curves of figure 10 and the probable isothermal sketches of figure 11, the temperature changes taking place during the first few hours of cooling are readily apparent.

[2] Occasionally a melt was produced in which a cloud of seeds formed during the last few minutes of stirring; at times it migrated from the center of the pot toward the edge and on subsequent inspection of the glass was found to occupy the same region as the main striae band.

At the time of removal from the furnace the central and lower portions of the melt were considerably hotter than the top, but horizontal gradients were relatively slight. One-half hour later the top edges had become considerably colder than even the top center. As cooling continued, the top edges and sides cooled more rapidly than the bulk of the glass, but nearly 2 hr elapsed before the bottom showed any appreciable drop in temperature below the center portion.

When the cooling can was lowered to the floor, there was a definite change in the rate of cooling of the various portions of the melt (see fig. 10). About 3½ hr later, the top center (curve T. C. 20) had become the hottest portion. The rapid cooling of the top edges during the early stages was regarded as the cause of the observed convection currents due to changes in density.

2. Tracing Convection Currents

In order to trace the motion of the glass in a cooling pot, a coloring agent was introduced into the melt just after removal from the furnace. Copper oxide, wrapped with copper screen to form balls about ¾ in. in diameter, was used to provide the color. Two of these balls, each weighted with a steel ball in the center, were permitted to sink to the bottom of the pot, and two were suspended from a bar across the top of the pot, so that they would hang about 4 in. below the surface of the glass. The balls were positioned in the melt so that there would be one ball in each quadrant, approximately half way between the center and edge of the pot.

The copper oxide was readily dissolved by the glass, giving a dark blue or black color. The colored streamers formed by the glass flowing past the copper oxide balls provided the means for determining the direction and magnitude of the convection currents.

Copper oxide balls were placed in 13 melts, each of which had a somewhat different cooling treatment either during the last hours of melting or just after their removal from the furnace and before placing them under the cooling can. Beginning with the second melt, the cooling can was provided with windows so that the migration of the colored streamers could be observed. The final positions of these streamers were traced after the pot of glass was cold and opened for inspection.

The various cooling treatments and the results are discussed in the following paragraphs in the order in which they were made.

Melt 1. Exit temperature 1,025° C.[3] The only observation made on this melt was just before lowering the cooling can to the floor. The colored streamer from ball D (see fig. 12) was found to have gone down the sides of the pot, across the bottom and up the center. Those from A and B had traveled up the center, across the top, down the sides and then curved upward again. One streamer had formed a definite loop, such as shown in figure 12. This loop was formed by the flow of glass crossing and displacing the colored streak left by the copper oxide ball sinking to the bottom of the pot. (Observations on subsequent melts reveal the formation of this characteristic loop).

Melt 2. Exit temperature 1,075° C. The copper oxide balls were introduced immediately on removal of the melt from the furnace. Observation through the cooling can windows indicated that by the time the pot was placed on the cooling piers the balls that were to sink had already reached the bottom, leaving dark streaks behind them. The color from the suspended balls had gone a considerable distance, but had gone toward the center of the pot, then down. About 10 min later, the directions appeared to have reversed; the original colored streaks had come back up the center, leaving a blotch of color on top, which was moving toward the sides. Then the streaks were observed to go down the sides and up the center, across the top and down the sides again. A slight clockwise motion around the pot was evident, causing the colored streaks to form spirals rather than plane loops. The amount of travel and twisting of the colored streamers soon made it impossible to follow them, but they appeared to make three or more loops. The appearance of the streamers, just before lowering the cooling can, is shown in figure 13. When the glass was opened for inspection, only the more prominent streaks (fig. 14) could be followed, but not too well. The photograph, figure 15, of both halves of the melt when cold, shows clearly the excessive movement that occurred.

Melt 3. Exit temperature 1,025°C; water-cooled rod in center of pot. A water-cooled rod was placed

[3] Exit temperature is the temperature at which the melt was removed from the furnace. Unless otherwise stated, the temperatures given here are those indicated by an optical pyrometer sighted on the surface of the melt through the stirring rod opening in the door of the melting surface.

in the center of this melt after removal from the furnace. Observation of the colored streaks indicated that the movement of the convection currents was slightly less than in other melts removed from the furnace at 1,025° C, and the direction of travel was reversed. The streaks, as located in the cold glass, are shown in figure 16. Due to somewhat unsymmetrical cooling, the streamer from A appears to bend back on itself. However, it is practically the same as that from B but is directed along the pot wall rather than toward the center. Color from the suspended balls C and D moved very little.

Melt 4. Exit temperature 1,025° C; water-cooled. Immediately after removal from the furnace the copper oxide balls were placed in the pot, the melt then placed on a cooling rack and sprayed with water [4] on the bottom and on the sides up to the pot knuckle, or shoulder. The water spray was applied for 30 min. and the pot then transferred to the regular cooling piers. The balls A and B were somewhat slow in sinking to the bottom, due to the chilled surface of the glass, which was not covered during the spraying period. On sinking, these balls left streaks of color behind which, after a few minutes, curved inward at a position about two-thirds of the way down. After about 45 min. these curved portions had formed loops that had progressed toward the center of the pot and upward. The formation of these loops gives the effect of double streamers. They are caused by the flow of glass from near the pot wall crossing the color paths left by the balls in sinking. The formation of these loops is illustrated by the sketches in figure 17. Figure 18 shows the final position of the colored streamers in melt 4.

Melt 5. Exit temperature 1,025° C; water-cooled, with lid. This melt was covered immediately on removal from the furnace with a lid made of insulating brick 4½ in. thick to prevent rapid chilling of the top surface of the glass while the melt was being water cooled. Due to the lid, observations were necessarily delayed until after the water cooling was finished. At the time of the first observation, the loops in the color streamers had reached the top of the pot and gave the appearance of being double streamers originating from the submerged balls. These streamers did not rise directly in the center of the pot, but slightly to one side, and those portions near the surface were also displaced, indicating unsymmetrical cooling.

The paths of the observed currents are shown in figure 19. The dotted portions shown in the top views represent those portions of the streamers across the bottom of the pot. The final positions of the colored streamers are shown in figure 20.

Melt 6. Exit temperature 1,025° C; air-cooled, with lid. The lid was placed on this melt for the first half hour of cooling in the belief that it would be more effective than the suspended can in keeping the top surface from chilling.

After removal of the lid it was noted that the color from the suspended balls (C and D) had traveled across the top, down the sides, across the bottom, and up the center in much the same manner as in melt 1. The balls A and B sank in a straight line to the bottom of the pot, leaving colored streaks behind. A and B were placed too close to the edge, so that the flow of glass did not displace the streamers as much as in previous melts. As judged subsequently by observations through the top of the insulated can, the positions of these bands at different times were approximately as shown in figure 21. The positions in the cold pot are shown in figure 22.

Melt 7. Exit temperature (975° C); regular cooling, as in melt 1. This melt was cooled in the furnace, with stirring, to 975° C. The copper oxide balls were placed in the melt. But those that were supposed to sink stayed on the surface, and the suspended balls remained stationary. No color streaks developed from any of them. At this temperature the glass was sufficiently viscous that the motion, if any, could not be observed by the use of the copper-oxide balls. The melt was full of striae, which appeared to have been dragged from the pot walls by the action of the stirrer.

Melt 8. Exit temperature 1,050° C; remained in furnace 2 hr at 1,050° C. The holding period at 1,050° C was intended to establish uniform temperature throughout the melt before removal from the furnace. This was based on the previous temperature probe and would be about equivalent to the normal exit temperature of 1,025° C without the holding period. The motion as shown by A and B, figure 23, was practically the same as in melts removed at 1,025° C. However, colors developed at C and D moved very little due to the chilling of the surface.

[4] An ordinary shower head, inverted, provided the spray for the bottom of the pot. A tubular ring perforated with a large number of small holes, suitably directed, provided the spray for the sides of the pot.

Melt 9. Held 2 hr at 1,050° C; surface raised to 1,075° C within 15 min before removal. The raising of the surface temperature at the end of the holding period at 1,050° C was effective in reducing the chilling of the top surface immediately after removal from the furnace. The observed movement of the glass was essentially the same as in the previous melt, except that the color from C and D moved farther. The rapid raising of the temperature to 1,075° C had very little effect on the magnitude of the convection currents. The cooling was very unsymmetrical, due mostly to an improperly hung can, so that the streamers went down one side of the pot and up the opposite side, rather than rising at the center. The appearance of the streamers as viewed from the top is shown in figure 24. Also in figure 24 are shown the final positions of the colors in the cold pot.

Melt 10. Held 1½ hr at 1,000° C surface raised to 1,025° C in 15 min before removal. As may be seen from figure 25, the movement of the glass due to convection currents was considerably less than in melts removed from the furnace at 1,025° C.

The melt had considerable striae, which appeared to have been dragged from the pot wall by the action of the stirrer.

Melt 11. Exit temperature 950° C; stirring stopped and rod removed at 1,025° C. The stirring of this melt was discontinued at 1,025° C, and the melt cooled in the furnace to 950° C. The one copper-oxide ball used was placed in the glass along the right side of the pot as viewed from the front of the furnace, as soon as the stirring rod was removed at 1,025° C.

On removing the melt from the furnace, it was found that the color from the copper-oxide ball had migrated toward the front of the pot in a spiral form. The amount of travel was not great, considering that 1½ hr had elapsed since the end of the stirring. However, the spiral path taken by the streamer shows that some convection currents were present. As viewed from the top, the colored tracer appeared as shown in figure 26. No motion was observed after the melt was removed from the furnace.

Melt 12. Exit temperature 950° C; stirring stopped at 1,050° C; cooling ports in back of furnace. This melt was similar to melt 11, except for additional cooling of the bottom of the pot provided by openings in the back of the furnace.[5] Stirring was stopped at 1,050° C, and a copper oxide ball was placed in the melt, at the front edge of the pot, when the temperature reached 1,025° C. One and one-half hours later, when the melt was removed from the furnace, the colored tracer appeared to have made three-fourths of a loop. The color progressed from the copper-oxide ball across the bottom of the pot, rising near the far side, then across the top toward the front of the pot. A separate streak, caused by oxide left behind as the ball sank, was also visible. This streak was not connected to the main tracer, but gave the appearance of completing the loop. Only a very slight movement was observed after the melt was removed from the furnace. This was shown by a slight migration of the top portion of the streak toward the side of the pot. The positions of the colored streaks in the cold pot were as shown in figure 27.

Melt 13. Exit temperature 1,050° C; cooling ports in back wall of furnace opened. Melt 13 was cooled with the back wall ports open and removed at 1,050° C. The movement of the glass was such that in 40 min the color streaks had made a complete turn, and a half hour later had made the second revolution. They were soon too difficult to follow. Inspection of the cold pot showed the main streamer from ball D to have made 2½ turns, and was accompanied by a few secondary streamers caused by disintegration of the copper oxide ball. The streamers from the other balls were too confused to trace properly. The position of the main streamer from ball D only is shown in figure 28.

V. Discussion

The introduction of color into melts of optical glass has provided a means of tracing convection currents in the glass during the cooling process. The positions taken by the colored tracers have been found to be similar to, and frequently identical to, the positions occupied by the main striae bands. This correspondence between the observed paths of the colored tracers and the striae bands shows that the convection currents are responsible for the striae distribution. The source of these striae appears to be the glass next to the

[5] These openings were 8 in. by 8 in., spaced 3 ft. apart and about level with the bottom of the pot.

walls and bottom of the pot, with the greater amount originating from the bottom of the pot where the stirring is least effective (see fig. 4).

The top horizontal band *A* in figure 5, which seems to be unrelated to the main striae bands, can also be accounted for by convection currents. There is frequently a movement of the surface glass (melt 2) toward the center of the pot immediately on removal from the furnace; this movement reverses direction when the melt is placed beneath the cooling can. The early motion toward the center could carry glass of different composition from the pot walls and spread it across the top of the melt near the surface where it would be frozen in before the direction of motion was reversed. The heavy band *B* in figure 6 shows a distinct loop, which could also be explained by this reversal of direction.

The various procedures tried for control of convection currents were only modifications of the standard cooling procedure. Of the various modifications tried, the lowering of the exit temperature was by far the most effective. However, this procedure could be carried out only to a limited extent. When the exit temperature was reduced below 1,025° C (melts 7 and 10), striae were dragged into the glass from the pot walls by action of the stirrer.[6]

In regular production, melts of borosilicate glass were removed from the furnace at 1,050° C whenever the cooling ports in the back wall of the furnace were used to increase the cooling of the bottom portion of the pots. It was found, however, that these ports were not effective for the purpose intended, and that the higher exit temperature tended to increase the convection currents (see melt 13).

The procedure of cooling the glass in the furnace after discontinuing the stirring reduced the convection currents, but some striae were still evident and appeared to be deeper in the glass. This procedure may be more effective if the stirring could be carried to a temperature well below 1,025° C.

[6] Further reduction of the exit temperature may be possible by the use of a slower speed than that now available, namely, 6 rpm.

The use of the water-cooled rod in the center of the melt provided too much local cooling and reversed the direction of the convection currents. Although the amount of motion was reduced, the heavy bands of striae were directed downward approximately half way between the center and the walls of the pot, resulting in a more than the usual loss of glass.

Water-cooling the outside of the pot for ½ hr had practically no effect on the magnitude of the convection currents. The use of the insulating lid only served to direct the striae closer to the pot walls and the surface of the glass.

It was found that the paths of the colored streamers, and consequently the striae layers, depend to a great extent on the symmetry of cooling. To avoid excessive loss of glass from striae, considerable care must be taken to assure that the cooling can is properly placed and the melt allowed to cool symmetrically.

The loss of glass due to the introduction of color was not significant, unless the motion of the glass during cooling was excessive. The colored streaks follow paths taken by the striae and are located in the portions of the melt that would normally be discarded on account of striae.

VI. Conclusion

The striae distribution in pots of borosilicate 517/645 optical glass was determined and the role of convection currents in causing this distribution established.

Of the various modifications of the cooling procedure employed, that of lowering the exit temperature formerly used, namely 1,075° C, about 50 deg C was found to be the most effective in reducing convection currents. Stirring could not be continued much below 1,025° C, as striae from the pot walls would be dragged into the melt.

The use of copper oxide balls, introduced into the melt after removal from the furnace, proved to be satisfactory for tracing convection currents, and thereby judging the efficacy of the cooling technique employed.

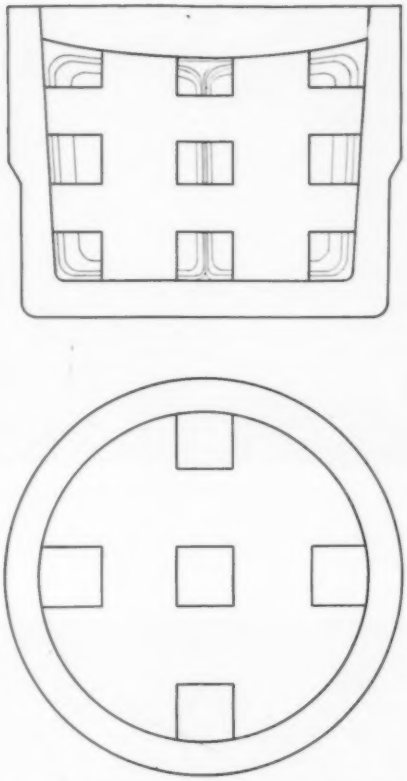

FIGURE 1. *Diagrams showing the location of the 15 samples chosen for inspection and the approximate location of the main striae bands.*

FIGURE 2. *Sample from the middle level showing striae bands along the left side of the pot and the end of loop caused by convection currents.*

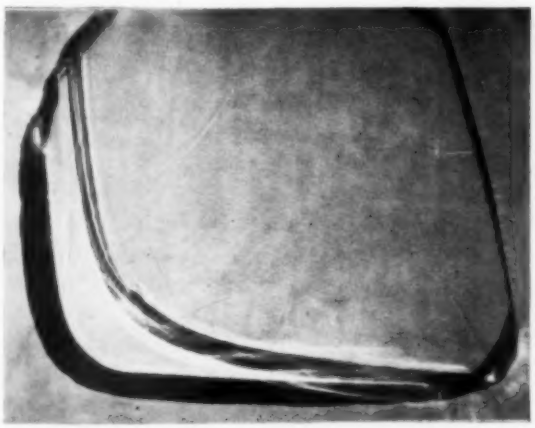

FIGURE 3. *Heavy striae band curving around lower left corner of pot.*

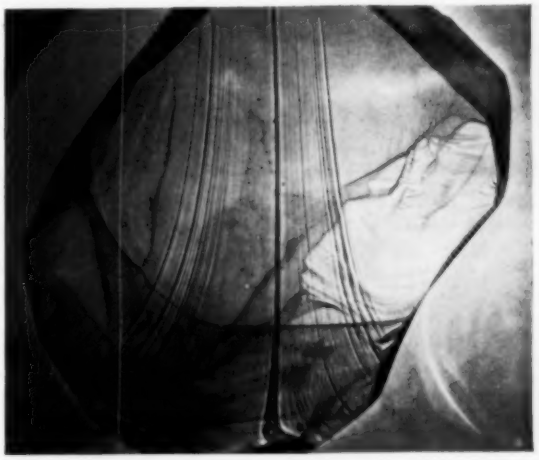

FIGURE 4. *Sample from bottom center of a melt showing the origin of the heavy vertical striae band.*

819237—49——6

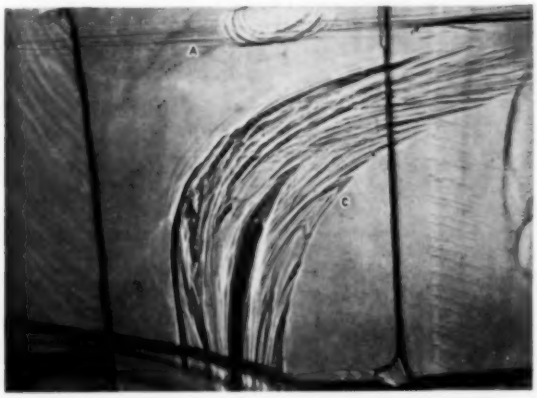

FIGURE 5. *Sample from top center of a melt showing the horizontal surface striae band (A), and the curving of the heavy vertical band (C) toward the right side of the pot.*

FIGURE 6. *Sample from top right side of a melt showing a band of striae (C) curving downward into the melt, and a heavy band (B), very close to the pot wall.*

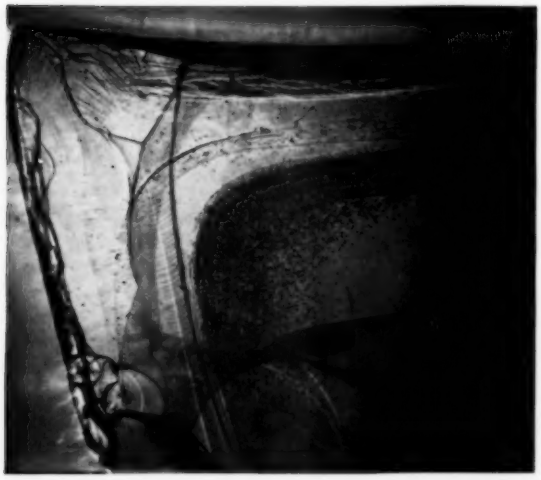

FIGURE 7. *Sample from top left side of a melt showing a cloud of seeds associated with a heavy band of striae.*

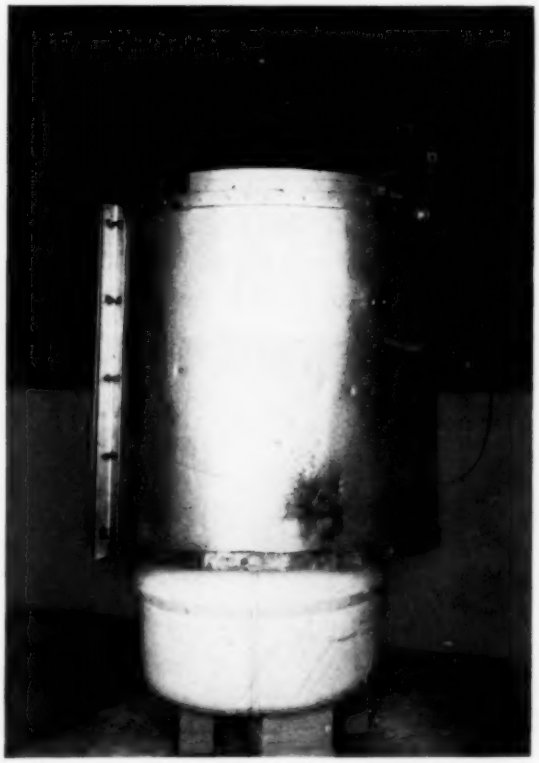

FIGURE 8. *Cooling cover in suspended position over a pot of glass.*

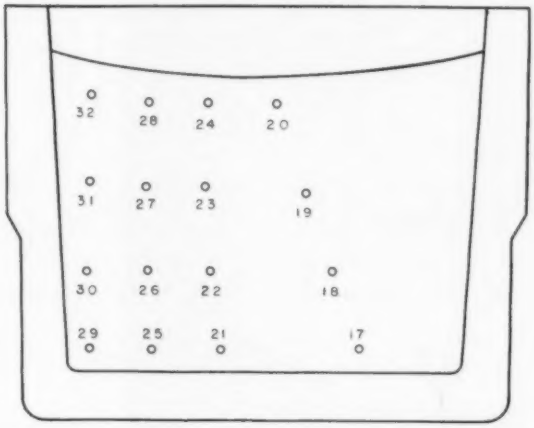

FIGURE 9. *Position of thermocouples employed for the study of the temperature distribution in a pot of glass.*

The numbers used here refer to the numbers on the recorder to which the thermocouples were connected.

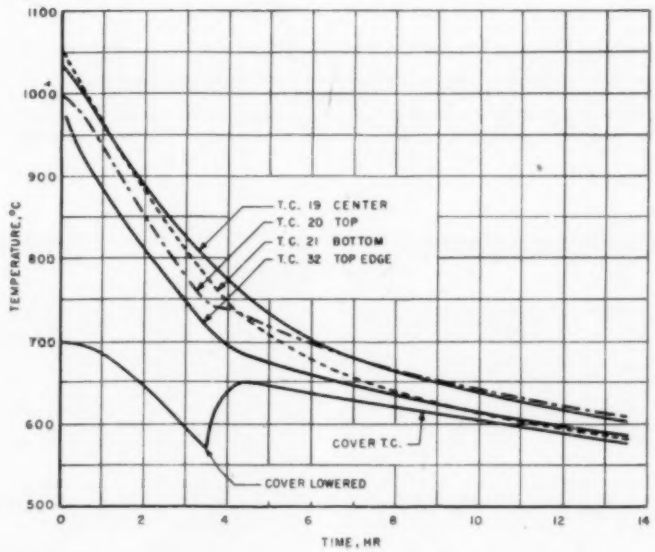

FIGURE 10. *Time-temperature relations in various portions of the glass as shown by thermocouples 19, 20, 21, and 32.*

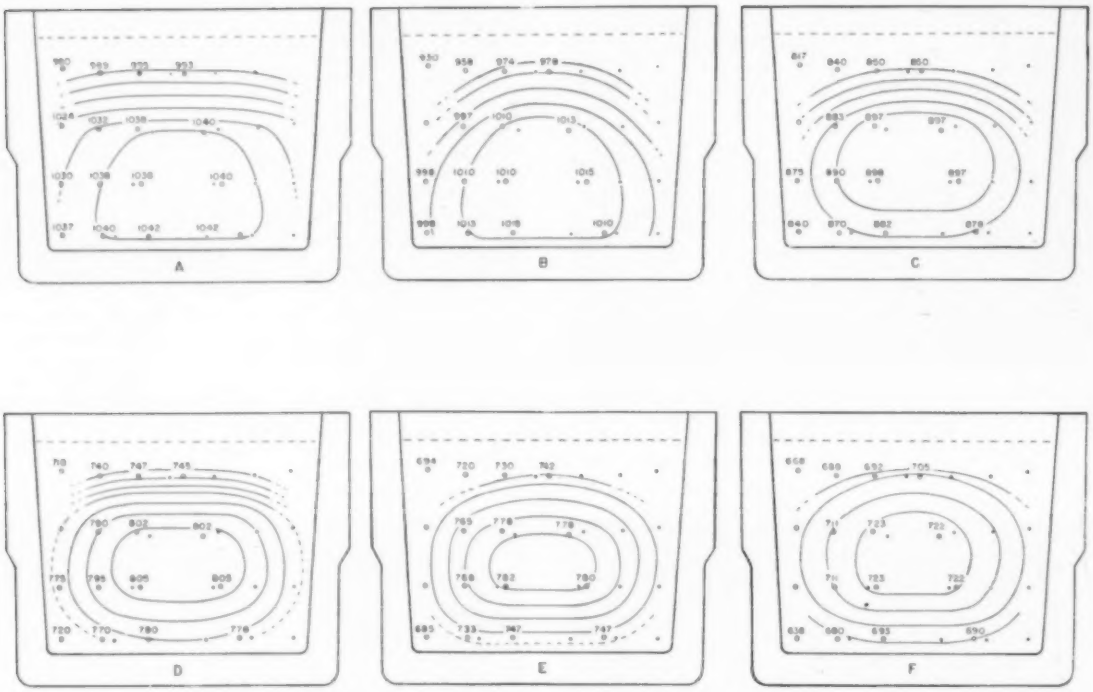

FIGURE 11. *Probable isotherms in a pot of glass during cooling.*

a, 10 min after removal from the furnace; b, ½ hr after removal from the furnace; c, 2 hrs after removal from the furnace; d, 3½ hrs after removal from the furnace (the cooling cover was lowered to the floor at this time); e, ½ hr after lowering cooling cover; f, 2 hrs after lowering cooling cover.

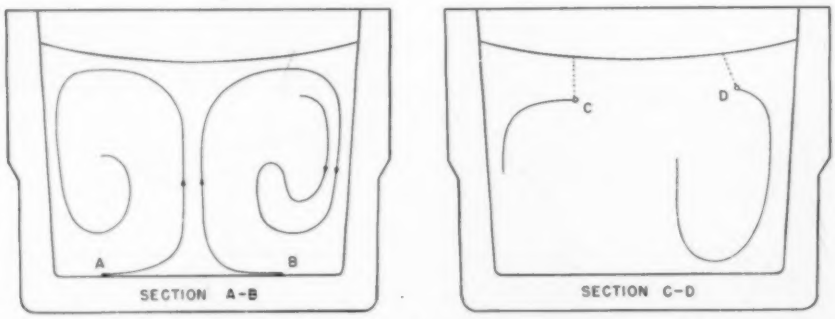

FIGURE 12. *Final position of the copper-oxide tracers in melt 1.*

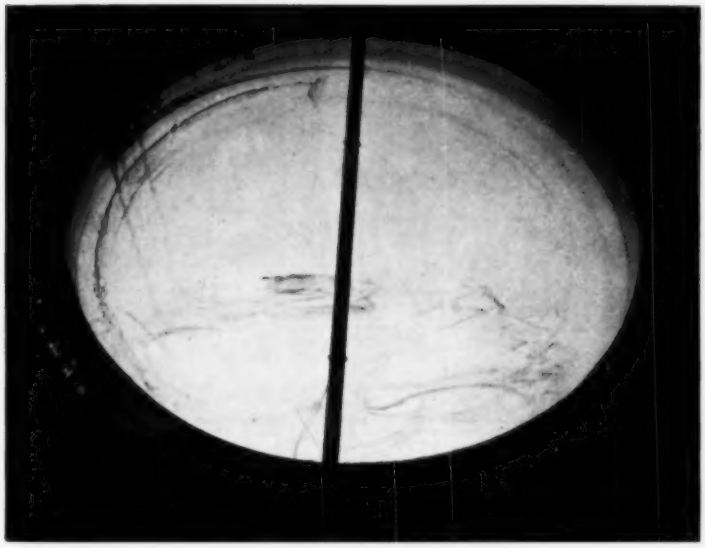

FIGURE 13. *Copper-oxide tracers in melt 2.*

The portions of the tracers deep in the glass show up as light streaks; those near the surface are dark.

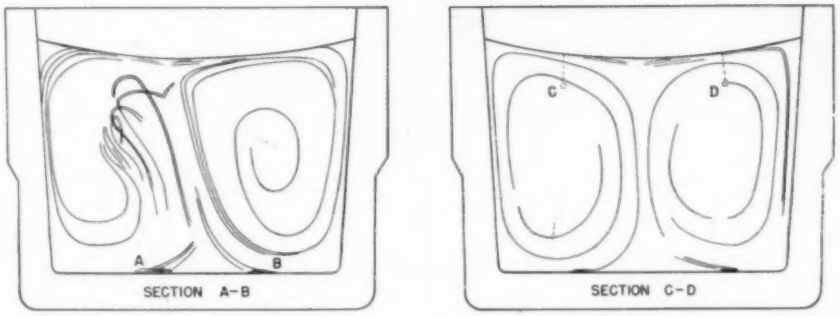

FIGURE 14. *Approximate location of the main portions of the copper-oxide tracers in melt 2 when cold.*

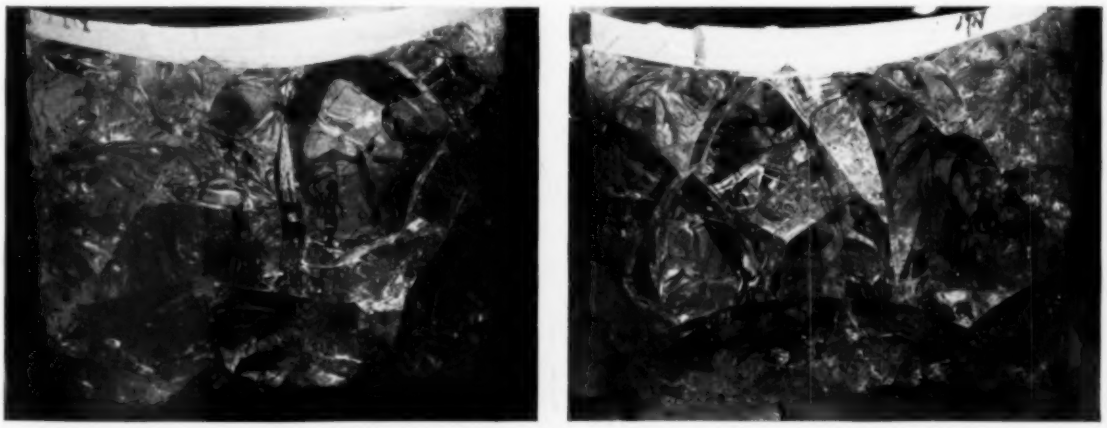

FIGURE 15. *Melt 2 when opened for inspection.*

The numerous streaks from the copper-oxide tracers and their tangled condition illustrate the excessive motion that occurred.

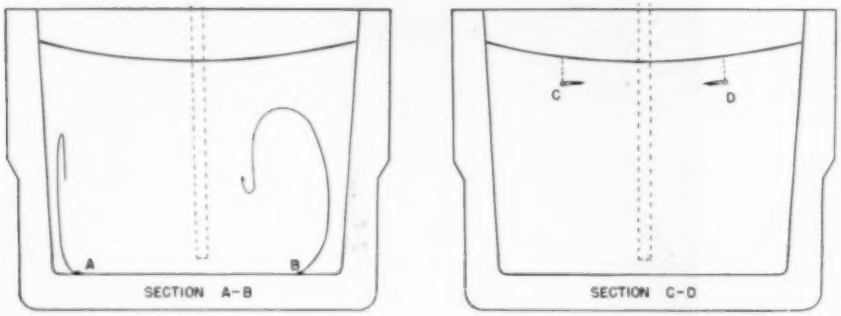

FIGURE 16. *Final positions of the copper-oxide tracers in melt 3 with the water-cooled rod in the center.*

The streak from A is similar to that from B, but is directed along the pot wall instead of toward the center of the pot.

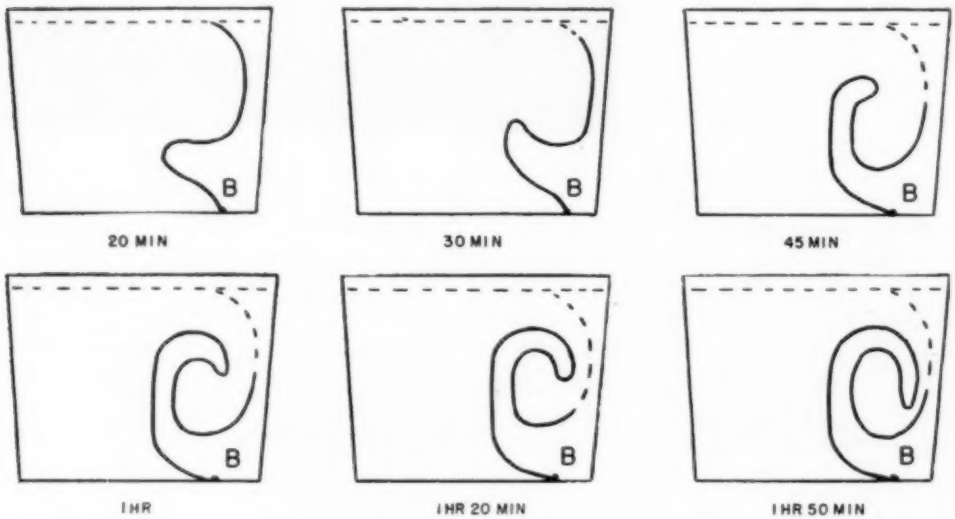

FIGURE 17. *Sketches of tracer from ball B drawn from observations of melt 4 during cooling, showing the formation of loops in the tracers.*

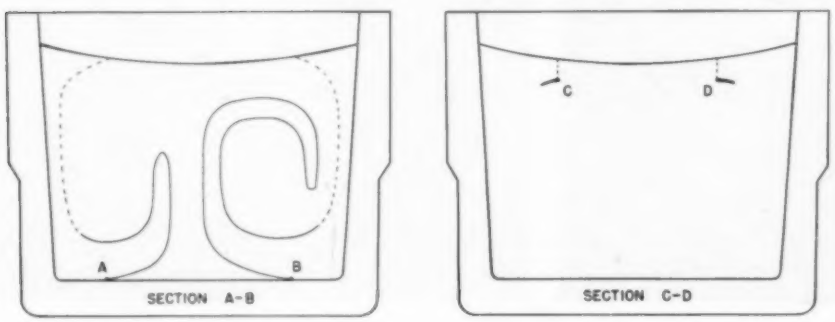

FIGURE 18. *Final position of the copper-oxide tracers in melt 4.*

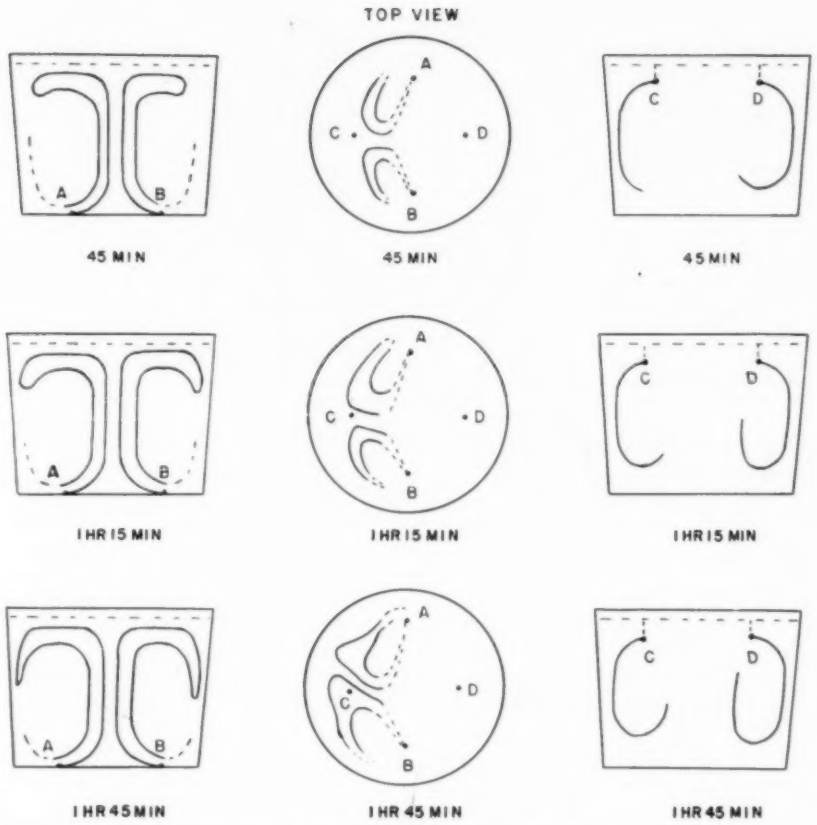

FIGURE 19. *Sketches drawn from observations of the copper-oxide tracers in melt 5 during cooling.*

The dotted portions shown in the top views represent those portions of the streamers across the bottom of the pot, and the ends of the loops going downward.

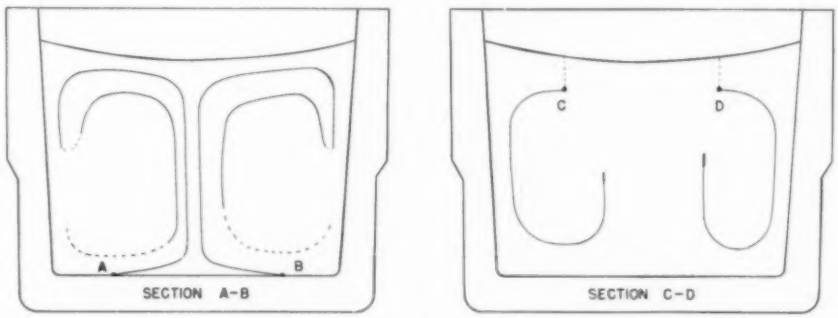

FIGURE 20. *Final position of the copper-oxide tracers in melt 5.*

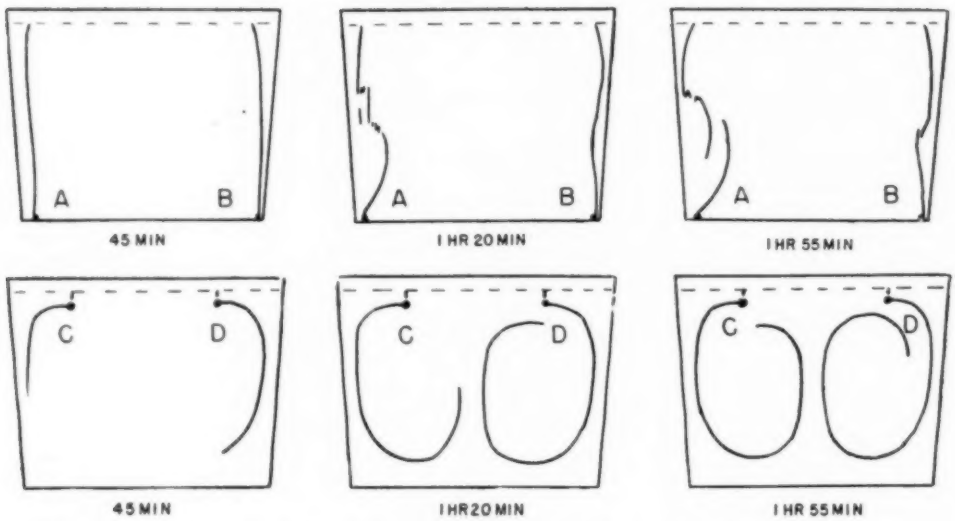

FIGURE 21. *Sketches drawn from observation of the copper-oxide tracers in melt 6 during cooling.*

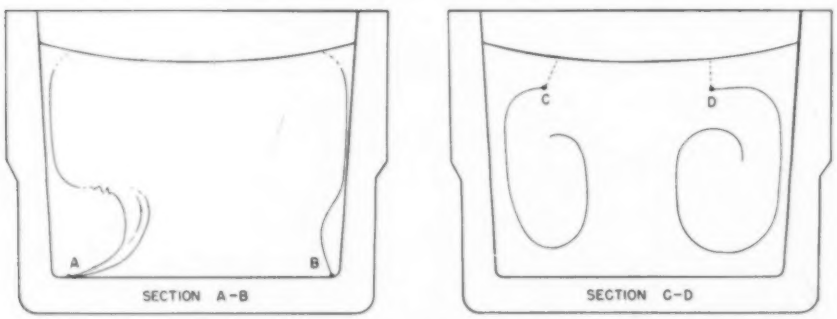

FIGURE 22. *Final positions of the copper-oxide tracers in melt 6.*

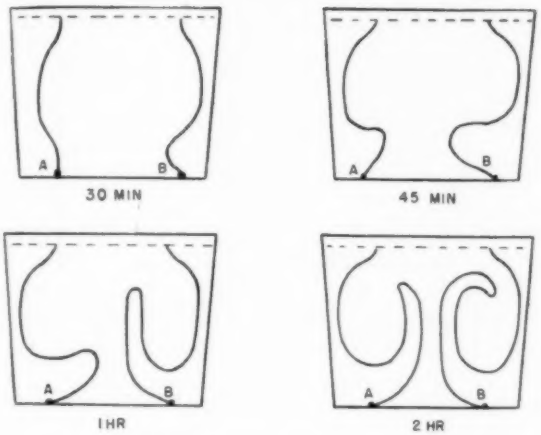

FIGURE 23. *Sketches drawn from observations of melt 8 during cooling.*

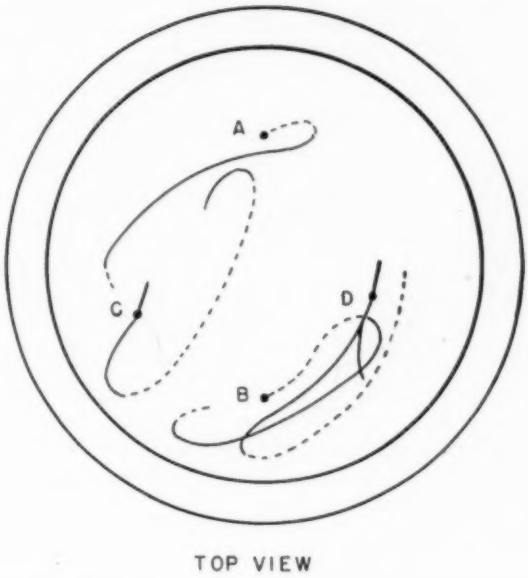

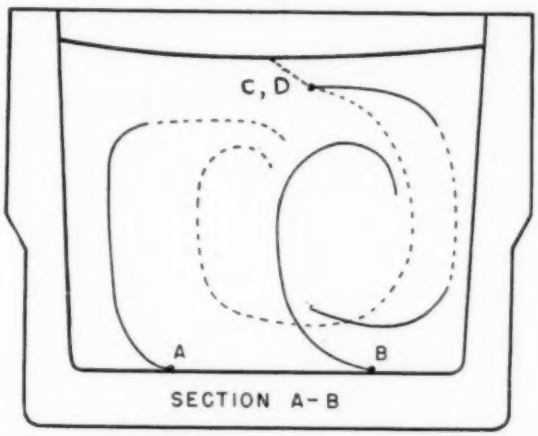

FIGURE 24. *Position of the copper-oxide tracers in melt 9.*

The top view represents the last observation made through the cover after all motion of the glass had ceased. The dotted lines indicate the portions of the tracers deep in the melt. Section A–B shows the final positions of the tracers in the cold melt. The solid lines show the portions of the tracers visible in the half of the pot containing ball D, and looking toward D. The dotted lines indicate portions of the tracers in the other half of the pot.

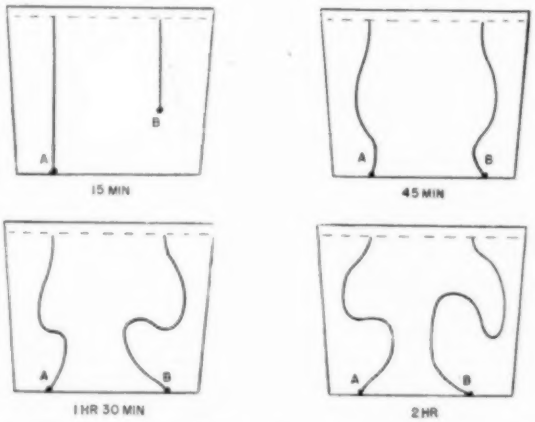

FIGURE 25. *Sketches drawn from observation of melt 10 during cooling.*

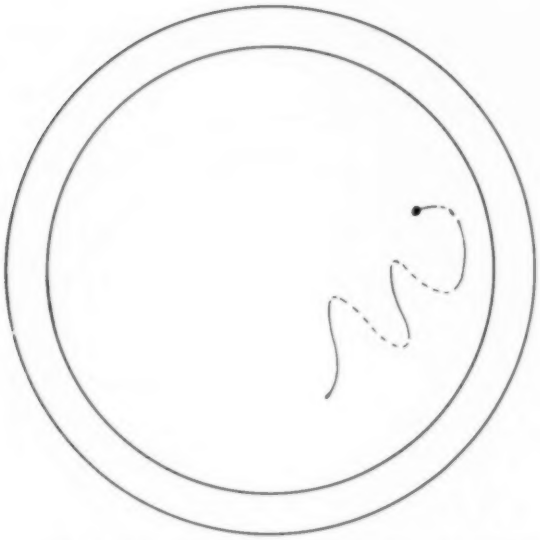

FIGURE 26. *Top view of the copper-oxide tracer in melt 11.*

The dotted lines indicate the lower portions of the spiral and the solid lines indicate the upper portions.

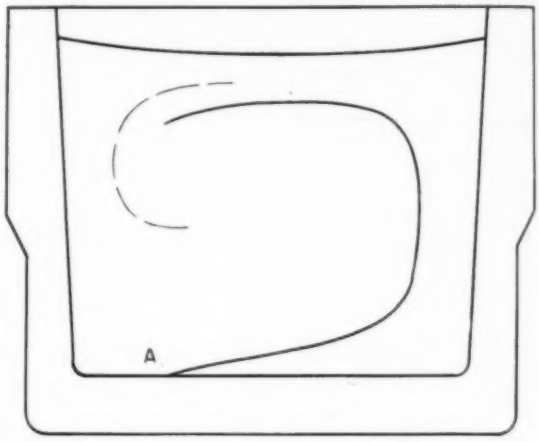

FIGURE 27. *Final position of the copper-oxide tracer in melt 12.*

The dotted lines indicate portions of the tracers in the other half of the pot.

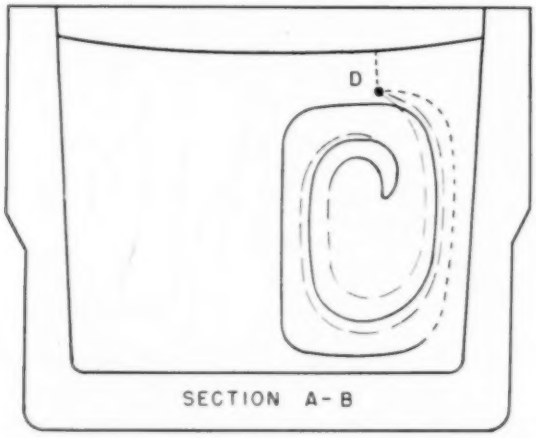

FIGURE 28. *Final position of the copper-oxide tracer from ball D in melt 13.*

The dotted lines indicate portions of the tracers in the other half of the pot.

VII. References

[1] C. N. Fenner, The technique of making optical glass, J. Am. Ceram. Soc. **2,** 102 (1919).

[2] H. S. Roberts, The cooling of optical glass melts, J. Am. Ceram. Soc. **2,** 543 (1919).

[3] F. E. Wright, Manufacture of optical glass and of optical systems, Ordnance Department Document 2037, Government Printing Office, Washington 25, D. C.

[4] W. H. Parsons and Herbert Insley, Attack on refractory clay pots by optical glass, J. Research NBS **36,** 31 (1946) RP1689.

[5] Francis W. Glaze and Clarence H. Hahner, Optical glass at the National Bureau of Standards, NBS Circular 469 (1948); Glass Ind. **29,** 562 (1948).

[6] Hans Jebsen-Marwedel, Glastechnische Fabrikationsfehler (Julius Springer, Berlin, 1936).

WASHINGTON, October 26, 1948.

U. S. Department of Commerce
National Bureau of Standards

Research Paper RP1960
Volume 42, February 1949

Part of the Journal of Research of the National Bureau of Standards

Expansion Effects of Annealing Borosilicate Thermometer Glasses

By Arthur Q. Tool and James B. Saunders

The expansivity of many glasses can be increased almost 10 percent by increasing the equilibrium temperature from 150 to 200 deg C above the lowest such temperature attainable by long annealing treatments in the lower part of the annealing range. By changing the equilibrium temperatures of a number of the better known borosilicate thermometer glasses, the increase in expansivity per degree increase in equilibrium temperature was found to be about 2.4×10^{-9} at 100° C. Also, it was found that the average values of the change in volume per degree Centigrade change in the equilibrium temperature approximated 7.8×10^{-8} when the volumes were measured at room temperature. As these effects concern the performance of thermometers, the results obtained are used to demonstrate their relation to certain ice point fluctuations that are observed in thermometers. It is shown that under particularly adverse conditions the ice point reading may be changed by as much as 30 deg C. Under more normal conditions of use, this source of error is considerably diminished, but it still remains important in precise work. Also, small changes in the value of the graduations anywhere along the stem may result from changes in the expansivity of the glass as its equilibrium temperature is changed by use at temperatures in the annealing range.

I. Introduction

The expansivity and specific volume of all glasses can be changed appreciably by heating the glasses to temperatures within their annealing ranges. In thermometer glasses these changes can be quite important, because their development by heating a thermometer into the annealing range of its glass often raises or lowers its ice point by several degree intervals on the scale graduated on the stem. Such a treatment may also cause a measureable change in the scale length of the degree intervals. These effects are the result of a shift in the equilibrium temperature of the glass. As long as a thermometer is not heated to its annealing range, appreciable shifts of this nature are never induced. The graduations of many thermometers extend to temperatures that are well within the annealing range of the glass from which the thermometers are made. For instance, thermometers made from borosilicate glasses that are similar to the old and once well-known Jena 59^{III} have often been graduated to 520° C, although these glasses can be annealed at temperatures as low as 450° C [1, 2].[1]

Annealing one of these thermometers for a long period of time at 450° C reduces the specific volume and the expansivity of the glass to about the lowest values obtainable without employing impractical annealing schedules. Treatments of this kind considerably increase the stability of the glass and, if the ice point and calibration are

[1] Figures in brackets indicate the literature references at the end of this paper.

determined while the glass is in this stable condition, the thermometer functions well as long as it is not heated above 450° C. In fact, it can be heated for short periods to temperatures near 520° C without seriously affecting its calibration. However, continuous use at temperatures near and above 500° C ultimately increases the expansivity and specific volume. These changes cause an appreciable ice point lowering and a slight reduction in the distance between the ice and boiling points. Most of these conclusions can be deduced from an earlier investigation by H. C. Dickinson [2] on the stabilization of thermometers made of a borosilicate glass.

To learn something more of the magnitude and effect of the changes caused in the expansivity and specific volume of thermometer glasses by heat treatment, a number of such glasses were investigated. Those discussed in this paper include some glasses used in thermometers for the determination of temperatures above 450° C.

II. Sources of Glasses

The data reported in this paper were obtained on samples of Jena 59^{III}, similar Corning borosilicate glasses, Jena 2954^{III}, and a glass that is designated by the number 172 and is used for thermometers indicating temperatures that greatly exceed the highest point safely registered by ordinary borosilicate thermometers. Since fresh samples of Jena 59^{III} were unavailable, samples of this glass were procured from old thermometers. From the appearance of these thermometers, their bulbs seemed to have been blown from the capillary tubing of the stem. Consequently, all tests on this type of glass were made on the stem glass, but the results are considered as representative of the bulb glass also. Of the Corning glasses, that designated by G80 was obtained directly from the Corning Glass Works. Although this glass was supposed to be similar to the capillary tubing used for stems of borosilicate thermometers, it was in the form of ordinary tubing with an outside diameter of about 10 mm. Capillary and bulb tubing of the Corning borosilicates were obtained from the Taylor Instrument Co., and are designated as glasses TS and TB, respectively. Capillary and bulb tubing of the Jena 2954^{III} were supplied by the Fisch-Schurman Corporation and are designated as glasses JS and JB. The capillary tubing of glass 172 was submitted by the Precision Thermometer and Instrument Co. The samples of bulb tubing were generally so thin walled and small in diameter that suitable test specimens were prepared from them with difficulty.

III. Thermal Expansion Tests

The first step in an investigation of the effects caused by heat treatment is the location of the annealing ranges of the glasses to be tested. The annealing range can be determined from graphs showing the linear thermal expansion of a glass as a function of temperature. Figures 1, 2, and 3 show such graphs for expansions determined by an interferometric method. The upper third of the annealing range (see fig. 3) corresponds approximately to the temperature range that extends upward from a temperature *A* (the approximate beginning of the rapid expansion range of a glass on heating) and ends at a temperature *B* (the beginning of noticeable inelastic deformation under light stress). The location of the temperatures A and B is an easy matter if thermal expansion curves are obtained on annealed glasses by the interferometric method. All details for obtaining such curves have been fully discussed in a previous paper [3]. A desirable

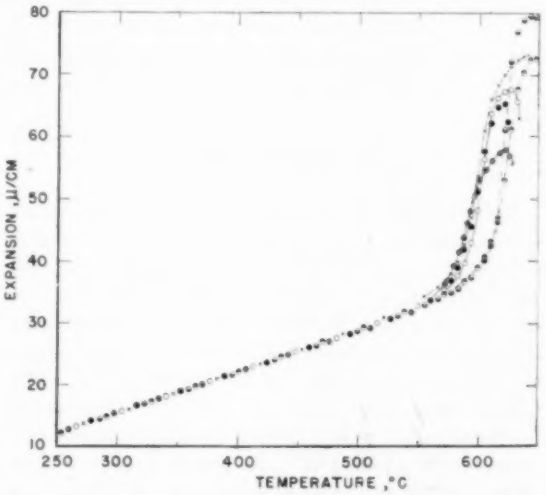

FIGURE 1. *Expansion curves of annealed thermometer glasses.*

Glasses annealed for 30 days at 500° C. Curves TS, TB, and G80 represent expansions of Corning thermometer glasses, and curves 59^{III}, JS, and JB represent expansions for Jena glasses. ○, TB; ●, TS; ⊕, G80; ×, 59^{III}; ◒, JS; ◓, JB.

form of test specimen is either a ring- or T-shaped spacer placed between the interferometer plates. However, with one exception, the nature of the above-mentioned glass samples made it necessary to use three tripod spacers in this investigation.

As received, most of the glasses were indifferently annealed. After procuring preliminary thermal expansion curves on the glasses in this condition, it was estimated that a treatment of 30 days at 500° C should be sufficient to bring six of the seven glasses to equilibrium at that temperature. It appeared that a corresponding temperature for glass 172 exceeded 650° C. Samples of the six glasses were then subjected to the treatment that seemed necessary to establish equilibrium at 500° C. This treatment was followed by rapid cooling to room temperature from which the expansion tests began. The thermal expansion curves shown in figure 1 for the six glasses resulted from these tests. These curves show that the annealing ranges of the Jena 2954[III] glasses, JB and JS, are about 20 deg C higher than those of the other four glasses. This is obvious because of the relative positions of the beginning points, A, of the rapid expansion (see table 1). The curves also show that the interferometrically determined deformation points, B, of all six glasses lie between 600° and 650° C. These results for B made it apparent that it would be useless to attempt to cool any of the six glasses so rapidly from any treating temperature above 625° C that a condition of equilibrium corresponding to the treating would be maintained.

TABLE 1. *Temperatures determined in locating annealing ranges*

Glass	Temperatures			
	°C C[a]	°C D[a]	°C A[b]	°C B[c]
TS	443	[a] 567	[b] 583	[c] 621
TB	435	569	590	626
JS	449	575	610	644
JB	449	578	609	646
59III	448	571	585	642
G80	448	563	572	622
172	665	715	730	795

[a] Temperatures at which contraction of chilled samples began and ended, respectively.

[b] Temperatures at which rapid expansion of annealed samples began according to a graphical determination demonstrated in figures 3.

[c] Temperatures at which inelastic deformation appeared according to a rather similar graphic determination. At these temperatures, the rate of deformation approximated that of thermal expansion.

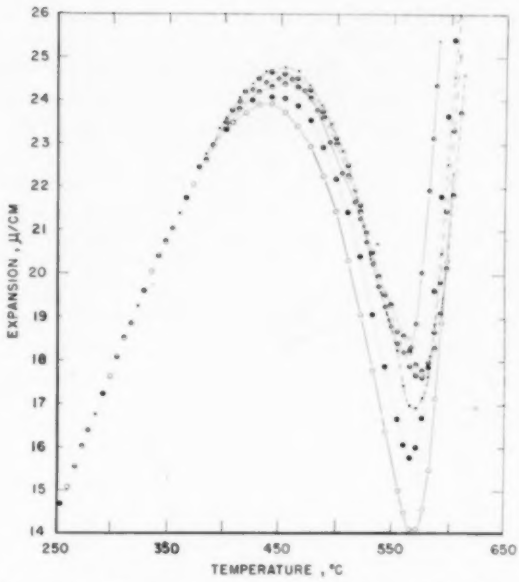

FIGURE 2. *Expansion curves of chilled thermometer glasses.*

Glasses cooled rapidly from 800° C. Designations for curves are explained under figure 1 and in text. ○, TB; ●, TS; ⊕, G80; ×, 59III; ◒, JS; ◓, JB.

To gain more information concerning the lower limit of the practical annealing range, undercooled samples of the six glasses were prepared by heating them to 800° C and cooling them as rapidly as possible in air. Such a treatment probably left the samples in an undercooled condition corresponding to equilibrium at undetermined temperatures not far below 700° C. The thermal expansion curves in figure 2 were obtained on these samples. These curves show the contraction that takes place as the equilibrium temperature [4] of a severely undercooled glass decreases while being heated through its annealing range. The temperature C at which the contraction begins marks the approximate lower limit of the annealing range. Accordingly, it appears that all six of the glasses can be brought to equilibrium at temperatures as low as 450° or 475° C, provided they are subjected to heat treatments that continue for several months at such temperatures. This estimate of the time required to establish equilibrium at low annealing temperatures is based on previous experience with other glasses under similar conditions. Similar experience has also shown that the necessary duration of treatments for establishing equilibrium at various tempera-

tures within the annealing range increases by a factor approximating 2 for each 8 deg C decrease in temperature. In procuring the data on the change in expansivity as the equilibrium temperature is changed, the periods of treatment at the various annealing temperatures were determined in accord with this experience. They ranged from about 4 months at low annealing temperatures to less than an hour above the upper limit of the annealing range.

In figure 3, curves similar to those in the previous figures are presented for glass 172. In this case, the undercooled sample was heated to 1,000° C before chilling and the well-annealed sample was treated 23 weeks at 650° C.

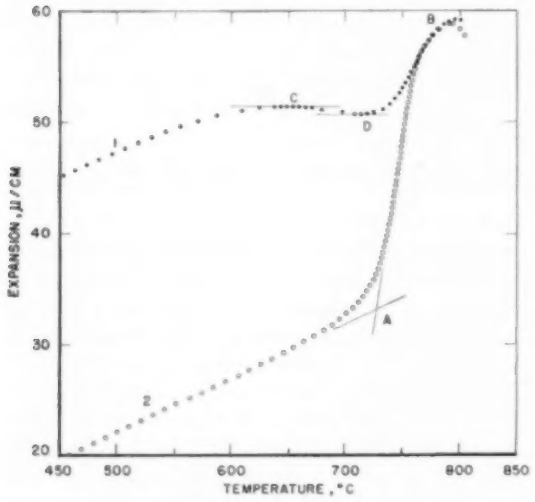

FIGURE 3. *Expansion curves of thermometer glass 172.*

Curve 1, glass cooled rapidly from 1,000° C. Curve 2, glass annealed for 23 weeks at 650° C. Points C and D represent beginning and end, respectively, of the contraction shown by chilled sample. The respective points A and B approximately represent the beginning of rapid expansion and of appreciable deformation shown by annealed sample.

Figure 3 is also used to show something of the significance of the temperatures A, B, and C and to show how they are determined. The determination of a temperature D is also demonstrated; this is the temperature that marks the end of the contraction of a chilled glass as it is being heated through the annealing range. In some respects, D as well as A appears to mark the beginning of the rapid expansion effect. However, D is in the region of undercooled glass, whereas A is in the region of superheated glass. At D, the contraction caused by a decreasing equilibrium temperature is just balanced by the normal expansion caused by an increasing actual temperature. At A, the expansion caused by an increasing equilibrium temperature adds appreciably to the normal expansion.

The temperature A can be determined only from expansion curves for samples that have been moderately or well annealed. Its value depends somewhat on the degree of annealing and also on the rate of heating. Temperature B is little affected by the degree of chilling or annealing, but it is affected by the rate of heating and the character of the contact points between the sample and the interferometer plates. Temperatures C and D are both affected by the rate of heating and by differences in the effectiveness of the chilling. Consequently, repeated observations show considerable variations. Despite the various causes for deviations in the determined values of A, B, C, and D, these temperatures are very useful in locating the annealing range and in devising annealing procedures.

IV. Change in Expansivity as Equilibrium Temperature Changes

For determining the change in expansivity as the equilibrium temperature of the six first-mentioned glasses was changed, treating temperatures, usually at 25- or 30-deg intervals, from 450° (or 475°) to 630° C. were chosen. At each of these temperatures the samples were held for periods that were deemed sufficient to establish equilibrium. The samples were then cooled rapidly to room temperature. Rapid cooling is unnecessary from low-treating temperatures, but it is necessary in cooling from high-treating temperatures if the downward drift of the equilibrium temperature is to be prevented. Since rapid cooling from the treating temperatures has no harmful effects on expansion measurements below the annealing range, the same cooling procedure was followed in all cases of heat treatment.

After these treatments, expansion curves from room temperature to 250° C. were obtained on the samples (see curve 1, fig. 4, for a typical curve). The tests were stopped at 250° C., because heating to that point certainly did not affect the equilibrium condition of the glass. This certainty made

it possible to use both heating and cooling data in determining the expansivity and also to repeat the test on a sample as many times as repetition seemed necessary.

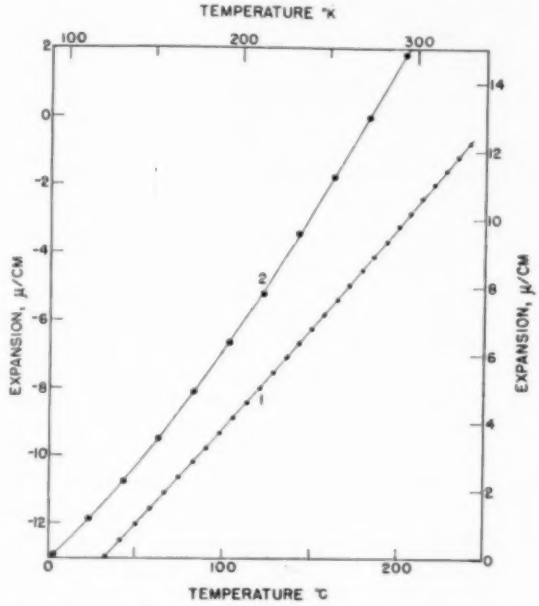

FIGURE 4. *Comparison of experimental and computed linear expansion data.*

Solid lines and dots represent computed and experimental data, respectively. Curve 1, glass annealed for 6 months at 475° C., ordinates on the right and abscissas in degrees Centigrade at bottom of figure. Curve 2, experimental points based on expansivity data obtained by H. G. Dorsey on crown glass tubing, ordinates on the left and abscissas in degrees Kelvin at top of figure.

In order to compute the expansivity at any desired temperature, attempts were made to fit various formulas to the data. These formulas included the usual parabolic and cubic equations but the best results were obtained by using the equation

$$\Delta L = A + BT + CT \ln T \qquad (1)$$

In this equation, ΔL is the expansion per unit length caused by heating from some absolute temperature T' to another absolute temperature T, and A, B, and C are constants, although A naturally depends on the choice of T'. The expression for the slope of the expansion curve is

$$dL/dT = B + C(\ln T + 1) = C \ln(T/T_0) \qquad (2)$$

In eq 2, the absolute temperature T_0 is that at which dL/dT becomes zero.[2]

As is well known, this condition for maximum density is found in vitreous silica at a temperature that is not far above −100° C. Below this temperature, the expansivity is negative, because the glass increases in length as temperature decreases. Every glass probably reaches a minimum specific volume at some low temperature that may be even nearer absolute zero. This temperature T_0 at which the expansivity is zero has its analogues in the temperatures at which the temperature coefficients of refractivity become zero. These temperatures, at which the refractivities reach a minimum, range from atmospheric temperatures downward [6]. Thermal expansion is an important factor but not the only one in determining the temperature coefficients of refractivity. This is obvious because increasing the density of a glass by cooling would increase the refractivity if no other factor were involved. Consequently, the temperatures for minimum volume and for minimum refractivity are by no means the same. Moreover, the temperature for minimum refractivity varies with the wavelength of the refracted light.

Equation 1 was fitted to the expansion data by means of the so-called method of averages. As an example of the results, a computed curve, together with the observed results is presented as curve 1 in figure 4. The constants, B and C of eq 1, which were obtained by this computation were introduced into eq 2 for computing the expansivity at any temperature at which the glass might behave as a solid. Samples of computed results for a wide temperature range are shown by the linear expansivity curves in figure 5.

The linear expansivities (cm/cm °C) shown in figure 6 were computed for 100° C (373.2° K) and plotted as functions of the equilibrium temperatures of the glass samples. The temperature, 100° C, was chosen, because it was reasonably remote from the limits, room temperature, and

[2] The slope of the expansion curve becomes zero at some low temperature, which according to eq 2 is given by the relation $\ln T_0 = -(B/C) - 1$. Using the values obtained for B and C as a result of the computations required in fitting experimental data of curve 1 in figure 5, it was found that $T_0 = 16.2$°K. Because of the range of the extrapolation, a value so computed has limited significance. By using the same method of analysis on expansivity data obtained by Dorsey [5] on a crown glass, a value $T_0 = 32.0$°K was obtained. As his data extended downward to 93°K, the range of extrapolation is considerably less in this case. For results based on his data see curves 2, figures 4 and 5.

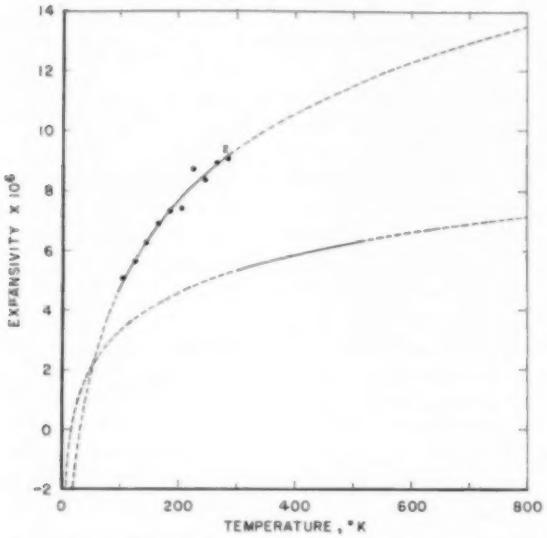

FIGURE 5. *Computed linear expansivities for wide range of temperatures.*

Curve 1, computed linear expansivities corresponding to curve 1 of figure 4. Curve 2, computed expansivities corresponding to curve 2 of figure 4. Solid parts of curves cover temperature ranges of the experimental data. Broken parts of curves represent extrapolated results computed for temperatures ranging from 10° K to points near or within the annealing ranges of the glasses. Dots plotted along curve 2 indicate Dorsey's results.

250° C., of the range used for the expansion tests. As many thermometers made from these glasses are ungraduated from 5° to some point between 200° and 300° C., the range of the tests approximately coincides with this ungraduated range. However, the temperature used in this investigation for expansivity determinations is a matter of little importance, because the only purpose of the investigation was to learn to what extent the expansivity at some standard temperature is changed by making definite changes in the equilibrium temperature. It was not intended to attempt the more difficult study of the manner in which changing the equilibrium temperature effects the increase in expansivity as the temperature of the glass is increased. Furthermore, this last-mentioned change in expansivity is of relatively little importance as far as thermometers are concerned.

The change caused in the expansivity at 100° C by changing the equilibrium temperature 150 deg C was found to be nearly 6 percent of the average expansivity. This finding agrees reasonably well with some results obtained on other glasses. In view of results obtained in this laboratory, it appears that the expansivity of most glasses can be increased almost 10 percent by increasing the equilibrium temperature from 150 to 200 deg C above the lowest such temperature attainable by long annealing treatments.

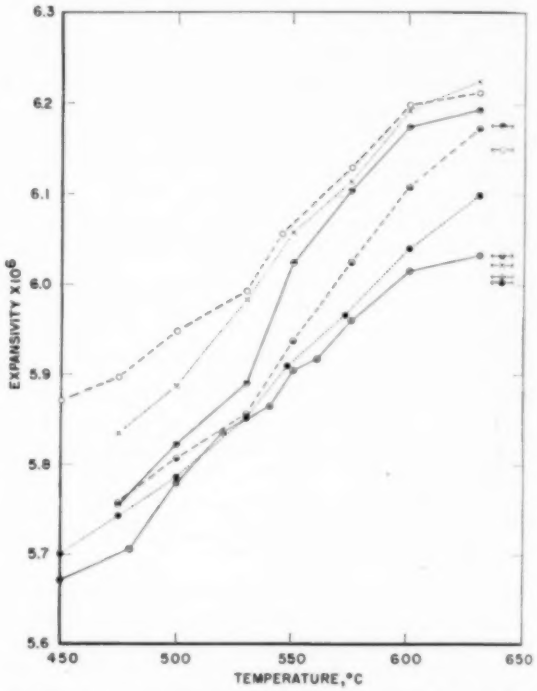

FIGURE 6. *Changes caused in linear expansivity by changing the equilibrium temperature.*

Computed linear expansivities for 100° C are plotted against the temperature of annealing treatment. Expansivities of the original or untreated glasses are indicated by the double arrows at the upper right of the figure. A treatment of 1 hr. was ample to establish equilibrium at 600° C. At 500° C. a treatment approximating 30 days usually seemed necessary. Some of the glasses appeared to require treatments of almost 6 months duration at 475° C. It is unlikely that equilibrium was established in any of the glasses at 450° C., as even 475° C is a very low annealing temperature for most of them. After some tests, it seemed that treatments of a year or more might be required to approximate equilibrium in the bulb glasses at the lower temperature. ○, TB; ●, TS; ⊕, G80; X, 59III; ◒, JS; ◓, JB.

When the tests were repeated several times on any sample without changing its equilibrium temperature, it was found that the spread of the results seldom exceeded ½ of 1 percent, or about 3×10^{-8}(cm/cm°C). However, when the results obtained on samples treated at different temperatures are considered, it is obvious that errors in the determinations of the treating temperatures and uncertainties concerning the adequacy of the

treatments will become apparent. These factors seemed to increase the uncertainty of a single determination to at least 1 percent when determining the expansivity of a sample after any particular treatment. As this uncertainty is about one-seventh of the change caused in expansivity by reducing the equilibrium temperature to the extent of 100 deg C, the failure of the results to indicate smooth curves when presented as in figure 6 is easily understandable.

Because of the irregularity of the results, neighboring points for the same glass were joined by straight lines merely to distinguish more clearly between the results obtained on the various glasses. The results as presented in figure 6 show that the expansivities of the stem glasses (JS, TS, and G80) are generally lower than those of the bulb glasses (59^{III}, JB, and TB). The expansivities of the glasses JS and JB are respectively the highest and lowest of the two groups. This fact indicates that there is less difference between these two glasses than there is between T_S and T_B. As far as can be determined from the results, the increase in the expansivity as the equilibrium temperature increases is roughly linear and not greatly different for the six glasses. Apparently, the equilibrium temperature coefficient of the expansivity (the change in linear expansivity per degree Centigrade change in the equilibrium temperature) is about 2.4×10^{-9}.

According to the tests made on glass 172, the linear expansivity of this glass at 100° C increased from about 3.5×10^{-6} to about 3.7×10^{-6} as the equilibrium temperature was increased from 650° to 800° C. The expansivity of the glass as received was about 3.6×10^{-6}, which was found to be the value that corresponded to an equilibrium temperature approximately 750° C. The equilibrium temperature coefficient of the linear expansivity appeared to be somewhat less than 1.1×10^{-9} for this glass.

V. Volume Change Caused by Annealing

As already stated, a glass expands or contracts whenever it is held at an annealing temperature that differs from the equilibrium temperature established by the preceding annealing treatment. Any such contraction or expansion caused by heating a thermometer into the annealing range of its glass not only results in a corresponding raising or lowering of the reading for the ice point but also for any other temperature. Whenever a thermometer is both poorly annealed and graduated into the annealing range, these changes in readings may be quite large. Holding the temperature of such a thermometer for a considerable time at low annealing temperatures but still within the range of the graduations causes a contraction that results in an ice point rise that may be equivalent to 30° C or more according to the graduated scale. The lower limit of the annealing range of glasses similar to the Jena 16^{III} glass [3] is near 350° C, and that for glasses similar to the Jena 59^{III} is somewhat below 450° C. Thermometers made of these glasses are sometimes graduated to temperatures that are 70° C above these limits, and they are therefore subject to considerable ice point changes if used frequently within the annealing ranges.

In view of these considerations, measurements were made on the volume change caused by changing the equilibrium temperatures of the glasses. For these measurements, the equilibrium temperature of samples from each glass, excepting glass 172, was established at 500° C. For other samples of the same glasses, this temperature was established at 620° C. At the lower temperature, a treating period exceeding 2 months was employed to establish what appeared to be a close approach to equilibrium. At the other temperature, a period of only a few hours appeared to be sufficient for the same purpose, but it was necessary to cool very rapidly in order to prevent a downward shift of the equilibrium temperature.

The volume change caused by increasing the equilibrium temperature from 500° to 620° C was determined for the six glasses by obtaining expansion curves for both samples of each glass and by treating these curves as shown in figure 7. In this interferometric method of measuring the volume change caused by heat treatment, the expansion curves for the samples were determined from room temperature to 578° C. Then, measurements both on the expansion of the annealed sample and on the contraction of the chilled sample were continued at this temperature as equilibrium was approached. These measurements were continued until it seemed that no further significant change would take place.

[3] For a discussion of the properties and compositions of Jena 16^{III} and 59^{III} see H. Hovestadt, Jena Glass (English translation, MacMillan and Co., Limited, London (the MacMillan Co., New York) 1902).

The end points of the resulting expansion curves for the chilled and annealed samples were then made to coincide at B, as shown in figure 7, which presents results obtained on glass JS. By this construction, the change in length at room temperature caused by the 120° C difference in equilibrium temperature between the two samples is given by the difference in the ordinates of curves 1 and 2 at room temperature. According to figure 7, the change in length for this pair of samples was 32 μ for a sample 1 cm long. In terms of volume change, this result is equivalent to 0.96 percent for a 120° C change in equilibrium temperature.

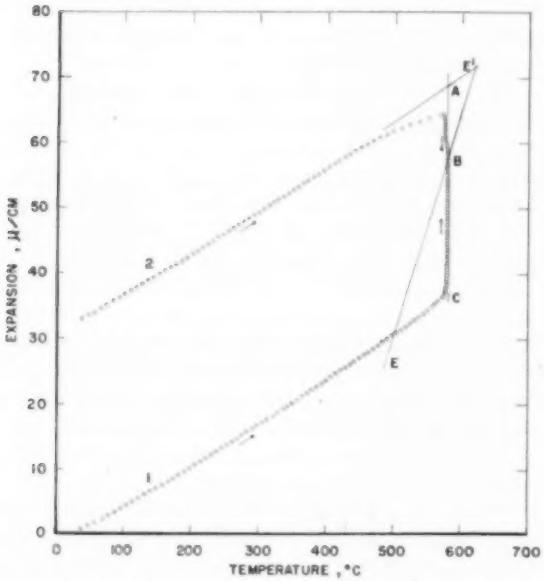

FIGURE 7. *Change in length as glass is held at constant annealing temperature.*

Expansion curves of glass JS when heated to and held at temperature 578° C. Curve 1, sample previously annealed until equilibrium was established at 500° C. Curve 2, sample previously treated and chilled to establish and maintain a condition of equilibrium at 620° C. Curve EE′, length-temperature equilibrium curve, which presumably represents the expansion curve that the annealed sample would have followed had it been heated at a very low rate from 500° to 620° C.

The corresponding change in length at 578° C can be estimated by extrapolating curve 2 from a point near 400° C to point A and with a slope slightly greater than that between 300° and 400° C and also by extrapolating curve 1 from 500° C to point C. The difference in the ordinates of A and C gives an approximation for the change in length at 578° C when the change in equilibrium temperature is 120° C. When the curves were extrapolated as shown in figure 7, it was found that this difference was also 32 μ. In view of the larger expansivity of chilled glass compared to annealed glass, it appears that a somewhat larger value should have been obtained for the change in length at 578° C. Possibly, the estimated value at 578° C is no larger in this case, because the slope of the extrapolation of curve 2 from 400° C to point A was not made large enough.

For most glasses, the change in length while being annealed is practically proportional to the change in equilibrium temperature. In other words, any increase in the equilibrium temperature of a sample in equilibrium at 500° C should produce about the same change in length as the same increase would produce if the sample were in equilibrium at 600° C. Because of this near proportionality, the equilibrium curve (represented in fig. 7 by line EE′) may be considered to approximate a straight line, over a range of about 100° C, to the same degree that curves 1 and 2 approximate straight lines over an equal range in the neighborhood of 200° C. For the same reason, the ratio $(620-578)/(578-500)$ approximates the ratio AB/BC.

As the equilibrium temperature of an annealed glass does not change materially until it is exceeded by the actual temperature, the equilibrium curve must intersect curve 1 of the annealed sample at 500° C. It must also pass through point B, which was obtained when the glass reached equilibrium. Line EE′ in figure 7 represents the approximate course of such an equilibrium curve. Also, if the curvature of the equilibrium curve is very slight as supposed, continuing it as a straight line beyond B should cause it to intersect the line AE′ at 620° C. When expansion curves, obtained on samples that are in equilibrium at such different temperatures, meet the demands of such constructions, confidence in the determinations of the volume changes by the interferometri- method is enhanced. The results obtained by this method on six glasses are shown in table 2.

For five of the glasses, the volume change as determined by this interferometric method for a 120° C difference in equilibrium temperature ranged from 0.94 to 1.05 percent. As the departure from an average does not exceed the uncer-

tainty of such results, it seems that the probable volume change for all of these five samples is approximately 1 percent.

TABLE 2. *Volume changes caused by a change of 120 deg C in equilibrium temperature*

Glass	Method of testing	Percentage of volume change
G80	Interferometric	0.95
	Archimedean	.91
59III	Interferometric	1.05
TS	Interferometric	0.98
	Archimedean	.97
TB	Interferometric	1.02
JS	Interferometric	0.94
	Archimedean	.95
JB	Interferometric	.84
	Archimedean	.86
	Pycnometer	.82

For the sixth glass, Jena 2954 III bulb, all results obtained by the interferometric method were lower, and averaged 0.84 percent. As this tubing was less than 3 mm in diameter and very thin walled, it was difficult to construct spacers for the interferometer that were entirely satisfactory. Because it was feared that the unsatisfactory spacers affected the results adversely, larger spacers were made by fusing the glass into large beads. The results remained the same. As a further check on the results obtained, determinations of the change in volume for a 120° C change in equilibrium were also made on some of the glasses by finding the apparent loss of weight when the samples were weighed in a liquid of known density. These determinations were made by E. L. Peffer of the capacity and density laboratory of this Bureau. His results are listed in table 2 as being obtained by the Archimedean method. Determinations on the glass JB were also made by the pycnometer method. No determination of this volume change was made for glass 172.

From an average of the results given in table 2 for the change caused in a unit volume by a change of 120° C in equilibrium temperature, it appears that the average volume change per unit volume per degree change in this temperature is near 7.8×10^{-5}. According to density data presented in a previous paper [7], the same equilibrium temperature coefficients for some optical glasses range from 4.8×10^{-5} to 12.4×10^{-5}.

VI. Rate of Expansion at Constant Temperature

In an earlier paper [8], it was suggested that the exponential integral equation

$$Ei(y)-Ei(y_0)=-Kte^{T/k} \qquad (3)$$

approximately represents the progress of density changes at constant annealing temperatures. In this equation, t represents time and $Ke^{T/k}$ is constant if the temperature T remains constant. For a linear expansion as the equilibrium temperature increases, the arguments y and y_0 of the exponential integrals represent $(L_\infty-L)/CL_0$ and $(L_\infty-L_0)/CL_0$, respectively. In these expressions, L is the length at any time t, and L_∞ and L_0 are the lengths when t is infinite and zero respectively. The constant C is the product of the equilibrium temperature coefficient of expansion (slope of curves in fig. 6), and a constant h which is related to Twyman's constant k appearing in eq 3.[4] The change in thermometer readings with time as a thermometer is held at an annealing temperature T is therefore a function of the change in the argument y with time.

As the expansions are generally computed in terms of microns per centimeter length at room temperature, and as the total expansion in heating from room temperature to points in the annealing range seldom reaches 100 μ, the length L_0 at the beginning of a treatment at a constant annealing can be assumed to be 1 cm or 10^4 μ without introducing appreciable error. As indicated in the above citation, the other constants (Ke^T/k, $L_\infty-L_0$, and C) can be determined by approximation methods and subsequent adjustments.

By following the method outlined in connection with eq 3, curve 1 (as indicated by a continuous line) in figure 8 was obtained. The dots lying along this line are observed points and correspond to the points that are in line with and between the points B and C in figure 7. This correspondence between expansion and time is known, because the time was recorded for each observation during the annealing periods in which the

[4] According to Twyman's empirical equation concerning the change in the viscosity of a glass as the temperature changes, $K_T=Ke^{T/k}$ is the reciprocal of the relaxation time at any temperature T, if K is the extrapolated value of K_T for $T=0$. The relation between the presumably constant temperature intervals k and h is shown in a previous publication [4]. The interval h has a significance only when the equilibrium temperature changes.

data used for curves such as 1 and 2 in figure 7 were procured. The data for curve 2 in figure 8 were computed by means of the logarithmic equation

$$\ln (L_\infty - L) - \ln (L_\infty - L_0) = Kte^{T/k}, \qquad (4)$$

and on the assumption that the curve must coincide with the experimental data at two points at least. As usual, the results obtained by the use of eq 3 are more satisfactory than those obtained by the use of eq 4.

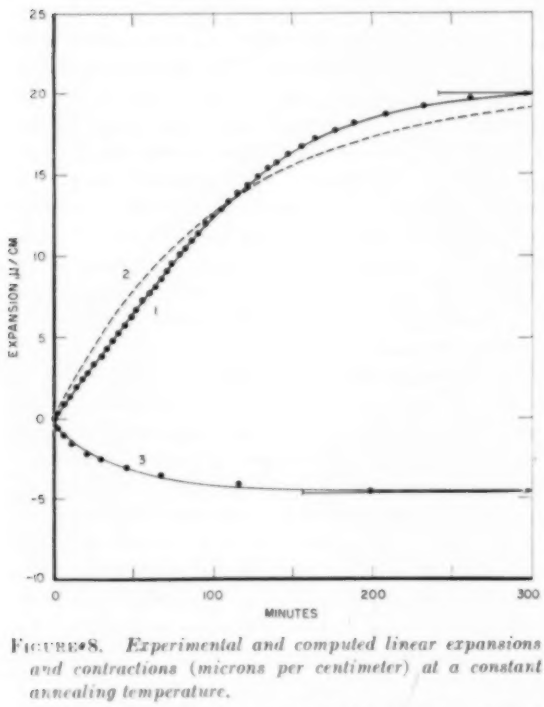

FIGURE 8. *Experimental and computed linear expansions and contractions (microns per centimeter) at a constant annealing temperature.*

Curve 1, solid line represents computed results, dots represent experimental points corresponding to points on curve 1 between C and B in figure 7. Curve 2, presents results computed on the assumption that the expansion is a logarithmic function of time. Inset curve 3, computed and experimental results corresponding to points on 2 between A and B in figure 7. At infinite time, curves 1 and 3 are tangent to fletched lines.

After computing curve 1 (fig. 8), the same values for the constants (CL_0 and $Ke^{T/k}$) were used to compute curve 3 of figure 8. This curve represents the approach of the chilled sample to equilibrium at 578° C after that temperature was approximated in the test yielding curve 2 of figure 7. However, the time of observation was recorded for the last ten observations only. Consequently, the first five points showing the vertical drop of curve 2 (fig. 7) are not represented in curve 3 (fig. 8). For curve 3 as for curve 1, the value assumed for $L_\infty - L_0$ is indicated by a fletched line to which the curve becomes tangent after an infinite time.

VII. Relation of Results to Performance of Thermometers

To simplify the discussion of the relation between the performance of thermometers and the data obtained on the borosilicate glasses tested, it will be assumed that the bulbs alone are affected by annealing or by occasional heating into the lower part of the annealing range of the glass. It will also be assumed that all second-order effects resulting from changes in the actual and equilibrium temperatures are relatively negligible when compared to the first-order effects. Generally, the uncertainties introduced by these assumptions are less than those resulting from uncertainties in the data procured on expansivity and volume changes.

With regard to the thermometer used as an example for the discussion, it will be considered that the borosilicate glass of which it was made possesses the average expansion coefficients for this type of glass. It will also be considered that the glass was thoroughly annealed at 450° C before graduating the stem and making the calibration. According to results that are exemplified by the curves presented in figures 5 and 6 for linear expansivity, it appears that the average volume expansivity in the temperature range from 0° to 100° C approximates 16.4×10^{-6} for a borosilicate thermometer glass in such a condition. Furthermore, according to data and an equation appearing in the International Critical Tables [9], it appears that the corresponding average coefficient is about 182.5×10^{-6} for the volume expansion of mercury. Consequently, for each unit volume of the bulb, a volume of mercury averaging approximately 166.1×10^{-6} will be forced into the capillary of the stem for every degree Centigrade rise in temperature. This result of the differential expansion is the average volume of the capillary between the degree graduations in the range from 0° to 100° C, if the volume of the bulb is unity.

The expansivity and specific volume of the

glass are increased appreciably if the thermometer is used or treated in such a manner that its equilibrium temperature is raised from 450° C to some other temperature, such as 500° C. According to the results of the previously described tests, the increases in volume and volume expansivity are, respectively, 7.8×10^{-5} and $3\times2.4\times10^{-9}$ per degree increase in equilibrium temperature. For a 50-deg increase, the changes in volume and volume expansivity are therefore 3.9×10^{-3} and 3.6×10^{-7}, respectively. Moreover, the average volume expansivity between 0° and 100° C becomes 16.8×10^{-6}. This increase in expansivity reduces the volume of mercury forced into the capillary to 165.7×10^{-6} per unit volume of the bulb and per degree rise in temperature. However, if the original volume of the bulb were unity, the 50-deg C increase in the equilibrium temperature increases the bulb volume to 1.0039. The product of this volume and the new differential expansivity, 165.7×10^{-6}, is about 166.4×10^{-6}. In other words, increasing the equilibrium temperature of the bulb glass of a completed thermometer increases the volume of mercury forced into the capillary for each degree rise in temperature. This increase is sufficient to cause a noticeable effect in those parts of the stem that are unaffected by usage or heat treatment.[5]

To demonstrate the relative importance of the ice-point lowerings, produced by these changes in volume and expansivity, it will be assumed for the moment that no volume change took place at 500° C during the treatment that raised the equilibrium temperature from 450° C to that point. That is, only the change in expansivity is supposed to have taken place. However, in such a case, the volume of the bulb is reduced at all temperatures below 500° C. At 0° C, this reduction amounts to $500\times3.6\times10^{-7}$ or 180×10^{-6}, provided the increase in expansivity persists throughout the range, 500° to 0° C. Consequently, the increase in the expansivity of the glass probably causes an ice-point lowering that somewhat exceeds 1 deg C.

Compared to this ice-point shift, the one caused by the neglected volume change is far more important. According to the value given above for this change, it causes an ice-point lowering or depression that approximates $3.9\times10^{-3}/1.66\times10^{-4}$, or 23.5° C. Consequently, the total effect of increasing the equilibrium temperature by 50 deg C is probably an ice-point lowering of 24+ deg C.

Many thermometers of borosilicate glasses of the kind tested have been graduated to 520° C. In such cases, it is easily possible to increase the equilibrium temperature from 450° to 520° C. As the change in volume at constant actual temperature is approximately proportional to the change in equilibrium temperature, it follows that the volume change produced by an increase of 70 deg C. will cause a lowering or depression of 33+ deg C in ice point and that the total effect will approximate 35 deg if the effect caused by the change in expansivity is added. As already indicated, negative depressions or elevations of this order have been obtained by annealing poorly annealed thermometers at temperatures that were low enough to require treatments approximating 3 weeks in duration before equilibrium was established. Such cases are exceptional and merely show that the maker failed for some reason to age the thermometers for a sufficient time at a suitable annealing temperature.

Under normal conditions of usage, ice-point shifts of the magnitudes found in this demonstration are not likely to develop in properly annealed thermometers. However, it is difficult to avoid small effects whenever a thermometer is graduated to and used at temperatures that can be regarded as low or medium annealing temperatures. In such cases, frequent ice-point determinations or their equivalent should be made. The calibration of the thermometer can then be adjusted in accord with the results of such checks.

VIII. Summary

The changes caused in expansivity by changing the equilibrium temperature of some borosilicate thermometer glasses were determined in this investigation. For some of these glasses that are

[5] In normal usage, a considerable portion of a thermometer stem is immersed and thus receives about the same treatment as the bulb. Consequently, the volume of the capillary per degree of the graduations on the immersed portion of the stem is changed to about the same percentage as the volume of the bulb, provided the glass and the initial conditions are the same for both immersed parts. Hence, the average volume of the capillary between degree graduations on the immersed portion of the stem is increased from the original value, 166.1×10^{-6}, to 166.8×10^{-6}. In other words, a degree change in the temperature of the bulb is indicated as slightly less than a degree on the scale of the immersed portion of the stem, whereas it is indicated as slightly more than a degree on the scale of the unaffected part. For a change of 100 deg in the reading, these discrepancies amount to a few tenths of a degree.

commonly used in thermometers, the increase in expansivity per degree increase in equilbrium temperature was found to be about 2.4×10^{-9}.

The changes in volume per degree change in equilibrium temperature were also determined for some of the glasses. A method of determining these changes from expansion curves for two or more differently treated samples is demonstrated. The average value of the changes approximated 7.8×10^{-5} per unit volume.

Measurements were made on the time rates of expansion and contraction while the glasses were being held at constant temperature in their annealing ranges. It is demonstrated that a previously proposed equation that involves exponential integrals applies satisfactorily to the experimental results of these measurements.

A discussion of the relation of the various results to the performance of mercury glass thermometers is included. In this discussion, it is shown that the volume and expansivity changes resulting from changes in equilibrium temperature are sufficient to account for ice-point elevations observed when poorly annealed thermometers are used at moderately high annealing temperatures.

IX. References

[1] J. B. Saunders and A. Q. Tool, Bull. Am. Ceram. Soc. **16**, 94 (1937).

[2] H. C. Dickinson, BS Bull. **2**, 189 (1906) S32.

[3] J. B. Saunders, J. Research NBS **23**, 179 (1939) RP1227.

[4] A. Q. Tool, J. Research NBS 34, 199 (1945) RP1637.

[5] H. G. Dorsey, Phys. Rev. **25**, 98 (1907).

[6] F. A. Molby, J. Am. Opt. Soc. **36**, 350 (1946).

[7] A. Q. Tool, L. W. Tilton, and J. B. Saunders, J. Research NBS **38**, 519 (1947) RP1793.

[8] A. Q. Tool, J. Am .Ceram. Soc. **31**, 183 (1948).

[9] International Critical Tables **2**, (McGraw-Hill Book Co., New York, N. Y., 1927).

Washington, September 28, 1948.

U. S. Department of Commerce
National Bureau of Standards

Research Paper RP 1961
Volume 42, February 1949

Part of the Journal of Research of the National Bureau of Standards

Zeeman Effect and g-Values for Neutral Nitrogen and Oxygen

By Carl C. Kiess and George Shortley *

Zeeman patterns of red and infrared lines of nitrogen and oxygen, as observed in magnetic fields of 35,000 and 86,000 gausses, at the National Bureau of Standards and the Massachusetts Institute of Technology, respectively, show various degrees of distortion due to Paschen-Back interaction. The interpretation of these patterns has afforded an interesting application of quantum theory to the elucidation of the Paschen-Back effect. The g-values derived for the energy levels of N I and O I are the first to be announced for neutral atoms of atomic number less than neon, 10, and are found to conform with those required for LS-coupling despite the fact that the term intervals do not conform with the Landé ratios.

I. Introduction

Although various observers have investigated the Zeeman effect of elements in the first two rows of the periodic table, the results, for the most part, are qualitative, most of the published measurements referring apparently to unresolved patterns. It was in the spectra of helium and oxygen that Paschen and Back [1][1] first encountered the distorted patterns that appear for close multiplet lines when excited in strong fields. The only Zeeman effects for elements of atomic number below Ne 10 from which g-values can be derived are those published by Mihul [2] for O II, and by Green and Maxwell [3] for N II.

During the past 10 years, at the National Bureau of Standards, Zeeman-effect observations have been made of the infrared spectra of several metals including chromium, molybdenum, columbium, tantalum, and uranium. On nearly all the spectrograms there are registered the magnetic patterns of the red and infrared lines of atmospheric nitrogen and oxygen, as well as those of the metal lines. Similar spectrograms of molybdenum, manganese, and columbium, secured with the spectrographs and magnet of the Massachusetts Institute of Technology, have been made available to us by G. R. Harrison. All of these plates have been measured and reduced, and the collected results are presented in this paper.

Because the Zeeman patterns considered here all show various degrees of Paschen-Back interaction, it is necessary to consider this effect in detail in order to derive g-values from the measurements. We discuss, therefore, not only the method of obtaining the g-values from distorted magnetic patterns, but also the method of computing theoretically the wavelength and intensity shifts arising from Paschen-Back interaction, and give comparisons of the theoretical with the observed results.

II. Experimental Procedure

The procedure employed in making the MIT spectrograms has been described frequently by Professor Harrison and collaborators [4]. The National Bureau of Standards observations were obtained with a large, water-cooled Weiss magnet in conjunction with spectrographs in which are mounted concave gratings that were ruled with 15,000 and 30,000 lines per inch by R. W. Wood [5]. These instruments have dispersions of 5.0

*Mendenhall Laboratory of Physics, Ohio State University; the analysis reported in this paper was made by Dr. Shortley while employed at the Bureau during the summer of 1947.

[1] Figures in brackets indicate the literature references at the end of this paper.

819237—49——7

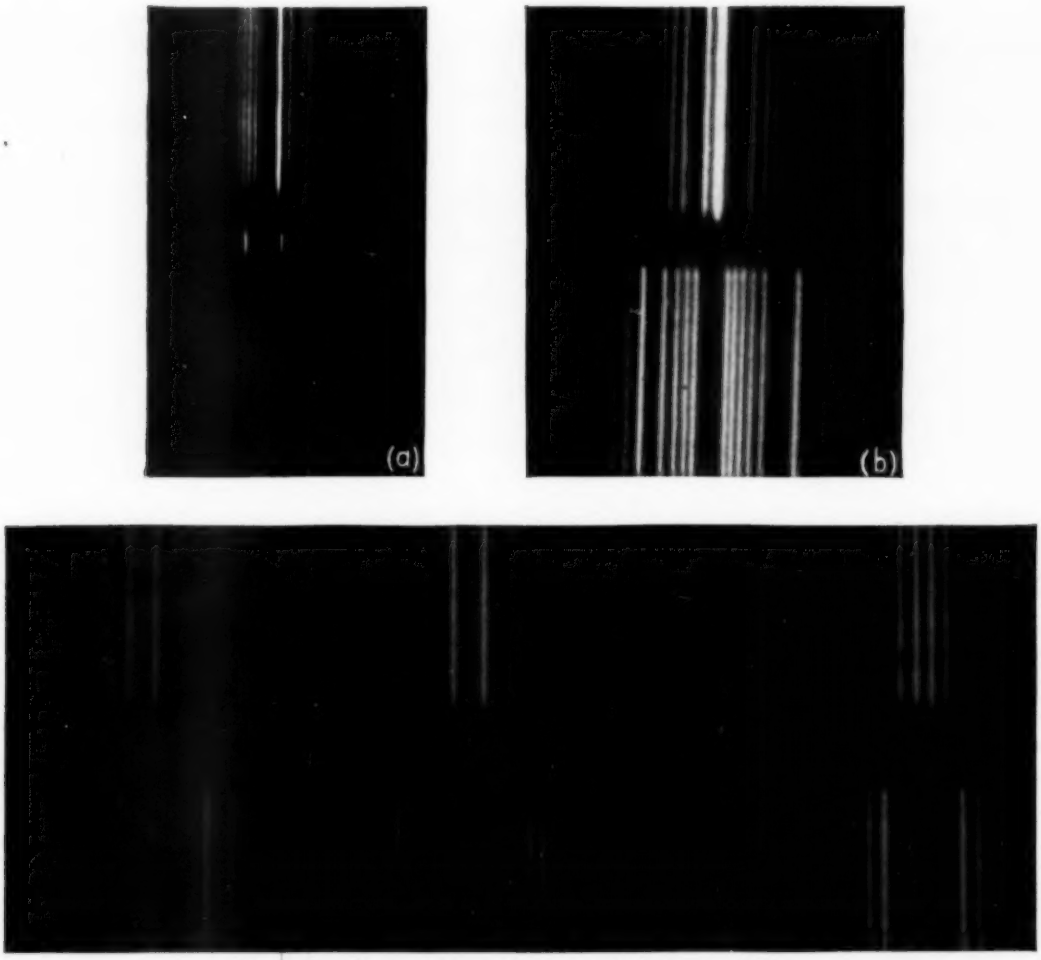

FIGURE 1. *Zeeman patterns of oxygen and nitrogen multiplets.*

Above, the O I quintet 7771 to 7775 A with fields of (a) 34,600 and (b) 85,400 gausses. Below, the N I quartet 7423 to 7468 A with a field of 85,400 gausses. Wavelengths increase from left to right.

and 1.8 A/mm, respectively, in the first-order spectra, whereas that of the MIT spectrograph is 1.6 A/mm. The light source was a Back [6] lamp in which an interrupted direct-current arc was operated on 1 ampere at 220 volts, the air pressure within the arc enclosure being reduced to one-sixth atm. The gap between the iron pole-pieces of the magnet was about 6 mm, so that with currents of 160 amp applied to the coils, fields of approximately 35,000 gausses were attained. For calibrating the fields, the spectrograms were exposed also to arcs between other electrodes to secure resolved patterns of known separations.

The National Bureau of Standards gratings are in Wadsworth mountings [7], in which the grating is illuminated by parallel light. Because of the stigmatic properties of a grating mounted in this manner, it was possible to photograph simultaneously both polarizations of the Zeeman pattern, one above the other, by separating them with a Wollaston prism. This prism, of quartz, was placed between the pole-gap of the magnet and the lens that projected the light onto the slit of the spectrograph. A movable occulting bar in front of the slit and between the two polarized images reserved an unexposed strip on the photographic plates for recording the spectrum without the magnetic field.

III. Results

The Zeeman patterns of the N I lines are presented in tables 1 and 2. The entries in table 1 are weighted mean values derived from two to five NBS spectrograms for all the lines except the first three, which were measured on only one plate. The nine lines of the table, of wavelength longer than 8,500 A, were measured only on spectrograms with a dispersion of 5 A/mm and, therefore, are not so accurately determined as the others. At magnetic field strengths of approximately 35,000 gausses, employed in the NBS observations, no striking anomalies in the spacing or the intensities of the components in the Zeeman patterns are apparent. These patterns, closely resembling those given by Landé's procedure for *LS*-coupling, are given in the last column of table 1.

On the MIT spectrograms, however, taken at fields in excess of 85,000 gausses, distortions of the patterns both as to spacing and intensity of the components are apparent, even to casual inspection. This is illustrated in figure 1 in the case of the line at 7,442 A. Measurement of the three available MIT spectrograms has yielded the data entered in detail in table 2.

In the first column of table 2 are given the term combinations of the lines, their undisturbed wavelengths according to Edlén [8], and the value in angstrom units of one-half the normal Lorentz triplet corresponding to these wavelengths for the field strengths used. The wavelengths entered in the second column are mean values and probably are in error by a small amount, since there were on the plates no standards between which to make accurate interpolations. On only one of the plates is a no-field exposure available in juxtaposition with both the σ- and π-components. In the discussion in section VIII, therefore, each pattern is referred to the arbitrary origin of wavelength listed with its components, since we are concerned only with wavelength differences within a pattern. The third column contains the estimated intensities of the magnetic components. In the last three columns of table 2 are listed the polarizations of the components and the transitions to which they are due, the distances in Lorentz units of the components from their origins, and, finally, their distances from the centers of their patterns. The centers can be located only after the positions of the magnetic levels have been fixed according to the procedure discussed below.

TABLE 1. *Zeeman patterns of* N I *lines from NBS spectrograms.*

Wavelengths	Term combinations	Observed Zeeman patterns
8718. 82	$3s\ ^4P_{2\frac{1}{2}}-3p\ ^4D^0_{3\frac{1}{2}}$	(0.57) 1.48
8711. 69	$3s\ ^4P_{1\frac{1}{2}}-3p\ ^4D^0_{1\frac{1}{2}}$	(0.78) 0.89, **1.50**, 2.01
8703. 24	$3s\ ^4P_{0\frac{1}{2}}-3p\ ^4D^0_{0\frac{1}{2}}$	(1.33) 1.33
8686. 13	$3s\ ^4P_{0\frac{1}{2}}-3p\ ^4D^0_{1\frac{1}{2}}$	(0.73) **0.45**, 1.89
8683. 38	$3s\ ^4P_{1\frac{1}{2}}-3p\ ^4D^0_{2\frac{1}{2}}$	(**0.16**, 0.52) **0.83**, 1.17
8680. 24	$3s\ ^4P_{2\frac{1}{2}}-3p\ ^4D^0_{3\frac{1}{2}}$	(**0.12***w*) 1.03 ⩘
8629. 24	$3s\ ^2P_{1\frac{1}{2}}-3p\ ^2P^0_{1\frac{1}{2}}$	(0.00) 1.32
8594. 01	$3s\ ^2P_{0\frac{1}{2}}-3p\ ^2P^0_{0\frac{1}{2}}$	(0.00) 0.64
8567. 74	$3s\ ^2P_{0\frac{1}{2}}-3p\ ^2P^0_{1\frac{1}{2}}$	(0.30) 1.05, **1.66**
8223. 07	$3s\ ^4P_{1\frac{1}{2}}-3p\ ^4P^0_{0\frac{1}{2}}$	(0.47) **1.25**, 2.20
8216. 28	$3s\ ^4P_{2\frac{1}{2}}-3p\ ^4P^0_{2\frac{1}{2}}$	(0.00) 1.59
8210. 64	$3s\ ^4P_{1\frac{1}{2}}-3p\ ^4P^0_{1\frac{1}{2}}$	(0.00) 1.73
8200. 31	$3s\ ^4P_{0\frac{1}{2}}-3p\ ^4P^0_{0\frac{1}{2}}$	(0.00) 2.66
8187. 95	$3s\ ^4P_{0\frac{1}{2}}-3p\ ^4P^0_{1\frac{1}{2}}$	(0.47) **1.28**, 2.20
8184. 80	$3s\ ^4P_{1\frac{1}{2}}-3p\ ^4P^0_{2\frac{1}{2}}$	(0.00*w*) 1.48 ⩘
7468. 29	$3s\ ^4P_{2\frac{1}{2}}-3p\ ^4S^0_{1\frac{1}{2}}$	(**0.20**, 0.61) **1.01**, 1.42, 1.80, 2.19
7442. 28	$3s\ ^4P_{1\frac{1}{2}}-3p\ ^4S^0_{1\frac{1}{2}}$	(0.16, **0.39**) 1.61, **1.88**, 2.16
7423. 63	$3s\ ^4P_{0\frac{1}{2}}-3p\ ^4S^0_{1\frac{1}{2}}$	(0.34) **1.68**, 2.35

In the spectrum of the neutral oxygen atom, two multiplets are easily excited in arcs-in-air between metallic electrodes: that at 8,446 A, representing the term combination $2p^3\ 3s\ ^3S^\circ-3p\ ^3P$, and that at 7,771 to 7,775 A from $2p^3\ 3s\ ^5S^\circ-3p\ ^5P$. In each of these multiplets, the no-field spacing of the three lines is less than the magnetic splitting of the levels, even for moderate fields, so that their Zeeman patterns all exhibit Paschen-Back interaction. In the case of the 8,446 lines, the interaction is essentially complete. In a field of 35,000 gausses the pattern, as measured on a spectrogram taken with the 15,000 lines/inch grating, is $\pm$(**0.00***w*, 0.99)**0.99**, with strong σ-components and very weak π-components at the separation of the normal Lorentz triplet. The strong, widened π-component appears as an unresolved group of two or more lines. On an

TABLE 2. *Zeeman patterns of* N I *lines from M1T spectrograms*

Term combination No-field wavelength Lorentz factor in A	Observed Zeeman pattern in A	Intensity	Polarization and transition	Distance in L. U. to origin	Distance in L. U. to center
$3s\ ^4P_{2\frac{1}{2}}-3p\ ^4P^o_{1\frac{1}{2}}$ 8242.34 L. U. = 2.708 A	8247. 326	1−	$\sigma -3/2\rightarrow -1/2$	6. 398	−1. 857
	8246. 709	1	$\sigma -1/2\rightarrow +1/2$	6. 170	−1. 629
	8246. 219	10	σ {+1/2→+3/2, +3/2→+5/2}	5. 989	−1. 448
	8242. 982	1	$\pi -3/2\rightarrow -3/2$	4. 794	−0. 253
	8242. 418	2	$\pi -1/2\rightarrow -1/2$	4. 586	−0. 045
	8242. 297		Center	4. 541	
	8241. 988	4	π {+1/2→+1/2, +3/2→+3/2}	4. 427	+0. 114
	8238. 595	7	$\sigma -3/2\rightarrow -5/2$	3. 174	+1. 367
	8238. 027	3	$\sigma -1/2\rightarrow -3/2$	2. 964	+1. 577
	8237. 615	2	σ {+1/2→−1/2, +3/2→+1/2}	2. 812	+1. 729
	8230. 000		Origin		
$3s\ ^4P_{1\frac{1}{2}}-3p\ ^4P^o_{0\frac{1}{2}}$ 8223.07 L. U. = 2.696 A	8229. 394	4	$\sigma -1/2\rightarrow +1/2$	10. 903	−2. 308
	8226. 759	10	$\sigma +1/2\rightarrow +3/2$	9. 926	−1. 331
	8224. 774	9	$\pi -1/2\rightarrow +1/2$	9. 189	−0. 594
	8223. 172		Center	8. 595	
	8222. 346	10	$\pi +1/2\rightarrow +1/2$	8. 289	+0. 306
	8219. 927	8	$\sigma -1/2\rightarrow -3/2$	7. 391	+1. 204
	8217. 636	6	$\sigma +1/2\rightarrow -1/2$	6. 542	+2. 053
	8200. 000		Origin		
$3s\ ^4P_{2\frac{1}{2}}-3p\ ^4P^o_{2\frac{1}{2}}$ 8216.28 L. U. = 2.691 A	8220. 546	25	$\sigma -n/2\rightarrow(-n+1)/2$	7. 635	−1. 588
	8216. 339	40	$\pi \pm n/2\rightarrow \pm n/2$	6. 072	−0. 025
	8216. 272		Center	6. 047	
	8211. 997	35	$\sigma +n/2\rightarrow(n-1)/2$	4. 458	+1. 589
	8200. 000		Origin		
$3s\ ^4P_{1\frac{1}{2}}-3p\ ^4P^o_{1\frac{1}{2}}$ 8210.64 L. U. = 2.688 A	8215. 376	1	$\sigma +1/2\rightarrow +3/2$	5. 720	−1. 737
	8215. 144	2	$\sigma -1/2\rightarrow +1/2$	5. 634	−1. 651
	8214. 946	3	$\sigma -3/2\rightarrow -1/2$	5. 560	+1. 577
	8210. 706	12	$\pi \pm n/2\rightarrow \pm n/2$	3. 983	0. 000
	8210. 706		Center	3. 983	
	8206. 198	4	σ {−1/2→−3/2, +3/2→+1/2}	2. 306	+1. 677
	8205. 826	3	$\sigma +1/2\rightarrow -1/2$	2. 167	+1. 816
	8200. 000		Origin		
$3s\ ^4P_{0\frac{1}{2}}-3p\ ^4P^o_{0\frac{1}{2}}$ 8200.31 L. U. = 2.681 A	8207. 525	3	$\sigma -1/2\rightarrow +1/2$	6. 537	−2. 708
	8200, 479	10	π {+1/2→+1/2, −1/2→−1/2}	3. 909	−0. 080
	8200. 266		Center	3. 829	
	8193. 428	5	$\sigma +1/2\rightarrow -1/2$	1. 279	+2. 550
	8190. 000		Origin		
$3s\ ^4P_{0\frac{1}{2}}-3p\ ^4P^o_{1\frac{1}{2}}$ 8187.95 L. U. = 2.673 A	8193. 487	1−	$\sigma -1/2\rightarrow +1/2$	5. 046	−2. 054
	8191. 278	9	$\sigma -3/2\rightarrow -1/2$	4. 219	−1. 227
	8188. 846	10	$\pi +1/2\rightarrow +1/2$	3. 309	−0. 317
	8187. 998		Center	2. 992	
	8186. 442	8	$\pi -1/2\rightarrow -1/2$	2. 410	+0. 582
	8184. 496	10	$\sigma +3/2\rightarrow +1/2$	1. 682	+1. 310
	8181. 709	2	$\sigma +1/2\rightarrow -1/2$	0. 639	+2. 353
	8180. 000		Origin		

TABLE 2. *Zeeman patterns of* N I *lines from MIT spectrograms*—Continued

Term combination No-field wavelength Lorentz factor in A	Observed Zeeman pattern in A	Intensity	Polarization and transition	Distance in L. U. to origin	Distance in L. U. to center
	8189.479	1—	$\sigma+1/2\rightarrow+3/2$	7.293	−1.733
	8189.317	1	$\sigma-1/2\rightarrow+1/2$	7.232	−1.673
	8188.928	3	$\sigma-3/2\rightarrow-1/2$	7.087	−1.528
	8188.505	6	$\sigma-5/2\rightarrow-3/2$	6.928	−1.369
	8185.274	4	$\pi+3/2\rightarrow+3/2$	5.718	−0.159
$3s\ {}^4P_{1\frac{1}{2}}-3p\ {}^4P_{2\frac{1}{2}}$	8185.038	6	$\pi+1/2\rightarrow+1/2$	5.630	−0.071
8184.80	**8184.848**		Center	5.559	
L. U.=2.671 A	8184.660	7	$\pi-1/2\rightarrow-1/2$	5.489	+0.070
	8184.209	5	$\pi-3/2\rightarrow-3/2$	5.320	+0.239
	8181.067	8	$\sigma+5/2\rightarrow+3/2$	4.143	+1.416
	8180.763	3	$\sigma+3/2\rightarrow+1/2$	4.030	+1.529
	8180.390	2	$\sigma+1/2\rightarrow-1/2$	3.890	+1.669
	8179.892	1—	$\sigma-1/2\rightarrow-3/2$	3.704	+1.855
	8170.000		Origin		
	7473.347	3	$\sigma-3/2\rightarrow-1/2$	6.001	−2.253
	7472.441	5	$\sigma-1/2\rightarrow+1/2$	5.594	−1.846
	7471.484	6	$\sigma+1/2\rightarrow+3/2$	5.164	−1.416
	7470.565	12	$\sigma+3/2\rightarrow+5/2$	4.750	−1.002
	7469.734	8	$\pi-3/2\rightarrow-3/2$	4.377	−0.629
$3s\ {}^4P_{2\frac{1}{2}}-3p\ {}^4S_{1\frac{1}{2}}$	7468.870	12	$\pi-1/2\rightarrow-1/2$	3.988	−0.240
7468.29	**7468.336**		Center	3.748	
L. U.=2.224 A	7467.989	10	$\pi+1/2\rightarrow+1/2$	3.592	+0.156
	7467.075	8	$\pi+3/2\rightarrow+3/2$	3.181	+0.567
	7466.109	12	$\sigma-3/2\rightarrow-5/2$	2.747	+1.001
	7465.262	8	$\sigma-1/2\rightarrow-3/2$	2.366	+1.386
	7464.396	5	$\sigma+1/2\rightarrow-1/2$	1.977	+1.771
	7463.511	2	$\sigma+3/2\rightarrow+1/2$	1.579	+2.169
	7460.000		Origin		
	7447.142	6	$\sigma-3/2\rightarrow-1/2$	7.764	−2.158
	7446.565	10	$\sigma-1/2\rightarrow+1/2$	7.502	−1.896
	7445.840	8	$\sigma+1/2\rightarrow+3/2$	7.174	−1.568
	7443.214	15	$\pi-3/2\rightarrow-3/2$	5.985	−0.379
$3s\ {}^4P_{1\frac{1}{2}}-3p\ {}^4S_{1\frac{1}{2}}$	7442.720	2	$\pi-1/2\rightarrow-1/2$	5.761	−0.155
7442.28	**7442.378**		Center	5.606	
L. U.=2.208 A	7442.096	1—	$\pi+1/2\rightarrow+1/2$	5.478	+0.128
	7441.460	12	$\pi+3/2\rightarrow+3/2$	5.190	+0.416
	7438.790	5	$\sigma-1/2\rightarrow-3/2$	3.981	+1.625
	7438.302	7	$\sigma+1/2\rightarrow-1/2$	3.760	+1.846
	7437.722	6	$\sigma+3/2\rightarrow+1/2$	3.497	+2.109
	7430.000		Origin		
	7428.795	3	$\sigma-1/2\rightarrow+1/2$	8.555	−2.282
	7427.324	6	$\sigma-3/2\rightarrow-1/2$	7.885	−1.614
	7424.385	7	$\pi+1/2\rightarrow+1/2$	6.548	−0.277
$3s\ {}^4P_{0\frac{1}{2}}-3p\ {}^4S_{1\frac{1}{2}}$	**7423.777**		Center	6.271	
7423.63	7422.911	7	$\pi-1/2\rightarrow-1/2$	5.877	+0.394
L. U.=2.197 A	7419.949	6	$\sigma+3/2\rightarrow+1/2$	4.528	+1.743
	7418.509	2	$\sigma+1/2\rightarrow-1/2$	3.873	+2.398
	7410.000		Origin		

MIT spectrogram, taken at 82,000 gausses, the π-component and the σ-component of shorter wavelength are split into two lines of unequal intensities, separated respectively by 0.047 and 0.034 Lorentz unit. The σ-component of longer wavelength is perceptibly broadened, but unresolved. No faint π-components appear at the normal triplet position.

The 7,771 to 7,775 multiplet, however, bears no resemblance either to a weak-field pattern or to a Lorentz triplet. The distortions produced by Paschen-Back interaction due to two fields of 34,660 and 85,400 gausses are shown in figure 1. The data given in table 3 are the wavelengths and estimated intensities of the π- and σ-components and their shifts from the undisturbed positions of the lines in terms of the normal Lorentz triplet spacing. The shifts, in columns (a), (b), and (c) of the table, were calculated from the observed wavelengths by the procedure described in the following section. As with the nitrogen lines, no attempt has been made to express the wavelengths on the correct I. A. scale, because of the absence of standards on the spectrograms. They differ from this by a small constant amount which is of no importance in the interpretation of the pattern. The tabulated wavelengths are mean values derived from measurements of two NBS spectrograms at 34,660 gausses and three MIT spectrograms at 85,400 gausses. For purposes of comparison, the wavelengths from both sets of spectrograms are referred to the same origin at 7771.950 A. The separations 2.220 A and 1.220 A adopted for the oxygen lines

TABLE 3. *Zeeman pattern of* O I *multiplet at 7771 to 7775 A*

Wavelength	Intensity	Lorentz spacing $H=34{,}660$			Wavelength	Intensity	Lorentz spacing $H=85{,}400$		
		(a)	(b)	(c)			(a)	(b)	(c)
π components					π components				
					7769. 972	3	−0. 821		
7771. 230	4	−0. 736			7770. 451	6	−0. 622		
7771. 494	8	−0. 466			7770. 980	7	−0. 403		
7771. 784	10	−0. 170			7771. 649	8	−0. 125		
7771. 950		Origin			**7771. 950**		Origin		
7772. 110	12	+0. 164			7772. 917	13	+0. 401		
7772. 486	12	+0. 548			7773. 475	6		−0. 288	
					7773. 579	7		−0. 245	
7773. 929	50*w*		−0. 247		7773. 695	10		−0. 197	
					7773. 796	7		−0. 155	
7774. 170			Origin		**7774. 170**			Origin	
7774. 590	15		+0. 428						
7775. 359	10			−0. 032					
7775. 390				Origin	**7775. 390**				Origin
7775. 764	8			+0. 382	7775. 598	8		+0. 593	
7776. 077	4			+0. 702	7776. 354	7			+0. 400
					7776. 904	5			+0. 629
					7777. 376	4			+0. 824

TABLE 3. *Zeeman pattern of* O I *multiplet at 7771 to 7775 A*—Continued

Wavelength	Intensity	Lorentz spacing $H=34{,}660$			Wavelength	Intensity	Lorentz spacing $H=85{,}400$		
		(a)	(b)	(c)			(a)	(b)	(c)
		σ components					σ components		
7769. 575	1−−	−2. 428			7765. 620	1−	−2. 628		
7769. 819	1−	−2. 178			7766. 146	1	−2. 409		
7770. 148	2	−1. 842			7766. 815	3	−2. 131		
7770. 555	4	−1. 426			7768. 122	8	−1. 589		
					7768. 660	3		−2. 287	
					7768. 770	4		−2. 241	
					7768. 876	3		−2. 198	
7770. 995	8	−0. 976			7769. 552	25	−0. 995		
					7770. 798	15		−1. 400	
					7771. 544	10			−1. 597
7771. 950		Origin			**7771. 950**		Origin		
7772. 045	5*w*		−2. 173		7772. 112	10			−1. 361
7772. 658	5		−1. 547		7772. 592	10			−1. 161
7772. 933	7	+1. 005							
7773. 177	5	+1. 254							
7773. 440	7	+1. 523		−1. 993					
7773. 728	2	+1. 818							
7773. 809	4			−1. 616					
7774. 141	5			−1. 277					
7774. 170			Origin		**7774. 170**			Origin	
					7774. 370	12	+1. 005		
					7774. 794	10	+1. 181		
					7775. 269	10	+1. 378		
7775. 390				Origin	**7775. 390**				Origin
7775. 930	10*w*		+1. 798		7775. 812	12	+1. 603		
7777. 308	1			+1. 961	7776. 482	15	+1. 881		
7777. 785	1−			+2. 448	7778. 291	5		+1. 711	
					7778. 388	8		+1. 751	
					7778. 492	8		+1. 794	
					7778. 582	5		+1. 831	
					7781. 193	1			+2. 409
					7781. 744	1−			+2. 638
					7782. 177	1−−			+2. 817

in their no-field positions are mean values from the present series of measurements and from the wavelengths in the solar spectrum as reported by Meggers [9] and by the observers of the Mt. Wilson Observatory [10].

The g-values that have been obtained from the data of tables 2 and 3 are given in table 4. The method used to determine g-values of the perturbed terms is discussed in detail in a later section of this paper. The g's entered in the table for the doublet terms of N I are only estimated values, which is indicated by enclosing them in parentheses. The three measured doublet patterns do not yield the g's of the doublet terms uniquely, but they are sufficiently close to the patterns of LS-coupling to justify the conclusion that the g's do not deviate appreciably from the Landé values.

TABLE 4. *Observed g-values for energy levels of* N I *and* O I

Values in pure LS-coupling are given for comparison

N I				O I			
Term	J	g_{obs}	g_{LS}	Term	J	g_{obs}	g_{LS}
$3s\ ^4P$	2½	1. 603	1. 600	$3s\ ^5S°$	2	1. 999 ± 0. 002	2. 000
	1½	1. 735	1. 733				
	0½	2. 670	2. 667	$3p\ ^5P$	3	1. 666 ± 0. 001	1. 667
$3s\ ^2P$	1½	(1. 33)	1. 33		2	1. 836 ± 0. 003	1. 833
	0½	(0. 67)	0. 67		1	2. 506 ± 0. 005	2. 500
$3p\ ^4D°$	3½	1. 44	1. 43				
	2½	1. 36	1. 37				
	1½	1. 19	1. 20				
	0½	0. 002	0. 00				
$3p\ ^4P°$	2½	1. 598	1. 600				
	1½	1. 737	1. 733				
	0½	2. 671	2. 667				
$3p\ ^4S°$	1½	2. 004	2. 000				
$3p\ ^2P°$	1½	(1. 33)	1. 33				
	0½	(0. 67)	0. 67				

IV. The $^5P \rightarrow {}^5S$ Multiplet of O I

The three lines of the O I multiplet $2p^3\ 3p\ ^5P \rightarrow 3s\ ^5S°$ are so close that large Paschen-Back perturbations occur with any field large enough to resolve the Zeeman components. The patterns at 34,660 and 85,400 gausses are shown in figure 1. These patterns are so distorted by Paschen-Back perturbations that they bear little resemblance to weak-field patterns.

The correct assignment of components to states was first determined for the 85,400-gauss pattern by making an entirely theoretical computation of component positions and (strengths)$^{1/2}$, by using the observed no-field positions of the levels and assuming strict Russell-Saunders coupling in determining the g-values and the matrix components that give the Paschen-Back interaction. The method of making these computations will be discussed in detail in sections VI and VII. The computed values are compared with the observed wavelengths and estimated intensities in table 5 and figure 2. Although this pattern is wide for a Zeeman pattern, yet it covers a sufficiently small range of wavelength so that within the observational error it is appropriate to assume that wave-number differences are proportional to wavelength differences, and use a mean value (at 7,773 A) of the ratio of $\Delta\nu$ to $\Delta\lambda$ to determine the Lorentz splitting factor in angstroms. Because wave-number and wavelength differences have opposite signs, the energy-state pattern of table 5 seems upside down. The scale has been turned over in plotting figure 3, although angstrom units are retained.

The agreement between the computed and observed wavelength intervals and intensities in

table 5 and figure 2 is excellent. Apart from the clustered, or very weak components bracketed in table 5, the maximum wavelength discrepancy is 0.026 A; the average of the discrepancies, all counted positive, is only 0.013 A. This agreement shows that the coupling must be exceedingly close to Russell-Saunders. This fact is of considerable theoretical interest since the ^{5}P term does not obey the Landé interval rule, the intervals being in the ratio 3:1.65 in place of 3:2. Since the quantum numbers of the term must be quite accurately those of ^{5}P, the departure from the interval rule is undoubtedly to be accounted for by some type of magnetic interaction other than the ordinary spin-orbit.

The fact that visual estimates of intensity correspond quite accurately to the square roots of the line strengths rather than to the strengths themselves was first pointed out by Russell [11]. There are certain interesting discrepancies in this inten-

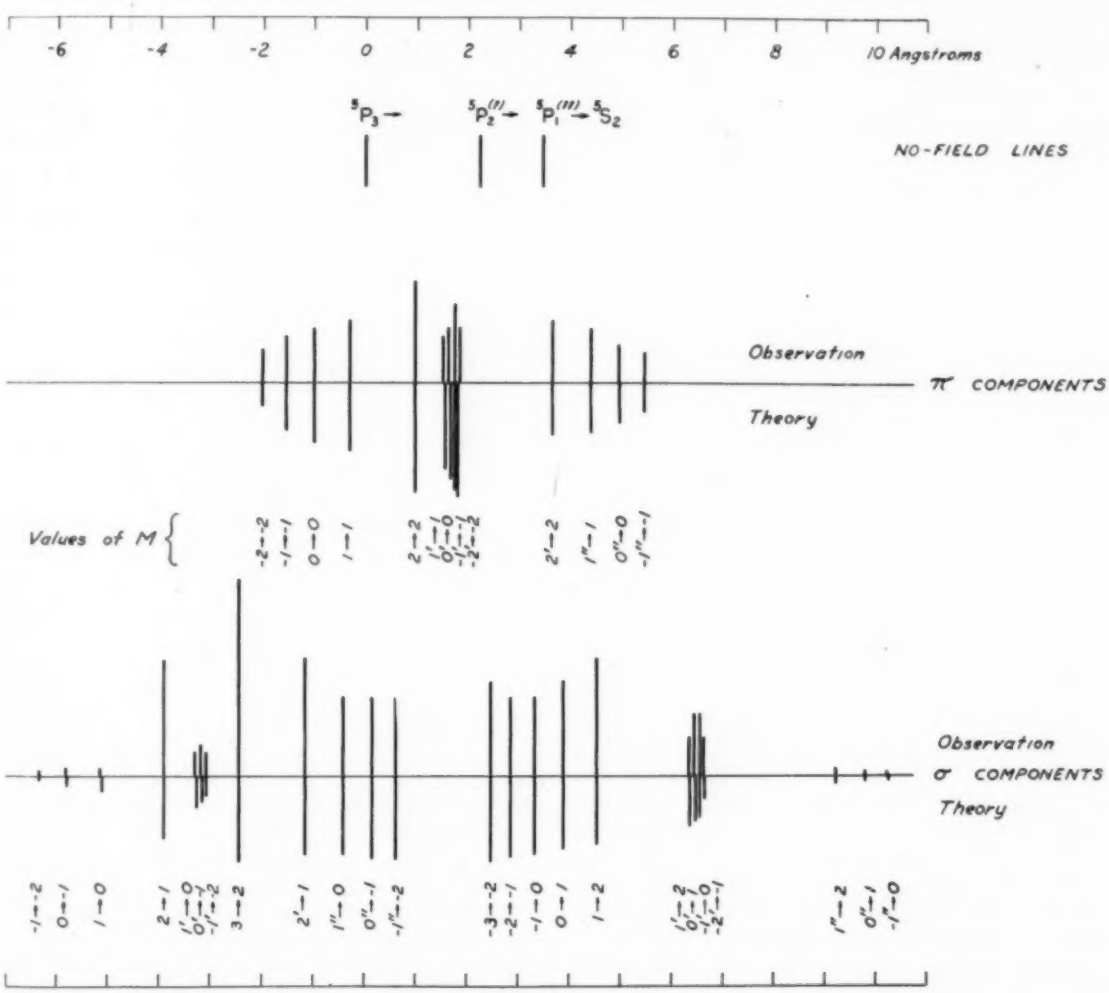

FIGURE 2. *Zeeman patterns of the* O I *miltiplet* $2p^3\ 3p\ ^5P \rightarrow 3s\ ^5S$ *in a field of 85,400 gausses*

Comparison of observation and theory. The theoretical positions were computed by using the no-field positions observed on the same plate and strict *LS*-coupling matrix components. The lengths of the bars show computed relative values of the square roots of the component strengths below and visual intensity estimates above.

TABLE 5. *Paschen-Back pattern for* O I $2p^3\ 3p\ {}^5P \rightarrow 3s\ {}^5S$ *(7771 to 7775 A) at 85,400 gausses*

	$M \longrightarrow$		$^5S_2$ 2	1	0	−1	−2
			−9.636	*−4.818*	*0*	*4.818*	*9.636*
			−9.632	−4.816	0	−4.816	9.632
	3	*−12.045*	*−2.409(11.0)*			$g(^5S_2) = 1.999 \pm 0.002$	
		−12.030	−2.398(25)				
	2	*−8.658*	*0.978(14.0)*	*−3.840(4.8)*			
		−8.654	0.967(13)	−3.828(8)			
	1	*−5.109*	*4.527(8.8)*	*−0.291(8.8)*	*−5.109(2.0)*		
$^5P_3$		−5.117	4.532(15)	−0.301(8)	−5.135(3)		
No-field position 0	0	*−0.966*		*3.852(9.4)*	*−0.966(7.6)*	*−5.784(1.3)*	
		−0.971		3.862(12)	−0.970(7)	−5.804(1)	
	−1	*3.308*			*3.308(10.0)*	*−1.510(6.2)*	*−6.328(0.7)*
		3.318			3.319(10)	−1.499(6)	[−6.330(1−)]
	−2	*7.651*				*2.833(10.5)*	*−1.985(4.4)*
		7.657				2.844(10)	−1.978(3)
	−3	*12.045*	$g(^5P_3) = 1.666 \pm 0.001$				*2.409(11.0)*
		12.052					2.420(12)
	2′	*−5.984*	*3.652(6.7)*	*−1.166(9.9)*			
		−5.976	3.648(8)	−1.152(15)			
	1′	*−3.267*	*6.369(6.5)*	*1.551(11.1)*	*−3.267(4.0)*		
$^5P_2$		−3.290	[6.341(5)]	[1.525(6)]	−3.290(3)		
No-field position 2.220	0′	*1.660*		*6.478(5.5)*	*1.660(12.5)*	*−3.158(3.5)*	
		1.636		[6.438(8)]	[1.629(7)]	−3.188(4)	
	−1′	*6.550*			*6.550(4.5)*	*1.732(13.7)*	*−3.086(2.5)*
		6.558			[6.542(8)]	[1.745(10)]	−3.074(3)
	−2′	*11.433*	$g(^5P_2) = 1.836 \pm 0.003$			*6.615(3.1)*	*1.797(14.8)*
		11.463				[6.632(5)]	[1.846(7)]
	1″	*−0.414*	*9.222(0.9)*	*4.404(6.2)*	*−0.414(10.0)*		
		−0.406	9.243(1)	4.394(7)	−0.406(10)		
$^5P_1$	0″	*4.970*		*9.788(0.7)*	*4.970(5.1)*	*0.152(10.3)*	
No-field position 3.440		4.966		[9.794(1−)]	4.954(5)	0.162(10)	
	−1″	*10.258*	$g(^5P_1) = 2.506 \pm 0.005$		*10.258(0.4)*	*5.440(3.7)*	*0.622(10.6)*
		10.258			[10.227(1−−)]	5.426(4)	0.642(10)

sity comparison that seem to be a definite indication of nonisotropic excitation conditions. In particular, the σ-component $M=3\rightarrow 2$ is observed much too strong, and in fact definitely much stronger than $M=-3\rightarrow -2$. Since these two particular components suffer neither shift in position nor alteration in strength because of Paschen-Back interaction, they must remain of equal strength at any value of the field if the excitation is isotropic. They are of substantially equal strength on the NBS plates, but are strikingly unequal on the MIT plates, as can be seen even from the reproduction in figure 1.

With the components allocated to their proper boxes in table 5, a state analysis was made and g-values computed from the experimental data. Because the pattern is very wide, these g-values can be obtained with high accuracy, and are found to agree with the Russell-Saunders values (2 for $^5S_2$, 5/3=1.667 for $^5P_3$, 11/6=1.833 for $^5P_2$, 2.5 for $^5P_1$) within the estimated experimental error given in the tables. The method of obtain-

ing these g-values from the state analysis is given in the next section. The entries in table 5 printed in Roman type are the observed components and the energy states derived therefrom, measured in A from the no-field position of $^5P_3 \rightarrow {}^5S_2$, with the estimated intensities in parentheses. The bracketed components are poorly resolved or are very weak. The observed Lorentz splitting factor is 2.409 A. The entries in *italics* are the components, states, and square roots of the line strengths computed from the no-field positions of the lines, from the observed splitting factors, and from the LS-coupling g-values.

At the right of figure 3 is shown a comparison of the observed positions of the ^5P states, as given in table 5, with their unperturbed positions. By unperturbed position, we mean the position the state would have if there were no Paschen-Back perturbation by states belonging to neighboring levels. The unperturbed position is obtained by adding to the no-field position the quantity Mg times the Lorenz splitting factor. The difference between the observed position of the state (solid bar in figure 3) and the unperturbed position (broken bar) is the Paschen-Back perturbation.

It is only states of the same M-value that perturb each other. Theory shows rigorously that the sum of the Paschen-Back perturbations of the states of the same M-value must vanish. Thus in figure 3 there is only one state of $M=3$ and one of $M=-3$, so these are unperturbed. The two states of $M=2$ and the two of $M=-2$ should be shifted away from each other by equal amounts. The sum of the three perturbations of the three states of $M=1$, of $M=0$, and of $M=-1$ should be zero in each case. The data given on figure 3 agree with these statements within the accuracy with which the values of the positions can be obtained from the experimental data used.

V. Analysis of a Paschen-Back Pattern

Usually it is not necessary to make a theoretical computation in order to allocate properly the components of a well-resolved Paschen-Back pattern. In fact, such a theoretical computation is impossible unless the g-values and the type of coupling are already fairly well known.[2] Instead one looks for repeated differences, always between a π-component and a σ-component, and attempts to make a state-analysis of the components in the same way as an ordinary level-analysis is made of spectral lines, by making use of all available theoretical clues with regard to Paschen-Back perturbations and intensities. Table 6, which shows the same oxygen quintet as table 5, but at a much lower field, will serve as an example, although a difficult one because of unresolved components. The numbers in the table printed in Roman type are the observed wavelengths of the components decreased by 7,700, and, in parentheses, their estimated intensities. The differences of the π and σ components that correspond to the $^5S_2$ splitting are entered between the columns, the bracketed values being uncertain, owing to blending or weakness of the lines. Here the observed Lorentz splitting factor is 0.978 A. In *italics* are given the states and components computed from the differences between the states. The states for the blends in $^5P_2$ are in all cases placed so that the mean Paschen-Back perturbation is zero, as required by theory.

The analysis in table 6 is simplified by the fact that the lower term $^5S_2^\circ$ is unperturbed, since it contains only one level. Hence the interval between the states of $^5S_2^\circ$ occurs repeatedly, each π-component having a σ-component at this distance on one or both sides, according to its position in the table. This interval is easily picked up (average 1.947 A), and determines the g-value of $^5S_2^\circ$. There are, however, two fairly strong σ-components ($M=3\rightarrow2, -3\rightarrow-2$) that do not lie at this interval from any π-component. Furthermore, these two σ-components are equidistant from the no-field position of $^5P_3\rightarrow{}^5S_2^\circ$, which makes them easy to spot. In this way the $M=3,-3$ separation and the g-value of $^5P_3$ are determined, and the unperturbed positions of the other states of $^5P_3$ may be computed. The table is completed by using the following guides:

(a) Intensities. For a discussion of the effect of Paschen-Back perturbations on intensity patterns, see sections VII and VIII.

(b) The fact that the sum of the Paschen-Back perturbations on states of a given M-value vanishes. Since the $+M$ and $-M$ unperturbed states are equidistant from the no-field position, this guide is best used in connection with the mean

[2] The theory of the Paschen-Back effect in intermediate coupling has been discussed by J. B. Green and J. F. Eichelberger, Phys. Rev. **56**, 51 (1939).

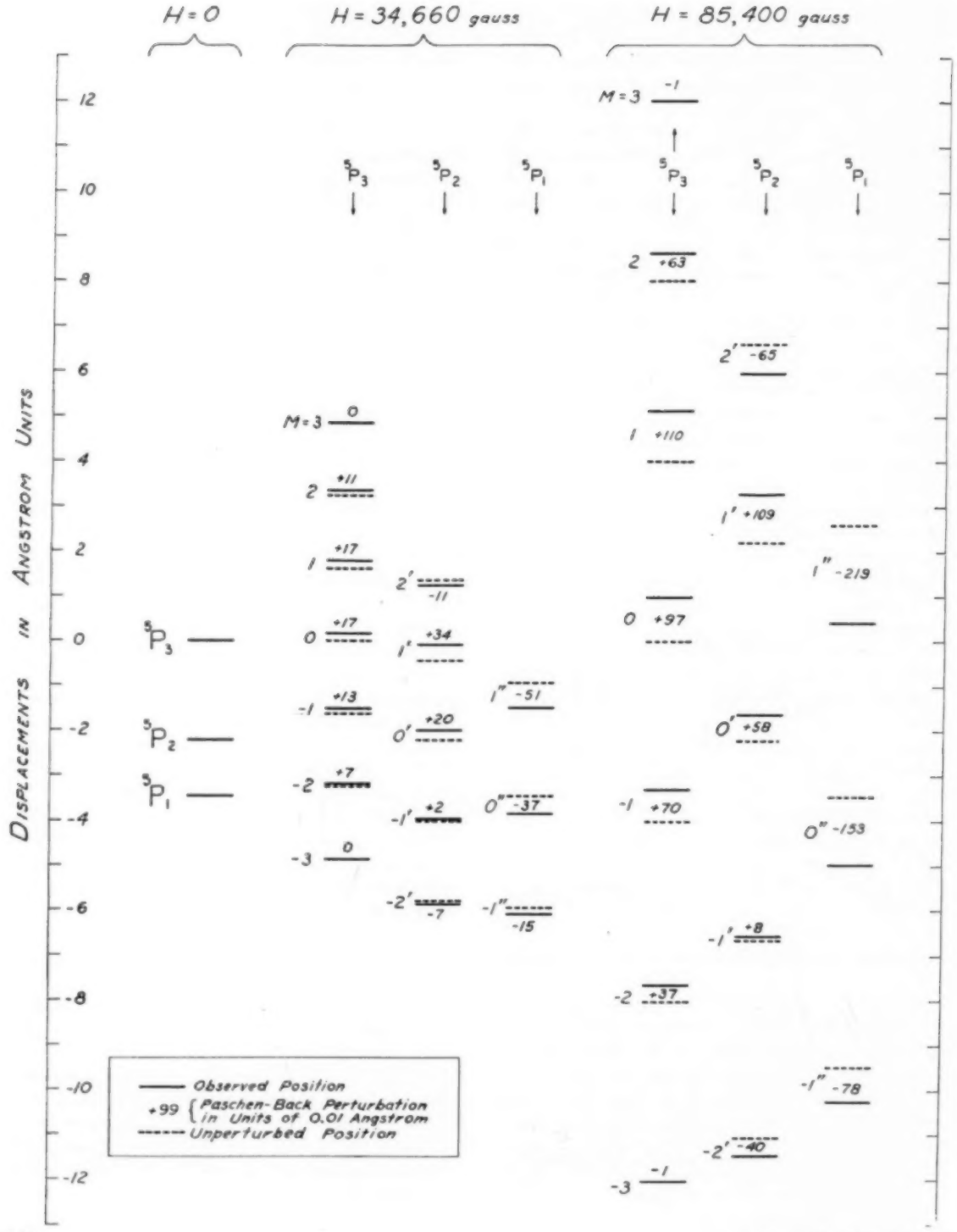
H = 0
H = 34,660 gauss
H = 85,400 gauss
DISPLACEMENTS IN ANGSTROM UNITS
12
10
8
6
4
2
0
-2
-4
-6
-8
-10
-12
$^5P_3$
$^5P_2$
$^5P_1$
M = 3
2
1
0
-1
-2
-3
+11
+17
+13
+7
+63
+110
+97
+70
+37
-1
+109
+58
+8
-40
-65
-219
-153
-78
+34
+20
+2
-11
-51
-37
-7
-15
Observed Position
+99 Paschen-Back Perturbation in Units of 0.01 Angstrom
Unperturbed Position

positions of perturbed states of opposite M-value. Thus, the mean of the states $M=3$ and $M=-3$ is the no-field position of $^5P_3$; the mean of the four states, $M=2, -2, 2', -2'$ is the mean of the no-field positions of $^5P_3$ and $^5P_2$, etc. (fig. 3). Thus, if we denote the mean positions of a set of states or no-field levels by $\langle\ \rangle$, we have for the ^5P of our example:

$$\langle 3,-3\rangle = {}^5P_3$$

$$\langle 2,-2,\ 2',-2'\rangle = \langle {}^5P_3,\ {}^5P_2\rangle$$

$$\langle 1,-1,\ 1',-1',\ 1'',-1''\rangle = \langle {}^5P_3,\ {}^5P_2,\ {}^5P_1\rangle$$

$$\langle 0,\ \ 0',\ 0''\rangle = \langle {}^5P_3,\ {}^5P_2,\ {}^5P_1\rangle$$

(c) When g-values are finally determined and unperturbed positions computed, the perturbations must be in the right direction and of the right order of magnitude. Thus, looking at the $H=$ 34,600-gauss part of figure 3, which shows the perturbations in the example in question, the single states of $M=3$ and $M=-3$ are unperturbed. The two states of $M=2$ and the two of $M=-2$ push each other apart by equal amounts, but the unperturbed states of $M=2$ are closer than those of $M=-2$, so the $M=2$ states suffer a greater perturbation. The perturbations are approximately in inverse ratio to the unperturbed separations. The three states of $M=1$ are more closely grouped than those of $M=-1$ so they suffer greater perturbations. In each case the top state must be pushed higher and the bottom state lower. The center state is pushed up more strongly by the closer state of the same M below it than it is pushed down by the more distant state above, so it suffers a net upward perturbation. The statement of this last sentence is not a rigorous requirement, because the matrix components determining the magnitude of the perturbation may, for example, be different for (1, 1') and (1', 1''). The states of $M=0$ behave similarly to those of $M=\pm 1$.

FIGURE 3. *Paschen-Back perturbations of the* $O\,1 2p^3 3p\,^5P$ *states at two field strengths.*

Solid bars show observed state positions as obtained from an empirical state analysis. The unperturbed positions shown by broken bars were computed by using the observed no-field positions and the empirical g-values obtained from the state analysis.

Determination of g-values. When a satisfactory state analysis is completed, the computation of the g-values, which give the weak field, or unperturbed, state positions, is straightforward. We can use the observed data in table 5, which give the best values for the oxygen quintet, as an illustration.

The $^5S_2$ splitting is 4.816 $\pm$0.004 A, determined from the 12 $\pi-\sigma$ intervals between unbracketed components. This splitting, divided by the Lorentz splitting factor, 2.409 A, gives $g(^5S_2)=$ 1.999 $\pm$0.002.

The probable errors that we give here are determined purely from internal consistency of the 12 $\pi-\sigma$ intervals, a possible error in the well-determined Lorentz splitting factor being neglected. On this basis a probable error of 0.010 A is assigned to each measured (unbracketed) wavelength, and from this the probable errors in the ^5P levels and the $g(^5P)$ are determined in straightforward fashion.

The $M=3, -3$ interval of 24.082 $\pm$0.018 A, divided by 6 gives 4.014 $\pm$0.003 A for the unperturbed $^5P_3$ splitting, and $g(^5P_3)=1.666\ \pm0.001$.

The observed $(2, -2)$ and $(2', -2')$ intervals are distorted by Paschen-Back perturbations, but because of the properties of these perturbations it is seen that the sum of these two intervals is the same as if there were no perturbation and can be used for deriving $g(^5P_2)$. The sum of these two intervals is 33.750 $\pm$0.018 A. Divided by 4, this gives 8.438 $\pm$0.005 A for the sum of the unperturbed $^5P_3$ and $^5P_2$ splittings and 8.438$-$4.014$=$ 4.424 $\pm$0.006 A for the $^5P_2$ splitting, corresponding to $g(^5P_2)=1.836\ \pm0.003$.

Similarly, the sum of the three observed intervals $(1, -1)$, $(1', -1')$, $(1'', -1'')$ must be the same as the sum of the unperturbed intervals. The sum of the observed intervals is 28.947 $\pm$0.022 A. Divided by 2, this gives 14.474 $\pm$0.011 A for the sum of the unperturbed $^5P_3$, $^5P_2$, $^5P_1$ splittings, or 14.474$-$8.438$=$6.036 $\pm$0.012 A for the $^5P_1$ splitting, corresponding to $g(^5P_1)=2.506\ \pm0.005$.

The g-values for the narrower pattern of table 6 were determined in exactly the same way but are less accurate, because the states of $^5P_2$ belonging to the blended lines are determined only roughly by the line positions and were actually placed as follows: $M=-2'$ was placed so that the average of $2, -2, 2', -2'$ coincided with the average of the no-field positions of $^5P_3$ and $^5P_2$. $M=0$ was placed

TABLE 6. *Paschen-Back pattern of* O I $2p^3\ 3p\ {}^5P \rightarrow 3s\ {}^5S$ *(7771 to 7775 A) at 34,660 gauss*

	$M \longrightarrow$		$^5S_2$ 2		1		0		−1		−2
	↓		−3.894		−1.947		0		1.947		3.894
	3	67.101	70.995(8) 70.995						$g(^5S_2) = 1.990 \pm 0.003$		
	2	68.600	72.486(12) 72.494	1.931	70.555(4) 70.547						
	1	70.156	Not obs. 74.050		72.110(12) 72.103	1.962	70.148(2) 70.156				
$^5P_3$ No-field position 71.950	0	71.784			73.728(2) 73.731	1.944	71.784(10) 71.784	1.965	69.819(1−) 69.837		
	−1	73.441					[a]73.440(7) 73.441	[1.946]	71.494(8) 71.494	[1.919]	69.575(1−−) 69.547
	−2	75.124							73.177(5) 73.177	1.947	71.230(4) 71.230
	−3	76.827	$g(^5P_3) = 1.657 \pm 0.002$								72.933(7) 72.933
	2′	70.703	74.590(15) 74.597	1.932	72.658(5) 72.650						
	1′	72.044	[b]75.930(10w) 75.938	[2.001]	[b]73.929(50) 73.991	[1.884]	[c]72.045(5w) 72.044				
$^5P_2$ No-field position 74.170	0′	73.967			[b]75.930 75.914		[b]73.929 73.967		[c]72.045 72.020		
	−1′	75.938					[b]75.930 75.938		[b]73.929 73.991		[c]72.045 72.044
	−2′	77.815	$g(^5P_2) = 1.827$						[b]75.930 75.868		[b]73.929 73.921
	1″	73.418	77.308(1) 77.307	1.949	75.359(10) 75.360	[1.919]	[a]73.440(7) 73.413				
$^5P_1$ No-field position 75.390	0″	75.760			77.785(1−) 77.707	[2.021]	75.764(7) 75.760	1.955	73.809(4) 73.813		
	−1″	78.030	$g(^5P_1) = 2.54_4$				Not obs. 78.030		76.077(4) 76.083	1.936	74.141(5) 74.136

[a]Entered twice. [b]Entered 4 times. [c]Entered 3 times.

so that the average of 0, 0′, 0″ coincided with the average no-field position of the three levels. $M=1'$ and $M=-1'$ were placed so that the average of the six states of $M=\pm 1$ coincided with the average of the no-field positions of the three levels and so that the states $M=1'$ and $M=-1'$ would give components of equal wavelength. This placement is in satisfactory agreement with observation but is undetermined to within the widths of the blends. Hence $g(^5P_2)$, derived from the ± 1 intervals, is particularly subject to error

The probable errors given for $g(^5S_2)$ and $g(^5P_3)$ in table 6 were determined in the same way as those in table 5, any error in the determination of the Lorentz unit being neglected. It will be noted that these two g-values in table 6 are smaller than those in table 5, and also smaller than the LS-values, by about 1 part in 200, which is outside of the probable errors given. In table 4 we adopt the values of table 5 from the MIT plates, because the Lorentz unit for the MIT plates is obtained from standard lines photographed simultaneously with the oxygen and nitrogen lines, whereas the NBS Lorentz unit is obtained from standard patterns photographed on the plate in a subsequent exposure. The NBS technique possibly introduces a slight error in the Lorentz unit because of slightly different field strength or different placement of the arc in the magnetic field when the standard lines are exposed.

VI. Theoretical Computation of Paschen-Back Patterns in Russell-Saunders Coupling

The method of computing theoretical Paschen-Back patterns in Russell-Saunders coupling is discussed in general terms by Condon and Shortley [12] and elsewhere. An attempt will be made here to give formulas and method, and sufficient detail on the oxygen ^5P example, to enable a spectroscopist unfamiliar with details of quantum-mechanical theory to make such computations, which are really quite straightforward. We shall plunge directly into the example of O I ^5P (7,773 A) at 85,400 gauss, giving general formulas as need for their use arises.

In the first place, it is most convenient to use as unit the normal Lorentz splitting, which gives half the width of a normal triplet. This Lorentz unit, in cm^{-1}, is 4.670×10^{-5} times H in gauss [13]. It is usually determined directly from known patterns on each exposure. The Lorentz unit in our case is experimentally determined as 2.409 A at 7,773 A. From the observed no-field wavelength differences, 2.220 A and 3.440 A measured from $^5P_3\rightarrow{}^5S_2$, we compute the no-field quintet energies in Lorentz units as $^5P_3=0$, $^5P_2=-0.922$, $^5P_1=-1.428$ L. U., placing them in the right order of energies to correspond to the erect quintet with least J-value lowest. As our starting point we compute the unperturbed pattern of states, which would obtain if there were no Paschen-Back perturbation, by adding the various values of Mg to the above energies, with $g(^5P_3)=1.667$, $g(^5P_2)=1.833$, $g(^5P_1)=2.500$. Using a superscript to denote the value of M, we find for the unperturbed energies:

$$^5P_3^3=3\times1.667=5 \text{ L. U.}$$

$$^5P_3^2=2\times1.667=3.333$$

$$^5P_3^1=1.667$$

$$^5P_3^0=0$$

$$^5P_3^{-1}=-1.667$$

$$^5P_3^{-2}=-2\times1.667=-3.333$$

$$^5P_3^{-3}=-3\times1.667=-5$$

$$^5P_2^2=-0.922+2\times1.833=2.745$$

$$^5P_2^1=-0.922+1.833=0.911$$

$$^5P_2^0=-0.922$$

$$^5P_2^{-1}=-0.922-1.833=-2.755$$

$$^5P_2^{-2}=-0.922-2\times1.833=-4.589$$

$$^5P_1^1=-1.428+2.500=1.072$$

$$^5P_1^0=-1.428$$

$$^5P_1^{-1}=-1.428-2.500=-3.928 \text{ L. U.}$$

These values, converted to angstroms by multiplication with 2.409, correspond to the broken bars on the right of figure 3.

We now need the nondiagonal matrix elements that determine the Paschen-Back interaction. These elements connect only states of the same M, the same L and S (i. e., states of the same term), and having J values differing by one unit. In Lorentz units, the interaction element connecting

*Entered twice. **Entered 4 times. ***Entered 3 times.

the state $SLJM$ and the state $SL,J-1$, M is

$$\sqrt{\frac{(J-L+S)(J+L-S)(J+L+S+1)(L+S+1-J)}{4J^2(2J-1)(2J+1)}}\sqrt{J^2-M^2}, \quad (1)$$

and is always positive. Substitution in this formula of $S=2$, $L=1$, $J=3$ gives the interaction elements connecting $^5P_3$ and $^5P_2$:

$M=+2, M=-2$: $\sqrt{2/3}=0.471$ L. U.

$M=+1, M=-1$: $4/3\sqrt{5}=0.596$ L. U.

$M=0$: $\sqrt{2/5}=0.632$ L. U.

Substitution of $S=2$, $L=1$, $J=2$ gives the elements connecting $^5P_2$ and $^5P_1$:

$M=+1, M=-1$: $3/2\sqrt{5}=0.671$ L. U.

$M=0$ $\sqrt{3/5}=0.775$ L. U.

Having computed the unperturbed states and the interaction elements, we proceed with the computation of the perturbed states as follows:

When there is just one state of given M, such as $M=\pm 3$, there is no perturbation, and the above unperturbed energies, converted to A, are entered in italics on the left of table 5 with sign changed.

When there are two states of the same M, such as $M=2$, let A and B be the upper and lower of the two unperturbed energy values ($A=3.333$ for $^5P_2^2$, $B=2.745$ for $^5P_2^2$ in our case); let C be the interaction element ($C=0.471$ from above). Then the energies of the perturbed states are given by the general formula

$$\tfrac{1}{2}A+\tfrac{1}{2}B\pm\sqrt{(\tfrac{1}{2}A-\tfrac{1}{2}B)^2+C^2}. \quad (2)$$

The higher of these two values goes with the state associated with the higher of the no-field states (nonerossing rule discussed below). Thus, in our case, with the notation of table 5 and figures 3 and 4, the perturbed energies for $M=2$ are

$$\left.\begin{matrix}2\\2'\end{matrix}\right\}=3.039\ \pm 0.555=\begin{cases}3.\ 594\text{ L. U.}=8.658\text{ A}\\2.\ 484\text{ L. U.}=5.984\text{ A}\end{cases} \quad (3)$$

which are the values entered (with sign change) in italics at the left of table 5, and which correspond to the observed energies of figures 3 and 4.

When there are three or more states of the same M, the calculation is more complicated. As an illustration take the case of $M=1$. Write down the matrix

$^5P_3^1$	1.667	0.596	0
$^5P_2^1$	0.596	0.911	0.671
$^5P_1^1$		0.671	1.072

(4)

in which the unperturbed energies are entered along the diagonal, the interaction elements each twice in the appropriate spaces.

From this, form the determinantal equation (the secular equation)

$$\begin{vmatrix}1.667-\lambda & 0.596 & 0\\ 0.596 & 0.911-\lambda & 0.671\\ 0 & 0.671 & 1.072-\lambda\end{vmatrix}=0. \quad (5)$$

When the determinant is expanded this equation becomes

$$-\lambda^3+3.650\lambda^2-3.477\lambda+0.497=0. \quad (6)$$

The three roots of this equation are the energies of the three perturbed states. In order of decreasing energy these should be designated as 1, 1′, 1″, associated with $^5P_3$, $^5P_2$, $^5P_1$, respectively. This association should be made in the same order as the no-field energies, not necessarily the order of the unperturbed energies. In this case, as the field is increased from 0 to 85,400 gausses, two of the unperturbed states of $M=1$ cross as shown in figure 4, so that they are no longer in the order of no-field energies; but if the perturbed energies were computed as a function of field strength, it would be found that states of the same M would never cross (see fine lines in fig. 4), so that the order of association of the perturbed states is to be the same as the no-field order. The three roots of eq 6 give the energies in Lorentz units:

$$\left.\begin{aligned}1\ &=2.121\text{ L. U.}=5.109\text{A},\\ 1'\ &=1.356\text{ L. U.}=3.267\text{A},\\ 1''&=0.172\text{ L. U.}=0.414\text{A}.\end{aligned}\right\} \quad (7)$$

These states are entered in table 5 with reversed sign, and correspond to the observed values of

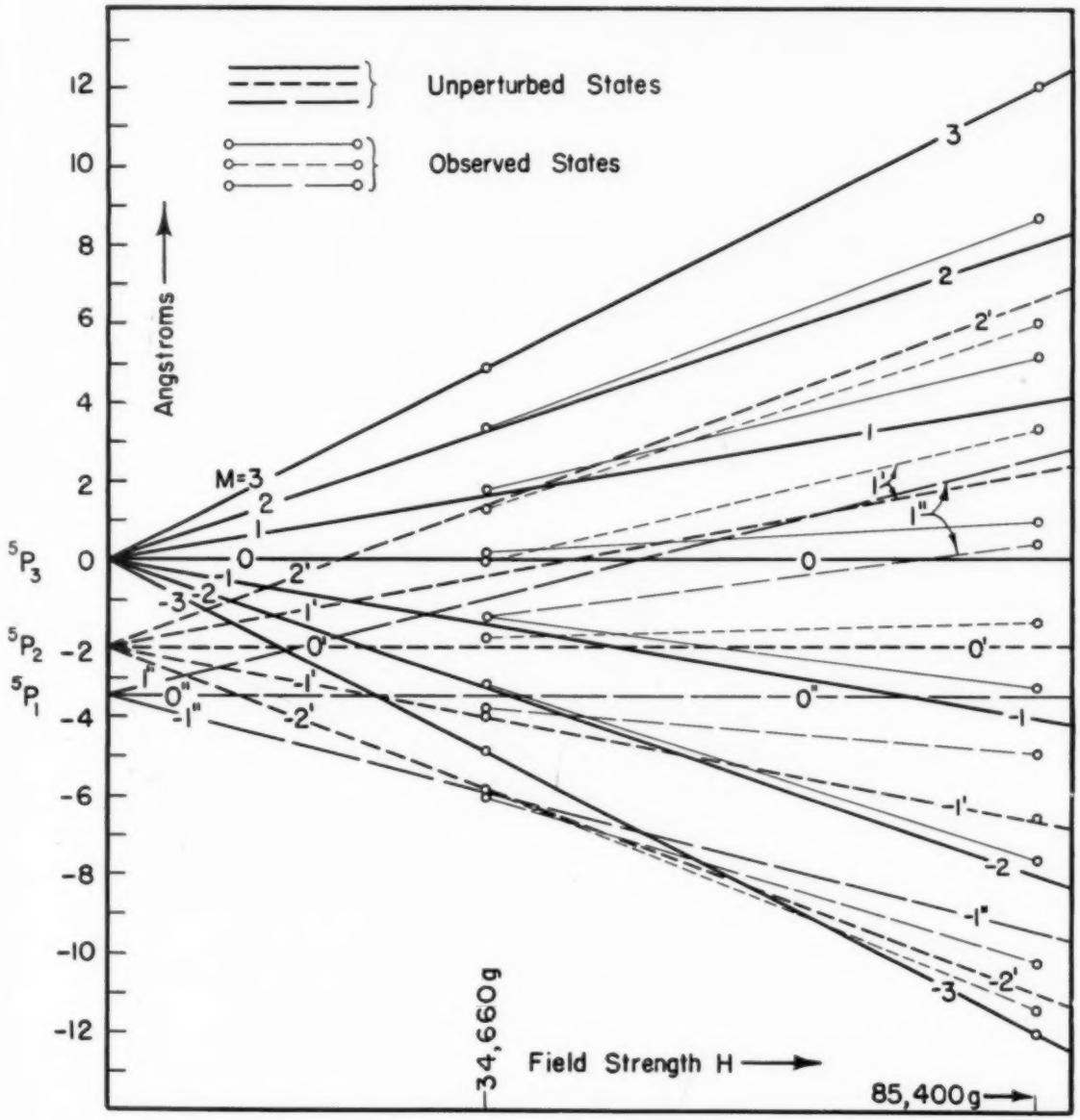

FIGURE 4.—*Zeeman effect of the* O I $2p^3\,3p\,{}^5P$ *to* m.

This figure shows (heavy lines) the positions the states would occupy if there were no Paschen-Back perturbation and illustrates, by the light lines connecting two observed points, the growth of the Paschen-Back perturbation with field-strength. Intermediate between the observed points, the actual state positions would, of course, lie on curved lines rather than on the straight lines drawn here. Because the g-values of the levels increase in going from $^5P_3$ to $^5P_2$ to $^5P_1$, the unperturbed states of the same positive M-value lie closer than those of the corresponding negative M-value and are more strongly perturbed. The crossing of the unperturbed states of $M=1$ and the noncrossing of the perturbed states is schematically illustrated.

819237—49——8

figures 3 and 4. The states for $M=0$ and -1 are obtained by exactly similar computations. The equation corresponding to eq 6 for $M=0$ is

$$-\lambda^3-2.350\lambda^2-0.317\lambda+0.570=0,$$

and that for $M=-1$ is

$$-\lambda^3-8.350\lambda^2-21.157\lambda-15.895=0.$$

The same procedure as that above will permit the computation of the Paschen-Back pattern of any term in *LS*-coupling.

VII. Theoretical Computation of Line Strengths in Paschen-Back Patterns in *LS*-Coupling

In quantum mechanics the strength of a line is defined [12, p. 98] as a quantity that must be multiplied by the fourth power of the frequency and by the number of atoms in any one of the initial states in order to obtain the radiated energy. Since all of the lines of our Paschen-Back pattern have closely the same frequency, we can compare relative strengths directly with observed

TABLE 7.—*Relative values of* $S^{1/2}$ *for components of an unperturbed* $^3P \rightarrow {}^3S$ *multiplet in transverse observation*

		$^3S_2$				
	$M \rightarrow$ / $\downarrow$	2	1	0	−1	−2
	3	$-\sqrt{120}=-10.95$				
	2	$\sqrt{80}=8.94$	$-\sqrt{80}=-8.94$			
	1	$\sqrt{8}=2.83$	$\sqrt{128}=11.31$	$-\sqrt{48}=-6.93$		
$^3P_2$	0		$\sqrt{24}=4.90$	$\sqrt{144}=12.00$	$-\sqrt{24}=-4.90$	
	−1			$\sqrt{48}=6.93$	$\sqrt{128}=11.31$	$-\sqrt{8}=-2.83$
	−2				$\sqrt{80}=8.94$	$\sqrt{80}=8.94$
	−3					$\sqrt{120}=10.95$
	2′	$\sqrt{160}=12.65$	$\sqrt{40}=6.32$			
	1′	$\sqrt{40}=6.32$	$\sqrt{40}=6.32$	$\sqrt{60}=7.75$		
$^3P_2$	0′		$\sqrt{60}=7.75$	0	$\sqrt{60}=7.75$	
	−1′			$\sqrt{60}=7.75$	$-\sqrt{40}=-6.32$	$\sqrt{40}=6.32$
	−2′				$\sqrt{40}=6.32$	$-\sqrt{160}=-12.65$
	1″	$\sqrt{72}=8.49$	$-\sqrt{72}=-8.49$	$-\sqrt{12}=-3.46$		
$^3P_1$	0		$\sqrt{36}=6.00$	$-\sqrt{96}=-9.80$	$-\sqrt{36}=-6.00$	
	−1″			$\sqrt{12}=3.46$	$-\sqrt{72}=-8.49$	$-\sqrt{72}=-8.49$

relative intensities under the assumption that all the close-lying upper states have the same excitation. The strength of a multiplet is defined as the sum of the strengths of its lines, and the strength of a line as the sum of the strengths of its components.

In making a transformation from one type of coupling to another, such as the transformation from the unperturbed states to the perturbed states in a Paschen-Back pattern (the perturbation mixes up states of different J), we must work not with the strength itself but with its square root, which we denote by $S^{1/2}$. This turns out to be quite convenient in our case, because visual intensity estimates give numbers that are actually close to the square roots of the relative strengths. It is to be noted that $S^{1/2}$ is a signed quantity and that it is very important to use the proper sign.

We need first the relative $S^{1/2}$ for the lines of a multiplet in LS-coupling. These are obtained by taking the square roots of the strengths as given by the familiar Kronig, Sommerfeld-Hönl, Russell formulas [12, p. 238], with the sign given below:

Sign of $S^{1/2}$ $(S, L, J;\quad S, L+\Delta L, J+\Delta J)$:

$$\Delta L=0,\quad \Delta J=0\begin{cases}+ \text{ if } S(S+1)<L(L+1)+J(J+1)\\ - \text{ if } S(S+1)>L(L+1)+J(J+1)\end{cases}$$

$$\Delta L=0,\quad \Delta J=\pm 1\ (-)$$

$$\Delta L=\pm 1,\ \Delta J=0\ (+) \tag{8}$$

$$\Delta L=\pm 1,\ \Delta J=\pm 1\ (+)$$

$$\Delta L=\pm 1,\ \Delta J=\mp 1\ (-)$$

In our case of ${}^5P_{3,2,1}\rightarrow{}^5S_2$, the strengths are in the ratio 7:5:3, and from the above sign rule we obtain the relative values

$$S^{1/2}({}^5P_3, {}^5S_2)=+\sqrt{7};\quad S^{1/2}({}^5P_2, {}^5S_2)=+\sqrt{5};$$

$$S^{1/2}({}^5P_1, {}^5S_2)=-\sqrt{3}. \tag{9}$$

We now need the formulas for the strengths of the unperturbed Zeeman components of a line in terms of the whole line strength, which is denoted by $S(J,J+\Delta J)$ in the formulas below, since these formulas are good for any line whether the coupling is Russell-Saunders or not. Per unit solid angle at angle θ $(0\leqq\theta\leqq\pi)$ with the magnetic field, these strengths are

$$\left.\begin{aligned}
S_\theta^{1/2}(J,M;J+1,M)&=2S^{1/2}(J,J+1)\sqrt{\frac{3}{32\pi}\frac{(J+1)^2-M^2}{(J+1)(2J+1)(2J+3)}}\sin\theta\\
S_\theta^{1/2}(J,M;J+1,M\pm1)&=\mp S^{1/2}(J,J+1)\sqrt{\frac{3}{32\pi}\frac{(J\pm M+1)(J\pm M+2)}{(J+1)(2J+1)(2J+3)}}\sqrt{1+\cos^2\theta}\\
S_\theta^{1/2}(J,M;J,M)&=2MS^{1/2}(J,J)\sqrt{\frac{3}{32\pi}\frac{1}{J(J+1)(2J+1)}}\sin\theta\\
S_\theta^{1/2}(J,M;J,M\pm1)&=S^{1/2}(J,J)\sqrt{\frac{3}{32\pi}\frac{(J\mp M)(J\pm M+1)}{J(J+1)(2J+1)}}\sqrt{1+\cos^2\theta}\\
S_\theta^{1/2}(J,M;J-1,M)&=2S^{1/2}(J,J-1)\sqrt{\frac{3}{32\pi}\frac{J^2-M^2}{J(2J-1)(2J+1)}}\sin\theta\\
S_\theta^{1/2}(J,M;J-1,M\pm1)&=\pm S^{1/2}(J,J-1)\sqrt{\frac{3}{32\pi}\frac{(J\mp M)(J\mp M-1)}{J(2J-1)(2J+1)}}\sqrt{1+\cos^2\theta}
\end{aligned}\right\} \tag{10}$$

In our particular problem, observation was made at $\theta=90°$, so the angle factor occurring last in eq 10 is unity in all cases. In the following discussion, transverse observation will be assumed, and we shall omit the subscript $\theta=90°$. Direct substitution of the line strengths (eq 9), and the state quantum numbers, in eq 10, gives the values of $S^{1/2}$ in table 7 after multiplication by the factor $\sqrt{640\pi}$ in order to get numbers comparable in magnitude to the estimated intensities. It is noted that the sums of the squares of the values in each of the three boxes of table 7 are proportional to the line strengths 7:5:3.

The unperturbed strength-pattern of table 7 is seen to be radically different from the observed pattern of table 5. Some of the weakest compon-

ents of table 7, and even the missing component, are among the strongest in table 5. Some of the moderately strong components of table 7 become very weak or are missing observationally. It is these pronounced differences for which the computation of the Paschen-Back perturbation must account. Table 7 furnishes the starting point for this computation, which leads to the perturbed values of $S^{1/2}$ in italics in parentheses in table 5 (the sign of $S^{1/2}$ is no longer retained in table 5, since this sign has no observable meaning but is only needed in the computation).

Since the states of $^5S_2$ are unperturbed, we need consider only the effect of the perturbation of the states of ^5P. Values of M occurring only once in ^5P suffer no perturbation ($M=3$ and -3), so intensities of components from these states are unperturbed. The value 10.95 for $3\rightarrow 2$ and $-3\rightarrow -2$ reappears in table 5 as (*11.0*).

For an M value that appears twice, such as $M=2$, the two components to the same lower state can transfer strength from one to the other. Designating unperturbed strengths by subscript *unp* and perturbed strengths by subscript p, we have from table 7

$$S_{unp}(2\rightarrow 2)=80, \quad S_{unp}(2'\rightarrow 2)=160, \qquad (11)$$

whereas the perturbed values entered in table 5, which will be computed presently, are

$$S_p(2\rightarrow 2)=(14.0)^2=196, \quad S_p(2'\rightarrow 2)=(6.7)^2=44. \qquad (12)$$

The sum of the strengths of the two components is unchanged by the perturbation, but the weaker has become stronger and the stronger weaker. The change is not always in this direction. If we look at the components $(-2\rightarrow -2)$ and $(-2'\rightarrow -2)$, which have the same unperturbed strengths as eq 11:

$$S_{unp}(-2\rightarrow -2)=80, \quad S_{unp}(-2'\rightarrow -2)=160,$$

the perturbed values of table 5 show the stronger component still stronger, the weaker still weaker:

$$S_p(-2\rightarrow -2)=(4.4)^2=20,$$
$$S_p(-2'\rightarrow -2)=(14.8)^2=220.$$

The signs of S_{unp} and the relative location of the levels are the factors that determine which way the intensity will shift.

The general formulas for making these computations are the following:

Let A be the upper, B the lower of two unperturbed energies, as in eq 2. Let $\Delta=A-B$ be the unperturbed energy difference ($\Delta>0$). Let A_p be the upper, B_p the lower of the two perturbed energies. Let $\Delta_p=A_p-B_p$ be the perturbed energy difference ($\Delta_p>0$). Then if $S^{1/2}(A\rightarrow X)$ and $S^{1/2}(B\rightarrow X)$ denote the unperturbed values of $S^{1/2}$ from A and B to the same lower state X, the strengths of the perturbed components are given by the formulas

$$\left.\begin{aligned} S_p^{1/2}(A_p\rightarrow X)&= \sqrt{\frac{\Delta_p+\Delta}{2\Delta_p}}S^{1/2}(A\rightarrow X)+\sqrt{\frac{\Delta_p-\Delta}{2\Delta_p}}S^{1/2}(B\rightarrow X) \\ S_p^{1/2}(B_p\rightarrow X)&= \sqrt{\frac{\Delta_p+\Delta}{2\Delta_p}}S^{1/2}(B\rightarrow X)-\sqrt{\frac{\Delta_p-\Delta}{2\Delta_p}}S^{1/2}(A\rightarrow X) \end{aligned}\right\} \qquad (13)$$

In our case, for $M=2$, in order to compute eq 13, we use $A=3.333$, $B=2.745$, $\Delta=0.588$, $A_p=3.594$, $B_p=2.484$, and $\Delta_p=1.110$, all in L. U., as given by eq 3 and the discussion preceding eq 3. Here A and B represent the states 2 and 2′ of ^5P. If X represents the state $M=2$ of ^5S, we need for the right side of eq 13 the unperturbed values $S^{1/2}(2\rightarrow 2)=8.94$, $S^{1/2}(2'\rightarrow 2)=12.65$, obtained from table 7. Substituting these and the coefficients

$$\sqrt{(\Delta_p+\Delta)/2\Delta_p}=0.875, \quad \sqrt{(\Delta_p-\Delta)/2\Delta_p}=0.485,$$

on the right of eq 13 we obtain the perturbed values

$$\left.\begin{aligned} S_p^{1/2}(2\rightarrow 2)&=0.875(8.94)+0.485(12.65)=14.0 \\ S_p^{1/2}(2'\rightarrow 1)&=0.875(12.65)-0.485(8.94)=6.7 \end{aligned}\right\} \qquad (14)$$

as in eq 12. The same coefficients, 0.875 and 0.485, are used in eq 13 to obtain the perturbed strengths of components $2\rightarrow 1$ and $2'\rightarrow 1$:

$$\left.\begin{aligned} S_p^{1/2}(2\rightarrow 1)&=0.875(-8.94)+0.485(6.32)=-4.8 \\ S_p^{1/2}(2'\rightarrow 1)&=0.875(6.32)-0.485(-8.94)=9.9 \end{aligned}\right\}, \qquad (15)$$

which are entered in table 5 with sign ignored.

From the form of eq 13 we see that when $S^{1/2}(A\rightarrow X)$ and $S^{1/2}(B\rightarrow X)$ have the same sign, the strength $S^{1/2}(A\rightarrow X)$ from the upper state is increased by the perturbation. This is the case in eq 14. On the other hand, when $S^{1/2}(A\rightarrow X)$ and

$S_{½}(B\to X)$ have opposite signs, as in eq 15, the strength from the upper state is ordinarily decreased, but this is not necessarily true.

When there are three or more states of the same M value, e. g., $M=1$, the computation takes a more complex form, of which the above is a special case. As an illustration of the method, let us compute the perturbed intensities $S_p^{½}(1''\to 2)$, $S_p^{½}(1''\to 1)$, $S_p^{½}(1''\to 0)$, which are interesting because their values in table 5 differ so strikingly from the unperturbed values of table 7.

Using the elements of the determinant eq 5 as coefficients, with the value of λ corresponding to $1''(\lambda=0.172$ from eq 7), we form the set of homogeneous linear equations

$$\left.\begin{aligned}(1.667-0.172)\alpha+0.596\beta=0,\\ 0.596\alpha+(0.911-0.172)\beta+0.671\gamma=0,\\ 0.671\beta+(1.072-0.172)\gamma=0.\end{aligned}\right\} \quad (16)$$

These equations are to be solved for α, β, γ subject to the normalization condition $\alpha^2+\beta^2+\gamma^2=1$. The first equation of eq 16 gives $\alpha=-0.399\beta$; the third gives $\gamma=-0.746\beta$. Whence $\alpha^2+\beta^2+\gamma^2=(0.159+1+0.557)\beta^2=1$, so $\beta=0.763$. It does not matter whether β is called + or −, but the relative signs of α, β, γ are important. Then

$$\left.\begin{aligned}\alpha&=-0.304\\ \beta&=+0.763\\ \gamma&=-0.569\end{aligned}\right\} \quad (17)$$

The second of the above homogeneous equations has not been used and will serve as a check

From the way in which eq 16 were formed from eq 4, it is seen that α, β, γ are associated respectively with the unperturbed $^5P_2^1$, $^5P_2^1$, $^5P_1^1$, i. e., with the unperturbed states 1, 1′, 1″. Quantum-mechanically, they are the coefficients in the wave function of the perturbed state 1″ when expressed in terms of the unperturbed states 1, 1′, 1″. The perturbed value of $S_p^{½}(1''\to X)$ from the perturbed state 1″ to any one of the states X of $^5S_2$ is then given in terms of the unperturbed values

$$S_{unp}^{½}(1\to X),\ S_{unp}^{½}(1'\to X),\ S_{unp}^{½}(1''\to X)$$

by using these coefficients in the simple relation

$$S_p^{½}(1''\to X)=\alpha S_{unp}^{½}(1\to X)+\beta S_{unp}^{½}(1'\to X)+\gamma S_{unp}^{½}(1''\to X). \quad (18)$$

Thus, using the values of α, β, γ of eq 17 and the unperturbed values of $S_{unp}^{½}$ read from table 6, we obtain

$$S_p^{½}(1''\to 2)=-0.304(2.83)+0.763(6.32)-0.569(8.49)=-0.9$$

$$S_p^{½}(1''\to 1)=-0.304(11.31)+0.763(6.32)-0.569(-8.49)=6.2$$

$$S_p^{½}(1''\to 0)=-0.304(-6.93)+0.763(7.75)-0.569(-3.46)=10.0$$

as entered in table 5. These values are strikingly different from the unperturbed values 8.5, 8.5, 3.5, but in striking agreement with the observational estimates 1, 7, 10.

Two similar computations, on replacing the 0.172 in eq 16 by 1.356 and 2.121 successively (eq 7), will give the perturbed components $1'\to 2$, $1'\to 1$, $1'\to 0$, and $1\to 2$, $1\to 1$, $1\to 0$, respectively. A check is furnished by the fact that the sum of the strengths of the components that get mixed up must be unchanged by perturbation. Thus, e. g.,

$$S_p(1\to 2)+S_p(1'\to 2)+S_p(1''\to 2)=S_{unp}(1\to 2)+S_{unp}(1'\to 2)+S_{unp}(1\to 2),$$

or from tables 5 and 7:

$$(8.8)^2+(6.5)^2+(0.9)^2=(2.8)^2+(6.3)^2+(8.5)^2, \text{ or } 120=120.$$

Computations similar to the above give the strengths of components from 0, 0′, 0″ and −1, −1′, −1″.

It should be pointed out that the method of computation sketched in this section needs no alteration whatsoever, except for reversing the arrows, if the combining term (^5S in this case) happens to lie above the perturbed term rather than below, as here. The strengths in the case in which both terms have Paschen-Back perturbations would be solved in two stages as follows: Start with the table similar to table 7 enlarged, which gives unperturbed values of $S^{½}$. Then apply exactly the above procedure to introduce the perturbation into the term on the left of the table, leaving the term on the top in its unperturbed condition, to get a new table. (Remember to keep signs.) As a second stage, introduce the perturbation into the term at the top, working with the new table in which the term at the left is already perturbed, to get a final table in which

both terms are perturbed. This two-stage procedure is equivalent to multiplication of the original table, considered as a matrix, in front by one matrix and behind by another. This matrix scheme makes it easier to keep track of the arithmetic, but does not involve less or different arithmetic from that in the above procedure.

VIII. Weak Paschen-Back Interaction in N I

The g-values given for the quartet terms of N I in table 4 were obtained by a procedure similar to that sketched above for O I. Although the Paschen-Back perturbations in N I are much less than those in O I (see fig. 1), yet they must be taken into account in determining g-values from the experimental data if full accuracy in determining them is to be realized. In the case of N I, the whole group of Zeeman components arising from transitions between the upper levels $2p^2\,3p\ {}^4S^\circ_{1\frac{1}{2}}$, ${}^4P^\circ_{2\frac{1}{2}}$, ${}^4P^\circ_{1\frac{1}{2}}$, ${}^4P^\circ_{0\frac{1}{2}}$ and the lower levels $2p^2\,3s\ {}^4P_{2\frac{1}{2}}$, ${}^4P_{1\frac{1}{2}}$, ${}^4P_{0\frac{1}{2}}$ were fitted into a rectangular array from which values of the energies in the magnetic field were derived for all the upper and lower states. The array was similar to table 5 or 6 considerably enlarged. From the energy values, the g-values were computed by exactly the procedure sketched above for the oxygen quintets.

We can verify that a weak Paschen-Back interaction in LS-coupling will account for the small positional asymmetries and intensity distortions by using the so-called second-order perturbation theory [12, p. 34].

According to this approximate theory, every pair of states of the same M but differing by one unit in J push each other *apart* by an amount equal to

$$\epsilon=\frac{\text{square of interaction element (eq 1)}}{\text{distance between states}}=\frac{I^2}{\Delta}, \quad (18)$$

all quantities being expressed in the same units. The energy perturbation (eq 18) is to be applied to each of the two states, in the repulsive direction. Where there are more than two interacting states, the perturbations of each pair may be assumed to act independently. Within the accuracy of eq 18, it does not matter whether the perturbed or unperturbed distance is entered in the denominator.

With regard to $S^{\frac{1}{2}}$, if A is the upper and B the lower of two interacting states that combine with a state X either above or below, one can show from eq 13 that to the same approximation

$$S_p^{\frac{1}{2}}(A,X)=S_{unp}^{\frac{1}{2}}(A,X)+(I/\Delta)\,S^{\frac{1}{2}}(B,X) \quad (19a)$$

$$S_p^{\frac{1}{2}}(B,X)=S_{unp}^{\frac{1}{2}}(B,X)-(I/\Delta)\,S^{\frac{1}{2}}(A,X) \quad (19b)$$

where I is the interaction element (eq 1), and Δ is the distance between states. In the last term, either the perturbed or the unperturbed $S^{\frac{1}{2}}$ may be used. Where a state is perturbed by two others, the changes of $S^{\frac{1}{2}}$ are additive to this approximation.

Conspicuous among the perturbations of the N I ${}^4S\rightarrow{}^4P$ of figure 1 are the four intervals of the six strong σ-components of the center line, which should be equal in the unperturbed case. The observed[4] wavelengths, intensities, and intervals for the σ-components of this line, ${}^4S_{1\frac{1}{2}}\rightarrow{}^4P_{1\frac{1}{2}}$, are given in the following array together with (at the left) the M-values of the transition to which they correspond:

$$\left.\begin{array}{lll} (1\tfrac{1}{2}\rightarrow\ \tfrac{1}{2}) & 7437.728\ \text{A} & (5) \\ & & 0.578\ \text{A} \\ (\tfrac{1}{2}\rightarrow -\tfrac{1}{2}) & 38.306 & (6) \\ & & 0.502 \\ (-\tfrac{1}{2}\rightarrow -1\tfrac{1}{2}) & 38.808 & (4) \\ & & \\ (\tfrac{1}{2}\rightarrow\ 1\tfrac{1}{2}) & 45.907 & (5) \\ & & 0.725 \\ (-\tfrac{1}{2}\rightarrow\ \tfrac{1}{2}) & 46.632 & (6) \\ & & 0.585 \\ (-1\tfrac{1}{2}\rightarrow -\tfrac{1}{2}) & 47.217 & (4) \end{array}\right\} \quad (20)$$

We shall use the above formulas to account for the interval-perturbations and the small, but definite, intensity-distortion exhibited here. As the Lorentz unit, when expressed in angstroms, differs by only 1 percent over the spread of the whole quartet pattern, we shall not change to wave numbers but shall use a mean Lorentz unit of 2.223 A. We shall express the interaction elements (eq 1) in angstrom units and work entirely in angstroms. These interaction elements connecting the states of ${}^4P$ are

[4] The data used in this section for illustrating the approximate theory of weak Paschen-Back interaction are obtained from the one plate reproduced in figure 1. These data do not agree exactly with those given in table 2, which represent the means of measurement of three plates.

$$\left.\begin{array}{rl} M=\pm 1\frac{1}{2}: I=0.490 \text{ L.U.}=1.09\,\text{A} & \\ {}^4P_{2\frac{1}{2}}, {}^4P_{1\frac{1}{2}} \quad M=\pm\ \frac{1}{2}: I=0.600 \text{ L.U.}=1.33\,\text{A} & \\ {}^4P_{1\frac{1}{2}}, {}^4P_{\frac{1}{2}} \quad M=\pm\ \frac{1}{2}: I=0.745 \text{ L.U.}=1.66\,\text{A} & \end{array}\right\} \quad (21)$$

The distances between states of ^4P needed in the denominator of eq 18 can be obtained with sufficient accuracy by taking the wavelength differences between components coming from the same state of ^4S. These distances are

$$\left.\begin{array}{lll} & {}^4P_{2\frac{1}{2}}-{}^4P_{1\frac{1}{2}} & {}^4P_{1\frac{1}{2}}-{}^4P_{\frac{1}{2}} \\ M=1\frac{1}{2}: & \Delta=25.7\ \text{A} & \\ M=\frac{1}{2}: & 25.9 & \Delta=17.8\ \text{A} \\ M=-\frac{1}{2}: & 26.2 & 19.9 \\ M=-1\frac{1}{2}: & 26.5 & \end{array}\right\} \quad (22)$$

The quartet is erect. The state $^4P_{1\frac{1}{2}}^{1\frac{1}{2}}$ has been pushed down by $(1.09)^2/25.7=0.046$ A by $^4P_{2\frac{1}{2}}^{1\frac{1}{2}}$ lying above. Similarly $^4P_{1\frac{1}{2}}^{-1\frac{1}{2}}$ has been pushed down by $(1.09)^2/26.5=0.045$ A. The states $^4P_{1\frac{1}{2}}^{+\frac{1}{2}}$ have suffered a net upward push, because the $^4P_{\frac{1}{2}}$ states below are closer and have larger interaction elements than the $^4P_{2\frac{1}{2}}$ states above. The net shift upward of $^4P_{1\frac{1}{2}}^{\frac{1}{2}}$ is $(1.66)^2/17.8-(1.33)^2/25.9=0.087$ A. The net shift upward of $^4P_{1\frac{1}{2}}^{-1\frac{1}{2}}$ is $(1.66)^2/19.9-(1.33)^2/26.2=0.072$ A.

When these Paschen-Back perturbations are removed from the wavelengths (eq 20), we find the unperturbed wavelengths and intervals

$$\begin{array}{rrrrr} & {}^4S_{1\frac{1}{2}}\rightarrow{}^4P_{1\frac{1}{2}}\ \text{(unperturbed)} & & & \\ (1\frac{1}{2}\rightarrow & \frac{1}{2}) & 7437.728-0.087= & 7437.641 & \\ & & & & 0.593 \\ (\frac{1}{2}\rightarrow- & \frac{1}{2}) & 38.306-0.072= & 38.234 & \\ & & & & 0.619 \\ (-\frac{1}{2}\rightarrow- & 1\frac{1}{2}) & 38.808+0.045= & 38.853 & \\ & & & & \\ (\frac{1}{2}\rightarrow & 1\frac{1}{2}) & 45.907+0.046= & 45.953 & \\ & & & & 0.592 \\ (-\frac{1}{2}\rightarrow & \frac{1}{2}) & 46.632-0.087= & 46.545 & \\ & & & & 0.600 \\ (-1\frac{1}{2}\rightarrow- & \frac{1}{2}) & 47.217-0.072= & 47.145 & \end{array} \quad (23)$$

The unequal intervals of eq 20 are seen to become quite equal within observational error when the Paschen-Back perturbation is removed. The asymmetries of position of the rest of the patterns are similarly accounted for by this theory.

In an unperturbed pattern, the six components of eq 20 should have values of $S^{\frac{1}{2}}$ approximately in the ratio 5:6:5:5:6:5 (from 10), with four components of equal intensity. We attempt to account for the inequality of these four components, as well as for the intensity-asymmetries in the balance of the pattern. The observed estimated intensities, to which have been attached the proper signs for the unperturbed $S^{\frac{1}{2}}$ taken from eq 8 and eq 10, are

		${}^4S_{1\frac{1}{2}}$ $M=1\frac{1}{2}$	$M=\frac{1}{2}$	$M=-\frac{1}{2}$	$M=-1\frac{1}{2}$
	$M=2\frac{1}{2}$	−10			
	$1\frac{1}{2}$	+11	−6		
	$\frac{1}{2}$	+2	+12	−3	
${}^4P_{2\frac{1}{2}}$	$-\frac{1}{2}$		+4	+12	−1
	$-1\frac{1}{2}$			+7	+10
	$-2\frac{1}{2}$				+10
	$M=1\frac{1}{2}$	+11	+5		
	$\frac{1}{2}$	+5	+0	+6	
${}^4P_{1\frac{1}{2}}$	$-\frac{1}{2}$		+6	−2	+4
	$-1\frac{1}{2}$			+4	−12
${}^4P_{\frac{1}{2}}$	$M=\frac{1}{2}$	+6	−6½	−3	
	$-\frac{1}{2}$		+2	−6	−7

(24)

We shall compute the last (perturbation) terms of eq 19 for each of these components and subtract them from the observed values to see if we regain a symmetrical pattern. In doing so we shall use for the S^{M} of the perturbing component in the last term of eq 19 just the observed intensity estimate of this component. Thus for $^4S_{1\frac{1}{2}}^{\frac{1}{2}} \rightarrow {}^4P_{1\frac{1}{2}}^{1\frac{1}{2}}$ the perturbation is by a state lying higher, so we use eq 19b, substituting from eq 21, 22, and 24 to get

$$+5 = S_p^{\frac{1}{2}} = S_{unp}^{\frac{1}{2}} - (1.09/25.7)(-6),$$

from which $S_{unp}^{\frac{1}{2}} = 4.7$. When we consider $^4S_{1\frac{1}{2}}^{-1\frac{1}{2}} \rightarrow {}^4P_{1\frac{1}{2}}^{-\frac{1}{2}}$, which should have equal unperturbed intensity, there is perturbation both from above and below. We use the correction term given by eq 19b for perturbation by the state above and that given by eq 19a for perturbation by the state below. Thus for this component,

$$+4 = S_p^{\frac{1}{2}} = S_{unp}^{\frac{1}{2}} - (1.33/26/2)(-1) + (1.66/19.9)(-7)$$

from which $S_{unp}^{\frac{1}{2}} = 4.5$. In a similar way all the unperturbed values of S^{M} are computed, and are collected in the following table:

$^4S_{1\frac{1}{2}}$

		$M=1\frac{1}{2}$	$M=\frac{1}{2}$	$M=-\frac{1}{2}$	$M=-1\frac{1}{2}$
$^4P_{2\frac{1}{2}}$	$M=2\frac{1}{2}$	−10			
	$1\frac{1}{2}$	*10.5*	−6.2		
	$\frac{1}{2}$	1.7	*12.0*	−3.3	
	$-\frac{1}{2}$		3.7	*12.1*	−1.2
	$-1\frac{1}{2}$			6.8	*10.5*
	$-2\frac{1}{2}$				10
$^4P_{1\frac{1}{2}}$	$M=1\frac{1}{2}$	*11.5*	4.7		
	$\frac{1}{2}$	4.5	*1.3*	6.1	
	$-\frac{1}{2}$		5.9	*−0.9*	4.5
	$-1\frac{1}{2}$			4.3	*−11.6*
$^4P_{\frac{1}{2}}$	$M=\frac{1}{2}$	6.5	*−6.5*	−2.4	
	$-\frac{1}{2}$		2.5	*−6.2*	−6.7

(25)

Comparison of eq 25 with eq 24 shows that in all cases the intensity-perturbation is in the right direction and of the right order of magnitude to account for the observed asymmetries. This is a definite check on the adequacy of this theory in connection with these intensity estimates, because particular care was taken in the estimates to note which of the pair of almost symmetrical components was the stronger. In the three cases where there was no detectable difference in the strength of such a pair, the computed Paschen-Back perturbation is seen to be 0.1 or less on this scale.

IX. Summary

Spectrograms of the Zeeman patterns of the red and infrared lines of various metals show the patterns of atmospheric nitrogen and oxygen lines as well. The nitrogen multiplets result from the term combinations $3s\ ^4P-3p\ ^4D^\circ$, $3s\ ^4P-3p\ ^4P^\circ$, $3s\ ^4P-3p\ ^4S^\circ$, and $3s\ ^2P-3p\ ^2P^\circ$, while those of oxygen result from the combinations $3s\ ^5S^\circ-3p\ ^5P$ and $3s\ ^3S^\circ-3p\ ^3P$. On spectrograms made at the National Bureau of Standards, with magnetic field strengths of 35,000 gausses, and on Massachusetts Institute of

Technology spectrograms, with fields in excess of 85,000 gausses, the nitrogen and oxygen patterns exhibit various degrees of distortion, both in the positions and in the intensities of the magnetic components. The nitrogen patterns exhibit only slight distortion or none at all. With the oxygen patterns the case is different: the quintet group, at 7771 to 7775 A, shows marked distortion at two different fields and bears no resemblance to either a weak-field pattern or to a Lorentz triplet; the triplet group, at 8446 A, however, shows a nearly perfect Lorentz triplet pattern with very weak π-satellites at the normal triplet separation. The interpretation of these patterns has afforded an interesting application of quantum theory to the elucidation of the Paschen-Back effect. The g-values that we have derived for the energy levels of N I and O I are the first to be announced for neutral atoms of atomic number less than 10, neon, and are found to conform, within observational error, with those required for *LS*-coupling, despite the fact that the term intervals, except those of $3p\ ^4D^\circ$ of N I, do not conform with the Landé ratios.

We thank Professor G. R. Harrison for placing at our disposal the MIT spectrograms, on which a large share of this investigation is based.

X. References

[1] F. Paschen and E. Back, Ann. phys. [4] **39,** 897 (1912) [4] **40,** 960 (1913).
[2] C. Mihul, Ann. phys. [10] **9,** 261 (1938).
[3] J. B. Green and H. N. Maxwell, Phys. Rev. **51,** 243 (1937).
[4] G. R. Harrison and F. Bitter, Phys. Rev. **57,** 15 (1940).
[5] R. W. Wood, Nature **140,** 723 (1937).
[6] E. Back, Ann. Physik. [4] **70,** 333 (1923).
[7] W. F. Meggers and K. Burns, BS Sci. Pap. **18,** 191 (1922) S441.
[8] B. Edlén, Bergstrand's Festskrift, p. 135 (1938).
[9] W. F. Meggers, Pub. Allegheny Observatory **6,** 13 (1919).
[10] C. E. St. John, et al., Carnegie Inst. of Washington, Pub. No. 396 (1928).
[11] H. N. Russell, Proc. Nat. Acad. Sci. **11,** 322 (1925).
[12] E. U. Condon and G. Shortley, Theory of atomic spectra (Cambridge University Press, 1935).
[13] R. T. Birge, Reports on progress in physics, VIII, p. 131 (London, 1941).

WASHINGTON, March 1, 1948.